Preface

Research Center for ELectron PHoton Science (ELPH), former Laboratory for Nuclear Science (LNS) was established in 1966 attached to Faculty of Science, Tohoku University. In 1967, a large-scale 300MeV electron linac was completed, and the 300MeV linac commenced to provide the beams to not only nuclear physics but many scientific fields. In addition to the higher beam energy, the 300MeV linac had been operated at a tremendous repetition rate such as 300pps, which is still marvelous for the current linac technology trend. The 300MeV linac played an important role in a new era of nuclear physics driven by high-energy electron beam electron beam, and left a number of significant results such as a study of giant resonance in deformed nuclei via electron inelastic scattering. Furthermore a pulsed-neutron from a dense target irradiated by the high-power electron beam was developed for solid-state physics and other related science, which was conducted by the first director of the Laboratory, Dr. Motoharu Kimura. This historical 300MeV linac is no longer here (the actual maximum energy was $\sim$220MeV due to deterioration of accelerating structure shunt impedance in its closing years). Major components of the 300MeV suffered serious damages due to the Great East Japan Earthquake on March 11, 2011. Since there was no technical support for the 44-year-old linac, recovering whole function was impossible any longer. Nowadays superconducting technology has been developed for high average power electron beam, so that the high-repetition normal conducting linac seems to be left behind. This means it may take a huge budget to re-construct a 300Hz - 300MeV linac. It was very difficult task to recover the functions of 300MeV linac. Consequently we have decided to separate major functions of the linac, i.e. production of radioisotopes and beam injection into a 1.2GeV booster synchrotron. Among five 25MW-klystron modulators, two adequate modulators were recovered as main power sources for a 300Hz - 60MeV linac. Other usable components and devices in the old linac have been stocked for possible malfunctions in the near future. A beam transport line into the 1st experimental room where there is a target station for the radioisotope production was also improved by introducing a new dispersive section and a dispersion-free beam line. The memorial linac was revived as an extremely high beam power linac dedicated to the radioisotope production. Accordingly handling of the high-power beam has been greatly improved, so that the stable beam can be provided to users in a short tuning time. Meanwhile, a 1.2GeV booster synchrotron, the so-called STB-ring, was also recovered and reincarnated as a 1.3GeV booster-storage ring (BST-ring) by introducing high-performance synchrotron tracking power supplies. Furthermore the BST ring is now able to store the high beam current more than 100mA theoretically because of replacing quadrupole magnets with sextupole-quadrupole combined magnets to cure the head-tail instability. A 90MeV injector linac was newly constructed in which an originally developed thermionic RF gun was introduced for reducing the linac cost. The role of old 300MeV linac is then distributed to the high-power linac and the injector linac so that parallel operation of two linacs is indeed possible. Detail of recovering from the disaster was reported in an issue “ELPH annual report 2011-2013”.

In 2014, reform of the research building was completed. This might be very much surprising for ones who know it used to be. The building looks fine and equips a new conference hall whose seating capacity is more than 100 people. In addition, utilities in the facility, such as electricity receiving and

transforming station, monitoring system for radiation safety, reservoir pool for polluted water and etc., were fixed and mostly improved. In addition to these facts, the alteration of the 300MeV linac, a symbol in the long history of ELPH and LNS, implies an opening of new era of the Laboratory.

Four years have already passed since the big earthquake and tsunami attacked. The scars left by the tsunami were still visible in every quarter. We should not forget contribution for the local area alongside of recovering our research activity. In 2014, we have embarrassed particularly by the steep rise of electricity price. However we are going to reverse the situation and let us be substantial parts of the next generation of the Laboratory. We sincerely ask facility users and related scientific field communities for strong supports and cooperation.

Director
Hiroyuki Hama

ELPH annual report, 2014

Contents

I. Papers

(ELPH Experiment : #2623, #2640, #2655, #2694)

Current status of meson photoproduction experiments with FOREST

T. Ishikawa[1], Q. He[1], Y. Honda[1], M. Miyabe[1], N. Muramatsu[1], H. Shimizu[1], Y. Tsuchikawa[1], and H. Yamazaki[1]

[1]*Research Center for Electron Photon Science (ELPH), Tohoku University, Sendai 982-0826, Japan*

Meson photoproduction experiments with an electro-magnetic calorimeter FOREST were carried out from May 2008 to May 2010. The main purpose of the FOREST experiments was to investigate a nucleon resonance $N^*(1670)$, which is a candidate of anti-decuplet pentaquark baryons, via the $\gamma n \to \eta n$ reaction. Ten series of long term FOREST experiments were made before the 2011 Earthquake, and measured the differential and total cross sections for the $\gamma p \to \eta p$, $\gamma d \to \eta p n$, and other reactions.

The photoproduction data were acquired with two STB circulating currents of 1200 and 920 MeV. The numbers of events collected were 2.13 G, 2.26 G, and 0.24 G events for hydrogen, deuterium, and empty targets in the high energy mode, and those were 211 M, 200 M, and 24 M events in the low energy one. In this report, the statuses of the analysis on the performance of FOREST from the fiscal year 2014 are presented.

§1. Introduction

Quark nuclear physics is a research field where we study the strong interacting matter to understand its properties and interactions coming from underlying fundamental theory Quantum Chromodynamics (QCD). It is a challenge to give an answer to the internal structure of the nucleon and its excited states in terms of effective degrees of freedom. Baryon resonance spectroscopy is an important testing ground for non-perturbative QCD calculations in the low energy scale. Meson photoproduction is utilized for baryon spectroscopy complementary to πN elastic scattering. The $\gamma p \to \pi^+ n$ and $\gamma p \to \pi^0 p$ reactions are intensively investigated at the first stage. Other meson photoproduction processes have been investigated in the second stage:

1. multi-meson photoproduction selecting highly excited baryons, and
2. meson photoproduction on the neutron.

A narrow resonance observed in η photoproduction on the neutron is of great interest.

It was observed at Laboratory of Nuclear Science (the former name of ELPH) [6], GRAAL [7], and CB-ELSA [8]. The resonance would be attributed to a member of anti-decuplet pentaquark baryons with hidden strangeness since no signature corresponding to this bump has been observed so far in the proton channel. Fig. 1 shows the baryon octet and anti-decuplet penta-quark baryons. Although the N_5^0 member can be photoproduced from the neutron, photoproduction of the N_5^+ member having a U-

spin of 3/2 is forbidden because the U-spin of the proton is 1/2 and that of the photon is 0. The baryon resonances including this bump has been studied with an electro-magnetic (EM) calorimeter FOREST at ELPH, Tohoku University by using various photoproduction reactions.

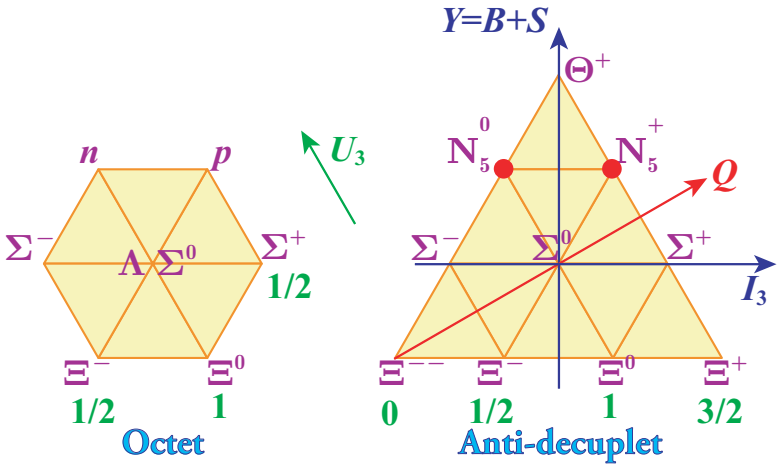

Fig.1. Octet baryons and anti-decuplet penta-quark baryons. The N_5^0 member can be photoproduced from the neutron, but photoproduction of the N_5^+ member is forbidden due to the U-spin conservation.

§2. Electromagnetic calorimeter FOREST

Meson photoproduction experiments with an electromagnetic calorimeter complex FOREST were carried out from May 2008 to May 2010 at ELPH, Tohoku University. Bremsstrahlung photons were used as a beam, being generated with a carbon fiber inserting into circulating 1200 or 920 MeV electrons in the STretcher booster (STB) ring. Each photon was tagged by detecting the corresponding post-bremsstrahlung electron inside a bending magnet of the ring. The details of the photon tagging counter STB-Tagger II are described elsewhere [9]. The energies of the tagged photon beam ranged from 740 to 1150 MeV for circulating 1200 MeV electrons, and from 580 to 880 MeV for 920 MeV ones.

Two γ rays from $\pi^0 \to \gamma\gamma$ or $\eta \to \gamma\gamma$ were detected with FOREST. The details of the design of FOREST are described elsewhere [10] and the status report of FOREST achieved in 2006–2013 can be found in Ref. [11–17]. Fig. 2 shows the schematic view of FOREST.

FOREST consists of different three EM calorimeters: the forward one 'SCISSORS III,' the central one 'LEPS Backward Gamma detector,' and the backward one 'Rafflesia II.' SCISSORS III is comprised of 192 pure CsI crystals, LEPS Backward Gamma detector is made up of 252 lead scintillating fiber modules, and Rafflesia II is composed of 62 lead glass Čerenkov counters. The energy resolution of each calorimeter is 3%, 7%, and 5% for 1 GeV photons, which was measured at the positron beamline for testing detectors at ELPH [18–22]. Plastic scintillator (PS) hodoscopes are placed in front of each calorimeter. The forward hodoscopes called 'SPIDER' consist of left and right-handed spiral-shaped PS's, and can determine the incident position of the detected particle. The central and backward hodoscopes called 'IVY ' and 'LOTUS' consist of 18 and 12 PS's, respectively.

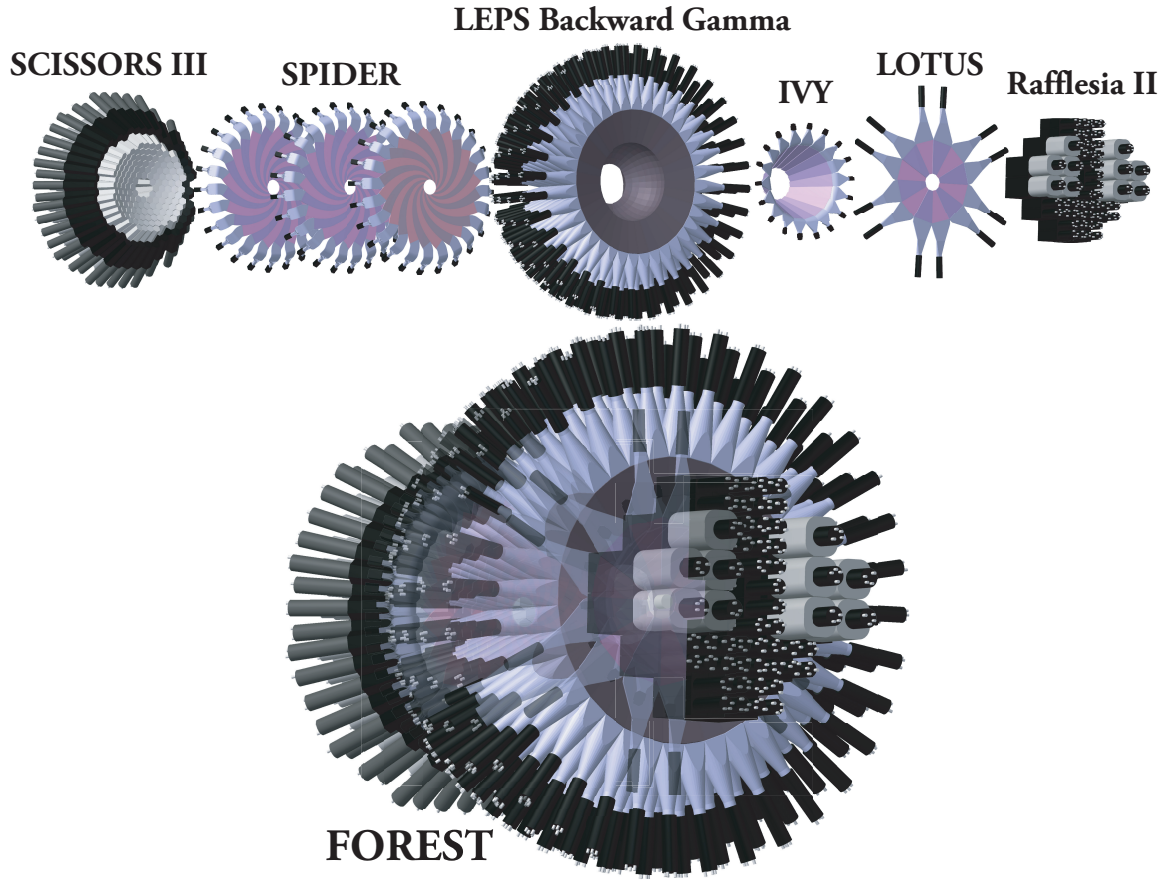

Fig.2. Schematic view of FOREST. It consists of three EM calorimeters: the forward one with 192 pure CsI crystals 'SCISSORS III,' the central one with 252 lead scintillating fiber modules 'LEPS Backward Gamma detector,' and the backward one with 62 lead glass Čerenkov counters 'Rafflesia II.' The energy resolution of each calorimeter is 3%, 7%, and 5% for 1 GeV photons. Plastic scintillator hodoscopes are placed in front of these calorimeters: SPIDER, IVY, and LOTUS. The photon beam comes from the right side.

Ten series of long term FOREST experiments were made before the 2011 Earthquake, and we call the periods 2008A–2008C, 2009A–2009E, 2010A, and 2010B. The developed FOREST cryogenic target system [23] enables us to change targets within 6 hours. The high speed data acquisition system (DAQ) FOREST-DAQ dedicated to the FOREST experiments [24] was used. The DAQ efficiency was 76% at the trigger rate of 2 kHz. The details of the FOREST experiments are described elsewhere [15]. The collected data in the FOREST experiments are summarized in Table 1 in Ref. [16]. Construction of Rafflesia II finished after the 2008A term ended, and the readout of signals from all the counters in Rafflesia II was ready from the 2008C. LOTUS was constructed just before the 2009D started. The data taking with the deuterium target started in the 2008C, and the data for both the hydrogen and deuterium targets were acquired in a term except for a short term 2009C. The circulating electron energy of the STB ring was 920 MeV for the 2009E and 2010A periods, and 1200 MeV for the other ones.

§3. Progress of the analysis in FY2014

The progress of the analysis in FY2014 is described in this section. The momentum, polar, and azimuthal angle reconstruction for the proton were updated for SPIDER and SCISSORS III [25–27]. The trigger formation probability especially for SCISSORS III was checked [28, 29]. The energy response to the proton and photon were investigated in detail [31–33]. The momentum, polar, and azimuthal angle reconstruction for the photon was also updated for Backward Gamma [30]. The geometry of the Rafflesia II in the simulation was updated [34, 35]. The knotting process (clustering of the responding plastic scintillators) was modified [36–38]. The geometries of SCISSORS III and SPIDER including the frame of SCISSORS III were also updated [39–43]. The energy response of SCISSORS III was modified [44], and the target center was also adjusted [45].

3.1 Update of the response of Lead/SciFi modules to the photon

The average number of responding Lead/SciFi modules as a function of photon energy is different between the experimental and simulation data when a photon injects onto Backward Gamma. The lateral broadening of the EM shower in Lead/SciFi was adjusted in the simulation so that the average number of responding Lead/SciFi modules in the experimental data were reproduced by the simulation. Figure 3 shows the photon energy distribution generating one and two blocks together with the probability of generating two blocks as a function of photon energy in response to a photon after the simulation code has been modified.

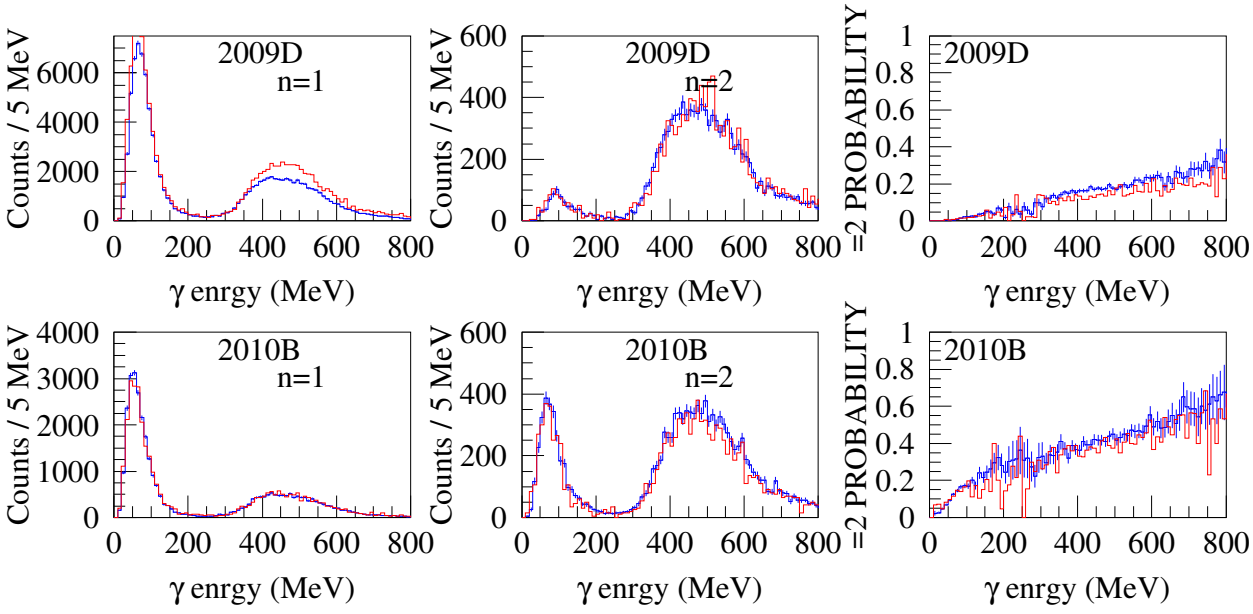

Fig.3. Photon energy distribution generating one (left) and two (right) blocks, and the probability of generating two blocks as a function of photon energy in response to a photon after the simulation code has been modified. These are estimated by using the $\gamma p \to \eta p$ events. The blue and red histograms show those for the experimental and simulation results, respectively. The upper and lower panels show the FOREST2009D and 2010B results.

3.2 Check of the trigger formation probability

The trigger logic for the data acquisition system could change more or less the acceptance for the specified reaction events. Therefore, the trigger formation probability was checked in the various points of view: effective threshold of the calorimeter modules and SCISSORS II blocks, and the responding probability of the blocks. It has been discussed in §3.1 as for the responding probability of the Backward Gamma blocks.

3.3 Update of the Rafflesia II geometry

The preliminary results for the differential cross sections of the $\gamma p \to \pi^0 p$ reaction differ between BB and BR, where BB stands for the events that both the two photons are detected with Backward Gamma, and BR shows the events that they are detected with Backward Gamma and Rafflesia II. This difference is thought to come from the discrepancy of the solid angles of Rafflesia II between the experimental and simulation data. The global z shift of Rafflesia II was adjusted so that the ratio of BR and BB events in the experimental data was reproduced by the simulation for the $\gamma p \to \pi^0 p$ reaction.

3.4 Update of the SPIDER geometry

A discrepancy between the experimental and simulation data exists in the placement of SPIDER plastic scintillators. The measured polar angles were estimated for the experimental and simulation by using the $\gamma p \to \eta p$ events. Figure 4 shows the centroid of the measured polar angle distribution for the most outer overlaps between the first and the second (third) layer of the SPIDER plastic scintillators. The measured polar angle in the simulation is always larger than that in the experimental data, and the difference seems constant.

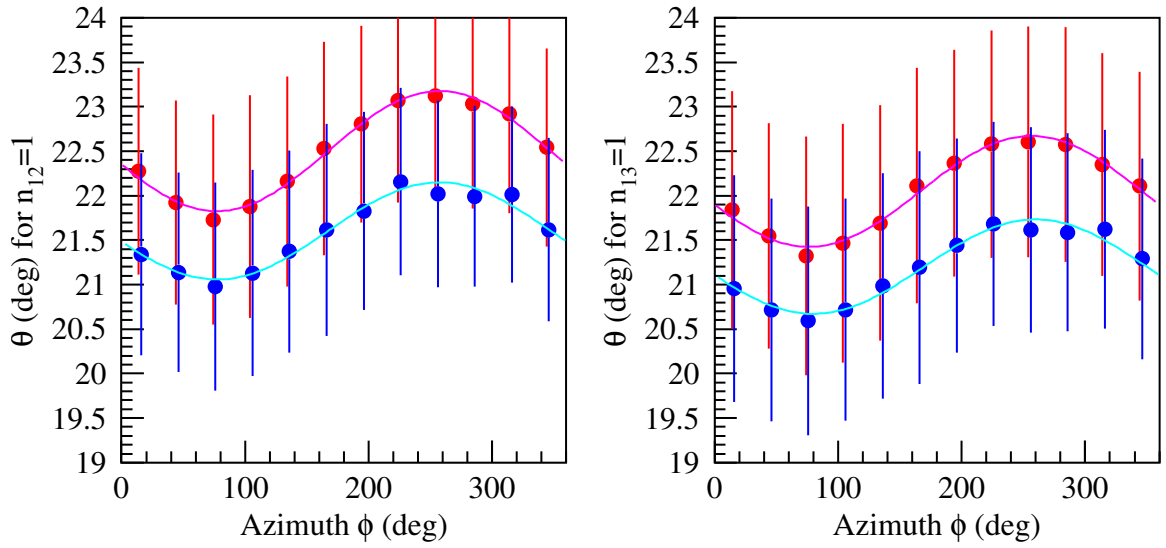

Fig.4. Centroid of the measured polar angle distribution for the most outer overlaps between the first and the second (third) layer of the SPIDER plastic scintillators. The blue and red histograms show those for the experimental and simulation results, respectively. The vertical bar shows the width (σ) of the measured polar angles.

After the modification of the placement of SPIDER plastic scintillators and the global shift of SCISSORS III in z axis, the good agreement between the experimental and simulation data was obtained. Figure 4 shows the centroid of the measured polar angle distribution for the most outer overlaps between the first and the second (third) layer of the SPIDER plastic scintillators after the simulation code was modified. The details of the analysis were described elsewhere [41].

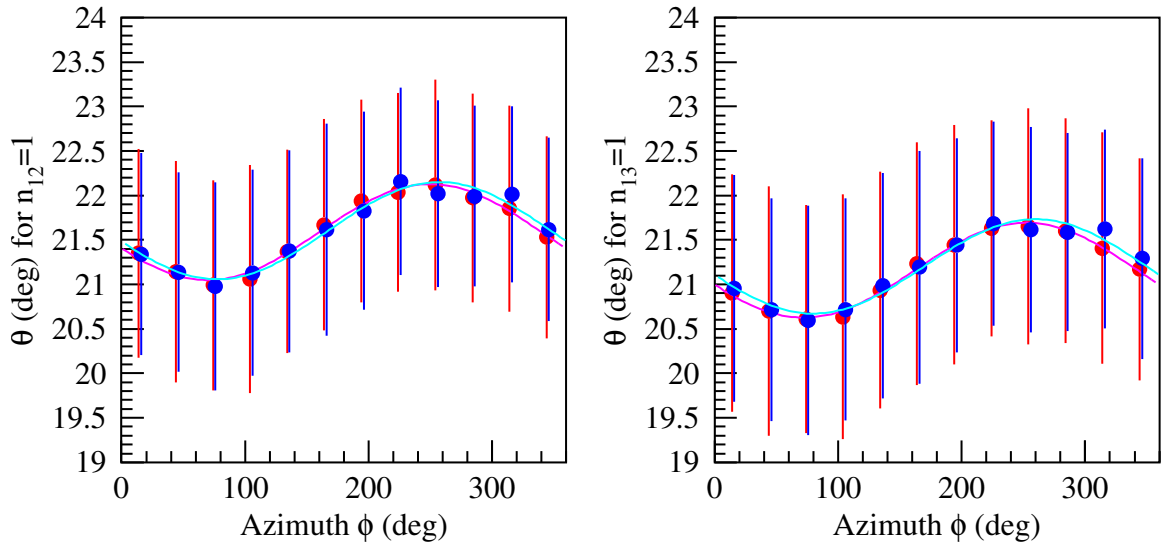

Fig.5. Centroid of the measured polar angle distribution for the most outer overlaps between the first and the second (third) layer of the SPIDER plastic scintillators after the simulation code was modified.

3.5 Update of the geometry of SCISSORS III and its frame

A discrepancy between the experimental and simulation data seemed to exist in the proton detection efficiency with SCISSORS III at large polar angles. At first the proton detection efficiency with SCISSORS III was estimated by using the $\gamma p \to \eta p$ and $\gamma p \to \pi^0 p$ events that two photons are detected with Backward Gamma and the proton is detected with SPIDER. The detection efficiency was estimated the cluster existing ratio in the selected events. Figure 6 shows the proton detection efficiency as a function of the momentum for each polar angle that is estimated by using the $\gamma p \to \eta p$ reaction, and Figure 7 shows that estimated by using the $\gamma p \to \pi^0 p$ reaction. In the $\gamma p \to \eta p$ reaction, A discrepancy between the experimental and simulation data appears in the momentum range less than 800 MeV/c in the polar angle larger than 20°. No discrepancy was observed in the $\gamma p \to \pi^0 p$ reaction since no protons with a momentum less than 800 MeV/c are detected with SPIDER.

The events are classified into four by using the azimuthal angle of the proton detection. The azimuthal angle regions are defined as 1, 2, 3, and 4 for $[0, 15°)$, $[15, 45°)$, $[45, 75°)$, and $[75, 90°)$ in the first quadrant, and the regions are defined in the other quadrant by assuming symmetry against the x and y axes. Figure 8 shows the proton detection efficiency as a function of the kinetic energy for each polar angle and each azimuthal angle that is estimated by using the $\gamma p \to \eta p$ reaction. It seems that low kinetic energy protons are likely to be blocked by some material.

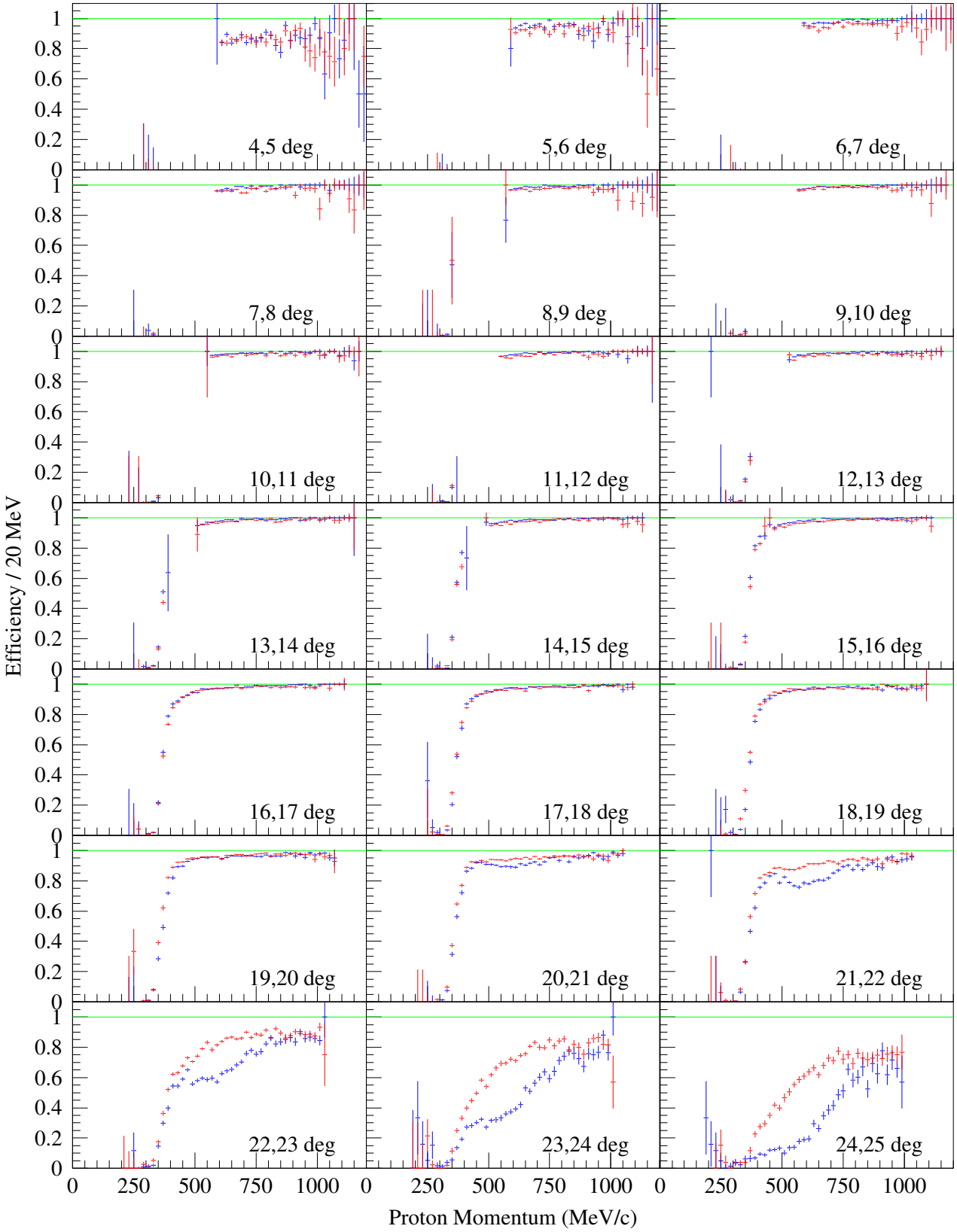

Fig.6. Proton detection efficiency as a function of the momentum for each polar angle before changing the geometry of the SCISSORS III frame, which is estimated by using the $\gamma p \to \eta p$ reaction. The blue and red histograms show those for the experimental and simulation results, respectively. The polar angle is described in each panel. A discrepancy between the experimental and simulation data appears in the polar angle larger than 20°.

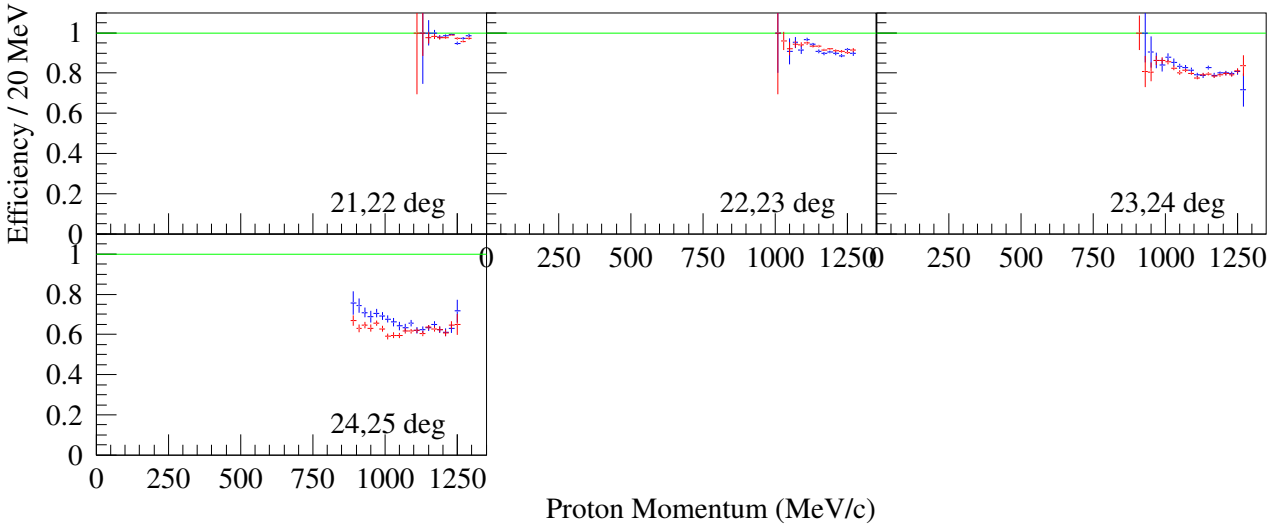

Fig.7. Proton detection efficiency as a function of the momentum for each polar angle before changing the geometry of the SCISSORS III frame, which is estimated by using the $\gamma p \to \pi^0 p$ reaction. The blue and red histograms show those for the experimental and simulation results, respectively. The polar angle is described in each panel. A discrepancy between the experimental and simulation data appears in the polar angle larger than 20°.

The implementation of the SCISSORS III frame made of the iron in the simulation was not realistic so far. This came from the unrealistic placement of the INS CsI crystals (most outer crystals in SCISSORS III). Therefore, the placement of all the CsI crystals was adjusted by changing the coordinates a little bit, and the geometry of the iron frame was changed to be realistic. Figure 9 shows the SCISSORS III frame. No overlap between the iron frame and SCISSORS III crystals was found.

The proton detection efficiency for the simulation data was re-estimated by using the modified code with a new geometries. Figure 10 shows the proton detection efficiency as a function of the momentum for each polar angle and each azimuthal angle after changing the geometry of the SCISSORS III frame that is estimated by using the $\gamma p \to \eta p$ reaction. The discrepancy between the experimental and simulation data disappears. The z coordinate of SCISSORS III was also adjusted again so that the position of the proton determined by SCISSORS III and that determined by the overlap of SPIDER scintillators agreed. The details of the analysis were described elsewhere [26, 27].

3.6 Modification of the knotting process

We call a cluster of the responding plastic scintillators in hodoscopes as a knot The knotting process is modified to incorporate the following together with bug fixes:

1. a charged particle penetrate both the IVY plastic scintillator and CsI crystal,
2. a charged particle penetrate both the IVY and SPIDER plastic scintillators, and
3. a charged particle only penetrate a plastic scintillator in SPIDER (the largest polar angle).

The details of the consideration were found elsewhere [36–38].

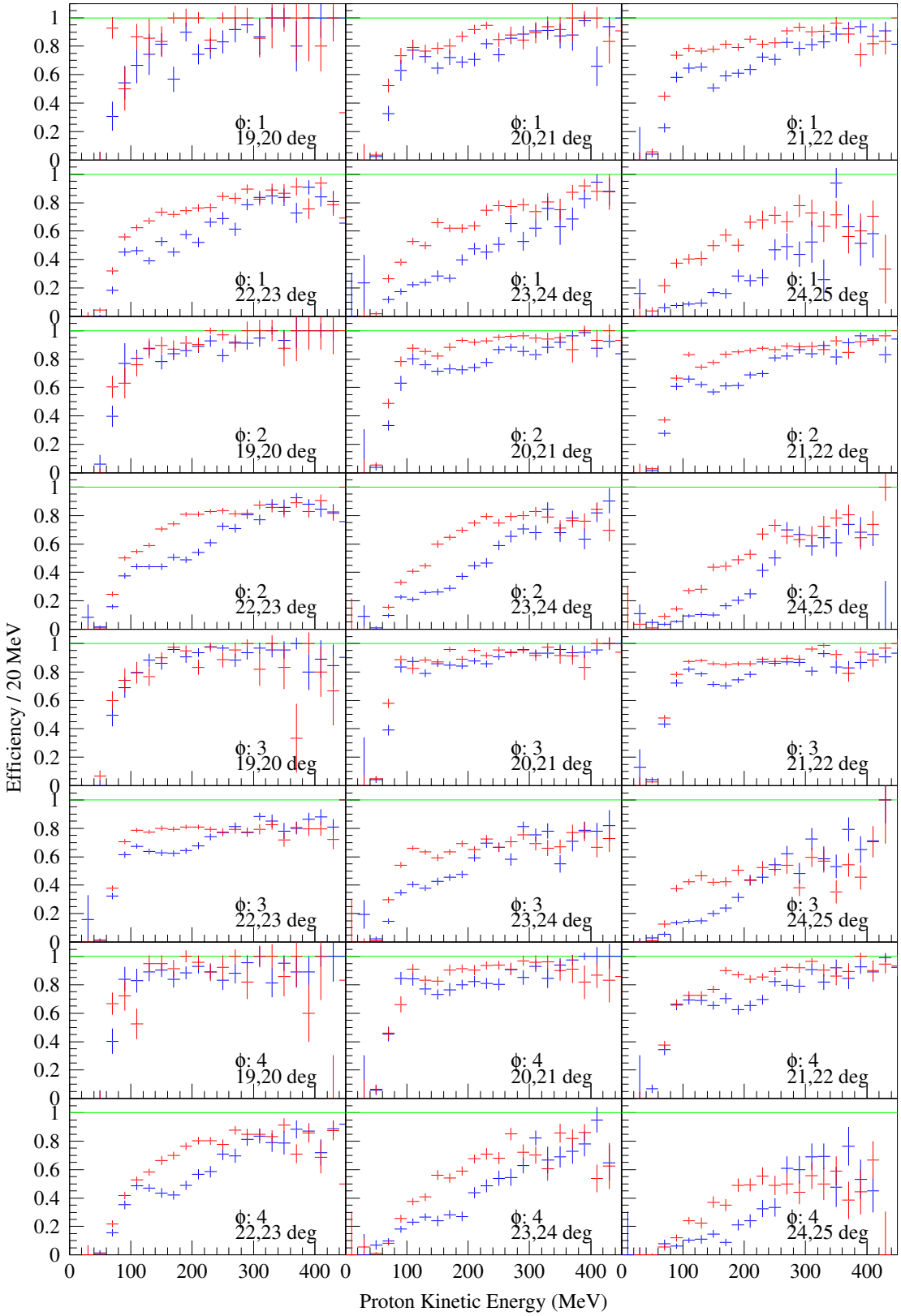

Fig.8. Proton detection efficiency as a function of the momentum for each polar angle and each azimuthal angle before changing the geometry of the SCISSORS III frame, which is estimated by using the $\gamma p \to \eta p$ reaction. The blue and red histograms show those for the experimental and simulation results, respectively. The polar angle is described in each panel. The discrepancy between the experimental and simulation data appears in the polar angle larger than 20°.

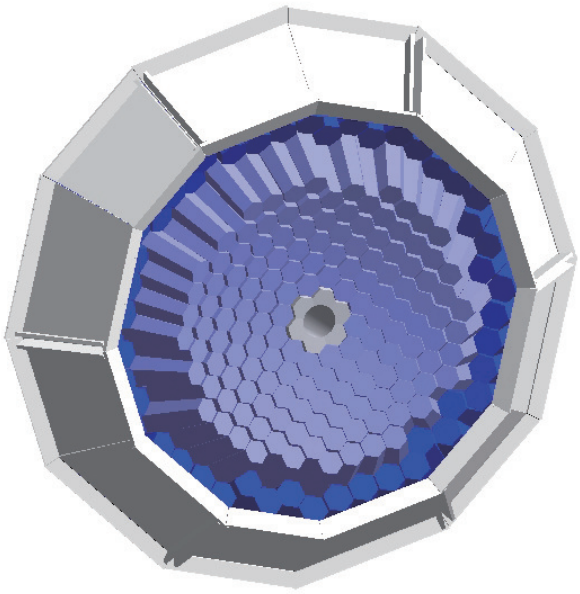

Fig.9. SCISSORS III frame. No overlap between the iron frame and SCISSORS III crystals is found.

3.7 Update of the determination of the proton kinematic variables

The determination of the proton kinematic variables (momentum, polar, and azimuthal angles) was updated for SPIDER and SCISSORS III [25–27]. The difference of the parameters between the experimental and simulation data became smaller.

3.8 Update of the energy response of CsI crystals to the proton

The measured energy distribution for each proton kinetic energy is different between the experimental and simulation data, which causes a wrong estimation of the proton detection efficiency in the experimental data. Therefore, the light output determination from the energy deposit was modified so that the measured energy distribution in the simulation reproduced that for the experimental data. Figure 11 shows the measured energy distribution for each 20 MeV kinetic energy bin in response to the proton after the simulation code has been modified. The measured energy distributions in the experimental data are well reproduced by the simulation The details of the consideration were found elsewhere [44].

§4. Summary

Ten series of meson photoproduction experiments with FOREST was carried out in 2008–2010. The main purpose of the FOREST experiments is to study a nucleon resonance $N^*(1670)$, which is a candidate of antidecuplet pentaquark baryons via η photoproduction on the neutron. The energy and timing calibrations of all the detectors have been finished. The software alignment of SPIDER, SCISSORS III, and Rafflesia II has been adjusted again. The estimation of the nucleon detection efficiency has been completed. The precise determination of the time of flight for the nucleon has also been updated. Now,

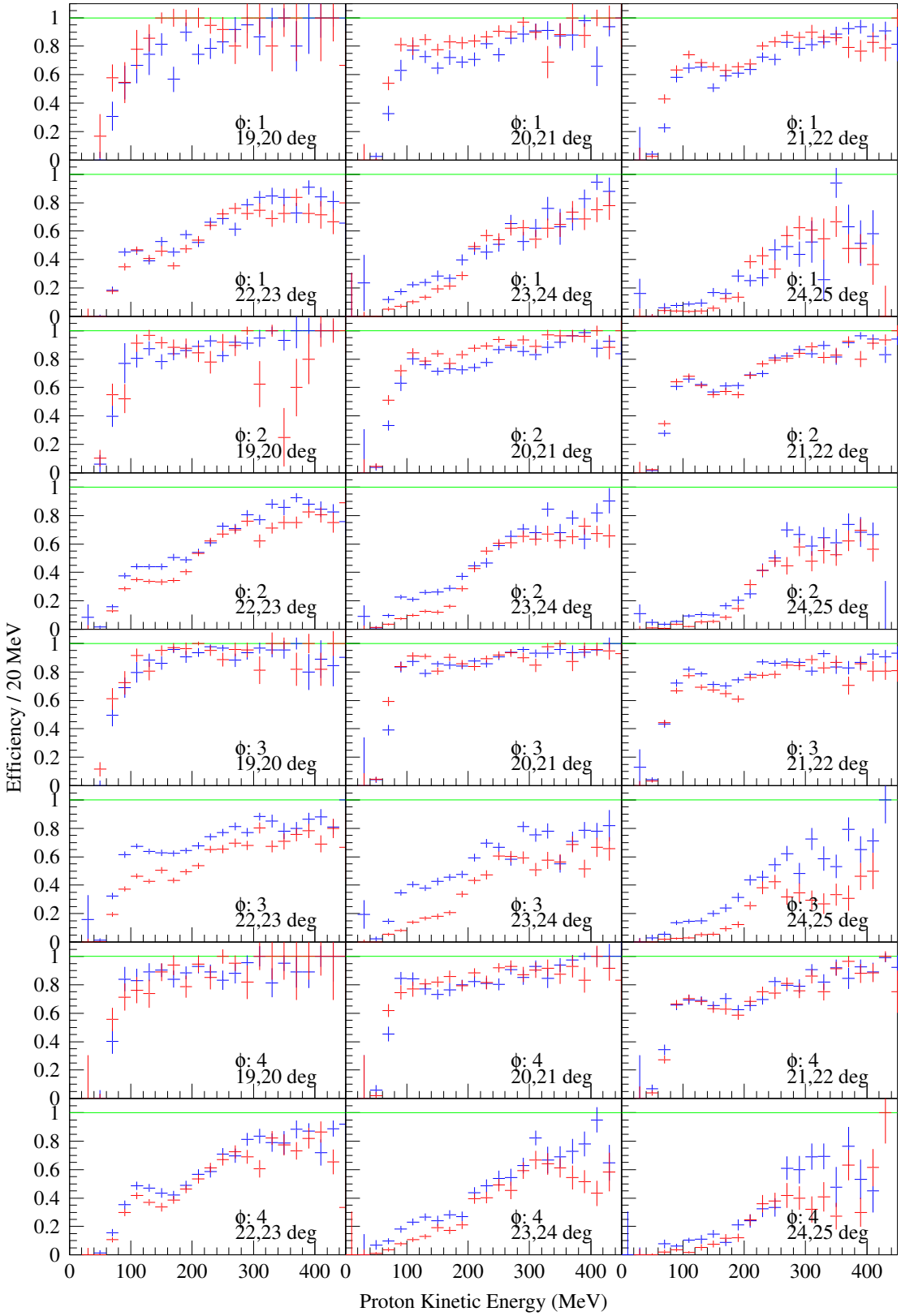

Fig.10. Proton detection efficiency as a function of the momentum for each polar angle and each azimuthal angle after changing the geometry of the SCISSORS III frame, which is estimated by using the $\gamma p \to \eta p$ reaction. The blue and red histograms show those for the experimental and simulation results, respectively. The polar angle is described in each panel. The discrepancy between the experimental and simulation data disappears.

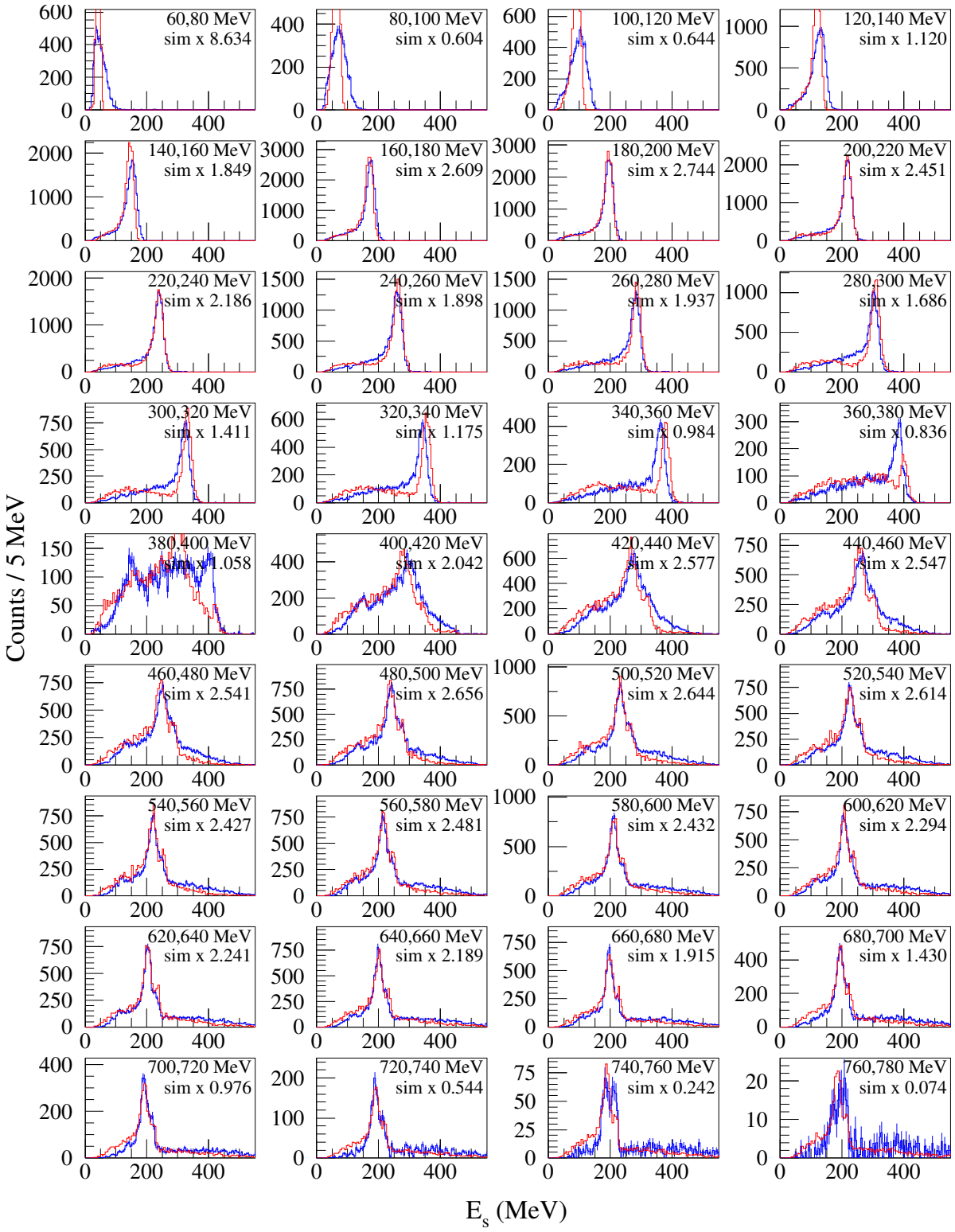

Fig.11. Measured energy distribution for each 20 MeV kinetic energy bin in response to the proton after the simulation code has been modified. The blue and red histograms show those for the experimental and simulation results, respectively.

we are working on the slight difference between the experimental and simulation data to finalize the FOREST data.

Acknowledgment

This work was supported in part by Grants-in-Aid for Scientific Research (B) (17340063), for Specially promoted Research (19002003), for Scientific Research (A) (24244022), and for Scientific Research (C) (26400287).

References

[1] S. Capstick and N. Isgur: Phys. Rev. D **34**, 2809 (1986);
S. Capstick and W. Roberts: Phys. Rev. D **47**, 1994 (1993);
S. Capstick and W. Roberts: Phys. Rev. D **58**, 074011 (1998);
S. Capstick and W. Roberts: Prog. Part. Phys. **45**, S241 (2000);
K. Nakamura *et al*. (Particle Data Group): J. Phys. G **37**, 075021 (2010).

[2] D. Jido, E. Oset, A. Ramos, and U.G. Meißner, Nucl. Phys. A **725**, 181 (2003).

[3] B.S. Zou, Nucl. Phys. A **790**, 110c (2007).

[4] T. Nakano *et al.*, Phys. Rev. C **79**, 025210 (2009), and references therein.

[5] M. Kaliner and H.J. Lipkin, Phys. Lett. B **575**, 249 (2003);
R.L. Jaffe and F. Wilczek, Phys. Rev. Lett. **91**, 232003 (2003).

[6] F. Miyahara *et al.*: Prog. Theor. Phys. Suppl. **168**, 90-96 (2007); H. Shimizu: talk at NSTAR2007.

[7] V. Kuznetsov *et al.*: Phys. Lett. B **647**, 23 (2007).

[8] I. Jaegle *et al.*: Phys. Rev. Lett. **100**, 252002 (2008).

[9] T. Ishikawa *et al.*: Nucl. Instr. and Meth. A **622**, 1 (2010).

[10] T. Ishikawa: Internal GeV-γ Analysis Note No. **130**$\mathcal{A}$ (2009).

[11] T. Ishikawa *et al.*, Research Report of LNS **39**, Tohoku University, 35 (2007).

[12] T. Ishikawa *et al.*, Research Report of LNS **40**, Tohoku University, 23 (2008).

[13] T. Ishikawa *et al.*, Research Report of LNS **40**, Tohoku University, 19 (2008).

[14] T. Ishikawa *et al.*, Research Report of LNS **41**, Tohoku University, 7 (2009).

[15] T. Ishikawa *et al.*: Research Report of LNS **42&43**, Tohoku University, 1 (2011).

[16] T. Ishikawa *et al.*: ELPH Annual Report **1**, Tohoku University, 1 (2012).

[17] T. Ishikawa *et al.*: ELPH Annual Report **2–4**, Tohoku University, 43 (2014).

[18] A. Nakamura, T. Ishikawa *et al.*: Research Report of LNS **42&43**, Tohoku University, 75 (2011).

[19] H. Sugai, T. Ishikawa *et al.*: Research Report of LNS **42&43**, Tohoku University, 88 (2011).

[20] K. Mochizuki, T. Ishikawa *et al.*: Research Report of LNS **40**, Tohoku University, 15 (2008).

[21] M. Sato, T. Ishikawa *et al.*: Research Report of LNS **41**, Tohoku University, 22 (2009).

[22] T. Ishikawa *et al.*: Research Report of LNS **42&43**, Tohoku University, 82 (2011).

[23] R. Hashimoto *et al.*: Research Report of LNS **41**, Tohoku University, 31 (2009).

[24] H. Fujimura *et al.*: Research Report of LNS **41**, Tohoku University, 26 (2009).
[25] T. Ishikawa: Internal GeV-γ Analysis Note No. **353**$\mathcal{F}$ (2014).
[26] T. Ishikawa: Internal GeV-γ Analysis Note No. **363**$\mathcal{F}$ (2014).
[27] T. Ishikawa: Internal GeV-γ Analysis Note No. **364**$\mathcal{F}$ (2014).
[28] T. Ishikawa: Internal GeV-γ Analysis Note No. **354**$\mathcal{F}$ (2014).
[29] T. Ishikawa: Internal GeV-γ Analysis Note No. **355**$\mathcal{F}$ (2014).
[30] T. Ishikawa: Internal GeV-γ Analysis Note No. **365**$\mathcal{F}$ (2014).
[31] T. Ishikawa: Internal GeV-γ Analysis Note No. **357**$\mathcal{F}$ (2014).
[32] T. Ishikawa: Internal GeV-γ Analysis Note No. **358**$\mathcal{F}$ (2014).
[33] Y. Tsuchikawa and T. Ishikawa: Internal GeV-γ Analysis Note No. **369**$\mathcal{F}$ (2014).
[34] T. Ishikawa: Internal GeV-γ Analysis Note No. **360**$\mathcal{F}$ (2014).
[35] T. Ishikawa: Internal GeV-γ Analysis Note No. **362**$\mathcal{F}$ (2014).
[36] Y. Tsuchikawa and T. Ishikawa: Internal GeV-γ Analysis Note No. **367**$\mathcal{F}$ (2014).
[37] Y. Tsuchikawa and T. Ishikawa: Internal GeV-γ Analysis Note No. **368**$\mathcal{F}$ (2014).
[38] Y. Tsuchikawa and T. Ishikawa: Internal GeV-γ Analysis Note No. **370**$\mathcal{F}$ (2014).
[39] T. Ishikawa: Internal GeV-γ Analysis Note No. **366**$\mathcal{F}$ (2014).
[40] T. Ishikawa: Internal GeV-γ Analysis Note No. **373**$\mathcal{F}$ (2015).
[41] T. Ishikawa: Internal GeV-γ Analysis Note No. **374**$\mathcal{F}$ (2015).
[42] T. Ishikawa: Internal GeV-γ Analysis Note No. **375**$\mathcal{F}$ (2015).
[43] M. Miyabe and T. Ishikawa: Internal GeV-γ Analysis Note No. **376**$\mathcal{F}$ (2015).
[44] T. Ishikawa: Internal GeV-γ Analysis Note No. **361**$\mathcal{F}$ (2014).
[45] T. Ishikawa: Internal GeV-γ Analysis Note No. **372**$\mathcal{F}$ (2015).

(ELPH Experiment : #2623, #2640, #2655, #2694)

$K^0\Lambda$ photoproduction studied with FOREST

Y. Tsuchikawa[1], R. Hashimoto[2], Q. He[1], T. Ishikawa[1], S. Masumoto[3], M. Miyabe[1], N. Muramatsu[1], H. Shimizu[1], Y. Tajima[2], H. Yamazaki[1], R. Yamazaki[1], and the FOREST collaboration

[1]*Research Center for Electron Photon Science, Tohoku University, Sendai, 982-0826, Japan*
[2]*Department of Physics, Yamagata University, Yamagata 990-8560, Japan*
[3]*Department of Physics, University of Tokyo, Tokyo 113-0033, Japan*

The photoproduction reaction $\gamma n \to K^0\Lambda$ has been studied with a 4 π electromagnetic calorimeter complex FOREST at Research Center for Electron Photon Science (ELPH), Sendai, Japan. The K^0 signals were clearly observed via its neutral decay mode: $K^0_S \to \pi^0\pi^0 \to \gamma\gamma\gamma\gamma$ with incident photon energy ranging from the reaction threshold to 1.15 GeV. We report the current status for the $\gamma d \to K^0\Lambda p$ photoproduction.

§1. Introduction

Baryon resonances have been experimentally studied by means of meson production reactions to understand low-energy scale quantum-chromo dynamics. Photoproduction is one of the useful tools to reveal the properties of excited baryons. Indeed, they have been intensively investigated via π, η, and multi-π photoproduction reactions. The K photoproduction reactions, which particularly include charged particles such as K^+, also have been well-studied nowadays. However, on the other hand, neutral kaon and neutral hyperon photoprodution reactions have not been studied enough, so that experimental studies are required to confirm some theoretical works. Moreover, $K^0\Lambda$ photoproduction may have the sensitivity to the prominent peak structure observed in the $\gamma n \to \eta n$ cross section. It is notable that all of the features on the peak reported by LNS [1], ELPH [2], GRAAL [3], CB-ELSA [4], and MAINZ [5, 6] were consistent with each other. Those results show (1) the center value of the peak is at $W \sim 1670$ MeV, (2) the width of the peak is about 20 MeV, and (3) the peak was observed only in the ηn cross section while no such structure was observed in $\gamma p \to \eta p$ reaction cross section. Because of its narrow width, it is questionable that the structure is made by a nucleon resonance. Indeed, many theoretical interpretations have been advocated. For example, there are possibilities of an exotic baryon [7], intrinsically narrow states [8], a KY threshold effect [9], and an interference effect of known resonances [10]. The variety of the scenarios indicates more constraints are needed to understand the structure. The $K^0\Lambda$ system has an isospin 1/2 and includes hidden strangeness which is same as the ηn system. Hence, confirmation of the prominent structure via the $\gamma n \to K^0\Lambda$ reaction is meaningful to reveal its mysterious nature.

§2. Experiment

The $K^0\Lambda$ photoproduced events were detected with an electromagnetic calorimeter complex FOREST [11]. The incident photon energy E_γ ranges from the $K^0\Lambda$ reaction threshold to 1.15 GeV [12]. FOREST consists of three parts of a calorimeter-hodoscope pair. Forward one consists of 192 pure CsI crystals and 72 plastic scintillators (PSs), central one consists of 252 Lead/Scintillating fiber modules and 18 PSs, and backward one consists of 62 Lead glass and 12 PSs. In total, FOREST covers over the entire steering angle range seen from the liquid deuterium target [13]. The energy resolutions of the calorimeters are 3% [14], 7% [15], 5% [16] for 1 GeV positrons [17].

§3. Current status of analysis

The $\gamma n \to K^0\Lambda$ events were identified by detecting four γs, proton p and π^- generated from below decay chains

$$K^0 \to \pi^0\pi^0 \to \gamma\gamma\gamma\gamma \text{ and} \tag{1}$$

$$\Lambda \to p\pi^-. \tag{2}$$

We analyzed the data taken with the liquid deuterium target ignoring the nucleon Fermi motion in this work. The proton inside a deuteron was assumed as a spectator during the $K^0\Lambda$ photoproduction reactions.

Four γs were identified as neutral clusters that were required to be coincident with each other within $[-2, 2)$ ns. Charge of the incident particle was An event timing criterion of the FOREST t_F was then given as an average timing of those. Event timing window was also set to [-5, +15) ns from t_F. Two charged particles generated by the Λ decay (Eq. (2)) are searched by means of the timing difference between its timing and t_F. No other neutral particles were required in this analysis. Thus, events which involved fifth neutral cluster or third charged cluster in the event timing window were rejected from the event selection. Figure 1 shows the timing difference distributions between the remaining particle and event timing criterion t_F. Additional particles (e.g. γ, n, $\pi^\pm$, p) are well observed in the timing difference distribution. In this energy region, $E_\gamma \leq 1.15$ GeV, the proton has lower velocity than that of the charged pion when it flies to forward angle because of the $\gamma n \to K^0\Lambda$ kinematics. Hence, on the charged particle case, if both of those were detected by the forward calorimeter, later one was regarded as proton and faster one was regarded as π^-. Figure 2 shows the energy correlation between E: measured energy by the forward calorimeter and ΔE: measured energy by the forward hodoscope for each particle regarded as the proton and π^-. It shows that the charged particles were well separated. Also the reaction kinematics confines the proton emission angle in the laboratory frame up to 30° which is just a boundary between the forward and central calorimeter. Thus, charged particles detected with the central or backward calorimeter was regarded as charged pions.

Measured energy, polar angle , and azimuthal angle of the four γs were kinematically fitted [18] to

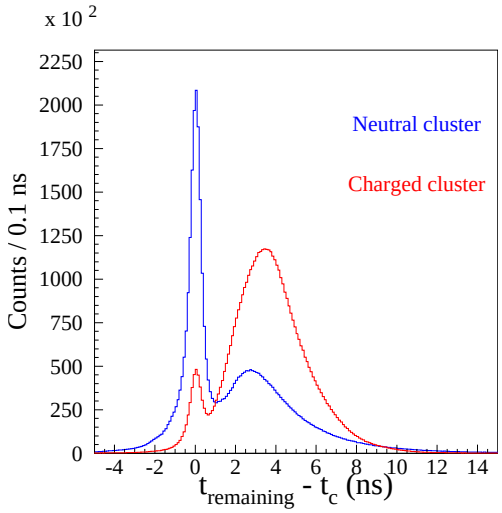

Fig.1. Timing difference distributions of remaining particles and event timing criterion t_F. The blue line shows the timing difference for neutral particles and red one shows that for the charged particles.

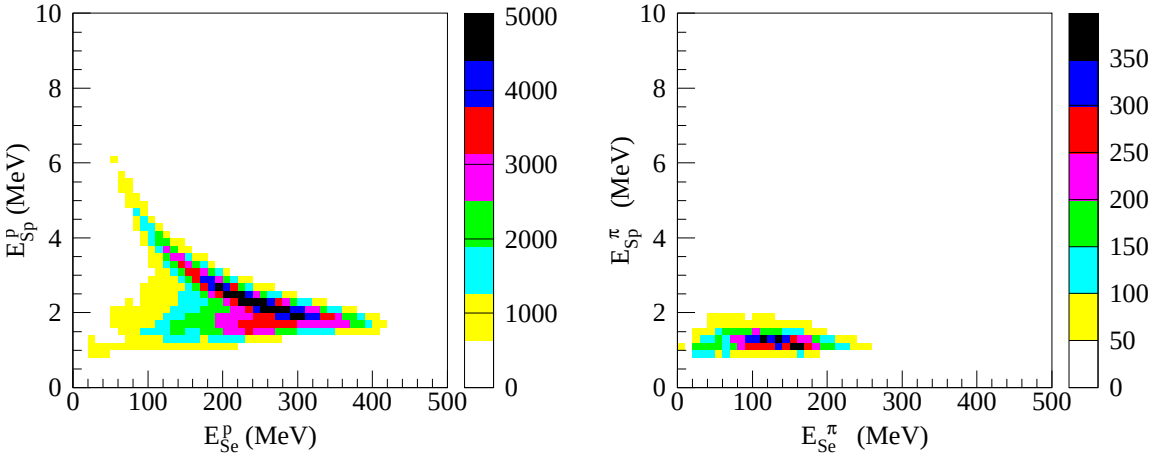

Fig.2. Energy correlation between E_{Sp}: measured energy by the forward hodoscope versus E_{Se}: measured energy by the forward calorimeter of the charged particles regarded as proton (left) and charged pion (right).

satisfy below three constraints

$$M^2(\gamma_1, \gamma_2) = m^2_{\pi^0}, \tag{3}$$

$$M^2(\gamma_3, \gamma_4) = m^2_{\pi^0}, \text{ and} \tag{4}$$

$$M^2_X(\gamma_1, \gamma_2, \gamma_3, \gamma_4, E_\gamma) = m^2_\Lambda. \tag{5}$$

where $M(\gamma_i, \gamma_j)$ is the invariant mass of γ_i and γ_j, M_X is missing mass as a function of the measured values of γ_i and incident photon energy E_γ. Momentum of the K^0 was then reconstructed by summation of its grandchild γs.

Accidentally triggered events contaminate to the selected events. Such events were subtracted by means of the sideband subtraction method by using timing difference between a photon tagging counter

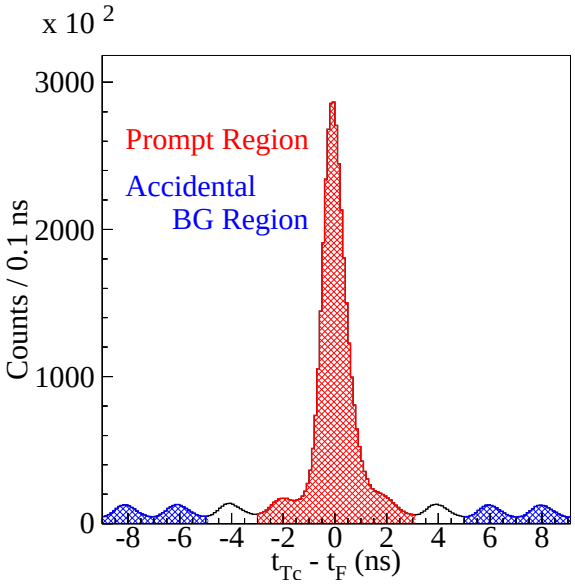

Fig.3. Timing difference distribution of Tagger and FOREST. The prompt region is shaded by red and the accidental background regions are shaded by blue.

and that of FOREST t_F. Figure 3 shows the timing difference between photon tagging counter: Tagger and FOREST. Figure 4 shows the 4 γ (*i.e.* $\pi^0\pi^0$ from here) invariant mass distribution obtained with kinematic fitted momenta. A clear peak around the K^0 mass (497.614 MeV/c^2 [19]) is observed with same width of the one expected from GEANT4 based Monte Carlo (MC) simulation. The K^0 yield was estimated about 10k by fitting the distribution with linear combination of 4th polynomial and gaussian functions.

The number of the $K^0\Lambda$ events were counted by subtracting a simulated background distribution from the $\pi^0\pi^0$ invariant mass distribution. Detailed studies proceed to reveal the contaminated reactions. This report shows the results on the assumption that the background distribution is originated by an non-resonant reaction $\gamma n \to \pi^0\pi^0\pi^- p$. The background distribution in the $\pi^0\pi^0$ invariant mass distribution was fitted by a simulated background distribution. Figure 5 shows the invariant mass distributions for different E_γ of each 50 MeV. The background distributions were almost reproduced by the simulated distributions for $\gamma n \to \pi^0\pi^0\pi^- p$ reaction.

The FOREST acceptance was examined by use of the MC simulation. Figure 6 shows the acceptance as a function of the kaon emission angle in the γn center-of-mass (CM) frame $\cos\theta_K^{\rm CM}$ for different photon beam energy E_γ. It shows that FOREST can detect overall emission angle of K^0.

Figure 7 shows differential cross sections as a preliminary result. The cross sections show enhancement as the kaon emission angle becomes backward in the higher E_γ region while they approach flatter distributions at the lower energies. This result supports the experimental remark in the experimental observation in the previous measurement of the $\gamma n \to K^0\Lambda$ reaction reported by K. Tsukada *et al.* [20]. This fact indicates that the u-channel exchange term may play an important role in this reaction.

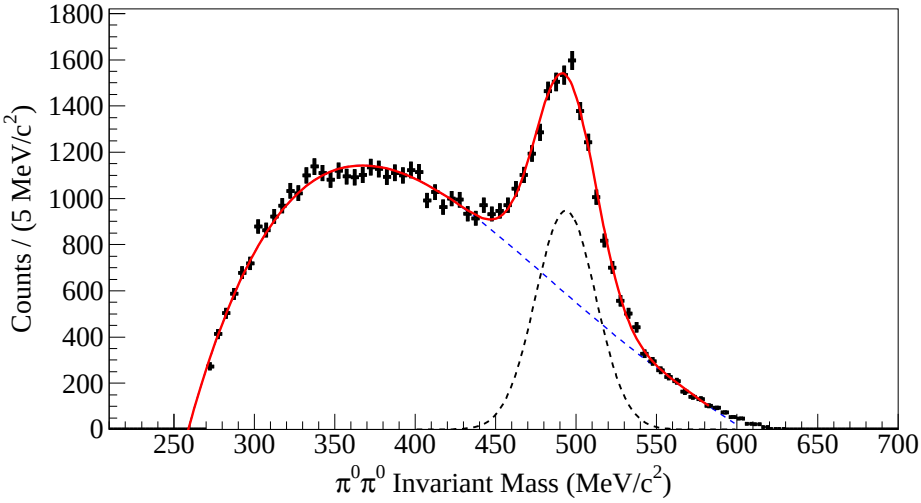

Fig.4. The $\pi^0\pi^0$ invariant mass distribution for different E_γ. Red line shows the fitted function. Blue dotted line shows only the 4th polynomial component and black dotted line shows only the gaussian function.

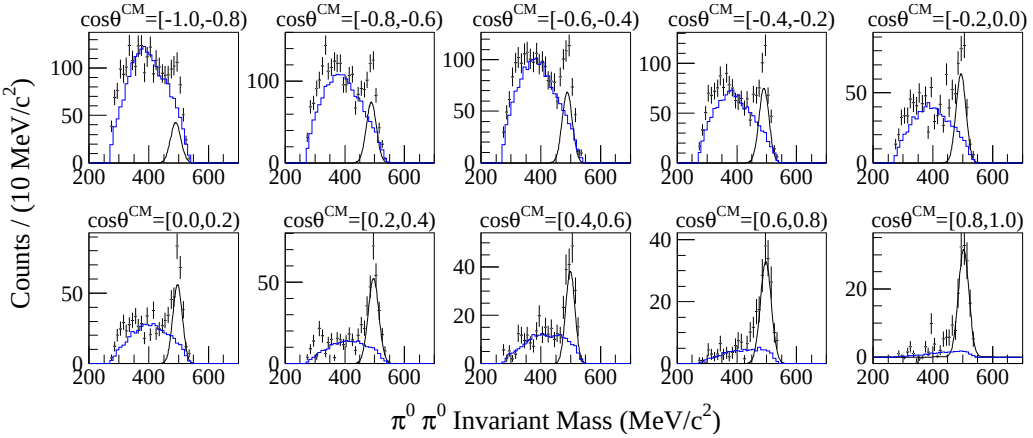

Fig.5. The $\pi^0\pi^0$ invariant masses at $E_\gamma = [950, 1000)$ MeV for different $\cos\theta_K^{\rm CM}$ bins. Blue line shows fitted background distribution made by MC simulation for the $\gamma n \to \pi^0\pi^0\pi^- p$ reaction.

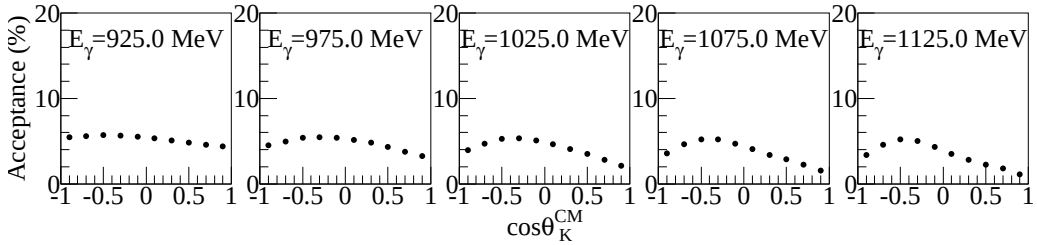

Fig.6. FOREST acceptance for the $K^0\Lambda$ photoproduction reaction as a function of $\cos\theta_K^{\rm CM}$ for different energy bins. A mean value of the incident photon energy is written in each panel in MeV unit.

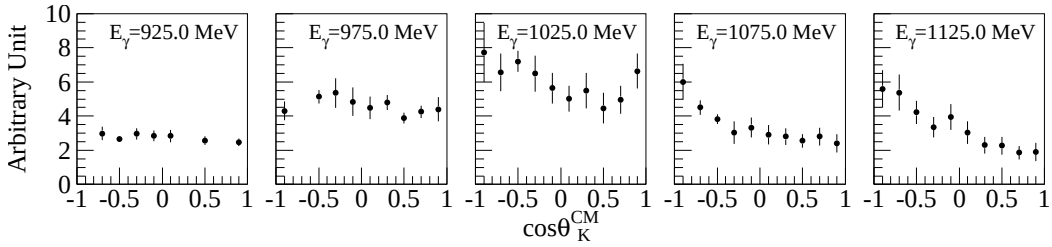

Fig.7. Preliminary result of $\gamma n \to K^0\Lambda$ differential cross sections as a function of kaon emission angle in the γn CM frame $\cos\theta_K^{\rm CM}$ for different photon energy E_γ. A mean value of an energy range of the photon beam is written in each panel in MeV unit. The y axis is scaled to an arbitrary unit.

§4. Summary

Meson photoproduction experiments were carried out at ELPH to study baryon resonances. The $\gamma n \to K^0\Lambda \to \pi^0\pi^0 p\pi^- \to \gamma\gamma\gamma\gamma p\pi^-$ events were studied with an electromagnetic calorimeter FOREST. About 10k $K^0\Lambda$ events were confirmed in the $\pi^0\pi^0$ invariant mass distribution. FOREST successfully detects K^0 at all of the emission angles in the γn CM frame. The $\gamma n \to K^0\Lambda$ differential cross sections showed backward enhancement in higher energy region. The preliminary results agree with the previous experimental remark reported by K. Tsukada *et al.* [20].

References

[1] F. Miyahara *et al.*, Progress of Theoretical Physics Supplement **168**, 90 (2007).

[2] T. Ishikawa, Talk at HADRON2013.

[3] V. Kuznetsov *et al.*, Phys. Rev. Lett. B **647**, 23 (2007).

[4] I. Jaegle *et al.*, Phys. Rev. Lett. **100**, 252002 (2008).

[5] I. Jaegle, *et al.*, Eur. Phys. J. A **47**, 89 (2011).

[6] D. Werthmüller *et al.*, Phys. Rev. C **90**, 015205 (2014).

[7] D. Diakonov *et al.*, Z. Phys. A **359**, 305 (1997).

[8] A. Fix *et al.*, Eur. Phys. J. A **32**, 311 (2007).

[9] M. Döring and K. Nakayama, Phys. Lett. B **683**, 145 (2010).

[10] V. A. Anisovich *et al.*, Eur. Phys. J. A **49**, 67 (2013).

[11] T. Ishikawa, Int. J. Mod. Phys. E **19**, 2393 (2010);
K. Suzuki *et al.*, Mod. Phys. Lett. A **24**, 978 (2009).

[12] T. Ishikawa *et al.*, Nucl. Instr. and Meth. **622**, 1 (2010).

[13] R. Hashimoto *et al.*, Research Report of LNS **41**, Tohoku University, 31 (2008).

[14] A. Nakamura, T. Ishikawa *et al.*, Research Report of LNS **42&43**, Tohoku University, 75 (2010);
H. Sugai, T. Ishikawa *et al.*, Research Report of LNS **42&43**, Tohoku University, 15 (2008).

[15] K. Mochizuki, T. Ishikawa *et al.*, Research Report of LNS **40**, Tohoku University, 15 (2008).

[16] T. Ishikawa *et al.*, Research Report of LNS **42&43**, Tohoku University, 82 (2011);

M. Sato, T. Ishikawa *et al.*, Research Report of LNS **41**, Tohoku University, 22 (2009).

[17] T. Ishikawa *et al.*, Research Report of LNS **40**, Tohoku University, 6 (2008);
Y. Tsuchikawa, T. Ishikawa *et al.*, ELPH Annual Report **1**, 107 (2010).

[18] T. Ishikawa *et al.*, ELPH Annual Report **2–4**, Tohoku University, 119 (2011-2013).

[19] K. A. Olive *et al.* (Particle Data Group), Chin. Phys. C, **38**, 090001 (2014).

[20] K. Tsukada *et al.*, Phys. Rev. C 78, 014001 (2008).

(ELPH Experiment : #2623, #2640, #2655, #2694)

A method to measure the size of hadrons

H. Shimizu[1], Q. He[1*], Y. Honda[1], T. Ishikawa[1], S. Kido[1], M. Miyabe[1], Y. Matsumura[1], N. Muramatsu[1], A. Tokiyasu[1], and Y. Tsuchikawa[1]

[1]*Research Center for Electron Photon Science, Tohoku University, Sendai, 982-0826*

A novel method to measure the size of hadrons is discussed. A Measurement of Bose-Einstein correlations (BEC) for identical mesons M makes it possible to extract the radius of hadron H decaying into MX in the $\gamma N \to MH \to MMX$ reaction. For example, the root mean square radius of $\Delta(1232)$ can be obtained from an experiment measuring $\pi^0\pi^0$ BEC by utilizing the Δ sequential decay process $\gamma N \to \pi^0\Delta \to \pi^0\pi^0 X$ at the $\pi^0\Delta$ photoproduction threshold.

§1. Introduction

In the study of hadron structure the information on the size of hadrons is of crucial importance. Hadron radii, however, are not well measured except for those of some stable hadrons such as the proton, the charge form factors of which have been measured precisely by means of electron-proton elastic scattering to yield the mean square radius of the proton [1]. Spectroscopy of atomic hydrogen gives also precise values of the proton radius [2]. As far as the measurement of the size of a particle is concerned, usually the size means the extent of the charge distribution inside the particle. Accordingly electromagnetic probes are employed as measuring tools. We are exploring another method to measure the size of hadrons, utilizing Bose-Einstein correlation (BEC) effects of two identical bosons.

We succeeded in extracting $\pi^0\pi^0$ BEC parameters from $2\pi^0$ photoproduction data obtained with the FOREST electromagnetic calorimeter in a baryon resonance region around 1 GeV [3]. This is the first observation of $\pi\pi$ BEC effects in such a low energy region where only a few pions are generated, unlike the case of BEC observations at high energies with large multiplicity. Here we have an idea to measure the size of the $\Delta(1232)$ resonance by applying a $\pi^0\pi^0$ BEC analysis to $\pi^0\Delta$ photoproduction on the nucleon.

§2. Bose-Einstein correlations of two identical bosons

In general, BEC effects may be expressed with two-particle correlation function $C_{BEC}(p_1, p_2)$ as

$$C_{BEC}(p_1, p_2) = \frac{P_{BEC}(p_1, p_2)}{P_0(p_1, p_2)}. \quad (1)$$

Here $P_{BEC}(p_1, p_2)$ denotes the probability density of two identical bosons, subject to Bose-Einstein symmetry, emitted from a source to space-time points y_1 and y_2 with momenta p_1 and p_2, respectively. The

*Present address: Institute of Fluid Physics, China Academy of Engineering Physics, Mianyang 621900, Sichuan, P.R. China

denominator $P_0(p_1, p_2)$ corresponds to that of two identical bosons in the absence of BEC. The probability density $P_{BEC}(p_1, p_2)$ is expressed as

$$P_{BEC}(p_1, p_2) = \int d^4r_1 d^4r_2 |\psi_2(p_1, p_2)|^2 \rho(r_1)\rho(r_2) \tag{2}$$

where $\psi_2(p_1, p_2)$ is a symmetrized two-particle plane wave function given by

$$\psi_2(p_1, p_2) = \frac{1}{\sqrt{2}} \left[e^{-ip_1(y_1 - r_1)} e^{-ip_2(y_2 - r_2)} + e^{-ip_1(y_1 - r_2)} e^{-ip_2(y_2 - r_1)} \right], \tag{3}$$

and $\rho(r)$ represents a normalized emitter source distribution. Here r_1, r_2 are the space-time points of two-boson emitted places in the source. We obtaine

$$|\psi_2(p_1, p_2)|^2 = 1 + \frac{1}{2} e^{-iq(r_1 - r_2)} + \frac{1}{2} e^{iq(r_1 - r_2)}, \tag{4}$$

with $q = p_1 - p_2$ and

$$\begin{aligned} P_{BEC}(p_1, p_2) &= \int d^4r_1 d^4r_2 \left[1 + \frac{1}{2} e^{-iq(r_1 - r_2)} + \frac{1}{2} e^{iq(r_1 - r_2)} \right] \rho(r_1)\rho(r_2) \\ &= 1 + |f(q)|^2, \end{aligned} \tag{5}$$

using the Fourier transform $f(q)$ of $\rho(r)$,

$$f(q) = \int d^4r e^{-iqr} \rho(r). \tag{6}$$

If the two particles are detected independently,

$$\begin{aligned} P_0(p_1, p_2) &= \int d^4r_1 d^4r_2 |\psi_0(p_1, p_2)|^2 \rho(r_1)\rho(r_2) \\ &= \frac{1}{2} \int d^4r_1 d^4r_2 \left[|e^{-ip_1(y_1 - r_1)} e^{-ip_2(y_2 - r_2)}|^2 + |e^{-ip_1(y_1 - r_2)} e^{-ip_2(y_2 - r_1)}|^2 \right] \rho(r_1)\rho(r_2) \\ &= \int d^4r_1 d^4r_2 \rho(r_1)\rho(r_2) \\ &= 1, \end{aligned} \tag{7}$$

which corresponds to the two-particle probability density without BEC. Therefore the two-particle correlation function can be written by

$$C_{BEC}(p_1, p_2) = 1 + |f(q)|^2. \tag{8}$$

It should be noted here that the BEC does not mean the correlation caused by the direct interaction between the bosons, but the correlation just due to the Bose-Einstein statistics.

If a Gaussian type distribution is employed, $\rho(r)$ can be expressed with a function of the world interval r^2 from the origin of the source,

$$\rho(r) = \frac{1}{(\sqrt{2\pi}\alpha)^4} \exp\left(\frac{-(\vec{r}^2 - t^2)}{2\alpha^2} \right), \tag{9}$$

with

$$r^2 = t^2 - \vec{r}^2. \tag{10}$$

The Fourier transform of $\rho(r_1)$ is then written by

$$f(q) = \int d^4r_1 e^{-iqr_1} \rho(r_1) = -i \exp\left(\frac{\alpha^2 q_0^2}{2} - \frac{\alpha^2 \vec{q}^2}{2} \right), \tag{11}$$

by means of the Wick rotation in the complex t plane ($it = t'$) and that of $\rho(r_2)$ likewise. Therefore we have

$$\int d^4r_1 d^4r_2 e^{-iq(r_1-r_2)}\rho(r_1)\rho(r_2) = |f(q)|^2 = \exp\left(\alpha^2 q_0^2 - \alpha^2 \vec{q}^2\right) = e^{-\alpha^2 Q^2}, \tag{12}$$

and

$$C_{BEC}(q) = 1 + e^{-\alpha^2 Q^2}, \tag{13}$$

where $Q^2 \equiv -q^2$. Experimentally we assume the two-particle correlation function can be expressed as

$$C_{BEC}(q) = 1 + \lambda e^{-\alpha^2 Q^2}, \tag{14}$$

since all the events do not come from the process under consideration. Here λ is introduced to describe chaoticity which measures the strength of the BEC effects.

§3. Application for Δ sequential decay processes

It is very much important to get Lorentz invariant BEC parameters in the measurement of the $\Delta(1232)$ radius. The parameter α given in the previous section has something to do with a Lorentz invariant world interval. The size of $\Delta(1232)$ can be measured with the $\pi^0\pi^0$ BEC method applied to $\pi^0\Delta$ photoproduction events under the following two assumptions.

1. Δ sequential decay dominance

   We assume Δ sequential decay dominance. As a matter of fact, our experimental data show that the Δ sequential decay process is dominated in $2\pi^0$ photoproduction on the nucleon in the vicinity of the $\pi^0\Delta$ photoproduction threshold [3],

   $$\gamma N \to R^* \to \pi^0\Delta(1232) \to \pi^0\pi^0 N, \tag{15}$$

   where R^* is an s-channel intermediate state decaying into $\pi^0\Delta$.

2. Space-time coordinates

   The space-time coordinates are defined so that the center of the Δ is the origin of the coordinates when the first π^0 and Δ appear simultaneously at $t = 0$, which is measured at the rest frame of the Δ. In this space-time coordinate frame, the first and second π^0s take place at r_1 and r_2,

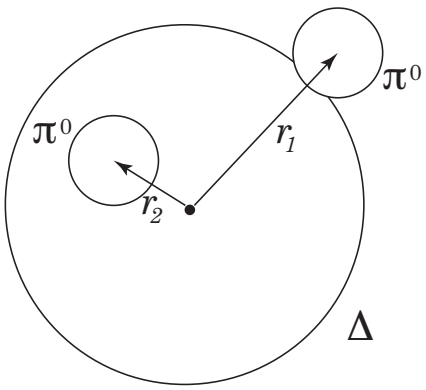

Fig.1. Space-time coordinates

respectively. And the emitter source distribution $\rho_1(r)$ for the first π^0 is assumed to be given as

$$\rho_1(r) = \frac{1}{(\sqrt{2\pi}\alpha)^4}\exp\left(\frac{-\vec{r}^2+t^2}{2\alpha^2}\right) \tag{16}$$

and $\rho_2(r)$ of the second π^0 as

$$\rho_2(r) = \frac{1}{(\sqrt{2\pi}\beta)^4}\exp\left(\frac{-\vec{r}^2+t^2}{2\beta^2}\right). \tag{17}$$

Each of the parameters α and β represents an extent of the distribution in terms of space-time interval $r^2 = t^2 - \vec{r}^2$.

Under these conditions, Eq. (2) becomes

$$\begin{aligned} P_{BEC}(p_1,p_2) &= \int d^4r_1 d^4r_2 |\psi_2(p_1,p_2)|^2 \rho_1(r_1)\rho_2(r_2) \\ &= \int d^4r_1 d^4r_2 \left[1+\frac{1}{2}e^{-iq(r_1-r_2)}+\frac{1}{2}e^{iq(r_1-r_2)}\right]\rho_1(r_1)\rho_2(r_2) \\ &= 1+\frac{1}{2}f_1(q)f_2^*(q)+\frac{1}{2}f_1^*(q)f_2(q) \\ &= 1+\exp\left(\frac{\alpha^2q_0^2}{2}-\frac{\alpha^2\vec{q}^2}{2}\right)\exp\left(\frac{\beta^2q_0^2}{2}-\frac{\beta^2\vec{q}^2}{2}\right). \end{aligned} \tag{18}$$

Therefore the correlation function may be written as

$$C_{BEC}(q) = 1+\lambda\exp\left(-\frac{\alpha^2+\beta^2}{2}Q^2\right), \tag{19}$$

for $2\pi^0$ emission. The parameter $(\alpha^2+\beta^2)/2$ is a Lorentz invariant quantity of the $2\pi^0$ system, where the secondly emitted π^0 coming from Δ decay is delayed due to the life time of Δ. This time component can be eliminated by a three-dimensional measurement of the distance between the $2\pi^0$ in the Δ rest frame. We are actually interested in the three-dimensional size of the $2\pi^0$ emitter. The three-dimensional mean square distance D^2 of $2\pi^0$ can be given as

$$\begin{aligned} D^2 &= \frac{1}{(\sqrt{2\pi}\alpha)^4}\frac{1}{(\sqrt{2\pi}\beta)^4}\int(\vec{r}_1-\vec{r}_2)^2\exp\left(\frac{-\vec{r}_1^2}{2\alpha^2}\right)\exp\left(\frac{-\vec{r}_2^2}{2\beta^2}\right)d^3\vec{r}_1 d^3\vec{r}_2 \\ &= 3(\alpha^2+\beta^2) \end{aligned} \tag{20}$$

in the Δ rest frame. Here the Δ shows up at the same time when the first π^0 appears at $t=0$. At this moment, the first π^0 event happens at $r_1 = (o, \vec{r}_1)$. (The origin of the space-time coordinates is defined at the center of Δ at rest.) The second π^0 appears somewhere in the Δ at the space-time point $r_2 = (\tau, \vec{r}_2)$. If the pion were a point-like object without dimension, D^2 would represent the mean square distance of two places in the Δ under the condition of $\alpha \approx \beta$. And the mean square radius R^2 of Δ can be obtained from the relation

$$D^2 = 2R^2. \tag{21}$$

We assume

$$R = R_\Delta + R_\pi, \tag{22}$$

where R_Δ and R_π denote the root mean square radii of Δ and π, respectively.

The $\pi^0\pi^0$ BEC size parameter obtained so far is $(\alpha^2+\beta^2)/2 = 0.828$ fm^2, which gives some information on the size of $2\pi^0$ emitter source but not exactly on the size of Δ because the $\pi^0\Delta$ event selection

is not completed for the moment. Nevertheless the obtained BEC parameter might yield a size close to the radius of Δ, since the Δ sequential decay process is dominated in the $\gamma N \to \pi^0\pi^0 X$ reaction at 1 GeV. Thus the root mean square radius of Δ can be obtained as

$$R_\Delta = \sqrt{\frac{3(\alpha^2+\beta^2)}{2}} - R_\pi = 1.58 \text{ fm} - 0.64 \text{ fm} = 0.94 \text{ fm}, \tag{23}$$

where we adopt the pion radius $R_\pi = 0.64$ fm. This is just a demonstration for our method to measure the Δ radius. A further data-analysis is going on to select $\pi^0\Delta$ events, which will provide $\pi^0\pi^0$ BEC parameters to extract the Δ radius properly.

Acknowledgment

This research was supported in part by the Ministry of Education and Science of Japan (Grant No. 19002003), and JSPS KAKENHI (No. 24244022).

References

[1] J.C. Bernauer *et al.*, Phys. Rev. Lett. 105 (2010) 242001; R. Hofstadter and R.W. McAllister, Phys Rev. 98 (1955) 217; R. Hofstadter, Rev. Mod. Phys. 28 (1956) 214; P. Lehmann *et al.*, Phys Rev. 126 (1962) 1183; L. N. Hand *et al.*, Rev. Mod. Phys. 35 (1963) 335; J. J. Murphy *et al.*, Phys. Rev. C9 (1974) 2125; X. Zhan *et al.*, Phys. Lett. B705 (2011) 59.

[2] B. de Beauvoir *et al.*, Phys. Rev. Lett. 78 (1997) 440; C. Schwob *et al.*, Phys. Rev. Lett. 82 (1999) 4960; R. Pohl *et al.*, Nature 466 (2010) 213; A. Antognini *et al.*, Science 339 (2013) 417.

[3] Q. He *et al.*, ELPH Annual Report (2011, 2012, 2013) 73.

(ELPH Experiment : #2769)

Performance Test of Thin Gap MWPC for In-beam Charged Particle Veto in KOTO Experiment

H. Nanjo[1], I. Kamiji[1], K. Nakagiri[1], M. Sasaki[3], N. Sasao[2], M. Sei[3], Y. Seki[3], S. Shinohara[1], Y. Tajima[3], and H. Yoshida[3]

[1]*Department of Physics, Kyoto University, Kyoto, 606-8502*
[2]*Research Core for Extreme Quantum World, Okayama University, Okayama 700-8530*
[3]*Department of Physics, Yamagata University, Yamagata 990-8560*

We developed and tested a Thin Gap Chamber with the gas mixture of CF_4 and n-Pentane. The efficiency and timing property for the electron beam were measured. The efficiency over 99.9% can be achieved for minimum ionizing particles with the time-jitter of 20 ns. No instability or no significant gain drop was observed under the high flux of electron up to 30 MHz/cm^2. It can satisfy the requirement of the KOTO experiment. We also developed an amplifier and shaper with three pole-zero cancellation circuits. It suppressed the $1/t$ tail of a MWPC signal and shaped it as narrow as 100 ns. It can resolve multi pulses in the high rate condition of the KOTO experiment.

§1. Introduction

We are conducting the KOTO experiment [1] at J-PARC to search for the rare CP-violating decay, $K_L \to \pi^0\nu\bar{\nu}$. The branching ratio is predicted to be 3×10^{-11} in the Standard Model (SM) with the theoretical uncertainty of $\sim$1% [2]. Such highly suppressed and well predicted process in the SM is suitable to detect new physics beyond the SM with some deviation from the prediction. There are some physics models which predict higher branching ratios as large as two orders of magnitude [3, 4]. We are searching for such new physics down to the sensitivity of the branching ratio $O(10^{-11})$.

The KOTO experiment uses a 30-GeV intense proton beam slowly extracted to the primary target in the Hadron Experimental Facility of J-PARC. From secondary particles produced at the target, long-lived neutral particles such as K_L, neutron, and gamma are selected with a 20-m-long KL beamline. In the beamline, two collimators shape the beam narrowly with a sharp edge within the solid angle of 7.8 μsr at a 16° direction with respect to the primary proton beam. A dipole magnet sweeps out charged particles. A lead absorber reduces gamma flux. Such neutral beam enters the KOTO detector as shown in Fig. 1 from the left to the right. Some K_L's decay in the decay volume, which is of our interest. We identifies the decay $K_L \to \pi^0\nu\bar{\nu}$ by detecting two gammas from the π^0 with an electromagnetic calorimeter, and by ensuring no other visible particle with a hermetic veto system. A charged-particle veto counter is needed also in the downstream in-beam area for such purpose.

Neutron and gamma in the neutral beam pass through the decay volume and enter the downstream in-beam counters. The in-beam charged veto counter should work under the high-flux neutron and

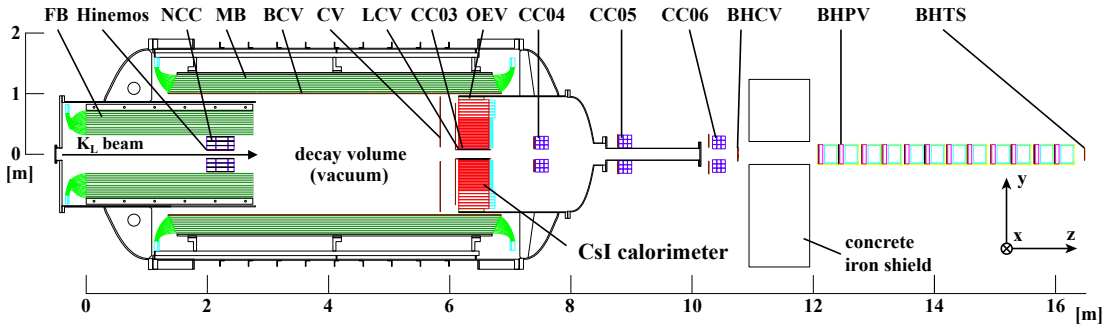

Fig.1. Cross-sectional view of the KOTO detector.

gamma, the rates of which are 0.6 GHz in $20 \times 20\,\mathrm{cm}^2$ area respectively. The required efficiency to detect charged particles from a K_L decay is 99.5% in order to reduce backgrounds, which come from $K_L \to \pi^+\pi^-\pi^0$, for example.

We prepared a 3-mm-thick plastic scintillator for the in-beam charged veto counter, named Beam Hole Charged Veto (BHCV) in 2013. It suffered from high counting rate from the beam gamma and neutron, which caused the signal acceptance loss due to accidental veto. Since larger acceptance loss was expected for planned increase of the beam power in the future, we decided to replace it with a thin MWPC. A gas chamber with thin film cathodes was adopted because such thin material reduces hits from gamma and neutron. Furthermore, we selected a MWPC with a shorter wire-cathode gap, Thin Gap Chamber [5, 6]. It enables fast collection of positive ions from the avalanche process of a MWPC, which reduces space charge effect, and hence suppresses a gain drop of a MWPC in a high-rate condition.

§2. Prototype module of Thin Gap Chamber

We constructed a prototype chamber with the following parameters, the wire spacing 1.8 mm, the wire-to-cathode gap 1.4 mm, and the wire diameter 50 μm. The relatively short gap and thicker wire realized higher electric field in larger volume.

We used the gas mixture of CF_4 and n-Pentane (C_5H_{12}), the mixing ratio of which was 55 : 45. The gas CF_4 was known as “fast gas” which realized fast electron-drift velocity. It enables fast response (short time-jitter) of the chamber. The gas n-Pentane acts as a strong quencher, which is the most efficient UV absorber among the hydrocarbon gas, and helps its stable operation with its high field in large volume.

The gas volume was $50\,\mathrm{mm} \times 50\,\mathrm{mm} \times 2.8\,\mathrm{mm}$, and 13 wires 50-mm long were stretched in the center. The tension of the wires was 300 gw in order to stabilize the positions against the electric force between the wires. The central 11 wires out of 13 wires were grouped, and the signal was read out as a single channel. The signal from the outer two wires were not read out, because the electric field of the edge wires was different.

The cathode was made of a Kapton film 50-μm thick. The inner surface was coated with graphite, which formed the cathode electrode. The thickness of the graphite layer was 30 μm, and the surface resistance was $1\,\mathrm{k}\Omega/\square$. This thin cathode is an essential part to reduce the counting rate from the interaction of neutral particles in the KOTO experiment. Compared to a metal cathode, the graphite

cathode reduces emission of electrons from the cathode due to the photoelectric effect of UV photons from the avalanche, thus it helps the stable operation. The Kapton film was stretched with the stress 15 MPa in order to keep the flatness against the electric static force between the wires and the cathode. The maximum difference of the gap was calculated to be less than 100 μm for the 30×30 cm^2 area which corresponds to the design of the actual chamber for the KOTO experiment. The stress was well within the elastic range of the Kapton to keep the long-term stability. The long-term stability of the Kapton film was also tested separately and no significant creep was observed with the stress of 30 MPa in 3 months.

Buffer gas volumes were made on the outside of the gas volume to share the same gas flow, which enables no pressure difference of the gas between the inside and outside of the cathode film. The buffer gas volume was closed with an aluminized PET films 12-μm thick, which also acts as an electrostatic shield covering the chamber.

The frame of the gas volume was made of G10 in order to keep electric isolation between the cathode ground and the high voltage applied on the anode wire. The frame of the buffer gas volume was made of aluminum. A photos for the construction is shown in where wires were soldered on the frame. Figure 2 right shows the final shape.

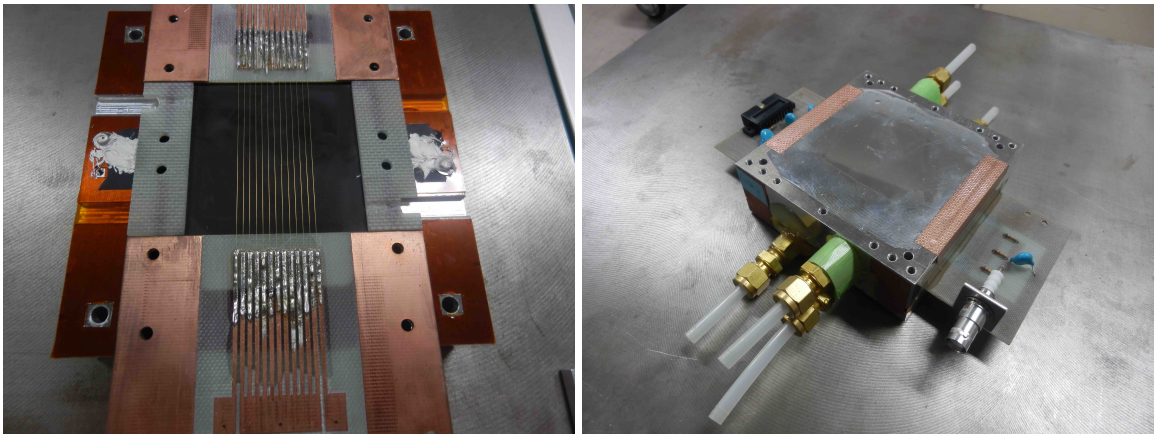

Fig.2. Photos of the prototype chamber. Wires were soldered on the frame (left). Construction was finished (right).

The signal was readout via a high-voltage-blocking capacitor (470 pF) with a custom-made pre-amplifier and shaper. The circuit diagram is shown in Fig. 3. A fast low-noise FET-input op-amp,

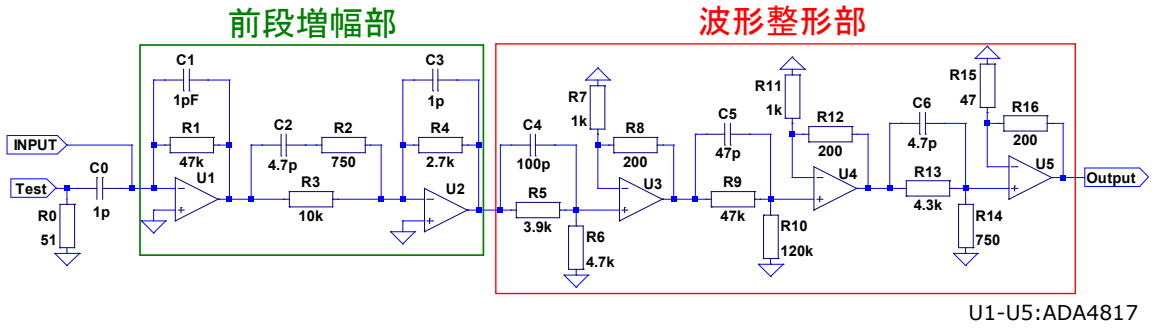

Fig.3. Circuit diagram of the pre-amplifier and shaper.

ADA4817 [7], was used for the core device, the features of which are shown in Table. 1. The first op-

Table 1. Typical performance of ADA4817 in the ± 5 V operation [7].

Gain-bandwidth product	> 410 MHz
Input voltage noise	$4\,\mathrm{nV}/\sqrt{\mathrm{Hz}}$
Input current noise	$2.5\,\mathrm{fA}/\sqrt{\mathrm{Hz}}$
Input offset voltage	0.4 mV
Input bias current	2 pA
Input bias offset current	1 pA

amp part corresponds to a pre-amplifier, which integrate the input current with the time constant of 47 ns. Then the pole-zero cancellation circuit with the second integration op-amp makes the effective integration time shorter to be 3.5 ns. The output of the chamber signal at this stage is shown in Fig. 4 left, where the long tail due to the so-called $1/t$ tail of a MWPC signal can be seen. The following three

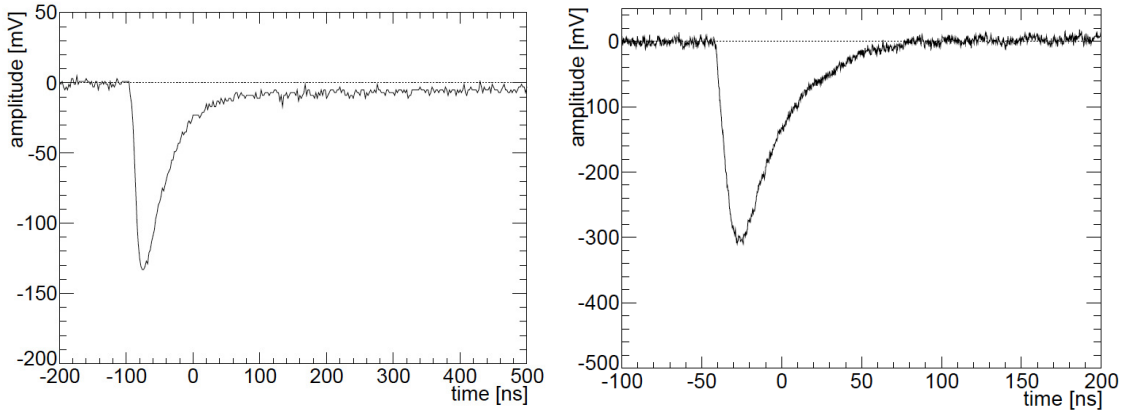

Fig.4. The output of the pre-amplifier part (left) and the output of the shaper (right) are shown.

pole-zero cancellation circuits and op-amps act as a shaper to reduce the $1/t$ tail of a MWPC signal. The output of the shaper is shown in Fig. 4 right, where the $1/t$ tail is totally vanished, and the width of the waveform is shortened to be ~ 100 ns.

§3. Performance test

3.1 Setup of the beam test

An electron beam with the energy of 500 MeV was used for this test. The setup is shown in Fig. 5. Three defining trigger counter, T1, T2, and T3 were used, which were plastic scintillators 5-mm thick with the area of $10 \times 10\,\mathrm{mm}^2$. A timing counter T4 or T5 was also used, which was a plastic scintillators 10-mm thick with the area of $50 \times 70\,\mathrm{mm}^2$. The signal was read out from the both ends to improve the timing resolution. The trigger was made with the coincidence of all the plastic scintillators. The timing was determined with the mean time of the both ends for the timing counter, where the timing resolution of 0.21 ns was obtained from the timing difference of the both ends.

We used the extraction of the electron beam with a 6-second extraction in a 12-second cycle for the test under a low counting rate. We also used a special extraction of the electron beam for the test under a

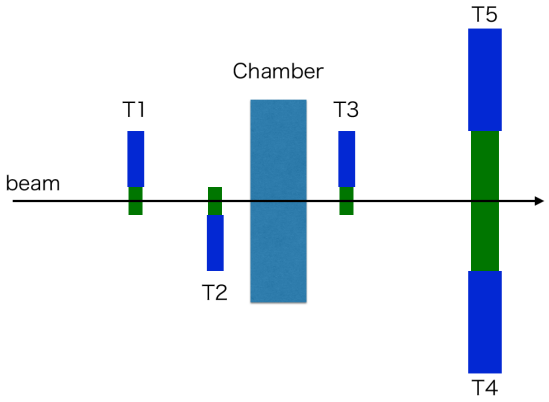

Fig.5. Set up of the beam test.

high counting rate condition. Here the smoothing of the beam was not applied and the extraction period was shortened.

3.2 Test under low counting rate

The output charge of the chamber at the high voltage of 2.9 kV was obtained with a CAMAC charge-sensitive ADC as shown in Fig. 6. A minimum ionization peak (MIP) can be seen at 56.8 pC. The efficiency of 99.95% was obtained with the threshold at 6 pC (separation from the pedestal by 3 times rms of the pedestal). The timing distribution at the high voltage of 2.9 kV was obtained with a CAMAC TDC as shown in Fig. 7. The "time-jitter" was defined with the time gate which contains 99.99% of the events excluding over-flow events. The time-jitter of 20 ns was obtained at the high voltage of 2.9 kV.

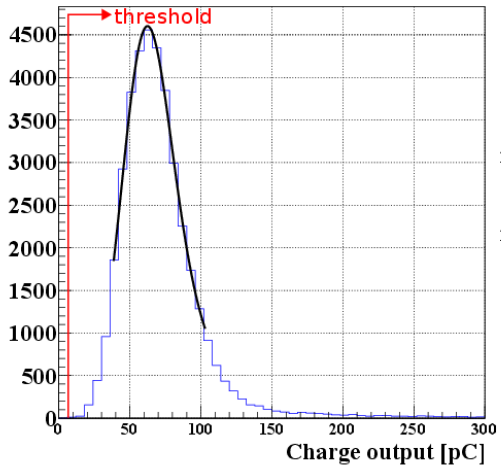

Fig.6. The output charge of the chamber at the high voltage of 2.9 kV measured with a CAMAC charge-sensitive ADC.

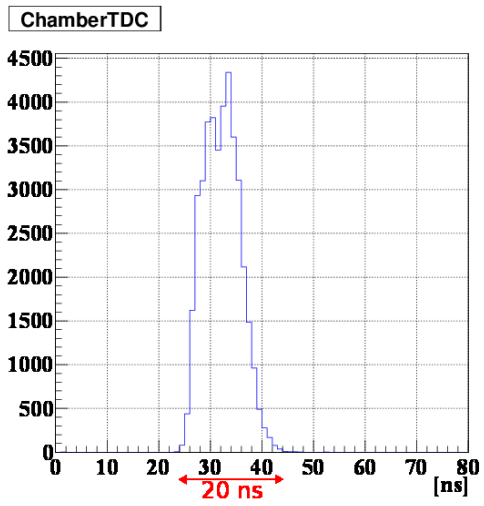

Fig.7. The timing distribution of the chamber at the high voltage of 2.9 kV obtained with a CAMAC TDC.

The high-voltage dependence of the output charge is shown in Fig. 8, where the charge corresponding to the MIP is used. It shows the saturating behavior compared to the expectation in the proportional

mode of a MWPC where an exponential dependence is expected. The operating mode seems to be the limited proportional mode. Proportionality is not important because this chamber is used for the veto. The limited proportional mode is rather suitable because it is robust against variation of the MWPC cell structure, such as wire-to-cathode gap, wire spacing, and so on. The high-voltage dependence of the time-jitter is shown in Fig. 9. The threshold and the definition are the same as in Fig. 7. It saturates ~ 20 ns at the high voltage 2.9 kV or more.

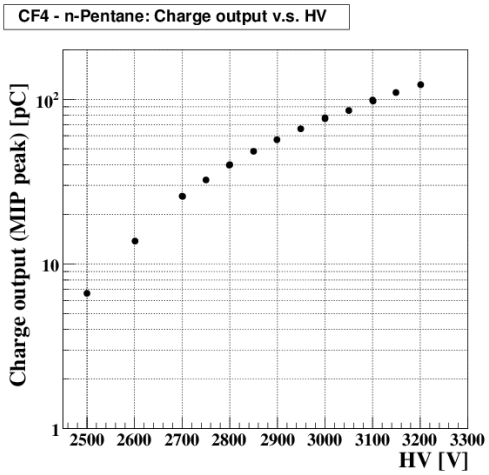

Fig.8. Output charge as a function of the high voltage.

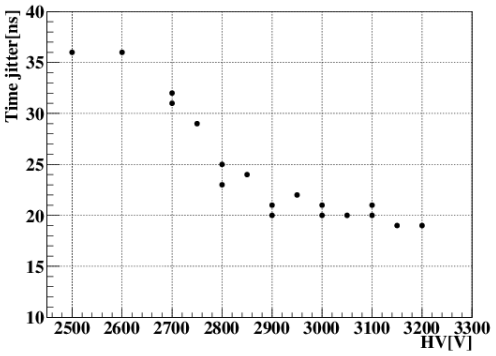

Fig.9. Time-jitter as a function of the high voltage.

The inefficiency (1 – efficiency) was calculated with the same threshold and the time gate as in the definition of the time jitter. The high-voltage dependence is shown in Fig. 10, where the required efficiency of 99.5% can be achieved at the high voltage of 2.7kV or more.

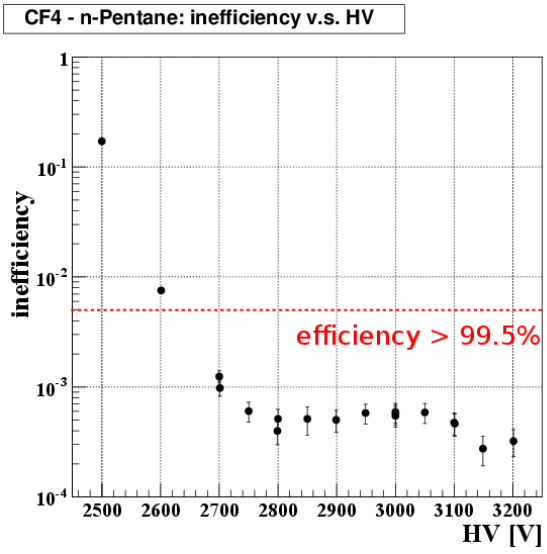

Fig.10. Inefficiency (1 – efficiency) as a function of the high voltage.

3.3 Test under high counting rate

The shorter beam spill was used to achieve high-counting rate condition. The electron incident rate was measured with the trigger counter nearest to the chamber (10-cm downstream of the chamber) with the area of $10 \times 10\,\mathrm{mm}^2$. The discriminated pulse was counted with a CAMAC scaler and the external clock was also counted with the CAMAC scaler simultaneously. The scaler counts as a function of the actual time for a spill are shown in Fig. 11. The extraction period was $\sim 0.1\,\mathrm{s}$ in this condition. The incident rate of the electron can be obtained with the differentiation of the scaler counts as shown in Fig. 12. The incident flux also can be obtained with the area of the trigger counter. The rate reached to 120 kHz or the flux reached to $120\,\mathrm{kHz/cm}^2$ during the spill.

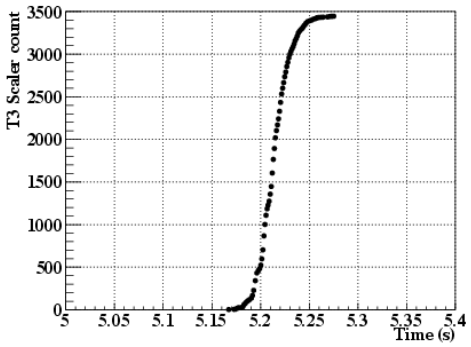

Fig.11. Scaler count of the trigger scintillator nearest to the chamber as a function of the actual time measured with a clock.

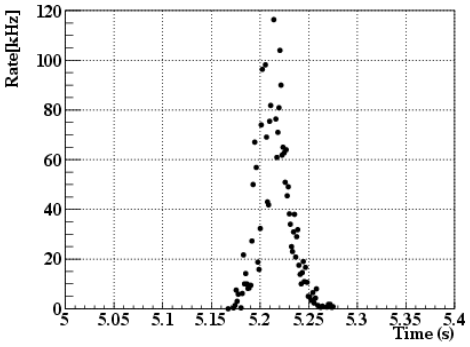

Fig.12. Incident rate of the beam electron. The vertical axis can be read as an incident flux ($\mathrm{kHz/cm}^2$) because the area was $10 \times 10\,\mathrm{mm}^2$.

The output charge of the chamber as a function of the incident rate is shown in Fig. 13, where no significant gain drop is observed. Figure 14 shows the output charge distributions for three incident rate conditions, less than $10\,\mathrm{kHz/cm}^2$, 10-20 $\mathrm{kHz/cm}^2$, and 20-30 $\mathrm{kHz/cm}^2$. Here no significant difference was observed. It shows the rate tolerance of the chamber up to $30\,\mathrm{kHz/cm}^2$, which is the expected maximum hit rate in the unit area for the KOTO experiment in the future.

In this performance test, we also used an ADC with 500-MHz sampling which was used in the actual KOTO experiment. Waveforms captured with the ADC in this high rate test are shown in Fig. 15. The stability of the base line can be seen and over-wrapped multi pulses in the right figure seems to be resolved. We simulated the high counting rate condition by overlaying the captured pulse. A pulse-fitting method was developed and the simulated waveforms were fitted. We still achieved 99.9% efficiency with the threshold of the 1/4-MIP level at the high voltage of 2.9 kV.

§4. Summary

The basic performance of the thin gap chamber with the gas mixture of CF_4 and n-Pentane was measured at the first time. We developed a chamber with the area of $5 \times 5\mathrm{cm}^2$. The wire spacing was 1.8 mm, the wire-to-cathode gap was 1.4 mm, and the wire diameter was 50 μm. The efficiency over 99.9% can be achieved for minimum ionizing particles with the time-jitter of 20 ns at the high voltage

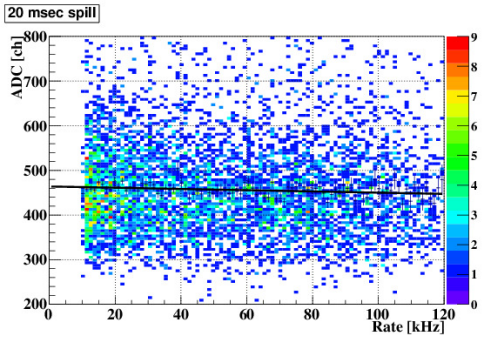

Fig.13. Output charge of chamber as a function of the incident rate in $10 \times 10\,\mathrm{mm}^2$.

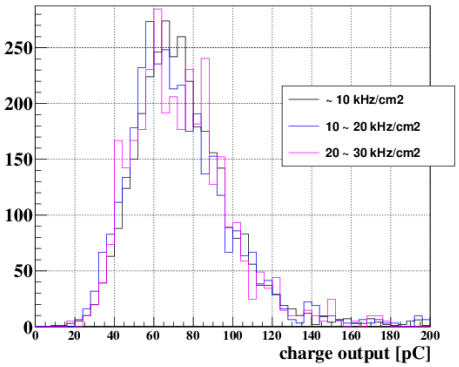

Fig.14. The distributions of the output charge for the incident fluxes of less than $10\,\mathrm{kHz/cm}^2$, 10-20 $\mathrm{kHz/cm}^2$, and 20-30 $\mathrm{kHz/cm}^2$.

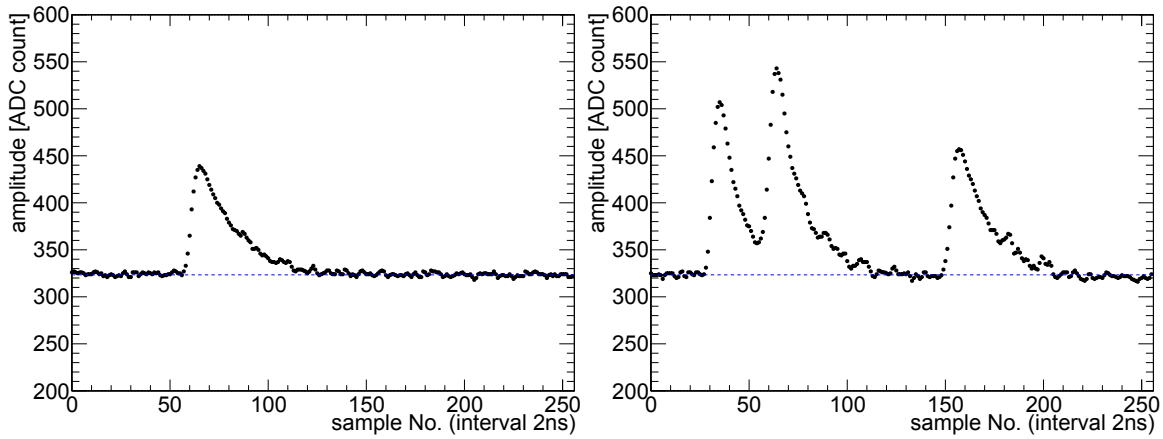

Fig.15. The waveforms captured with a ADC with 500-MHz sampling in this test. The ADC was an actual ADC used in the KOTO experiment.

of 2.7 kV or more. We plan to use three chambers in the KOTO experiment and take two-out-of-three logic, where the requirement of the efficiency for the single chamber can be lowered to be 90.5%. It is also robust against occasional sparking or trip of the high voltage, although there was no trip of the high voltage or observable sparking in this test. We didn't observed no instability or no significant gain drop under the high flux of electron up to $30\,\mathrm{MHz/cm}^2$, which is expected to be the maximum counting rate in the unit aria for the KOTO experiment. It guarantees that our chamber will work properly satisfying the requirement of the efficiency in the environment of the KOTO experiment.

We also developed an amplifier and shaper with three pole-zero cancellation circuits. It suppressed the $1/t$ tail of a MWPC signal and shaped it as narrow as 100 ns. We simulated the high rate condition of the KOTO experiment with overlaying the captured waveforms, and expected no significant increase of the inefficiency due to the pile up of the waveforms in the condition of the KOTO experiment. It guarantees that our amplifier and shaper will work properly in the environment of the KOTO experiment.

Based on the results, we already developed the actual thin gap chamber with the area of $30 \times 30\,\mathrm{cm}^2$

for the KOTO experiment. Three chambers were constructed and installed in the KOTO experimental site, and have worked in the physics run in April 2015. The long-term stability including the aging effect will be studied in the KOTO beam.

Acknowledgment

We would like to express our gratitude to staffs of the Research Center for Electron Photon Science. Part of this work was supported by JSPS/MEXT KAKENHI Grant Numbers 23224007 and 25400309.

References

[1] T. Yamanaka [KOTO Collaboration], PTEP **2012**, 02B006 (2012).

[2] A. J. Buras, D. Buttazzo, J. Girrbach-Noe and R. Knegjens, arXiv:1503.02693 [hep-ph].

[3] M. Blanke, arXiv:1412.1003 [hep-ph].

[4] M. Blanke, PoS KAON **13**, 010 (2013) [arXiv:1305.5671 [hep-ph]].

[5] S. Majewski, G. Charpak, A. Breskin and G. Mikenberg, Nucl. Instrum. Meth. **217**, 265 (1983).

[6] K. Nagai, Nucl. Instrum. Meth. A **384**, 219 (1996).

[7] Analog Devices, Inc., `http://www.analog.com/media/en/technical-documentation/data-sheets/ADA4817-1_4817-2.pdf`

(ELPH Experiment : #2779)

Development of new detector systems for J-PARC E07

S.H. Hwang[1], J.K. Ahn[2], B. Bassalleck[3], H. Ekawa[1,4], Y. Han[1], S. Hasegawa[1], S. Hayakawa[1,5], T. Hayakawa[5], K. Hosomi[1], K. Imai[1], M.H. Kim[2], S.H. Kim[2], R. Kiuchi[6], J.Y. Lee[7], T.J. Moon[7], K. Oue[5], H. Sako[1], S. Sato[1], H. Sugimura[1], K. Tanida[1], and T. Watabe[8]

[1]*Advanced Science Research Center, Japan Atomic Energy Agency, Tokai, Ibaraki 319-1195, Japan*
[2]*Department of Physics, Korea University, Seoul 136-713, Republic of Korea*
[3]*Department of Physics and Astronomy, University of New Maxico, NM 87131, USA*
[4]*Department of Physics, Kyoto University, Kyoto 606-8502, Japan*
[5]*Department of Physics, Osaka University, Toyonaka 567-0047, Japan*
[6]*Institute of Particle and Nuclear Studies (IPNS), High Energy Accelerator Research Organization (KEK), Tsukuba 305-0801, Japan*
[7]*Department of Physics and Astronomy, Seoul National University, Seoul 151-747, Republic of Korea*
[8]*Department of Physics, Nagoya University, Nagoya 464-8602, Japan*

We are developing a new large acceptance forward spectrometer, KURAMA, for systematic study of S = -2 system using the hybrid-emulsion method at J-PARC. We have developed new detector system, which is composed of a single-sided silicon micro-strip detector (SSD), a beam-hodoscope (BH), a beam-aerogel-Cherenkov=counter (BAC), a proton-veto-aerogel-Cherenkov-counter (PVAC) and a charge-hodoscope (CH). A test experiment was performed to evaluate performance of new detector systems with 500 MeV/c positron beams at the ELPH facility, Tohoku University in June 2014.

§1. Introduction

Double strangeness (S = -2) systems have gained considerable attention over the past decades, because of their important role to understand baryon-baryon (B-B) interaction in $SU(3)$ flavor. Also it plays a key role in the understanding of the multi-strangeness matter, such as the core of the neutron stars. For hyperon (Y) - nucleon (N) interaction (S = -1), where hyperon consists of three quarks including at least one strange quark, only 35 species of Λ-hypernuclei are known. However, for Y-Y (S = -2) interaction, only a few double-Λ hypernuclei have been reported. Among them, only one double-Λ hypernuclei event, called $NAGARA$ event, was clearly identified as the decay of ${}^{6}_{\Lambda\Lambda}He$ hypernuclei in the hybrid emulsion experiment [1]. The two-Λ binding energy ($B_{\Lambda\Lambda}$) and the Λ-Λ interaction energy ($\Delta B_{\Lambda\Lambda}$) were measured to be 6.91 $\pm$ 0.16 and 0.67 $\pm$ 0.17 MeV, respectively [2]. More samples are still desired to extend the understanding of Λ-Λ interaction in the nuclei. J-PARC proposed experiment E07 is systematic study of S = -2 systems by the hybrid-emulsion method and it is expected to obtain about

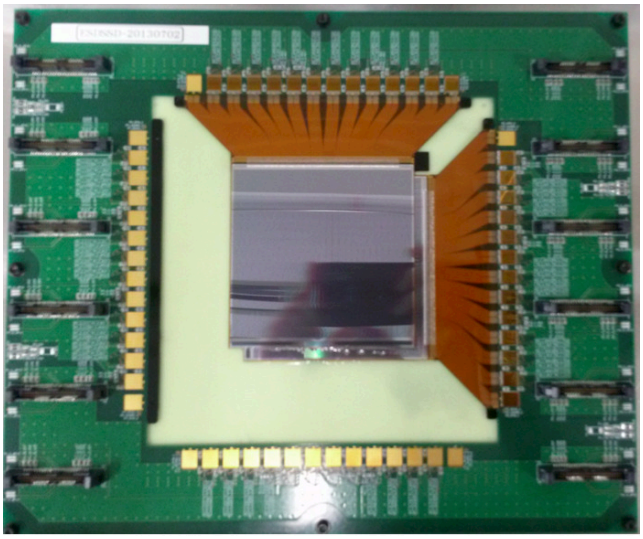

Fig.1. A picture of the test module of SSD.

100 double-hypernuclei candidates [3].

A new magnetic spectrometer, KURAMA, is developed to identify outgoing K^+ in the $C(K^-, K^+)\Xi^- X$ reaction at forward angles. Originally the KURAMA spectrometer was used for the experiments at the KEK-PS beamline. For the new experiment, E07, a pole gap of the KURAMA dipole magnet was increased from 50 cm to 80 cm to get a maximum acceptance at the forward scattered angles. To meet required acceptance, new detector systems were fabricated , which are a single-sided silicon micro-strip detector (SSD), a beam-hodoscope (BH), a beam-aerogel-counter (BAC), a proton-veto-aerogel-counter (PVAC) and a charge-hodoscope (CH). We performed a test experiment for new detector systems with 500 MeV/c positrons at the GeV gamma beamline at the ELPH facility, Tohoku University.

§2. New detector systems

This section deals with the new detector systems for the new KURAMA spectrometer.

2.1 A single-sided silicon micro-strip detector (SSD)

The hypernuclei can be found by themselves in the emulsion experiments, but it takes long time to analysis whole emulsion. Ξ^- particles are produced via (K^-, K^+) reaction in the diamond target and stopped in emulsion plates. In the hybrid emulsion method, the incident position of Ξ^- in the emulsion plate can be reconstructed with vertex information from SSDs together with information from other counters and trackers [4]. The silicon sensors are single-sided and a p-in-n type manufactured by Hamamatsu Photonics [5]. The sensor has total 1,792 strips with a strip pitch of 50 μm and 320 μm thick. Among them, 1,536 strips are bonded to 12 APV25 front-end chips and the total effective area is 77[W] $\times$ 77[H] mm^2.

One stack consists of 4 layers of sensors in $XYX'Y'$ order and the APVDAQ VME modules are used to acquire a pulse shape of SSDs. In the test experiment, the SSD module with two layers of SSDs

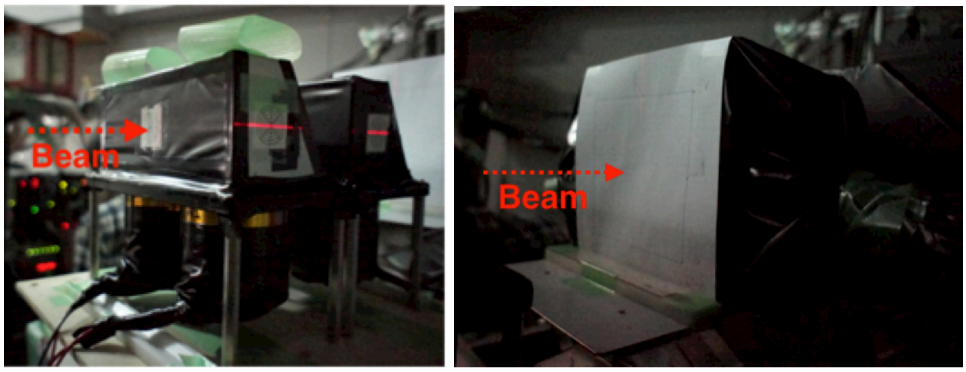

(a) BACs (b) PVAC

Fig.2. A picture of a beam-aerogel-Cherenkov counters (a) and a proton-veto-aerogel-Cherenkov counter (b).

with the XY configuration was fabricated to evaluate the operation of new sensors at the ELPH facility as shown in Figure 1.

2.2 A beam hodoscope (BH)

Time-of-flights (ToF) of charged particles are measured by a Beam-Hodoscope (BH) and a Time-of-Flight wall. A good ToF resolution is guaranteed for reliable particle identification, because the masses of the reconstructed charged particles can be calculated by the relation $m^2 = p^2(1-\beta^2)$, where $\beta = L/(c \cdot \mathrm{ToF})$. L is the flight length and c is the speed of light in vacuum, respectively. Two type of the plastic scintillators, Eljen EJ-212 and Eljen EJ-230 [6], were used and the size of scintillator is 40[H] $\times$ 120[W] $\times$ 6[T] mm^3. EJ-212 shows better light yield, while EJ-230 has good timing property. Fishtail light guides were coupled to the both upper and lower sides of the plastic scintillator. Two 2-inch-diameter PMTs, Hamamatsu H10570 and Hamamatsu H2431-50 [5], measures scintillation lights from the scintillator. A Teflon sheet in 200 μm thick or an aluminized Mylar were used for wrapping scintillators to optimize time resolution of BH's.

2.3 A beam aerogel counter (BAC)

A beam aerogel counter (BAC) is important to reduce backgrounds, such as pions, muons and electrons, at the online level. Two BACs are used at the online level trigger because knock-on electrons from K^- beams make an over-killing signal about 5 % for one counter. Figure 2 (a) shows the fabricated BACs. The size of window is 170[W] $\times$ 70[H] mm^2 and the diffusion box has an inclined plane with 61.3 degree. In side of the diffusion box, four layers of n = 1.03 aerogel radiators were stacked at the upstream of BAC. Two 3-inch fine-mesh PMTs (Hamamatsu R6683 MOD [5]), which were used for the belle experiment, were jointed in the bottom of the diffusion box. A single layer of GORETEX is used as reflector for one of the BAC, while a triple-layer Teflon sheet is covered for another BAC.

Fig.3. A photo of a charge hodoscope.

2.4 A proton veto aerogel counter (PVAC)

A high reflective index aerogel is recently developed by Chiba Univ.. The aerogel with high reflective index is used to identify the scattered K^+ from the Ξ^- production at forward angles. A prototype of PVAC was fabricated to study a design of diffusion box as shown in Figure 2 (b). The radiator of PVAC is an aerogel with high reflective index of 1.163 and 113[H] $\times$ 113[W] $\times$ 13[T] mm^3. The size of the diffusion box is 120[W] $\times$ 120[H] $\times$ 70[T] mm^3 and four 2.5-inch fine-mesh PMTs are attached to both sides to collect Cherenkov lights. 300 μm thick Teflon sheet was used at the up and downstream windows. On the other hand, the side of the diffusion box used 700 μm thick Teflon sheet.

2.5 A charge hodoscope (CH)

A charge hodoscope (CH) is used to identify the charge and rough naive momentum of the scattered particle by information of hit segment with both CH and ToF wall in the 1^{st} level trigger (matrix trigger) and the 2^{nd} level trigger (mass trigger and momentum trigger). The CH consists of 64 plastic scintillators with size of 2 x 11.5 x 450 mm^3 as shown in Figure 3. Each segment is overlapped with adjacent segments by 1 mm. The signal is read out by MPPC (multi-pixel photon counter) with wavelength-shifting-fiber (WLS-fiber). Since it is located inside of the KURAMA dipole magnet, high tolerance against strong magnetic field is needed for CH. The WLS-fiber is inserted in the 1mm-depth groove in a single side of scintillator. The 1x1 mm^2 MPPC with the Kuraray Y11 WLS-fiber [7] collects scintillation lights at a side. The SPIROC board is used in the read-out electronics and the logic signal from the SPIROC board is used in the 1^{st} and 2^{nd} level trigger.

§3. Test experiment

3.1 Experimental setup

Figure 4 shows an experimental setup at the GeV gamma beamline at the ELPH facility. All detectors were aligned along to the beam line. We prepared two large size of trigger counters, 144[W] $\times$ 44[H] $\times$ 10[T] mm^3, to estimate intrinsic time resolution, which large trigger counter used two Hamamatsu

H1949 PMTs and PMTs are coupled with both edges. In additional, small trigger counters, 9.3[W] $\times$ 9.4[H] $\times$ 4[T] mm^2 and 9.5[W] $\times$ 9.8[H] $\times$ 4[T] mm^2, used to estimate position dependency. Large counter and small counter were located most both up and downstream sides to identify positron beams. Among three SSDs, up and downstream SSDs are reference SSDs, which were used for the J-PARC E10 experiment [8]. A shower veto counter was located downstream of aerogel counters. The size of shower veto counter is 25 $\times$ 25 cm^2 and it has ϕ30 mm hole in the center of the scintillator. The hole was aligned to the beamline and it was used to suppress the shower events from positron beams.

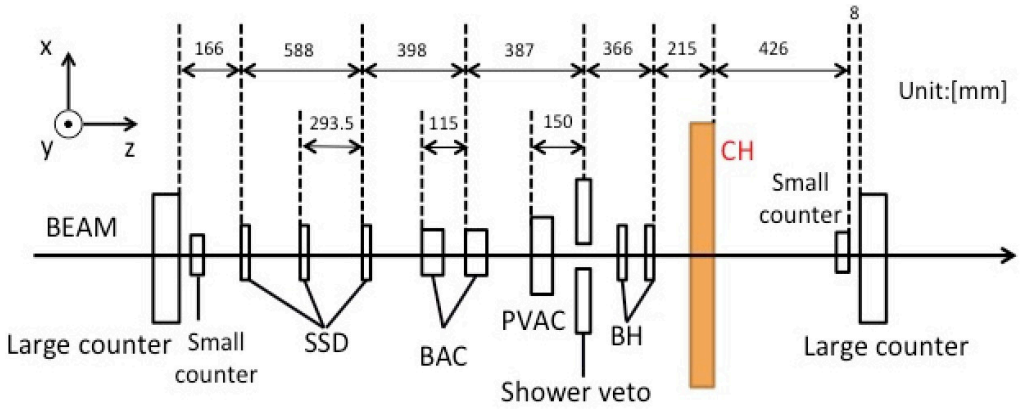

Fig.4. Experimental setup for a test experiment.

The trigger rate was 5000 count/spill (16s cycle) and about 1% events were survived by requiring hits on small counters and no showered events.

3.2 Results

3.2.1 SSD

The efficiency of SSDs are measured by comparing with the reference SSDs and these are estimated to be 98.7 % and 99.4 % for X-layer and Y-layer, respectively. However, X-layer has 10 dead strips in hit region, whereas those in Y-layer is 1 strip. It can reflect lower efficiency of X-layer. We found that high rms level of X-layer than that of Y-layer. It came from loose connection of the ground line between APV25 front-end chips and their power lines [4]. The problem has been solved to the final SSD modules. We successfully estimated the beam profile by hit pattern of new SSDs as shown in Figure 5. Figure 5 (a) shows the beam profile of positron beams. The x and y widths of beam are estimated to be 10.6 mm and 5.3 mm, respectively. By requiring no hit on shower veto counter, the beam profile became circle shape due to the hole shape of shower veto counter as shown in Figure 5 (b). Figure 5 (c) shows the beam profile by requiring small trigger counters. The shape of small trigger can be seen, but the boundary is not clear. It is caused by the multiple scattering of the positron beams.

3.2.2 BH

We estimated intrinsic time resolution of BHs depending on different positions and different type of scintillators. Small beam size was selected by requiring hits on the small trigger counters. The time-

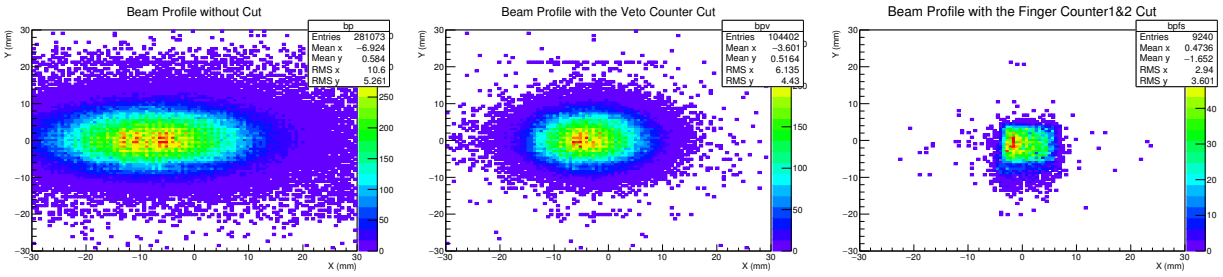

(a) Beam profile (b) Beam profile w/o shower veto counter hit (c) Beam profile w/ small trigger hits

Fig.5. Reconstructed beam profiles by new SSD

walk correction of the large counters was performed with the $TDC_{cor} = TDC_{raw} - a/\sqrt{ADC_{raw}} + b$ relation, where TDC_{cor} is the corrected TDC, TDC_{raw} is the raw TDC and ADC_{raw} is the raw ADC. a and b are fitting parameters. Three ToF's are defined as $ToF_{BH_{H10571}-Trig_2}$, $ToF_{BH_{H2431}-Trig_2}$ and $ToF_{BH_{H10571}-BH_{H2431}}$, where are the time-of-flight between BH_{H10571} and $Trig_2$, BH_{H2431} and $Trig_2$, BH_{H10571} and BH_{H2431}, respectively. The intrinsic time resolutions $\sigma_{BH_{H10571}}$, $\sigma_{BH_{H2431}}$ and σ_{Trig_2} can be estimated by the following equations,

$$\begin{aligned}
\sigma^2_{BH_{H10571}-Trig_2} &= \sigma^2_{BH_{H10571}} + \sigma^2_{Trig_2} \\
\sigma^2_{BH_{H2431}-Trig_2} &= \sigma^2_{BH_{H2431}} + \sigma^2_{Trig_2} \\
\sigma^2_{BH_{H10571}-BH_{H2431}} &= \sigma^2_{BH_{H10571}} + \sigma^2_{BH_{H2431}},
\end{aligned}$$

where σ shows resolution of time-of-flight of each combinations. The estimated intrinsic time resolutions depending on X-incident position are shown in Figure 6. BH with H10571 PMT (Figure 6 (a)) shows various intrinsic time resolutions than that of BH with H2431-50 PMT. It is caused by small light yield of EJ-230 and low gain of H10570 PMT. Reflector with an aluminized Mylar shows better timing properties, because Teflon is random reflector and the pass length of scintillation has large variation. In the case of H2431-50 PMT, the intrinsic resolutions show similar distributions for different type of scintillators and reflectors. The best timing resolution,however, shows 95 ps. We found that H10570 PMT with EJ-230 and an aluminized Mylar shows best intrinsic time resolution about 85 ps and almost no position dependency in X-position.

3.2.3 BAC

To normalize gain of two PMTs, we estimated single-photo-electron (SPE) channel in the LED test bench at the laboratory test. The SPE level was measured by the zero probability of the Poisson distribution with weak LED intensity as relating with $P_{zero} = e^{-\lambda}$, where λ is mean photoelectrons. Figure 7 shows the estimated number of photoelectrons for two BACs. Teflon reflector is better light collection efficiency than that of GORETEX, due to the 10 % better intrinsic reflectance for Teflon sheet. The estimated number of photoelectrons are more than 20 photoelectrons for positron beams. The inefficiency of BACs are negligible because the inefficiency of BAC from the Poisson distribution is $2.1 \times 10^{-}9$.

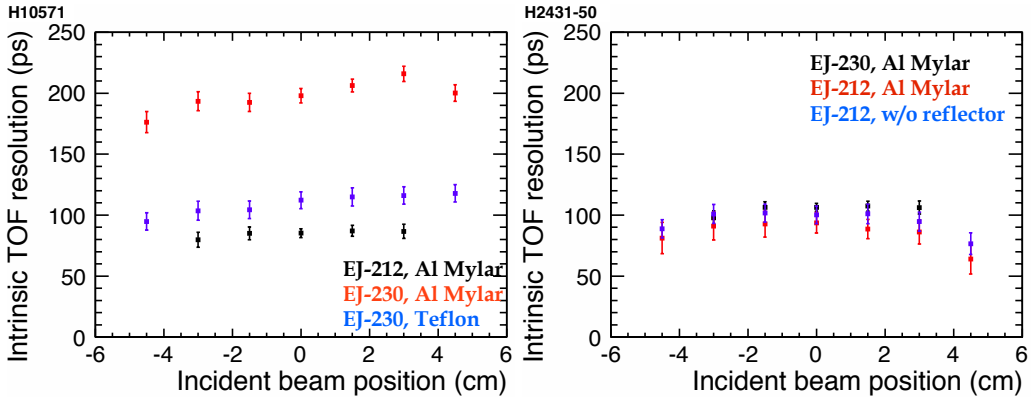

(a) H10570 PMT (b) H2431-50 PMT

Fig.6. Intrinsic resolutions for each condition. (a) shows the measurement with H10571 PMT and (b) is the measurement with H2431-50 PMT, respectively.

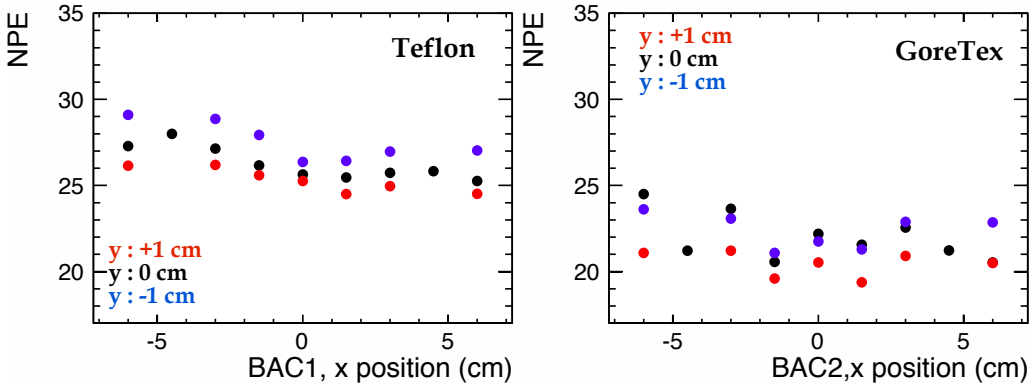

(a) BAC1, Teflon (b) BAC2, GORETEX

Fig.7. Distribution of number of photoelectrons at center position.

3.2.4 PVAC

SPE levels for 4 PMTs were estimated from the LED test bench as similar as the BAC's normalization method. Positron beams were irradiated for 5 positions at PVAC. Figure 8 (a) shows the reconstructed number of photoelectrons of PVAC, when positron beams inject at center. The estimated mean photoelectrons are 32.6 photoelectrons at center. The histogram has a large tail at high energy side compared to the Poisson distributions, but the peak position consistents to a result of Monte-Carlo simulation (20.8 photoelectrons). Other 4 positions were also irradiated as shown in Figure 8 (b). The estimated photoelectrons are 30.8, 31.7, 32.0 and 32.0 for (2.5 cm, -2.5 cm), (2.5 cm, -2.5 cm), (-2.5 cm, 2.5 cm) and (-2.5 cm, -2.5 cm) positions, respectively.

3.2.5 CH

MPPC shows very good photon counting characteristic and our MPPC module can clearly count more than 10 photoelectrons in the LED test bench. During the test experiment, all channels were normalized to 30 channel of SPE. Figure 9 shows gain dependency of all 64 channels. All channels show

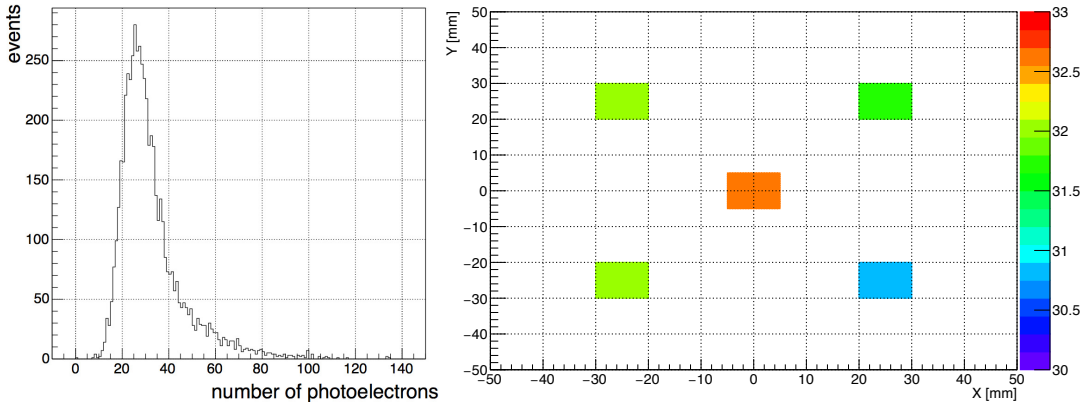

(a) Histogram of number of photoelectrons at center (b) Number of photoelectrons depending on the incident beam positions

Fig.8. Histogram of number of photoelectrons of PVAC at center (a) and the reconstructed number of photoelectrons depending on the beam positions (b).

more than 20 photoelectrons. Normally, MPPC has high dark counting rate, 600 kcps, and it needs a little high threshold level to reduce fake events from dark count. By assuming 4 SPE threshold level, efficiency can be estimated as 99.998 % in the Poisson distribution. The obtained number of photoelectrons meets our requirement. Efficiency was estimated in terms of Y-position and incident angle as shown in Figure 10 (a) and (b), respectively. The efficiency of Y-positions show about 99.98 % and it is almost closed to our expectation by the Poisson distribution.

We estimated efficiency depending on the incident angle of positron beams. Particles with large incident angle can hit corner of scintillators, since each segment is overlapped with adjacent segments by 1 mm. In additional, if adjacent segments have a space, the inefficiency will be increased. In the Figure 10 (b), the inefficiency is less than 0.1 %. The inefficiency is small, however this inefficiency is larger than that of our expectation. Because 1 mm overlapping can cover 20 degree of incident angle. This large inefficiency is mainly space problem between each segment.

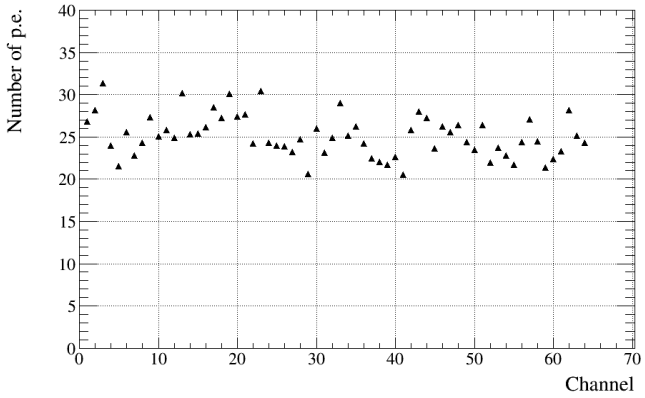

Fig.9. Distribution of number of photoelectrons at center position.

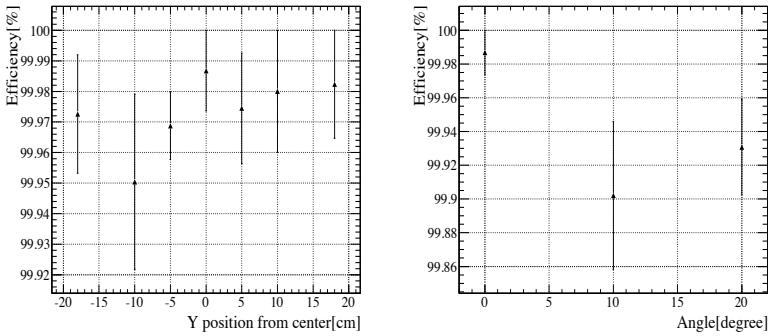

(a) (b)

Fig.10. Y-dependency (a) and angular dependency (b).

§4. Summary

We carried out a test experiment to evaluate the performance characteristics of SSD, BH, BAC, PVAC and CH for the J-PARC E07 experiment. The beam profile was clearly reconstructed by new SSD system and we have confirmed an operation of new SSD. The estimated intrinsic time resolution of BH is reached to 85 ps and it is good enough to identify the scattered K^- from the (K^-, K^+) reaction. Two aerogel counters,BAC and PVAC, were tested and the obtained gain expects good efficiency of these detectors. Number of photons of all channel of CH show more than 20 photons. The estimated characteristics of all new detectors meet our requirements to perform the J-PARC E07 experiment.

Acknowledgment

The authors gratefully acknowledge the contributions of the staff at the ELPH facility, Tohoku University.

References

[1] H. Takahashi *et al.*: Phys. Rev. Lett. **87** (2001) 212502

[2] J.K. Ahn *et al.*: Phys. Rev. C **88** (2013) 014003

[3] K. Imai, K. Nakazawa and H. Tamura *et al.*: J-PARC proposal E07, Systematic Study of double strangeness system by emulsion-counter hybrid method.

[4] J.Y. Lee *et al.*: Proceeding of J-PARC 2nd symposium., in press.

[5] Hamamatsu Photonics, ⟨http://www.hamamatsu.co.jp⟩.

[6] Eljen Technology, ⟨http://www.eljentechnology.com⟩.

[7] Kuraray Co., LTD., ⟨http://www.kuraraypsf.jp⟩.

[8] H. Sugimura, *et al.*: Phys. Lett. **B** 729 (2014) 39-44.

[9] S.H. Kim, *et al.*: Nucl, Instr. and Meth, in press.

(ELPH Experiment : #2781)

200 MeV/c陽電子ビームを用いたシリコンストリップセンサーおよび読み出し回路試作機の性能評価

西村昇一郎[1], 池田博一[2,3], 池野正弘[2,4], 上野一樹[2,4], 内田智久[2,4], 川越清以[5], 古浦新司[5], 高力孝[2,4], 齊藤直人[2,4], 佐々木修[2,4], 調翔平[5], 田中真伸[2,4], 東城順治[5], 長澤翼[5], 三部勉[2,4], 吉岡瑞樹[5], 他 J-PARC muon $g-2$/EDM コラボレーション

[1] 東京大学大学院理学系研究科 （113-0033 文京区本郷 7-3-1）
[2]Open-It （305-0801 つくば市大穂 1-1）
[3] 宇宙航空研究開発機構 （305-8505 つくば市千現 2-1-1）
[4] 高エネルギー加速器研究機構 （305-0801 つくば市大穂 1-1）
[5] 九州大学理学部 （812-8581 福岡市東区箱崎 6-10-1）
[6] 九州大学 RCAPP （812-8581 福岡市東区箱崎 6-10-1）

Evaluation of Test Silicon Strip Sensors and Readout ASICs with the 200 MeV/c Positron Beam

Shoichiro NISHIMURA[1], Hirokazu IKEDA[2,3], Masahiro IKENO[2,4], Kazuki UENO[2,4], Tomohisa UCHIDA[2,4], Kiyotomo KAWAGOE[5], Shinji KOURA[5], Takashi KOHRIKI[2,4], Naohito SAITO[2,4], Osamu SASAKI[2,4], Shohei SHIRABE[5], Manobu TANAKA[2,4], Junji TOJO[5], Tsubasa NAGASAWA[5], Tsutomu MIBE[2,4], Tamaki YOSHIOKA[5], and for the J-PARC muon $g-2$/EDM collaboration

[1]*Faculty of Science, The Univ. of Tokyo, Hongo 7-3-1, Bunkyo-ku, 113-0033*
[2]*Open-It, Tsukuba 305-0801*
[3]*Japan Aerospace Exploration Agency (JAXA), Sengen 2-1-1, Tsukuba-shi, 305-8505*
[4]*High Energy Accelerator Research Organization (KEK), Oho 1-1, Tsukuba-shi, 305-0801*
[5]*Faculty of Science, Kyushu Univ., Hakozaki 6-10-1, Fukuoka-shi Higashi-ku, 812-8581*
[6]*Kyushu Univ. RCAPP, Hakozaki 6-10-1, Fukuoka-shi Higashi-ku, 812-8581*

The muon $g-2$/EDM experiment at J-PARC (E34) aims to measure muon $g-2$ with a precision of 0.1ppm, and search for muon EDM with sensitivity down to 10^{-21} $e\cdot$cm. In this experiment, muon is accelerated to the 300 MeV/c and injected to the storage ring that supplies a 3 T precise magnetic field. We plan to measure a track of a decay positron by the highly-segmented positron tracking detector. The tracker is required to have high rate capability, high stability against a large rate change, good operation in a high magnetic field, and good position resolution. The silicon strip sensor is useful for our experiment. Two types of test sensors and test readout ASICs were produced and tested by the

*Present address: Research Center for Electron Photon Science, Tohoku University, Sendai, 982-0826

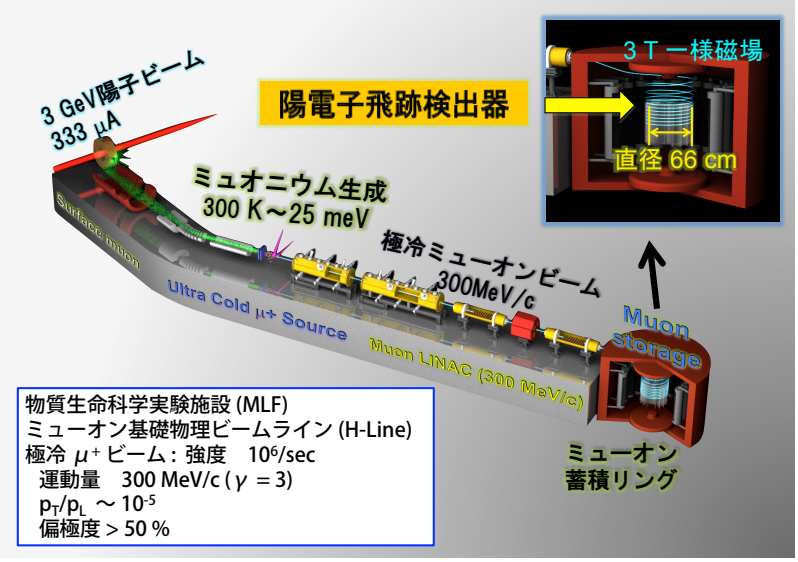

第 1 図　J-PARC E34 実験の全体概念図

200 MeV/c positron beam to check the signal-to-noise ratio and time resolution. As a result, signal-to-noise ratio satisfied the requirement of S/N>15 and time resolution was improved about twice by ToT time walk correction.

§1. 研究背景

ミューオンの異常磁気能率 $(g-2)$ はブルックヘブン国立研究所 (BNL) での E821 実験において 0.54ppm の精度で測定され、標準理論の予測値と 3.3σ の乖離がある [1]。また CP 非保存量であるミューオン電気双極子能率 (EDM) についても探索が行われ、現在の上限値は $1.8 \times 10^{-19}\ e \cdot \mathrm{cm}$ である [2]。J-PARC での新実験 (E34) では $g-2$ を 0.1 ppm の精度で、EDM を $10^{-21} e$·cm の感度での測定を目指している [3]。第 1 図は J-PARC E34 実験全体の概念図である。本実験では 300 MeV/c まで加速したミューオンを 3 T 一様磁場、軌道半径 333 mm の小型蓄積リングに蓄え、崩壊陽電子の飛跡をリング内側にある飛跡検出器により再構成し、ミューオンのスピン歳差運動を測定する。第 2 図は陽電子飛跡検出器の概念図である。陽電子飛跡検出器には高レート耐性が求められ、シリコンストリップセンサーの使用を検討している。飛跡検出器は 48 枚のベーンと呼ばれる羽根板からなり、1 ベーンに 24 枚のシリコンストリップセンサーを搭載する予定である。 これまで飛跡検出器の主要部分となるセンサーの開発と読み出し回路の開発が並行して進行し、テストセンサーと読み出し回路試作機の製作、実験室での基礎的な性能評価を行ってきた。今回、その次の段階として、ビームを使ってセンサーと読み出し回路を接続した状態での性能評価を行った。

1.1 シリコンストリップセンサー

第 3 図はシリコンストリップセンサーの仕様である。センサーは軸方向と動径方向の位置をそれぞれ読み出すために 2 種類のセンサーを用い、それぞれ A センサー、R センサーと呼ぶ。共に厚さは 320 μm、p-on-n のシングルサイドで、バイアス抵抗は 10 MΩ である。この仕様に基いて、それぞれのセンサー 64 strip に相当するテストセンサーを製作し、基礎特性の測定を行った。第 1 表はテストセンサーの仕様である。また基礎特性評価の結果を第 2 表にまとめた。テストセンサーが問題なく動作することを確認し、仕様から予

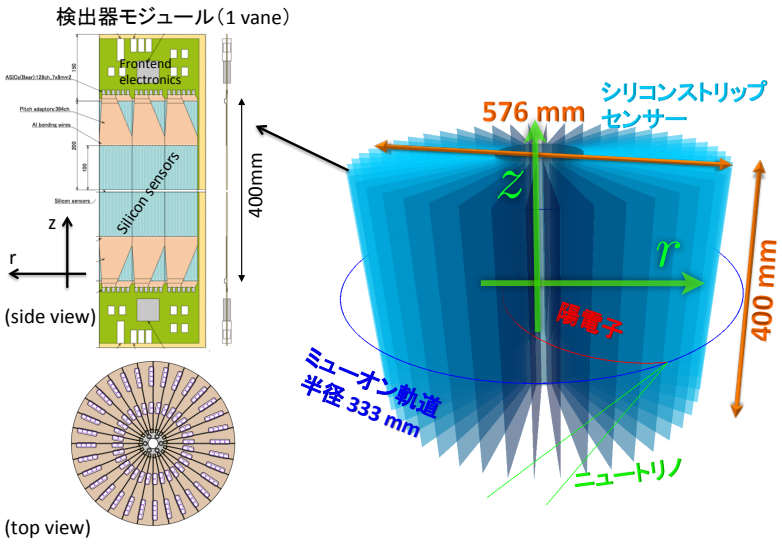

第 2 図　陽電子飛跡検出器の概念図

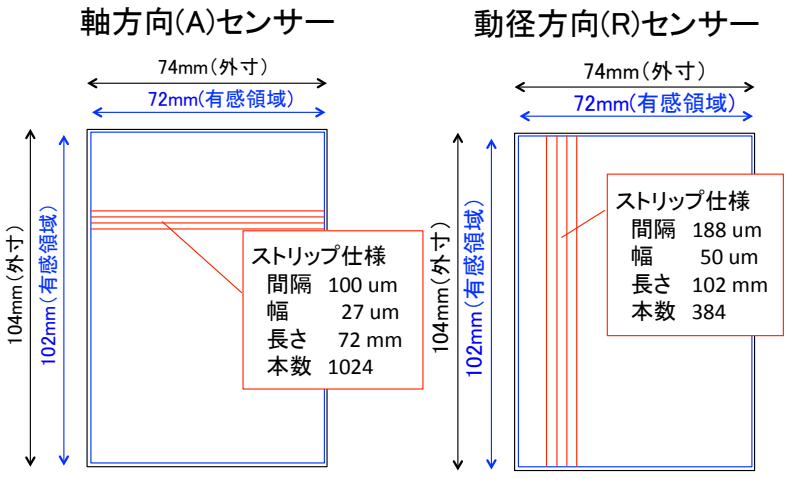

第 3 図　シリコンストリップセンサーの仕様

第 1 表　テストセンサー仕様

仕様	動径方向センサー	軸方向センサー
厚さ	0.320 mm	
ストリップ数	64	
読み出しストリップ	純アルミニウム	
読み出しストリップ厚さ	1.5 μm	
ストリップ間隔	0.188 mm	0.100 mm
ストリップ長さ	102 mm	72 mm
ストリップ幅	0.050 mm	0.027 mm
ストリップ間容量 (概算値)	約 6 pF	約 4 pF

第 2 表　基礎特性評価の結果

仕様	動径方向センサー		軸方向センサー	
	予想値	測定値	予想値	測定値
目視確認		異常なし		異常なし
I-V 特性		プラトー領域確認		プラトー領域確認
完全空乏化電圧		93 V		73 V
バルク容量	350 pF	360 pF	150 pF	170 pF
ストリップ間容量	6 pF	7.4 pF	4 pF	6.2 pF
検出器容量		23.4 pF		15.9 pF

想される性能通りの結果が得られた。

1.2　読み出し回路

E34 実験では測定時間構造に特化した独自のフロントエンド ASIC(SlitA) を用いる。第 4 図は SlitA のブロックダイアグラムである。今回は Analog part の試作機を製作し (SlitA2013)、性能評価を行った [4] [5]。第 5 図は製作した試作器の写真であり、32 チャンネルを同時に読み出すことができる。時間情報を測定するのに重要な項目として、ゲイン、ダイナミックレンジ、ノイズ (ENC)、パルス幅、タイムウォークの値を調べ、要求値と比較した。性能評価の結果を第 6 図にまとめた。この性能評価から概ね要求通りの性能が得られていることを確かめた。

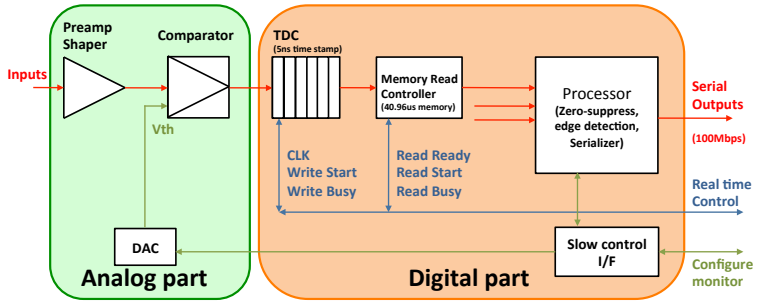

第 4 図　読み出し ASIC(SlitA) のブロックダイアグラム

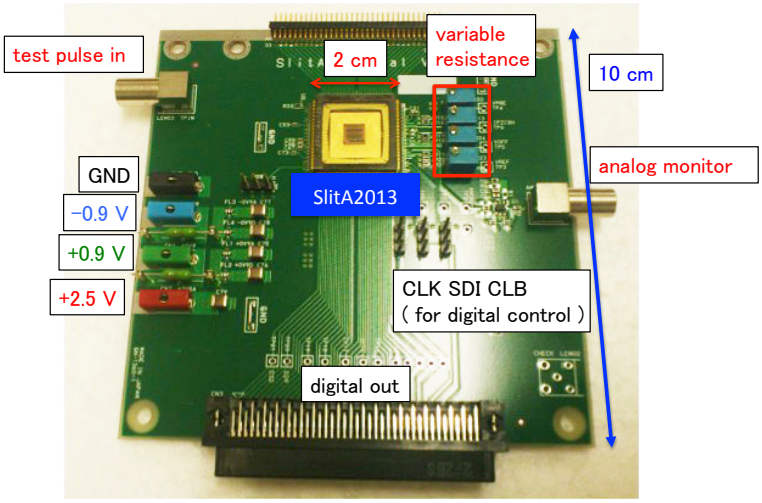

第 5 図　ASIC 試作器 (SlitA2013) の写真 [5]

parameter	Requirement	Measurement
ゲイン	> 70 mV/MIP	~ 50 mV/MIP
パルス幅	<100 ns	< 100 ns (50 ns@1 MIP)
ダイナミックレンジ	5 MIP	> 5 MIP
ノイズ@15pF	< 2000 e	1490 e
チャンネル数	128	64
タイムウォーク	<< 5 ns	15 ns
消費電力	5 mW/ch	~ 1.9 mW/ch

第 6 図　SlitA2013 の性能評価まとめ [5]

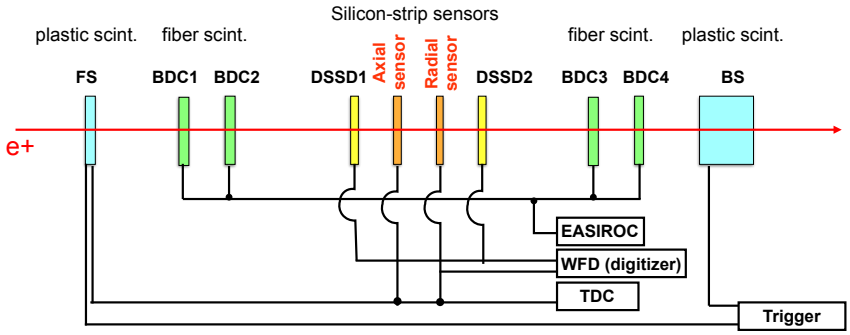

第 7 図　ビーム試験時のセットアップ

§2．研究目的

E34 実験では統計数と非対称度の関係から崩壊時のエネルギーが 200 MeV 以上の陽電子を信号とする。SN 比に対する要求値は 15 以上であり、まず、実際の実験環境下での SN 比を見積もるために、200 MeV 陽電子の信号波形を測定する。さらに本実験では時間情報のずれが誤差に効果を与えるため、時間情報の広がりとして時間分解能を測定する。また同時に Time over Threshold (ToT) を測定し、タイムウォーク補正がどの程度有効であるかを見積もる。

§3．実験セットアップ

第 7 図はビーム試験のセットアップである。テストセンサーのストリップ方向を x 軸、ストリップに鉛直な方向を y 軸、ビーム方向を z 軸と定義する。試験目的である A センサーと R センサーを中心に、陽電子飛跡を再構成するために Belle Ⅱ 用 DSSD と、10 本の 0.5 mm 角と 6 本の 1 mm 角のシンチレーションファイバーからなる BDC4 台を設置した。さらにトリガー用のシンチレーターを最上流と最下流に設置し、それぞれ FS と BS と呼ぶ。FS のサイズは (x, y, z)=(6 mm,5 mm,1 mm)、BS のサイズは (x, y, z)=(12 mm,10 mm,10 mm) である。それぞれの検出器のデータ取得には、汎用 MPPC 読み出しモジュールである EASIROC で BDC の波高を測定、Waveform Digitizer (WFD, CAEN V1742) で DSSD、テストセンサー、FS、BS の陽電子信号の波形を測定、TDC (CAEN V1190) でテストセンサーと FS、BS の陽電子ヒット時間を測定した。

§4．実験結果

4.1　実際の実験環境下での SN

第 8 図はビーム試験で得られたテストセンサーの典型的な波形と波高分布である。波高は BDC4 台でトラックが引けることを条件に課し、波形をフィッティングすることにより求めた。波高分布では最小イオン化粒子 (MIP) によるピークが観測され、波高は最頻値で A センサーで 88.0 mV、R センサーで 68.8 mV になり、SlitA2013 のゲインからセンサー上で生じた電荷量に逆算すると、A センサーで $2.1 \times 10^4 e$、R センサーで $1.7 \times 10^4 e$ となった。これに対して J-PARC MLF において測定されたノイズの大きさは A センサーで $\sigma_A = 1160e$、R センサーで $\sigma_R = 990e$ であったので、実際の実験環境下での SN 比は A、R それぞれ、18.5、17.7 となり、要求値 15 以上を満たすことが分かった [6]。

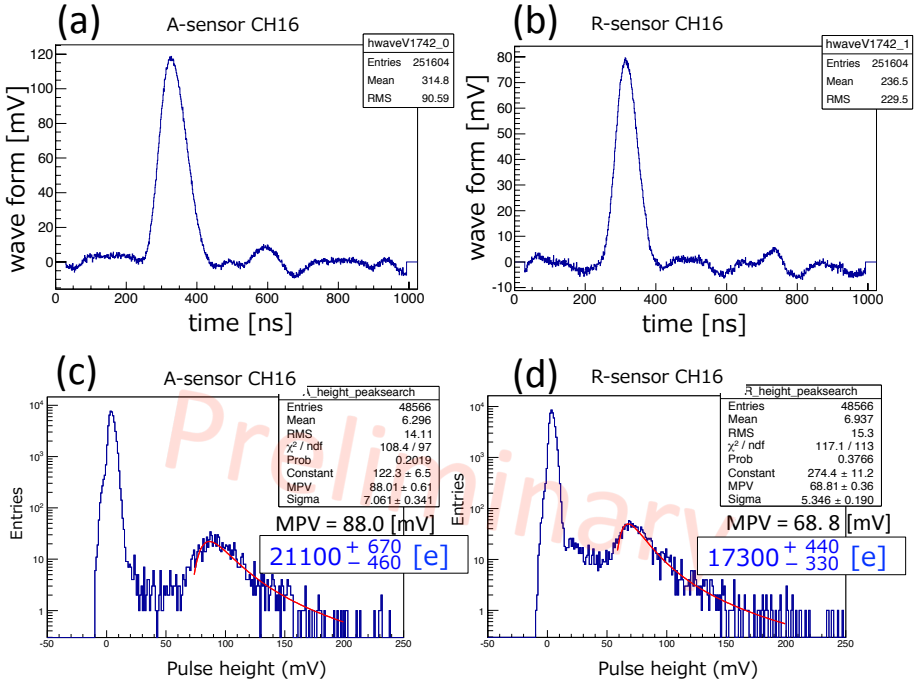

第 8 図　(a), (b) テストセンサーからの典型的な波形、(c)、(d) テストセンサーの波高分布

4.2 テストセンサーの時間分解能

第 9 図はテストセンサーで測定された ToT と時間分布の関係を表している。時間の基準には時間分解能が 140 ps の BS を使用した。また閾値はノイズの 5σ に設定した。ToT の違いによって 20 ns 以上のタイムウォークがあることが分かる。タイムウォークによる広がりは SlitA2013 性能評価の結果と無矛盾である。この結果から、得られた ToT に対してタイムウォークによる時間の広がりを補正すると時間分解能が改善できると予想される。第 10 図はタイムウォーク補正前後でのテストセンサーの時間分布である。補正前は σ_A=3.6 ns、σ_R=5.6 ns であり、補正後は $\sigma_{A\ corr}$=2.4 ns、$\sigma_{R\ corr}$=2.6 ns となった。このことから ToT によるタイムウォーク補正により、時間分解能が 1.5 倍から 2 倍改善し、実際の測定でも有効であることが分かった。

§5. ま と め

J-PARC E34 実験ではミューオン $g-2$ を 0.1ppm の精度で測定し、EDM を $10^{-21}\ e\cdot\mathrm{cm}$ の感度で探索することを目指している。実験に使用する陽電子飛跡検出器にはシリコンストリップセンサーの使用を検討しており、テストセンサーと読み出し回路試作機を製作した。信号となる 200 MeV 以上の陽電子に対する応答を調べるため、200 MeV/c の陽電子ビームを照射し、波形と時間を測定した。その結果、SN 比は実際の測定環境下において要求値 15 以上を達成することが見積もられた。また時間分解能は σ_A=3.6 ns、σ_R=5.6 ns であり、ToT によるタイムウォーク補正により $\sigma_{A\ corr}$=2.4 ns、$\sigma_{R\ corr}$=2.6 ns と一定の効果があることが分かった。タイムウォークは要求値よりも大きな値となっているが、この結果に対しては次期試作機である Slit128A において波高のゲインを増大させることにより、要求を達成する見込みである。

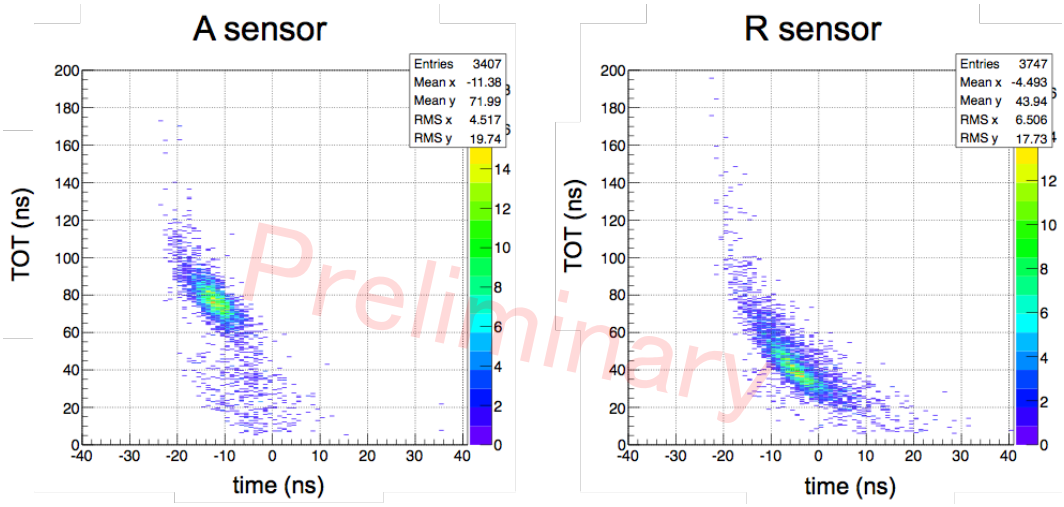

第 9 図　ToT と時間分布の関係

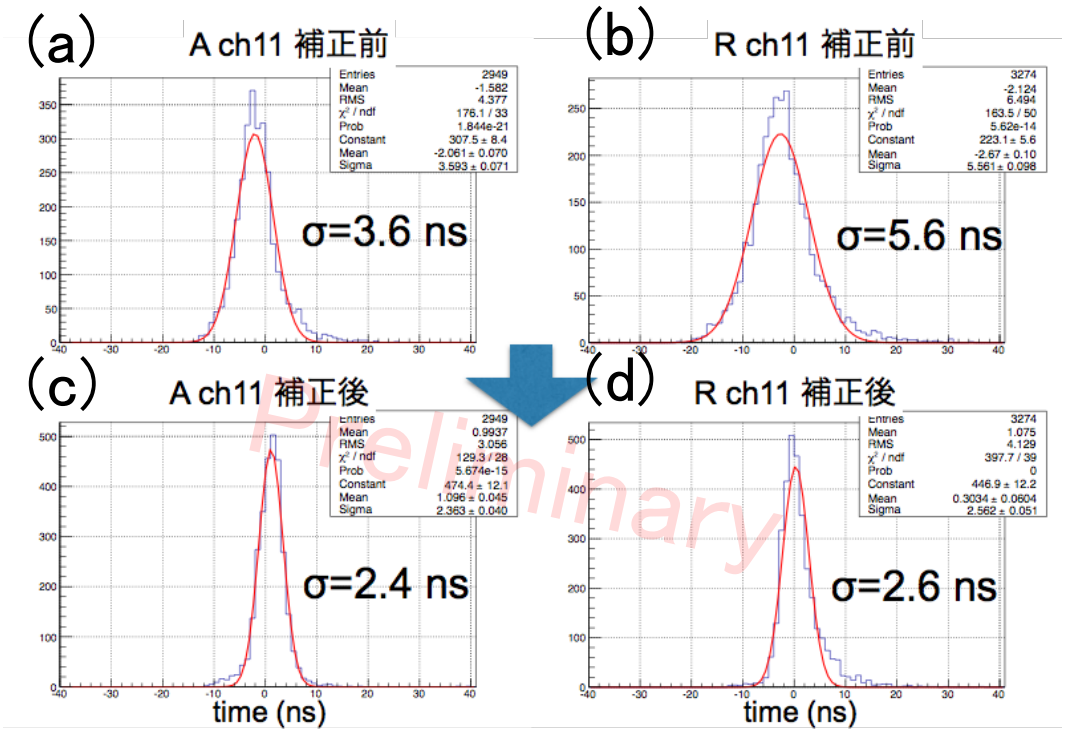

第 10 図　(a)、(b)ToT によるタイムウォーク補正前の時間分布、(c)、(d) 補正後の時間分布

謝　辞

本研究にあたって、石川 貴嗣さん、宮部 学さんを始め、東北大 ELPH の方々には大変お世話になりました。この場を借りて深く御礼申し上げます。

参　考　文　献

[1] G. W. Bennett *et al.*: Final report of the E821 muon anomalous magnetic moment measurement at BNL. Phys. Rev. **D73**, p. 072003, (2006).

[2] G. W. Bennett *et al.*: Improved limit on the muon electric dipole moment. Phys. Rev. **D80**, p. 052008, (2009).

[3] N. Saito *et al.*: Conceptual Design Report for The Measurement of the Muon Anomalous Magnetic Moment $g-2$ and Electric Dipole Moment at J-PARC, Conceptual Design Report (KEK), (2011).

[4] K. Ueno *et al.*: IEEE Nucl. Sci. Symp. Conf. Rec. (2013)

[5] 調 翔平、他: J-PARC ミューオン $g-2$/EDM 実験:シリコンストリップ検出器用 ASIC の性能評価, ICEPP Symp. 2014. (2014)

[6] 長澤 翼、他: J-PARC muon $g-2$/EDM 精密測定実験: シリコンストリップ検出器試作機のビームを用いた性能評価, 日本物理学会第 70 回年次大会 (2015)

(ELPH Experiment : #2784)

Performance evaluation of the readout electro circuit for the PWO counters in the J-PARC E13 experiment

M. Nakagawa[1], N. Ichige[2], T. Koike[2], Y. Sasaki[2], H. Tamura[2], M. Ukai[2], T. O. Yamamoto[2], and Y. Yamamoto[2]

[1]*Department of Physics, Osaka University, Toyonaka, 560-0043*
[2]*Department of Physics, Tohoku University, Sendai, 980-8578*

We are planning to perform a high-precision γ ray spectroscopy using the (K^-, π^-) reaction in the J-PARC K1.8 beam line (J-PARC E13). We use the PWO ($PbWO_4$) scintillation counters in order to suppress backgrounds in the γ ray spectrum from the excited states of Λ hypernuclei. At the same time, we aim to obtain the inclusive missing-mass spectrum for Λ and Σ hypernuclei via the (K^-, π^-) reaction at the beam momenta of 1.5 GeV/c and 1.8 GeV/c.

Thus, the excited state of Σ hypernuclei will be produced. Especially, we expect the observation of the excited state of Σ hypernucleus owing to a high momentum transfer. However, it could be difficult to clearly distinguish the excited state whose natural width is broad from a large amount of background events coming from the Σ quasi-free production in the missing-mass region. Thus, it is needed reduce the background coming from quasi-free events using energy deposit information of charged particles, which originate in hyperon decay, in the PWO counters.

In order to obtain the energy information, a conventional QDC will be used. We have to consider trigger latency of 1 μs in our DAQ system to obtain the ADC information. Then the analog signal of PMT collecting photons from PWO crystals is delayed by the delay chip. The readout circuits using three types of delay chips with different impedance (50, 100 and 300 Ω) were made in order to select the best chip. The signal from PMT is divided at ratio of 10 : 1 to a TDC line for the background suppressor and an ADC line for the energy measurement.

We tested the readout electro circuit at the electron beam line in the GeV-γ experimental area in the Research Center for Electron Photon Science (ELPH), in June 2014. We performed the on-beam experiment for performance evaluation of the ADC line and the off-beam experiment for performance evaluation of the TDC line. As the result of performance evaluation under the on-beam condition, it was difficult to discuss the energy linearity of the PWO counter. We assumed the saturation effect was seen in the high energy deposit side in the spectrum. In addition, we checked the difference of performance of the delay chips. The same energy resolution were obtained for all type of delay chips.

As the result of performance evaluation under the off-beam condition, performance deterioration of the TDC line due to the splitting of the PMT signal and the insertion of the delay chips was not seen for the detection of Compton scattered γ rays, which are backgrounds in a γ ray spectrum, in the off-beam measurement using a ^{60}Co source.

As these results, we concluded that the performance of the PWO counters was not changed if we used the delay chips. We will use the 300 Ω impedance delay chip because of usability in making the readout board.

§1. Introduction

The investigation of both Λ-$\boldsymbol{N}$ and Σ-$\boldsymbol{N}$ interaction is essential for the understanding of the YN interaction in the S=-1 sector. However, the Σ-$\boldsymbol{N}$ interaction is not understood precisely yet due to lack of experimental data. A Σ particle is basically not bound in nuclei except for the ${}^{4}_{\Sigma}$He hypernucleus because the spin-isospin averaged Σ-nucleus potential is repulsive [1]. Then, the ${}^{4}_{\Sigma}$He system was theoretically analyzed in order to reveal the property of the Σ-$\boldsymbol{N}$ interaction in each spin-isopin state. However, since the observed bound state was s-state (0^{+}), only the contribution from the s-wave of the Σ-$\boldsymbol{N}$ interaction was studied [2]. In order to extract the property of the p-wave, the experimental study of the exited state of this system was suggested [3]. Therefore, experimental studies of the exited state of this system are awaited in order to understand the property of the p-wave of the Σ-$\boldsymbol{N}$ interaction.

We are planning to perform a high-precision γ ray spectroscopy using the $(\boldsymbol{K}^{-}, \pi^{-})$ reaction in the J-PARC K1.8 beam line (J-PARC E13) [4]. The purpose of the J-PARC E13 experiment is to obtain the inclusive missing-mass spectrum for Λ and Σ hypernculei via the $(\boldsymbol{K}^{-}, \pi^{-})$ reaction at the beam momenta of 1.5 GeV/c and 1.8 GeV/c. The wide momentum acceptance of the pion spectrometer named the SKS-Minus system enables us to obtain such a inclusive spectrum. In addition, we simultaneously measure γ rays from excited states of Λ hypernuclei using the germanium detector array, Hyperball-J. In the J-PARC E13 experiment, a liquid helium target which is 3.0 g/cm^2 in thickness, will be irradiated with high momentum $\boldsymbol{K}^{-}$ beams. Hence, the momentum transfer will be changed from 200 MeV/c to 500 MeV/c depending on the reaction angle. The production of the exited state of ${}^{4}_{\Sigma}$He is expected. On the other hand, the production of the ground state of ${}^{4}_{\Sigma}$He is suppressed. Thus, an opportunity to study the excited state of ${}^{4}_{\Sigma}$He is given us by using the high-momentum $\boldsymbol{K}^{-}$ beams for the first time. However, it could be difficult to clearly observe the excited state whose natural width is broad because of a large amount of background events coming from the Σ quasi-free production in the same mass region. Thus, it is needed reduce the background coming from quasi-free events using PWO ($PbWO_4$) scintillation counters used as a background suppressor in Hyperball-J system. The PWO counters are installed around the germanium detectors to suppress background events in γ ray spectrum such as a Compton scattering or hadron penetration. Since the energy of decay particles coming from the $\Sigma\boldsymbol{N} \rightarrow \Lambda\boldsymbol{N}$ conversion in Σ-hypernucleus and an escaped Σ particle in the quasi-free Σ production are different, we are able to reduce the quasi-free events by measuring the energies of the decay particles by the PWO counters.

§2. PWO Counters

We introduce the PWO counters installed in the Hyperball-J system for the background suppression. The purpose of the germanium detectors is to measure the γ rays from the excited states of hy-

pernuclei. The one of background source is Compton scattering events in the germanium crystals. The PWO counters suppress the Compton background events by detecting γ rays originated from the Compton scattering. Hence, the germanium detectors are surrounded by the PWO counters.

The PWO counters consisted of $PbWO_4$ crystals and PMTs. The major feature of the PWO crystal is shown in Table1. The PWO crystal is often used as a calorimeter because of thier high effective atomic number and high density. The decay constant is 6 ns shorter than other inorganic scintillator. The scintillation lights are one hundredth in comparison with a NaI scintillator. Since the PWO crystal at the room temperature emits only 0.4 photo-electrons for 100 keV γ ray, we use the doped PWO crystal and decrease its temparature in the J-PARC E13 experiment in order to increase the number of photon.

Table 1. Features of the PWO crystal [5]

effective atomic number	76
density [g/cm^3]	8.28
radiation length [cm]	0.89
decay constant [ns]	6
photon number [NaI=100]	1
γ ray absorption [%]	67

Since the minimum energy of γ ray from the Compton scattering is as low as a few 100 keV, the threshold of the discriminator is set to a few 10 keV in order to detect such a low energy γ ray. In the original plan, we will use only the timing information for the background suppression . However, the energy of decay particles shuld be also measured in order to reduce the background coming from the quasi-free Σ production in the missing-mass spectrum. In addition, the energy of decay particles emitted from the hypernuclei and quasi-free Σ is as high as a few 100 MeV.

We need to understand the response of the PWO counters for high energy deposit. In addition, the change of the performance of the PWO counters as the Compton suppressor when we obtain the TDC and the ADC simultaneously.

§3. Readout electro circuit

In order to obtain ADC information, we have to consider trigger latency of 1 μs in our DAQ system. Although we usually use cables to wait a trigger, it is not realistic to prepare cables for such a requirement because the number of channels of the PWO counters is 214. Hence, we use delay chips instead of cables. In addition, when we use TDC and ADC simultaneously, the signal line has to be splited. If a signal split ratio of the TDC line and the ADC line is $1:1$, each signal height becames a half. In this situation, it is difficult to be discriminated with 0.5 p.e. threshold without amplification because of the small signal height. We have to keep the detection efficiency of the PWO counters as the Compton suppressor. Thus, the split ratio of the TDC line and the ADC line is set $10:1$.

Therefore, we prepared the electro circuit which splits signals and delay the signal in the ADC line. Most of all circuits usually have the input impedance of 50 Ω. If there is a delay chip with the input

impedance of 50 Ω and the delay time of 1 μs, such a delay chip should be selected. However, such a delay chip is not available as commercial products. Hence, we prepare three kinds of the delay chips, with different input impedance as summarized in Table 2. In this paper, three delay chips are labeled as

Table 2. Properties of the delay chips

	delay chips		
impedance [Ω]	50	100	300
delay/chip [ns]	100	300	1000
number of chips	9	3	1

the 50 Ω delay chip, the 100 Ω delay chip and the 300 Ω delay chip, respectively. Since our DAQ system require the delay time of 1μs, the number of needed delay chips are 9 for the 50Ω chip, 3 for the 100Ω chip, and 1 for the 300Ω chip in each channel. We prepared three kinds of electro circuits using these delay chips. In order to suppress signal reflection, impedance matching is taken into account for each circuit.

The purpose of the test experiment is to decide the most suitable delay chip by checking the performance of three kinds of the circuits, and to study the change of the performance of the PWO counters as a Compton suppressor.

§4. Experiment

We tested the readout electro circuit for the PWO counters with the beam and without the beam at the electron beam line in the GeV-γ experimental area in the Research Center for Electron Photon Science (ELPH), in June 2014.

We used the electron beam whose size is 20 mm^2 with the beam energy of 250, 450 and 650 MeV. In this experiment, the PWO counters are not able to stop the electromagnetic shower caused by the electron beam due to the small size of PWO crystals. The detectors used in this experiment, that is, the Shower Veto counter (SV), the trigger counter (T1), and the PWO counters (PWO) are shown in Fig 1. SV rejected the shower events before T1. SV was a plastic scintillation counter which consisted of a plastic scintillator whose size is 200×200×10 mm^3 and the PMT. T1 was also a plastic scintillation counter which consist of a plastic scintillator 10×10×5 mm^3 and PMT. The PWO counters consisted of the PWO crystal whose size of 40×200×20 mm^3 and PMT. The DAQ system recorded TDC and ADC of all detector with the T1 trigger. In addition, we also used FADC (Flash ADC) to record wave form. We took data to study the difference of the performance of the three types of delay chips (and cable delay) using the electron beam of 450 MeV, and data to check the energy linearity of the PWO counter at the beam energies of 250, 450 and 650 MeV.

We measured the change of the Compton suppressor performance using the NaI counters (NaI1 and NaI2) instead of the germanium detectors. Two NaI counters and three PWO counters were placed as shown in Fig 2. We used the radioactive source of ^{60}Co which emit the γ rays of 1173 and 1333 keV from cascade decay. The data taking required NaI1 and NaI2 coinsidence trigger which the γ rays of 1173

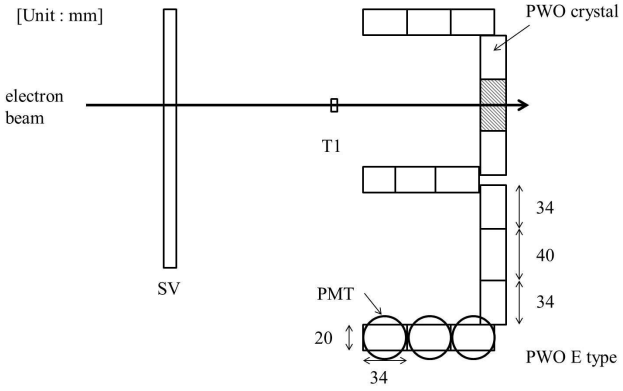

Fig.1. The schema of the setup for the performance evaluation using the electron beam.

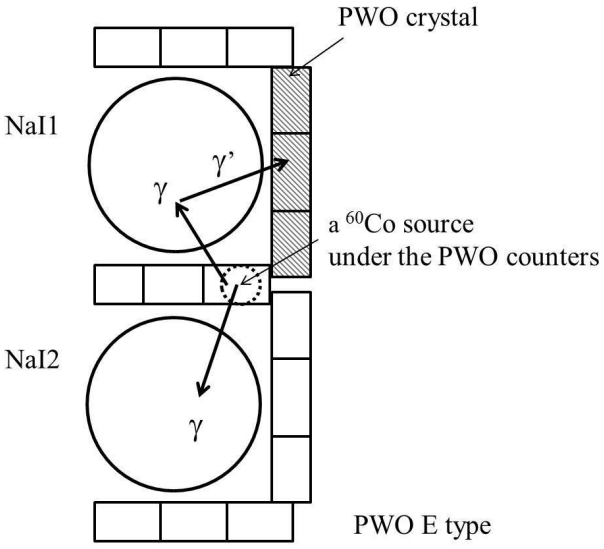

Fig.2. The schema of the setup of the measurement using a ^{60}Co source without the beam.

and 1333 keV irradiate NaI1 and NaI2 at the same time. In this measurement, ADC data for NaIs and TDC data for PWO counters were taken with this trigger by changing delay chips. In addition, reference data was taken without the ADC line of PWO counters.

§5. Analysis and result

In the analysis of data taken with the beam, we use the center segment of PWO counters as shown in Fig 1. In addition, we do not use data of SV because of almost no shower events after our analysis.

On the other hand, we use the three segments of PWO counters which is shown with shaded area in Fig 2 in the analysis of data taken without the beam.

The energy linearity

We took data at the beam energies of 250, 450 and 650 MeV. We used the 100 Ω delay chip in this measurement. The energy distribution for each data are shown in Fig 3. In addition, the correlation between the beam energy and the mean value of each energy distribution are plotted in Fig 4. It is difficult to discuss the energy linearity of the PWO counter. Then, we compare data of this experiment with data of the Geant4 simulation. In addition, simulation data is convoluted with Gaussian by considering electric noise in the actual condition. As a result, the experimental data is not reproduced by the convoluted simulation data. The experimental data have shorter tail structure in higher energy side than the simulation data. Thus, we assume the saturation effect is seen in the high energy deposit side in the spectrum.

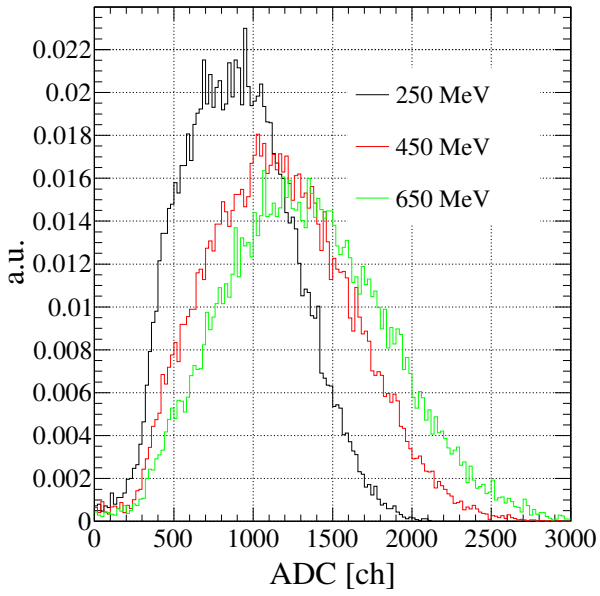

Fig.3. The energy distribution for each beam energy.

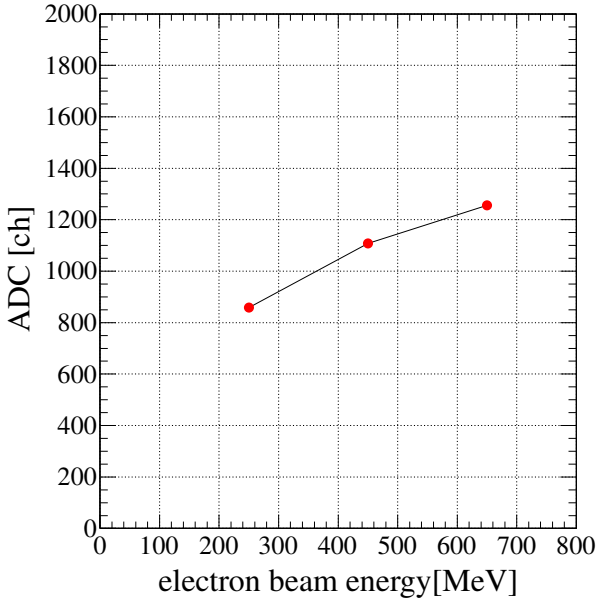

Fig.4. The correlation between the mean value of each energy distribution and the beam energy.

The difference of performance of the delay chips

We check the difference of the delay chips and cable delays as a reference. For this purpose, data taken with the beam energy of 450 MeV was analyzed. In Fig 5, the difference of performance of the delay chips and the cable delay is shown. The horizontal axis is the normalized energy when setting the peak value of the distribution for the cable delay to 1. In addition, the virtical axis is nomalized by the number of the total events. The performance of 50 Ω delay chip is consistent with the performance of the cable delay whose impedance is 50 Ω. In addition, the gain of the 100 Ω delay chip is high. In contrast, the gain of the 300 Ω delay chip is low.

As we mentioned in the previous section, the energy resolution of the PWO counter including the electro circuit is not obtained by the energy distribution directly, because those energy distribution are spread by the escape of a part of the electromagnetic shower. In order to obtain the change of the energy resolution, we compared shape of each distribution by normalizing all the peak position to 1 as shown in Fig 6. In addition, the virtical axis is nomalized by the number of the total events. Since all the shapes of distributions are the same, the energy resolution is not affected by delay chips.

The change of the Compton suppressor performance

We evaluated the effect to the TDC line, that is, the performance of the Compton suppressor from our electro circuits by changing delay chips. We analyzed data taken without the beam. In this analysis, the events lying around the photoelectric absorption peak of 1333 keV in the energy spectrum of NaI2 were gated in order to guarantee that γ ray of 1173 keV entered NaI1. Then, we check the energy distribution of γ rays which is detected by NaI1. Here, the suppression factor is defined as the energy

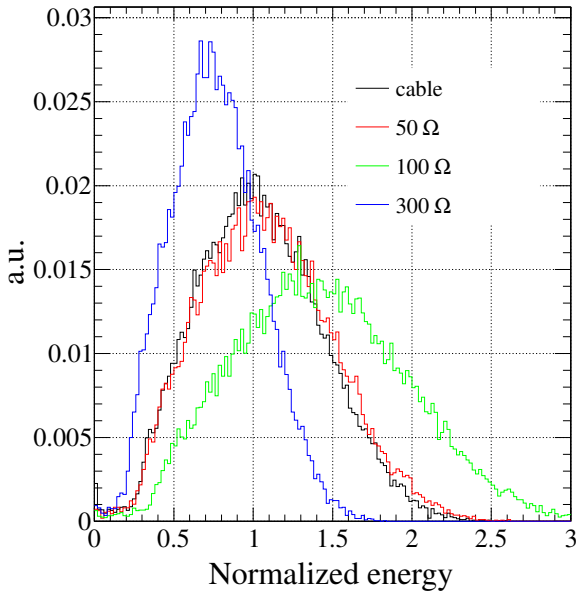

Fig.5. The normalized energy distribution using delay chips and the cable when setting the peak position for the cable delay to 1.

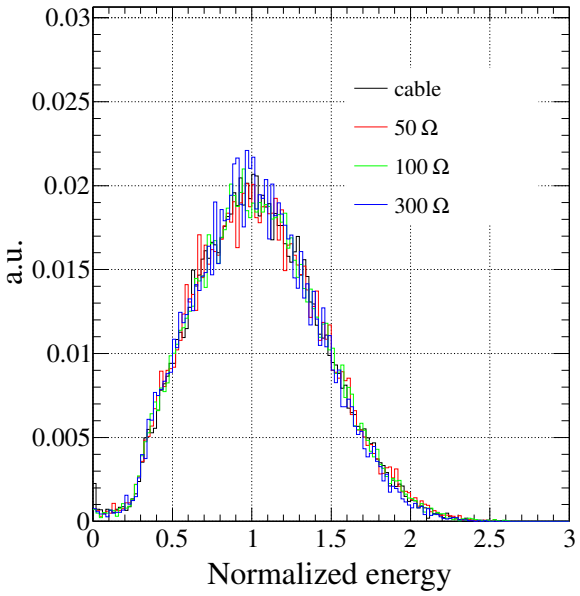

Fig.6. The normalized energy distribution when setting all the peak position to 1.

distribution of NaI1 ratio of requiring PWO counters hits and not requiring it. The suppression factor is shown in Fig 7. No divide (no delay chip) for the reference is also shown in this figure. The suppression factor is around 0.1 in Compton scattering region. The suppression factor decrease over 800 keV because the γ ray which caused back scattering hardly entered the PWO counters. However, the γ ray which caused mutiple scattering often entered the PWO counters.

From these results, we estimated performance deterioration of the Compton suppressor by adding our electro circuit. The change of Compton suppressor factor is defined as the ratio of the Compton suppressor factor using dividers and no divide. The change is shown in Fig 8. The deterioration of the Compton suppressor performance is not observed in each delay chip blow 800 keV. On the other hand, it is observed over 800 keV.

§6. Conclusion

We evaluted the three performances of the PWO counters. Although we were not able to obtain the energy linearity in this experiment, the saturation effect was implied because experimental data and the Geant4 simulation result are in disagreement in the high energy side. As a result that the PWO counter is irradiated by same electron beam in each circuit, the performance of the delay chips is same, whose gain is changed. The detection efficiency for the Compton scattering event is no affected by adding the readout electro circuit for all the delay chips. As these results, we conclude that the performance of the PWO counters is not changed if we use the delay chips. We will use the 300 Ω delay chip because of usability of making the readout board.

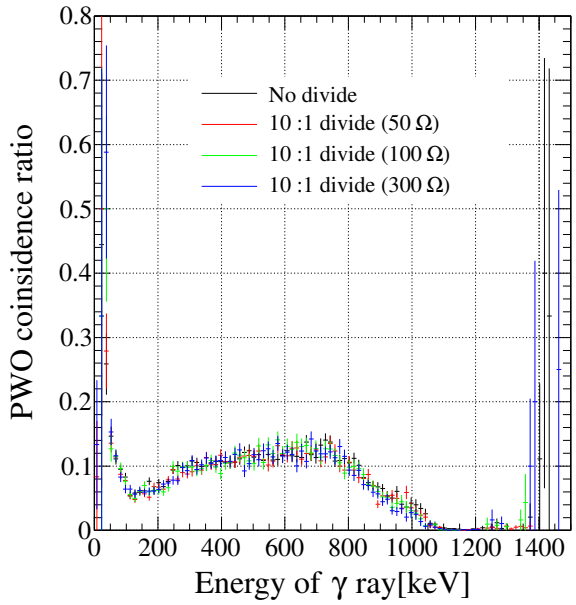

Fig.7. The PWO coinsidence ratio

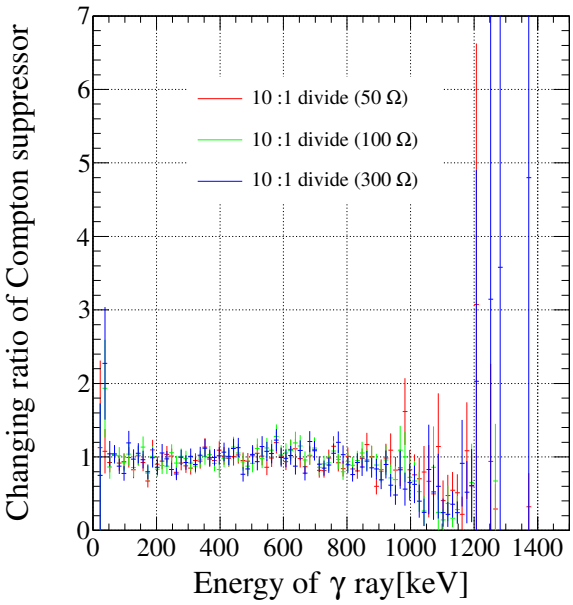

Fig.8. The change ratio of the Compton suppressor performance

Acknowledgment

We would like to acknowledge the staff of the ELPH group for their efforts of keeping the stable operation during the beamtime.

References

[1] T. Nagae *et al.*: Phys. Rev. Lett. **80** (1998) 1605.

[2] T. Harada *et al.*: Nucl. Phys. A**507** (1990) 715.

[3] T. Harada *et al.*: Phys. Lett. B**740** (2015) 312.

[4] H. Tamura *et al.*: J-PARC Proposal E13, Gamma-ray spectroscopy of light hypernuclei (2006) http://j-parc.jp/researcher/Hadron/en/pac 0606/pdf/p13-Tamura.pdf.

[5] M. Ishii *et al.*: Prog. Crystal Growth and Charact.23 (1991) 245.

(ELPH Experiment : #2798)

Development of drift chamber for the J-PARC E21 COMET experiment

H. Sakamoto[1], C. Wu[2,6], T. S. Wong[1], H. Yoshida[1], Y. Nakazawa[1], H. Katayama[1], T. Yamane[3], T. Ueda[1], D. Tsunemori[1], N. Yokoyama[1], H. Yong[6], A. Sato[1], Y. Kuno[1], J. Sato[3], Z. Zhang[2], R. P. Litchfield[4], and P. Dauncey[5]

[1]*Department of Physics, Osaka University, Toyonaka, 560-0045*
[2]*Institute of High Energy Physics (IHEP), China*
[3]*Department of Physics, Saitama University, Saitama, 338-8570*
[4]*University College London, UK*
[5]*Imperial College London, UK*
[6]*Nanjing University, China*

We carried out beam tests using prototypes of drift chambers for J-PARC E21 COMET experiment to measure gas gain, spatial resolution, and hit efficiency using three sets of gas mixtures, He:iC$_4$H$_{10}$(90:10), He:C$_2$H$_6$(50:50), and He:CH$_4$(73:27) using two prototype chambers with sense wire of ϕ25 μm and ϕ30 μm. Results of the beam test analyzed by May 2015 are described in this report.

§1. Introduction

1.1 J-PARC E21

A neutrino-less muon-electron conversion process in muonic atoms that violates charged lepton flavor is forbidden in the Standard Model (SM). Assuming massive neutrinos the probability to occur this process would be about 10^{-52}, which is too small to detect. Some models beyond the SM predict that probability to occur this process would be order of 10^{-15}. Current experimental upper limit of the muon-electron conversion process had been set to be 7×10^{-13} by SINDRUM-II experiment at Paul Scherrer Institute (PSI) in 1999. Signature of muon-electron conversion process in muonic atoms is to detect mono-energetic electrons emitted from muonic atoms. Major background is electrons decayed in orbit (DIO) from muonic atoms, whose energy spectrum is continuous up to the energy of signal. Therefore in order to achieve a high sensitivity a discrimination of DIO electrons is essential. J-PARC E21 experiment (COMET) aims to search for the muon-electron conversion process with 10000 times higher sensitivity than the current upper limit in two stages. The first stage (Phase-I) [1] will start from 2017 with a single event sensitivity of 10^{-15} and the second stage (Phase-II) will start from 2020 with a single event sensitivity of 10^{-17}. Schematic view of the beam line for Phase-I is shown in Fig.1.

1.2 COMET CDC

Cylindrical drift chamber (CDC) will be utilized to identify conversion electrons in Phase-I. CDC will be installed at the end of the muon beam line around muon stopping targets as shown in Fig.2. COMET CDC are required to measure momenta of electrons with an accuracy of about 200 keV/c (0.2%). Hit occupancy is required to be less than about 10% to suppress pile-up effects. To achieve high resolution on momentum measurement Helium-based gas mixture will be used to suppress multiple scattering. Sources contributing to hit occupancy are protons after muon capture, gamma rays after muon capture, DIO electrons, beam-related neutrons, and beam flash. Protons are easily discriminated using charge information. Most of DIO electrons of low energy with a high intensity cannot reach CDC region of inner radius of 50 cm. Beam-related neutrons and beam flash are suppressed by shielding around CDC.

A final design of the wire configuration had been determined in March 2014 according to comments by IPNS reviewer. We had selected three gas mixtures of CDC in Table 1. In view of multiple scattering, He:CH_4(80:20) prefers to others while in view of spatial resolution He:C_2H_6(50:50) prefers. In view of short drift time to reduce hit occupancy, He:C_2H_6(50:50) prefers.

Specification of sense and field wires is described in Table 2. Gas mixture and wire thickness are to be determined by prototype tests.

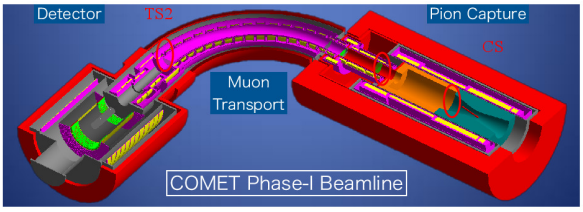

Fig.1. *Schematic view of beam line at Phase-I. A pion capture solenoid, 90 degree muon transport solenoid, and detector solenoid are installed.*

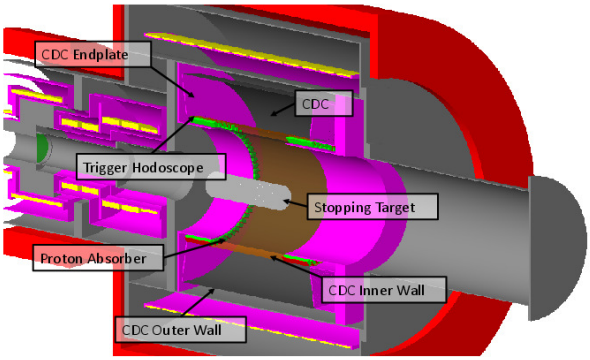

Fig.2. *Schematic view around CDC. CDC will be installed under 1 T solenoid to measure momenta of conversion electrons from muon stopping targets. [1]*

1.3 Prototype Chambers

We have built three sets of prototype chambers. First prototype had been built in October 2013 and cosmic-ray tests had been performed. Results of the cosmic-ray tests are described in the next section. Second and third prototype has been built in November 2014 for a beam test. Main differences of prototype I and II or III are stereo angle and field wire size. Prototype I and II are shown in Fig.4 and Fig.5, respectively. Specifications of each prototype are summarized in Table 3.

Table 1. *Comparison of different Helium-based low-Z gas mixtures, where* X_0 *is the radiation length,* W *is mean energy to generate one electron-ion pair,* dE^{MIP}/dx*,* n_T^{MIP}*, and* n_p^{MIP} *mean is energy loss per cm, the number of electron-ion pairs per cm, and the number of primary ions per cm for minimum ionizing particles, respectively. [1]*

Gas	X_0 (m)	W (eV)	$\frac{dE^{MIP}}{dx}$ (keV/cm)	n_T^{MIP} (cm^{-1})	n_p^{MIP} (cm^{-1})
He:iC_4H_{10}(90:10)	1310	39	0.88	29	14
He:C_2H_6(50:50)	630	32	1.63	60	27
He:CH_4(80:20)	2166	39	1.47	17	11

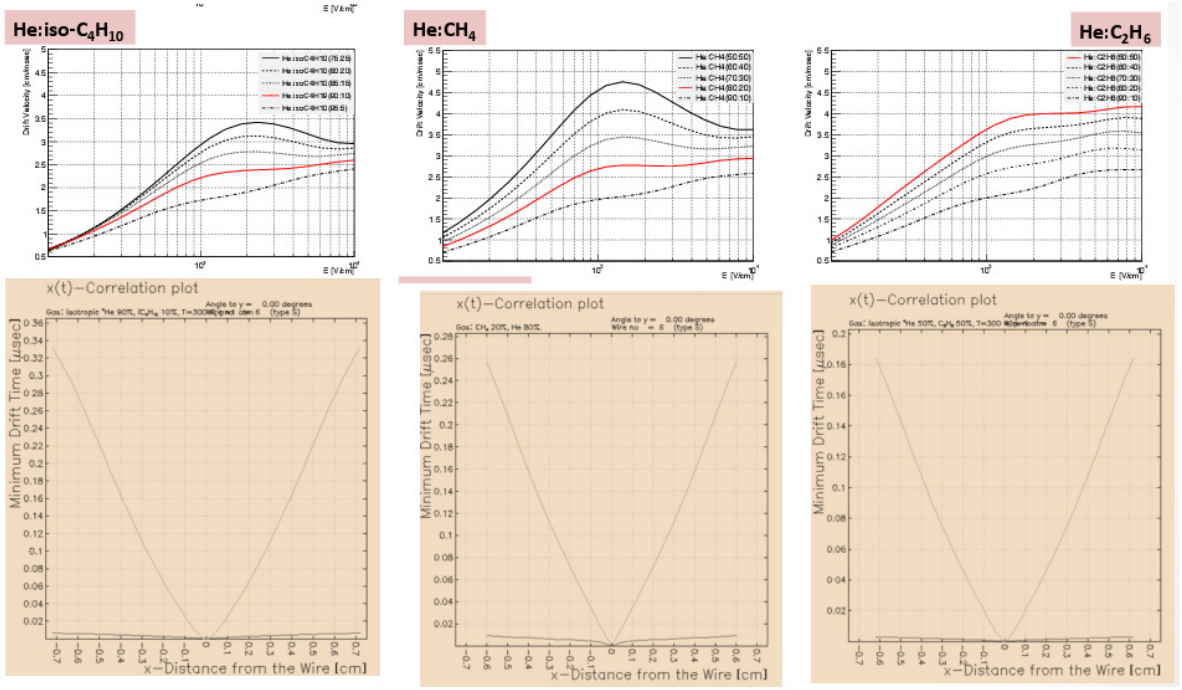

Fig.3. *Comparison of drift velocity as a function of electric fields in top and position-time relationship (XT curve) in bottom. [1]*

1.3.1 Cosmic-ray Tests by Prototype I

We have done cosmic-ray tests to measure spatial resolutions using prototype I without magnetic fields and with uniform magnetic fields of 1 T with cooperation of KEK cryogenic group in summer of 2014. Trigger counters of 20×20 cm with Multi-Pixel Photon Counter (MPPC) readout were set in top and bottom of the prototype. Four 64ch boards by REPIC with readout by optical cables were used to readout data. For all of the gas mixtures spatial resolutions (including tracking errors) under 1 T were measured to be less than 300 μm. The residual distribution is shown in Fig.6 and results on spatial

Table 2. *Main parameters of the CDC [1]*

Inner wall	Length	1490.3 mm
	Radius	496.0∼496.5 mm
Outer wall	Length	1577.3 mm
	Radius	835.0∼840.0 mm
Number of sense layers		20 (including 2 guard layers)
Sense wire	Material	Au plated W
	Diameter	25 μm
	Number of wires	4986
	Tension	50 g
Field wire	Material	Al
	Diameter	80 μm
	Number of wires	14562
	Tension	70 g
Cell	square	16.2-16.8 mm in azimuthal, 16mm in radial
	stereo layer	+/- 70mrad

Table 3. *Parameters of prototype chambers*

Prototype No.	I	II	III
Sense wire	ϕ30 μm Au plated W	ϕ25 μm Au plated W	ϕ30 μm Au plated W
Field wire	ϕ126 μm Al	ϕ80 μm Al	ϕ80 μm Al
Number of sense layers	11	11	11
Cell size	15 mm (w) $\times$ 16 mm (h)	16 mm (w) $\times$ 16 mm (h)	16 mm (w) $\times$ 16 mm (h)
Stereo angle	aprox. 25 mrad	aprox. +/- 70 mrad	aprox. +/- 70mrad
Wire length	60 cm	20 cm	20 cm
Wide angle coverage	30 deg.	8 deg.	8 deg.
Tension (sense, field)	50 g, 80 g	not measured	not measured
#/wires (sense, field)	199, 602	27, 72	27, 72
Readout board	64ch REPIC x4	48ch RECBE x1	48ch RECBE x1

resolutions are summarized in Table 5. In the cosmic-ray tests statistics were limited therefore we proposed to carry out a beam test to study hit efficiencies effectively.

§2. Beam Test

Purpose of the beam test is to test following items with He:iC$_4$H$_{10}$(90:10), He:C$_2$H$_6$(50:50), and He:CH$_4$(80:20) using prototype II (ϕ25μm sense wire) and prototype III (ϕ30 μm sense wire).

- Gas gain
- Position-time relation (XT curve)
- Spatial resolution
- Hit efficiency

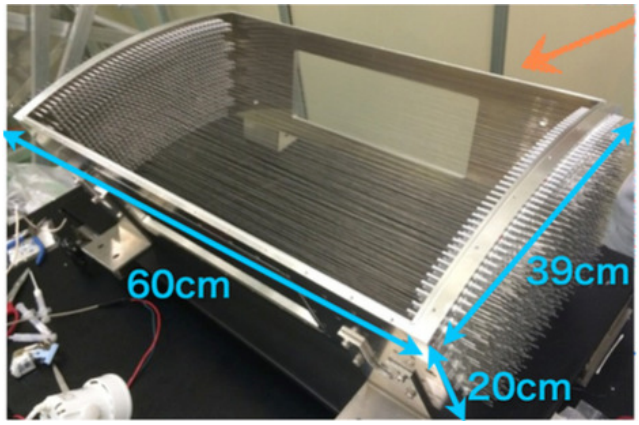

Fig.4. *Prototype I built at KEK*

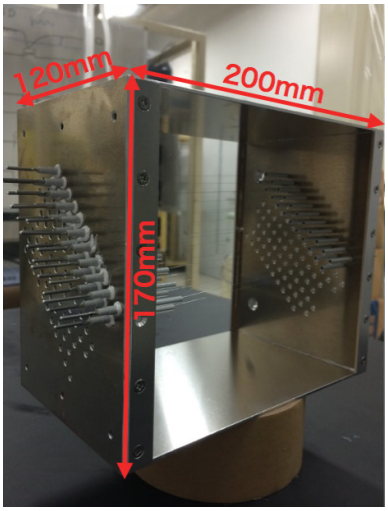

Fig.5. *Prototype II built at Osaka University*

Table 4. *Parameters of the cosmic-ray tests at KEK [1]*

Gas mixture	He:iC$_4$H$_{10}$(90:10)	He:C$_2$H$_6$(50:50)	He:CH$_4$(80:20)
HV of sense layers	1900 V	2600 V	2150 V
HV of guard layers	1200 V	1200 V	1200 V
Vth	3790 mV	3790 mV	3790 mV
Magnetic Fields	0 T, 0.6 T, 1.0 T	0 T, 1.0 T	0 T, 1.0 T

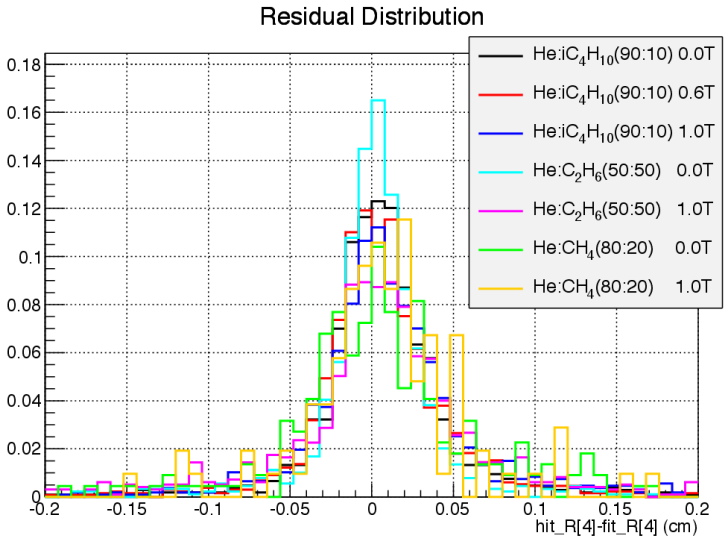

Fig.6. *Residual distribution measured at the prototype chamber I with cosmic-rays [1]*

Table 5. *Preliminary results on spatial resolutions measured by the prototype chamber [1]*

Gas mixture	Magnetic Fields	Spatial Resolution
He:iC$_4$H$_{10}$(90:10)	0 T	$225.1 \pm 11.2\ \mu m$
He:iC$_4$H$_{10}$(90:10)	0.6 T	$228.0 \pm 9.7\ \mu m$
He:iC$_4$H$_{10}$(90:10)	1 T	$265.9 \pm 18.0\ \mu m$
He:C$_2$H$_6$(50:50)	0 T	$186.1 \pm 7.6\ \mu m$
He:C$_2$H$_6$(50:50)	1 T	$249.8 \pm 16.3\ \mu m$
He:CH$_4$(80:20)	0 T	$232.1 \pm 91.5\ \mu m$
He:CH$_4$(80:20)	1 T	$266.9 \pm 59.4\ \mu m$

2.1 Setup

Momentum of electron beams was set to 460 MeV/c (Magnet current was set to 230 A). We used Tungsten of a thickness of 0.2 mm as a converter. Two prototype chambers II and III are installed in the beam line. Tracking chambers for reconstructing electron tracks were installed at upstream (T1X and T1Y) and downstream (T2X and T2Y) of the prototype chambers. P10 gas was used for tracking chambers. At the most upstream and downstream side scintillating counters of dimension of 30×30×3 mm and 30×30×5 mm were installed for making trigger signals. Distance of two scintillating counters was about 80 cm. Scintillating counters were read out by 1-inch PMTs. Each of prototype and tracking chambers was read out by a 48ch RECBE board developed by Belle II CDC group. In the underground NIM modules for trigger logic and power supplies of detectors, gas system, and a DAQ-PC were set. Trigger signal for monitoring trigger rates and Ethernet cable to log in the DAQ-PC were sent to the room on the 1st floor. Power supply for the tracking chamber was 2ch manual controlled module and 4ch remote controlled module by CAEN was used for prototype chambers. Schematic view of setup is shown in Fig.7.

2.2 Trigger Logic

Trigger signals were made by taking coincidence with the upstream and downstream PMTs. In order to avoid a high hit rate VETO of 100 μs long after beam injection was added in the trigger logic. Trigger signals were then delayed by 700 ns and sent to four readout boards. The diagram is shown in Fig.8.

2.3 Readout Board

For readout of prototype and tracking chambers, 48ch RECBE boards shown in Fig.9 were used. A RECBE board has eight ASD (Amp-Shape-Discriminator) chips, eight ADC chips, and a FPGA. Output of the ASD are an amplified analog signal and discriminated digital signal. Threshold of discriminator is common to all of 48ch. The analog signal is digitized by the following ADC chips then ADCs are recorded by the FPGA in every 32 ns. The digital signal is sent to the FPGA and its rising edge is measured using 1 ns clocks in the FPGA. Once a trigger signal is received ADCs and TDCs in a given window size with a event header is sent to SiTCP [4]. SiTCP sends data through TCP to a DAQ PC. SiTCP also

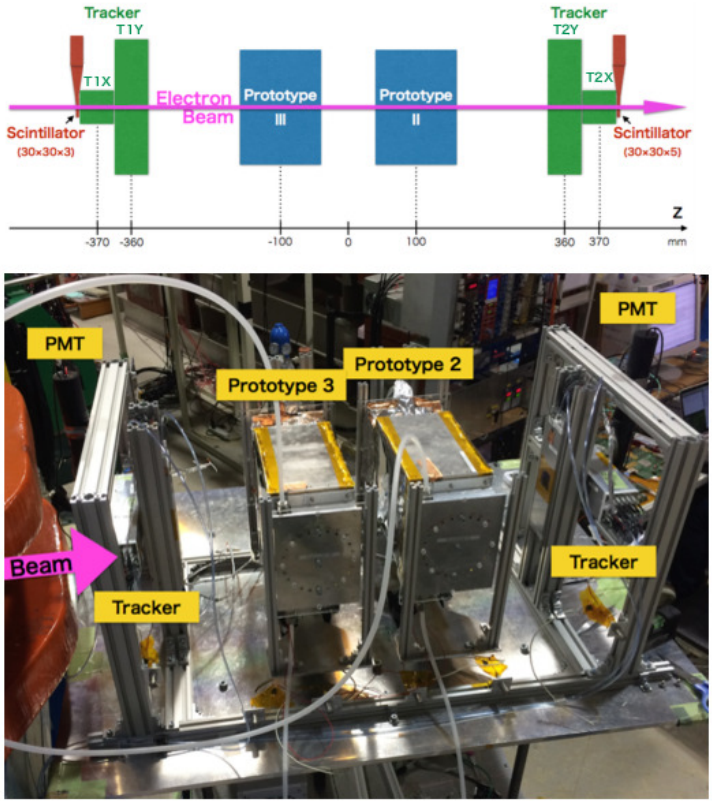

Fig.7. *Setup at beam test. Electron beam of 460* MeV/c *pass thorough from left and triggered by upstream and downstream PMT.*

communicates through UDP to realize a slow control. Threshold, window size, and window position can be set remotely by a slow control. In the beam test for the purpose of synchronizing clocks among four RECBE boards an external clock of 62.5 MHz of 2.5 V was used. Window size was set as 1 μs.

2.3.1 Firmware

There are three versions of firmwares in the RECBE board; raw mode, suppress mode, and semi-suppress mode. In raw mode, ADC and TDC at every 32 ns in a given window size for all channels are sent to PC. In suppress mode, summed ADC in a given window size and first two TDCs only for hit channels are sent to PC. In semi-suppress mode, all ADC in a given window size and first three TDCs only for hit channels are sent to PC. In the beam test it was required to record waveform with keeping data size small semi-suppress mode was used.

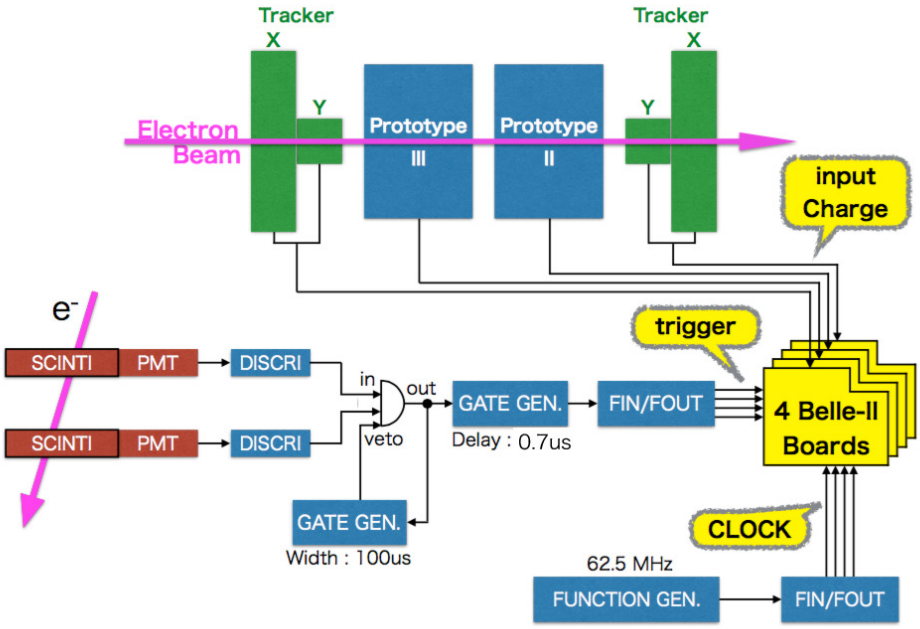

Fig.8. *Trigger logic at beam test. Coincidence of two PMTs with 100 μs VETO is sent to four RECBE boards [2]*

2.4 DAQ

DAQ-Middleware [5] developed by KEK online group was used to do online monitoring and save data in storage.

2.5 Gas System

P10 gas was flowed to the upstream and downstream tracking chambers in series with about 50 cc/min. Helium gas was mixed with $i C_4H_{10}$ or C_2H_6 or CH_4 using a mass flow controller by HORIBA. Flow rate was set to 200 cc/min at gas exchange then reduced to 20 cc/min after gas exchange finished. P10 and Helium-mixed gas lines were attached with each exhaust ports. In order to prevent backward flow bubblers were set before exhaust ports after the run in Dec 7.

2.6 Measurements

Five shifts assigned for this beam test are scheduled as follows.

Dec 5 Beam tuning and trigger logic check.

Dec 6 Noise reduction of tracking and prototype chambers

Dec 7 Data taking of He:$i C_4H_{10}$(90:10)

Dec 9 Data taking of He:C_2H_6(50:50)

Dec 11 Data taking of He:CH_4(73:27) and He:$i C_4H_{10}$(90:10)

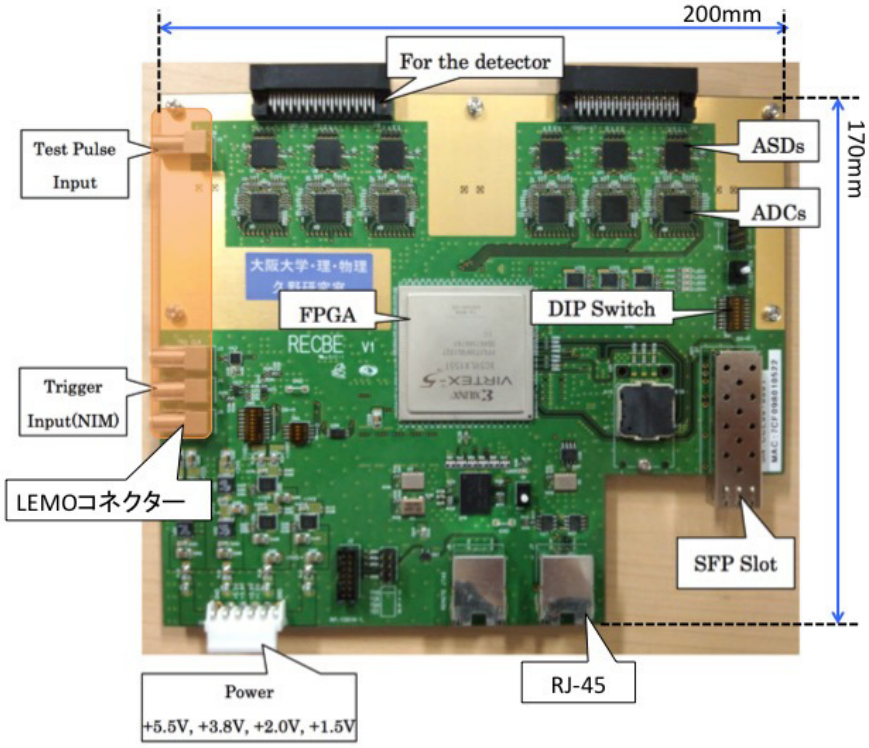

Fig.9. *48ch RECBE board developed by Belle II CDC group. Function is to amplifier signals and sample waveform and measure time of discriminated signals. Data is sent to DAQ PC via SFP slot where either copper twisted cable or optical cable can be attached. External clock and trigger signal are received from LEMO connectors or RJ-45. In the beam test LEMO connectors are used. Test pulse input is used to test ASDs.*

In the first day trigger rate was measured with adding VETO after beam injection to prevent high trigger rate. With 100 μs long VETO a trigger rate was about 800 Hz. Efficiency of data taking was more than 95% through runs. In the second day noise reduction of trigger and prototype chambers was performed mostly by improving grounding around chamber and RECBE boards. HV scanning and threshold scanning of tracking chambers were performed. In the third day data taking of He:iC$_4$H$_{10}$(90:10) was done. HV scanning and threshold scanning were performed. As described in Section 3.1 we had problem on ADC of prototype chambers therefore we requested one more shift at the end to take data of this day. In the fourth day data taking of He:iC$_2$H$_6$(50:50) was done. HV scanning and threshold scanning were performed. In the last day data taking of He:iCH$_4$(73:27) was done. Our proposed ratio of methane gas was 20% but set to 27% by mistake. HV scanning and threshold scanning were performed. After that data taking of He:iC$_4$H$_{10}$(90:10) was carried out. In the last, we moved prototype chambers to take data with different X positions and angles with respect to X axis and Y axis for testing dependency of cell shape and beam direction.

2.7 Analysis and Results

2.7.1 Gas gain

Gas gain is calculated as below.

$$\text{Gain} = \frac{N_t}{N_{pair}^{cell}},$$

$$N_{pair}^{cell} = N_{pair} \frac{dE^{cell}}{dE/dx}$$

where N_t is the number of total electrons measured, N_{pair}^{cell} is the number of primary ions generated by an electron beam in a cell, N_{pair} is the number of electron-ion pairs per cm, dE^{cell} is an energy deposit in a cell, and dE/dx is an energy deposit in a gas per cm. N_{pair} and dE/dx are described in Table 1. dE^{cell} is calculated by G4beamline simulation [3] as shown in Table 6. N_t is calculated from a peak of summed ADC which is converted into charge using a calibration data as shown in Fig.10. Measured gas gain curve for each gas mixtures at prototype II and III are shown in Fig.12.

Table 6. *Parameters used in gas gain calculation [2]*

Gas mixture	dE^{cell} (keV/cell)	N_{pair}^{cell} (1/cell)
He:iC$_4$H$_{10}$(90:10)	0.983	32.39
He:C$_2$H$_6$(50:50)	1.180	43.44
He:CH$_4$(80:20)	0.389	4.50

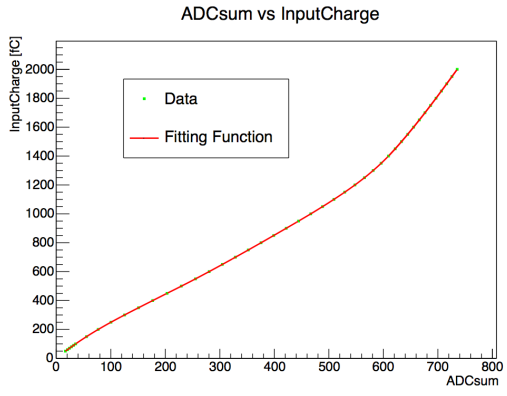

Fig.10. *Relationship between input charge and summed ADC taken by RECBE board [2]*

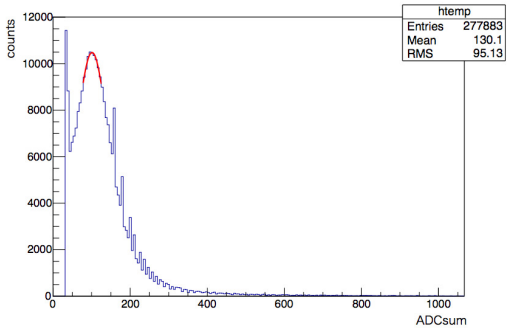

Fig.11. *Summed ADC distribution after pedestal subtraction of Prototype II with He:iC$_4$H$_{10}$(90:10) at 1730 V [2]*

2.7.2 XT Curve

A method of measuring position-time relationship is as follows. Position is estimated as closest approach of testing sense wire from an reconstructed track. In order to reconstruct tracks XT curve of tracking chambers should be calibrated firstly. Three hits at the upstream and downstream tracking chamber are used to make an track using a XT curve calculated by Garfield simulation. The track is extrapolated to a testing wire of tracking chamber to make its XT curve. By fitting the XT curve of the

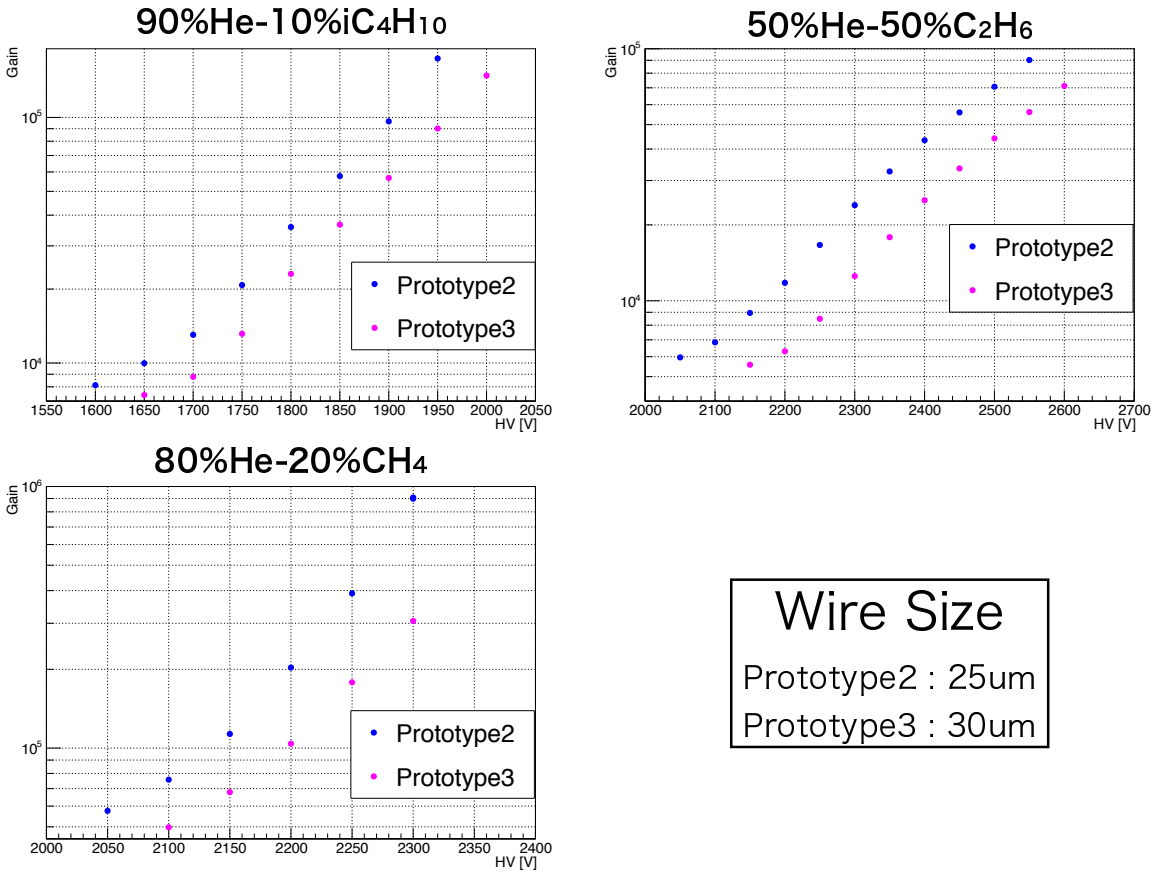

Fig.12. *Measured gain curve for each of gas mixtures. Gain of prototype II is roughly twice as large as that of prototype III [2]*

testing wire a new XT curve is estimated. Using the new XT curve track is again reconstructed and extrapolated to the testing wire. This iteration was done in three times. Chi-square distributions at each of iteration are shown in Fig.13. The XT curve of T1X of wire#0 obtained after three iterations is shown in Fig.14.

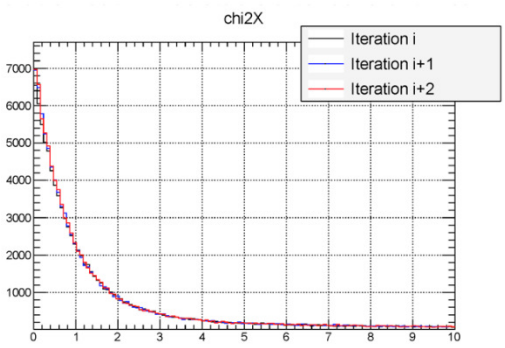

Fig.13. *Chi-square distributions of reconstructed tracks in X-axis at each iteration steps.*

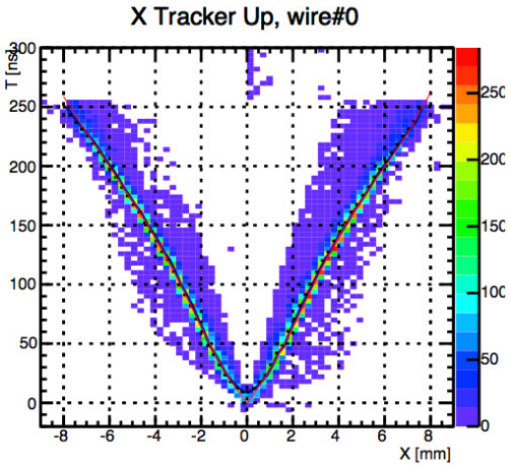

Fig.14. *XT-curve of wire#0 in T1X (upstream tracking chamber) after iterations.*

After that XT curves of all tracking chambers are calculated tracking was performed in each of X and Y directions individually. Residual distributions on X and Y with different chi-square cuts are shown in Fig.15. From this figure cut of chi-square at 7 is applied. Tracking efficiencies of X and Y tracker are about 50% so that net efficiency is about 25%.

Once X and Y positions at the upstream and downstream are determined, 3-dimensional track was made. Using the 3D-track closest approaches to wires at prototype chambers are calculated finally. XT curve of the prototype II of the central wire is shown in Fig.16.

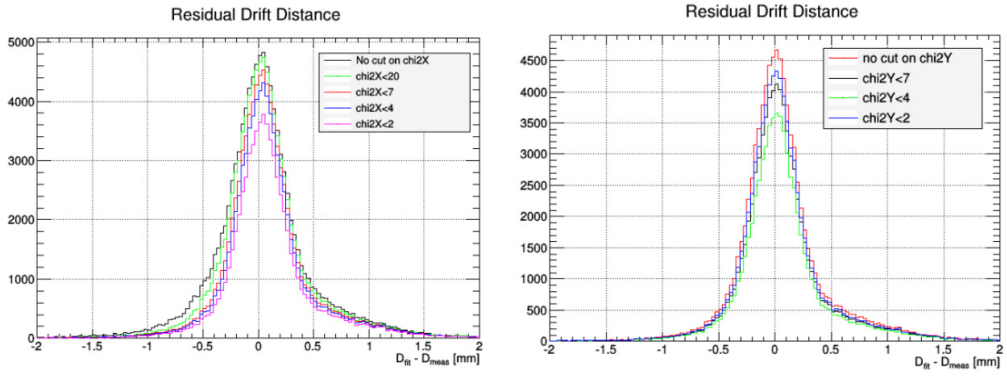

Fig.15. *Residual distribution on X (left) and Y (right) for different chi-square cuts.*

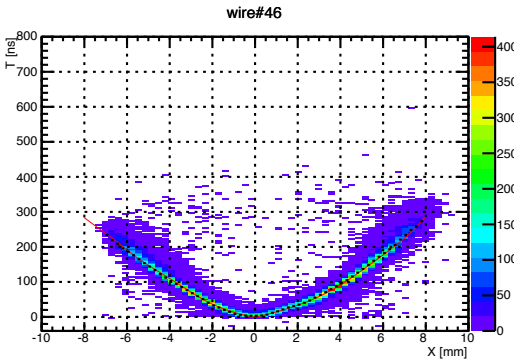

Fig.16. *XT curve of prototype II measured with He:C_2H_6(50:50) at 2500 V (Run#169).*

2.7.3 Spatial Resolution

Measured time is converted to position X_{meas} using the XT curve. Residual is calculated by subtracting X_{meas} from reconstructed X position. Spatial resolution is estimated by fitting the residual distribution with Gaussian distribution. The residual includes tracking errors. Fittings are done in each range of drift distance from 0 mm to 8 mm in 1 mm steps. Residual distribution measured with He:C_2H_6(50:50) is shown in Fig.17. Finally spatial resolutions in eight regions are averaged. At small drift distance a spatial resolution becomes worse due to statistics of primary ions, while at large drift distance it is due to a diffusion and an uncertainty of XT curve.

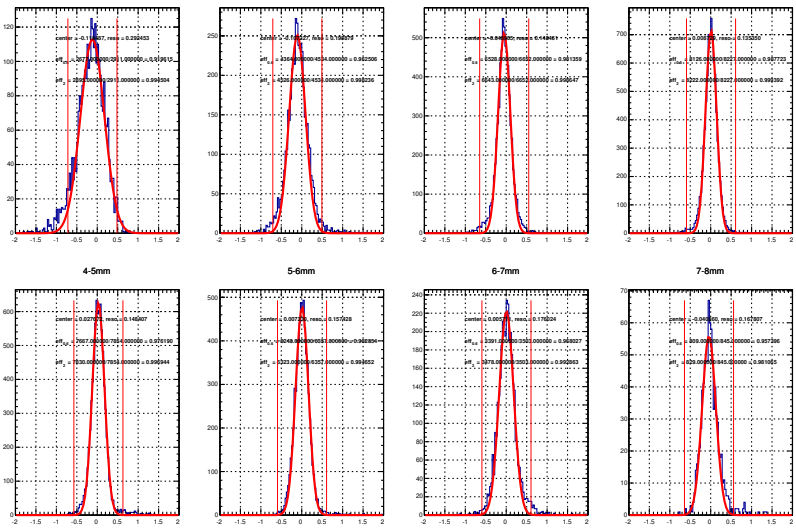

Fig.17. *Residual distributions measured with He:C_2H_6(50:50) at 2500 V (Run#169). Residual distribution is fitted with Gaussian distribution in range of drift distance from 0 mm to 8 mm in 1 mm steps*

2.7.4 Hit Efficiency

Hit efficiency is defined as the ratio of the number of events within 0.6 mm of residuals to the number of reconstructed events. Finally hit efficiencies in eight regions are averaged. Hit efficiency as a function of HV for each gas mixtures are shown in Fig.18. Efficiency of He:iC$_4$H$_{10}$(90:10) and He:C$_2$H$_6$(50:50) is about 95% while that of He:CH$_4$(73:27) is smaller than 95%. It is found that efficiency drop found at higher HV is due to oscillation of waveform. Details are explained in Section 3.2.

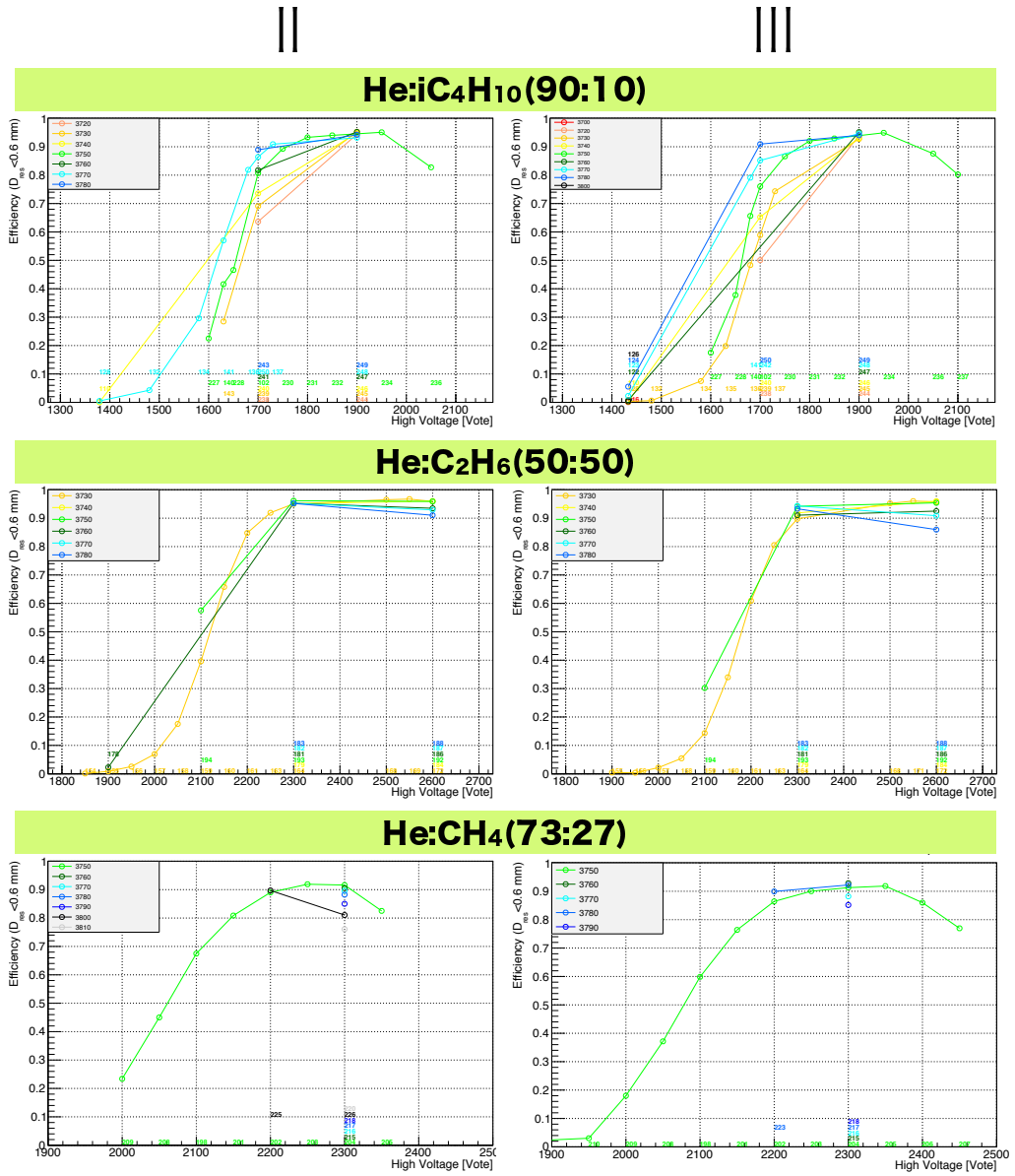

Fig.18. *Efficiency curves measured with prototype II (left side) and III (right) for gas mixtures of He:iC$_4$H$_{10}$(90:10) (top), He:C$_2$H$_6$(50:50) (middle), and He:CH$_4$(73:27) (bottom). Lines of different colors indicate different thresholds of the RECBE boards.*

2.8 Results of Spatial Resolution and Hit Efficiency

Results of spatial resolution and hit efficiency are summarized in Table 7.

Table 7. *Results of spatial resolution and hit efficiency of prototype II and III for each gas mixtures where hit efficiency is maximum.*

Prototype	Gas mixture	HV	Spatial resolution	Hit efficiency
II	He:iC$_4$H$_{10}$(90:10)	1900 V	191 μm	95%
III	He:iC$_4$H$_{10}$(90:10)	1900 V	177 μm	95%
II	He:C$_2$H$_6$(50:50)	2550 V	178 μm	97%
III	He:C$_2$H$_6$(50:50)	2550 V	182 μm	96%
II	He:CH$_4$(73:27)	2300 V	188 μm	92%
III	He:CH$_4$(73:27)	2300 V	186 μm	93%

2.9 Conclusion

We measured spatial resolution to be less than 200 μm including tracking errors for all gas mixtures and both prototype chambers. Efficiencies of about 95% were measured for all gas mixtures and both prototype chambers. These results suggests that both ϕ25 μm and ϕ30 μm can be used as sense wire.

§3. Investigation of Issues Found in Prototype II and III

3.1 Strange ADC Distribution

We found that ADC distributions of both of prototype chambers II and III showed spike structures in runs taken on Dec 7 as shown in Fig.19. ADC of tracking chambers looked fine so we thought RECBE board had no problems. We continued to taking data since TDC distribution of prototype chambers seemed normal. We didn't put a bubbler at the gas exhaust line by Dec 7, therefore we tried to put a bubbler after the shift on Dec 7 finished. We still saw strange ADC distributions in the morning runs on Dec 8. ADC distributions showed suddenly normal after the next run when DAQ crashed. We thought that the problem was fixed by adding the bubblers at that time. By off-line analysis after the beam test we found that ADC distributions are normal. Therefore we conclude that this problem would be caused by bugs somewhere in online analysis or Middleware.

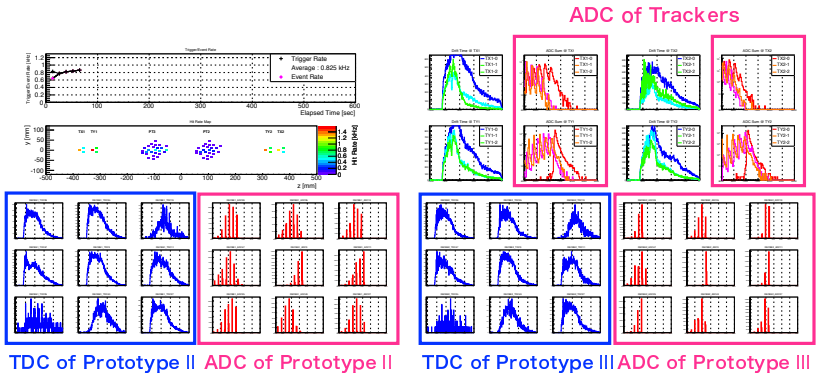

Fig.19. *Display of online monitor for Run#147 taken in the last on Dec 7. Summed ADC distributions of prototype II and III showed strange structures.*

3.2 Oscillation after Signal

When HV increased we observed similar XT curves at left and right hand side as shown in Fig.20. It seems that these dummy XT curves has some correlation with real one. It is found that hits on these dummy XT curves appear when a beam passes neighboring wires. When a neighboring wire has a signal an induced current of opposite sign is flowed in the central wire. Since induced current is opposite sign to signal it cannot be triggered. But as shown at top in Fig.21 waveform is oscillating just after the first signal arrived therefore it could be triggered. We found that pulse height of the oscillation increased when pulse height of signal increased. This is the reason to see dummy XT curves on both sides of the real XT curve. This effects make a precision of time measurement worse, resulting in expanding width of residual distribution. This is why an efficiency became small when HV increased as seen in Fig.18.

This oscillation is reproduced by measurements using ^{90}Sr with prototype chamber II and III at Osaka University. See bottom of Fig.21. After several trials such as enforcing shielding around RECBE board and end plates at HV side we successfully eliminate this oscillation by shielding signal cables from feed through to the RECBE board. Since shielding around end plates at prototype II and III seems not sufficient external noise would be picked up into the signal cables. We are planning to test the oscillation with a next prototype chamber IV where end plates are perfectly covered with aluminum boxes.

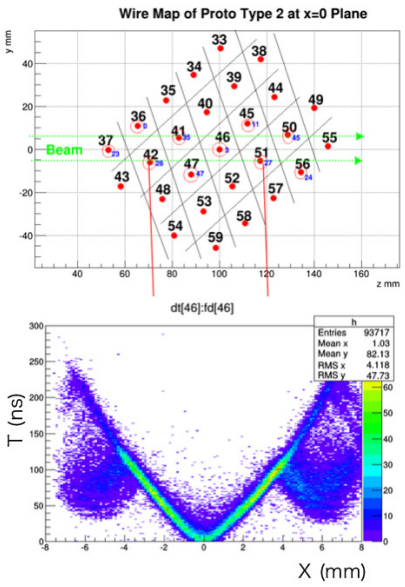

Fig.20. *Sense wire positions around beam passing area (top). XT curve measured at higher HV setting. Dummy XT curves are seen at both sides.*

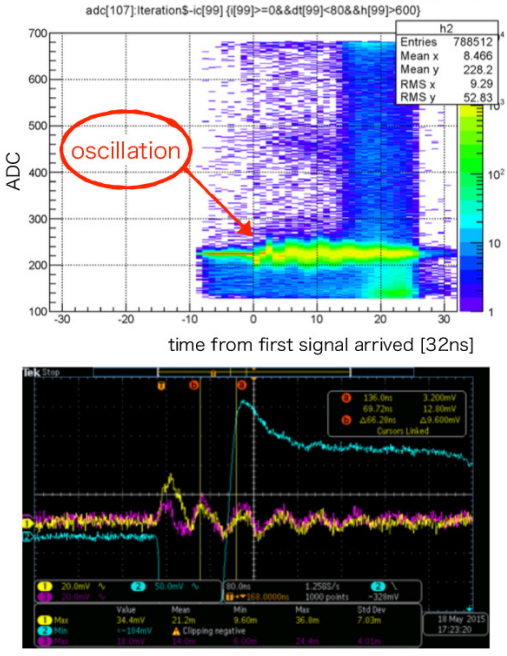

Fig.21. *Oscillation seen at the neighboring sense wire at the beam test (top). Reproduced oscillation using prototype chamber at Osaka University using ^{90}Sr beta source. (bottom)*

§4. Wire Size Decision after the Beam Test

Results of the beam test show good efficiencies of 95% and good spatial resolutions less than 200 μm for all of gas mixtures. From aging point of view, past experiments suggest to keep electric fields on the surface of field wires to be below 20 keV/cm not to accelerate aging speed. Magnitude of electric fields is mostly determined by size of field wire. In case of ϕ80 μm (prototype II and III) 20 kV/cm is reached at 1700 V, while in case of ϕ126 μm (prototype I) voltage can be increased up to 2600 V. From beam test results, efficiency at 1700 V is too small in case of He:C_2H_6(50:50) and He:CH_4(73:27). Even with He:$i C_4H_{10}$(90:10) an efficiency was around 90%, which still be less than the maximum efficiency of 95%. It is strongly recommended to follow this rule, therefore we had determined to use ϕ126 μm as field wire instead of ϕ80 μm. Size of sense wire had been chosen as ϕ25 μm in terms of suppressing multiple scattering and Lorentz angle. We have made a next prototype chamber IV using sense wire of ϕ25 μm and field wire of ϕ126 μm. Cosmic-ray tests under 1 T magnetic fields and beam test under 0 T using prototype IV are planned.

Acknowledgment

We would like to thank all members in ELPH for assistance and supporting kindly our beam test.

References

[1] COMET collaboration, Technical Design Report, http://comet.kek.jp/Documents_files/PAC-TDR-2014/PAC-Review-20141110.pdf

[2] Y. Nakazawa et al., COMET Phase-I CDC Prototype Beamtest 1, 70th JPS meeting at Waseda University, Mar. 21 2015

[3] http://www.muonsinternal.com/muons3/G4beamline

[4] http://research.kek.jp/people/uchida/technologies/SiTCP/

[5] http://daqmw.kek.jp

(ELPH Experiment : #2800)

Development of a photon tagger with counters based on MPPCs

Hiroki Kanda[1], Takao Fujii[1], Yu Fujii[1], Manami Fujita[1], Hiroki Homma[1], Kazuhisa Honda[1], Takatsugu Ishikawa[2], Masashi Kaneta[1], Yuma Kasai[1], Chigusa Kimura[1], Junichiro Kusaka[1], Kazushige Maeda[1], Sho Nagao[1], Satoshi N. Nakamura[1], Aki Ninomiya[1], Takashi Nishizawa[1], Kazuki Nochi[1], Keiichi Ozeki[1], Takayuki Sasaki[1], Hajime Shimizu[2], Yuta Takahashi[1], Kyo Tsukada[1], Ryouun Yagi[1], Fumiya Yamamoto[1], and Hirohito Yamazaki[2]

[1]*Department of Physics, Tohoku University, Sendai, 980-8578*
[2]*Research Center for Electron Photon Science, Tohoku University, Sendai, 982-0826*

We have been developing an internal photon tagger for the NKS2 experiment. Its electron detector consists of scintillation counters based on Multi-Pixel Photon Counter (MPPC) with newly developed read-out systems. The electron detector including a part of counter units was installed in a bending magnet (BM4) of BST ring and tested with a beam. Obtained time resolution was less than 40 ps in Gaussian σ at hit rates ranging from a few kHz to 200 kHz. A tagging efficiency was roughly 70%, which is consistent with the tagging efficiency obtained with STB Tagger. Further development and production are being continued.

We have been studying the meson photoproduction on deuteron with tagged photon beams and Neutral Kaon Spectrometer 2 (NKS2) at the Research Center for Electron Photon Science (ELPH), Tohoku University. NKS2 is a magnetic spectrometer for a charged particle detection. We have provided unique data in the neutral kaon photoproduction [1–3] and charged pion photoproduction [4] on the deuteron. We continue data analyses for kaon photoproduction [5] and double pion photoproduction [6–8].

We have been upgrading the electron detector of the photon tagger [9]. The electron detector detects momentum analyzed electrons after the bremsstrahlung and thus define timing and energy of radiated photons. By increasing number of channels of the electron detector, we aim at increasing its granularity and enlarging an energy range of tagged photon beams. With 1.3 GeV electron, a range of tagged photon energy is from 0.82 to 1.28 GeV with energy spans ranging from 1 to 6 MeV. The new electron detector consists of scintillation counters based on Multi-Pixel Photon Counters (MPPCs) supplied by Hamamatsu Photonics K. K. with newly developed read-out systems [10, 11]. We designed a electron detector of the photon tagger composed of counter units each of which has four position defining counters (TagF) and one timing counter (TagB). By a coincidence of a TagB counter and one of TagF counters, a trajectory of an electron can be selected to reduce an electromagnetic background from electrons, positrons or gamma rays coming from other sources.

In the first experiment, two counter units were aligned along a trajectory of scattered electrons after the bremsstrahlung. Thus their timing properties in the same environment as an actual electron detector of the tagger were measured. The prototype detector case were placed along a vacuum chamber of the accelerator in the pole gap of the bending magnet, BM4. We measured time resolutions of the TagB counters by electrons sequentially passing through them. In this measurement, we supposed identical time resolution for the two TagF counters. The time resolution was obtained as s $1/\sqrt{2}$ of a sigma of a fitted Gaussian to a time difference distribution between two TagBs. It exhibits that the time resolution is dependent on the bias voltage and its tuning is important (Fig. 1(a)). Sufficiently good time resolution and its weak dependence to the hit rate were obtained at 200 kHz which is the maximum expected hit rate (Fig. 1(b)).

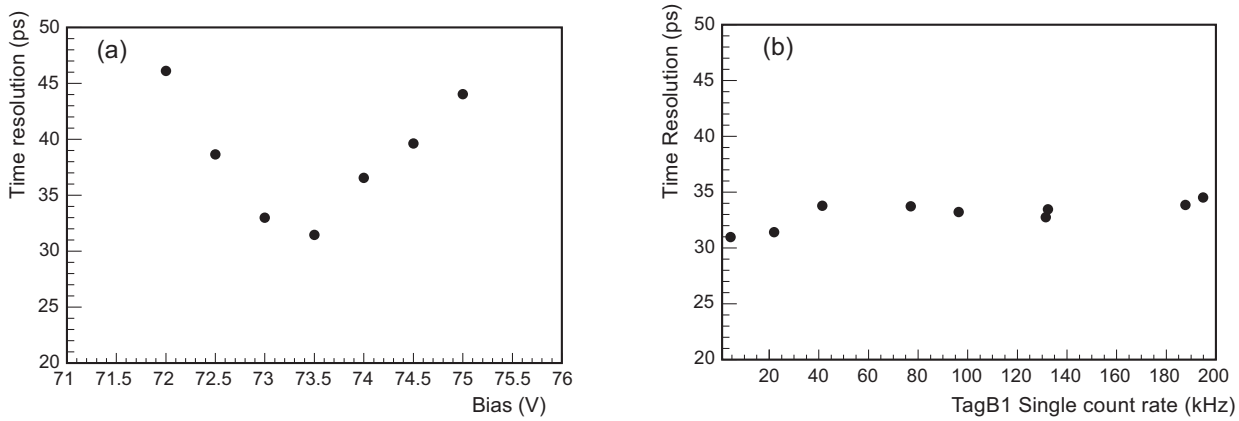

Fig.1. Time resolution of TagB (a) with regard to a bias voltage and (b) with regard to a hit rate.

In the second experiment, we fixed three counter units on an actual detector case which were placed in BM4. We tested a tagging efficiency of three counter units with a lead glass Cherenkov counter (LG) which was placed at the downstream of tagged photon beam line. The electron energy was set as 1.3 GeV. The tagging efficiency (ϵ_{tag}) was defined as a following equation:

$$\epsilon_{\text{tag}}(E_{e'}/E_e) = \frac{N_{LG\otimes B_i\otimes F_j}}{N_{B_i\otimes F_j}(\text{Radiator ON}) - N_{B_i\otimes F_j}(\text{Radiator OFF})} \tag{1}$$

where $E_{e'}$ is an expected electron energy detected by a coincidence of i-th TagB and j-th TagF, E_e is the incident electron energy, $N_{LG\otimes B_i\otimes F_j}$ is a number of hits on LG in coincidence with i-th TagB and j-th TagF and $N_{B_i\otimes F_j}$ is a number of coincident hits on i-th TagB and j-th TagF in each measurement period. The combinations of ith-TagB and j-th TagF in true coincidence for both STB Tagger and the present setup are $4(i-1)+1 \leq j \leq 4i$, where i and j are natural number. STB Tagger consisted of 12 TagBs and we placed 3 TagBs in our test setup. Description of "Radiator ON" and "Radiator OFF" in braces denote a status radiator motion. A remnant gas bremsstrahlung contributes to "Radiator OFF" hits, but it is known to be less than a few percent of "Radiator ON" hits in the previous studies of STB Tagger. In our measurement, it was ignored to obtain the tagging efficiency. The obtained tagging efficiencies are smaller tagging efficiencies obtained with STB Tagger at $E_e = 1.2$ GeV (Fig. 2). In general, the tagging efficiencies obtained with STB Tagger in the small $E_{e'}/E_e$ region are likely to be smaller than

those in a $E_{e'}/E_e \sim 0.2$ region. This tendency is caused by Møller scattered electrons, which does not emit photons but creates background hits to the electron detector. By considering this tendency, present tagging efficiencies are consistent with the ones obtained with STB Tagger. Detailed analyses of hits on the counters revealed that the coincidence of a TagF and a TagB effectively selects electrons after the bremsstrahlung.

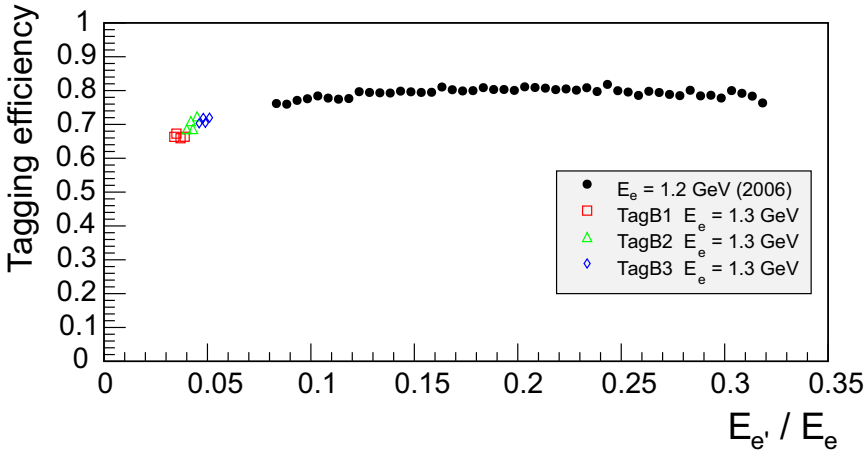

Fig.2. Tagging efficiency dependent on a ratio of a detected electron energy to an incident electron energy. Black circles show the efficiency measured with STB Tagger and colored makers show the efficiency measured with current setup. Red squares show the efficiency with TagB1 hit required; green triangles, with TagB2; blue diamond, with TagB3.

We assembled all the counter units and mounted them on the detector case (Fig. 3).

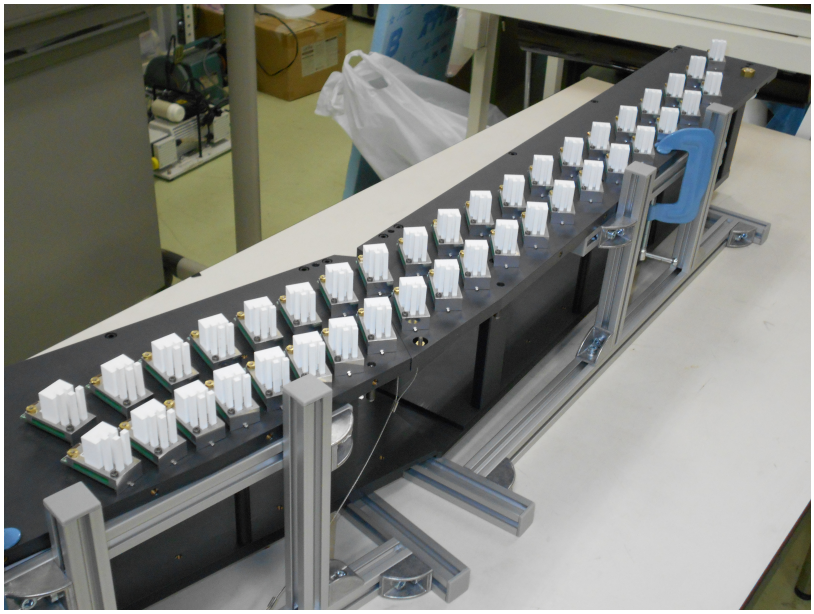

Fig.3. Photograph of the detector case of the tagger with all the counter units mounted on it.

Auxiliary circuits for signal transfer and data taking are being designed and developed. We continue working to complete the development of the new tagger. We plan to finish its commissioning in FY2015.

Acknowledgment

We would like to thank the administration and technical staff in ELPH and the faculty of science. This program was partly supported by Core-to-core program (21002), strategic young researcher overseas visits program for accelerating brain circulation (R2201), and KAKENHI Grant Number 23540334 by JSPS.

References

[1] K. Futatsukawa *et al.*: EPJ Web of Conferences **20** (2012) 2005.

[2] B. Beckford *et al.*: arXiv:1308.1649.

[3] M. Kaneta *et al.*: JPS Conf.Proc. 1 (2014) 013071, M. Kaneta *et al.*: Nucl.Phys. A914 (2013) 69-73.

[4] Y. C. Han *et al.*: Nucl. Phys. **A834** (2010) 596c-598c.

[5] T. Fujii *et al.*: Proceedings of J-PARC2014, to be published.

[6] C. Kimura *et al.*: Few Body Syst. 54 (2013) 1319-1322.

[7] F. Yamamoto *et al.*: JPS Conf.Proc. 1 (2014) 013072.

[8] H. Kanda *et al.*: JPS Conf.Proc. 1 (2014) 013075.

[9] H. Yamazaki *et al.*: Nucl. Instr. and Meth. 1 (2000) 10.

[10] T. Nishizawa *et al.*: IEEE trans. Nucl. Sci. **61** (2014) 1278.

[11] H. Kanda *et al.*: Conference Record, Nuclear Science Symposium and Medical Imaging Conference (NSS/MIC), 2013 IEEE.

(ELPH Experiment : #2802)

Test experiment of a prototype RICH counter for the J-PARC E50 experiment

T. Yamaga[1*], R. Honda[2], T. Ishikawa[3], K. Kato[4], M. Naruki[4], H. Noumi[1], K. Shirotori[1], and T. Takahashi[1]

[1]*Research center for nuclear physics, Osaka University, Osaka, 567-0047*
[2]*Department of physics, Osaka University, Osaka, 567-0047*
[3]*Research Center for Electron Photon Science, Tohoku University, Sendai, 982-0826*
[4]*Department of physics, Kyoto University, Kyoto, 606-8502*

In this experiment, we tested MPPC photo-detection plane for RICH counter. A prototype RICH counter has been constructed and tested with electron beam at GeV-γ experimental hall. The Cherenkov angle and its angular resolution was measured at different beam momentum, mirror set angle and refractive index of radiator. Clear Chrenkov ring was observed by selecting Chrenkov photons, and typical angular resolution was 3.0 mrad. As a results, MPPC can be used as photon sensor of RICH counter.

§1. Introduction

We are planning an experiment for studying charmed baryons via the $p(\pi^-, D^{*-})$ reaction at the J-PARC high-momentum beam line [1]. Charmed baryons will be measured by a missing mass method. Scattered D^{*-} will be reconstructed by selecting its decay chain of $D^{*-} \to \bar{D}^0\pi^- \to K^+\pi^-\pi^-$. Decay particles from D^{*-} and produced charmed baryon which have momenta of up to 16 GeV/c are detected by large acceptance spectrometer system. Particle pass is tracked by drift chambers located around dipole magnet, and its time of flight is measured by TOF wall. Particle identification (PID) is performed by using TOF and forward PID counter. The cross section of the $p(\pi^-, D^{*-})\Lambda_c$ is estimated to be at a level of nb. On the other hand, the cross section to produce at least a kaon in the final state is a few mb. A huge amount of events including K^+ and two π^-s will be able to be reduced by identifying not only D^{*-} but also $\bar{D}^0$. However, wrong identification of those particles increases a background level drastically. For example, wrong identification of positive pions or protons with positive kaons enhances the background level by a factor of about 20. Therefore, a high performance of the PID counter is desired for the charmed baryon spectroscopy. We designed a Ring imaging Cherenkov (RICH) counter with two radiators, aerogel and C_4F_{10} gas of refractive indices of 1.04 and 1.00137, respectively, in order to identify pions and kaons in a wide momentum range from 2 to 16 GeV/c [2]. The RICH counter contains radiators, photo-detection plane and focusing spherical mirror. Because the RICH counter is located at the most down stream of the spectrometer system, the counter size must be large to cover all acceptance.

*Present address: Research center for nuclear physics, Osaka University, Osaka, 567-0047

The PID performance of RICH counter is determined by angular resolution of the Cherenkov angle which depends on position resolution of photo-detection plane. In order to obtain enough resolution with large acceptance, 2 pieces of photo-detection plane which have size of 1.0×2.0 m constructed by more than 2000 photon sensors is needed.

We plan to use the multi-pixel photon counter(MPPC) as a photon sensor. The MPPC can detect 1 photon with very nice separation which is advantage to detect feeble Cherenkov photons. Furthermore, it is not affected by magnetic field as compared to the PMT. However, larger dark current rate of the MPPC which is typically 100 kHz/mm^2 may increase noise hit. Consequently, the PID performance may become worse.

In this experiment, performance of a prototype RICH counter using MPPC photo-detection plane is studied.

§2. Experimental setup and procedure

2.1 Setup

This experiment was performed at GeV-γ experimental hall. Electron beam which has momentum of up to 700 MeV/c was induced to a prototype RICH counter. Electrons which passes center of the counter is selected by trigger counters located upstream and down stream of the prototype RICH counter.

2.2 Prototype RICH counter

The prototype RICH counter contains a MPPC photo-detection plane and a focusing spherical mirror (see Figure 1). In this time, we used S12642-0808 module made by Hamamatsu Photonics. It has 64 segments (8×8), and each segment is size of 3.1×3.1mm^2. The total detection area is 25.8×25.8 mm^2.

The spherical mirror is used for focusing the Cherenkov photons and transferring photons to photo-detection plane. The curvature radius of mirror is 330 mm which was determined by size of detection area. The reflection surface is made by Aluminum which has reflectance of about 90% in visible light.

Air and CO_2 are used for radiator which has refractive indices of 1.000293 and 1.0005, respectively. The detector box is filled by each radiator one by one. Then, we can change Cherenkov angle even same particle velocity. The length of radiator can be modified from 90 cm to 190 cm by moving photon shield plate.

§3. Results

Figure 2 shows TDC distribution of photo-detection plane. In this experiment, two TDC information of leading and trailing edge of the signal were acquired. However, only leading timing is used in this analysis.

Clearly peak corresponding to Cherenkov photons is observed. In this analysis, time cut with 50 ch. window is used to separate between Cherenkov light and dark current. The hit pattern of photon-detection plane is shown in Figure 3. The Cherekov ring can be observed and S/N ratio become better by selecting the Cherenkov peak in TDC distribution.

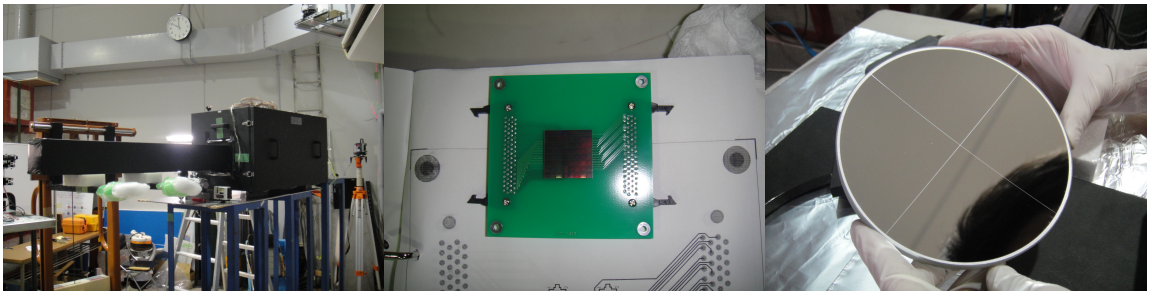

Fig.1. Prototype RICH counter. (left) Overview of the Prototype RICH counter. Electron beam comes from left side. (middle) MPPC photo-detection plane. MPPC is mounted on read board. (right) Spherical mirror.

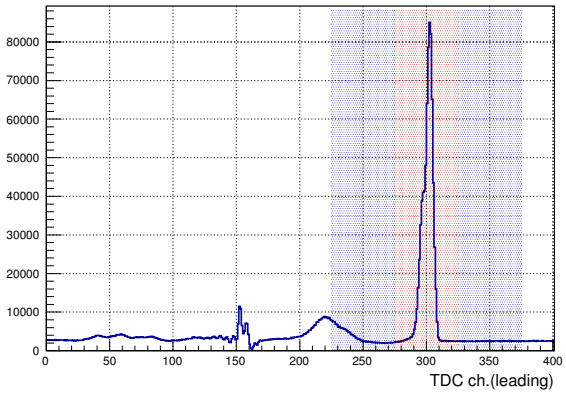

Fig.2. TDC timing distribution. A peak around 300 ch. is came from Cherenkov photons. Red and blue regions indicate cut window for Cherenkov photons and background from dark current, respectively.

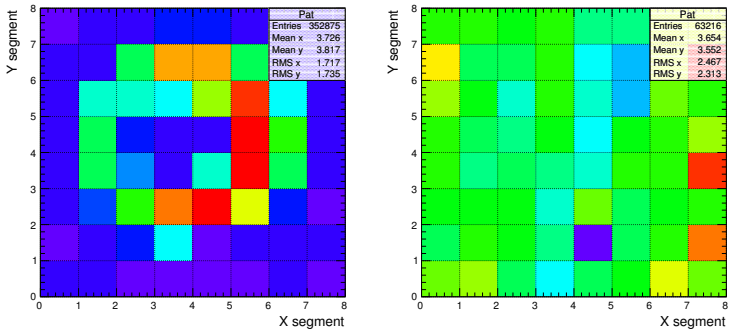

Fig.3. Hit pattern of photon-detection plane. (left) Cherenkov region is selected. The Cherenkov ring is clearly observed. (right) Dark current region is selected. There is no ring structure.

The Cherenkov angle is calculated by simple equation,

$$\theta_c = \mathrm{Tan}^{-1}\left(\frac{R_{ring}}{R_{mir}}\right) \tag{1}$$

, where R_{ring} and R_{mir} are radius of the Cherenkov ring and spherical mirror, respectively. Actually, incident angle of particle must be taken into account to calculate the Cherenkov angle. However, because particles which passes center of the RICH counter are selected, incident angle is fixed to be 0 degree for all event. All detected position in one triggered event are converted to the Cherenkov angle, then all of them are averaged to determine the measured Cherenkov angle for a particle. Figure 4 shows the Cherenkov angle distribution. There is clear peak around 25 mrad which corresponds to $\theta_{Air} = \mathrm{Sin}^{-1}(1/\beta\, n) = 24$ mrad, where β is particle velocity which is fixed 1.0 and n is refractive index of air. On the other hand, there is no peak structure when dark current region is selected. We can separate events from Cherenkov photons and dark current by using TDC timing. The angular resolution is obtained by a peak width in the Chrenkov angle distribution. In this time, evaluation of angular resolution is performed by using RMS value of the Cherenkov angle distribution.

Each data set are analyzed by the same way and evaluated its angular resolution.

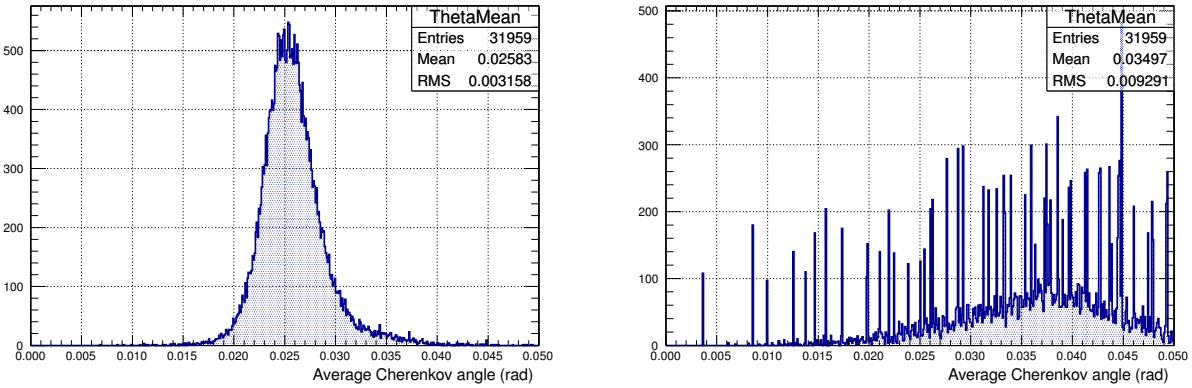

Fig.4. Average Cherenkov angle distribution. (left) Cherenkov region is selected. A peak from Cherenkov photons is clearly observed around 25 mrad. (right) Dark current region is selected.

3.1 Incident momentum dependence

Due to multiple scattering of incident particles, the angular resolution may becomes worse. We studied this multiple scattering effect by changing incident momentum of the electron beam. The angular resolution with electron momentum of 300, 500 and 700 MeV/c is measured. Figure 5 shows angular distribution at each incident momentum. The angular resolution does not depend on incident momentum. So, the effect from multiple scattering is small.

3.2 Geometry dependence

The spherical mirror is used for focusing the Cherenkov photons to improve angular resolution. Actually, the focusing by spherical mirror is not completely parallel to point focusing when mirror angle against incident particle becomes large. In order to evaluate this effect, set angle of mirror is changed.

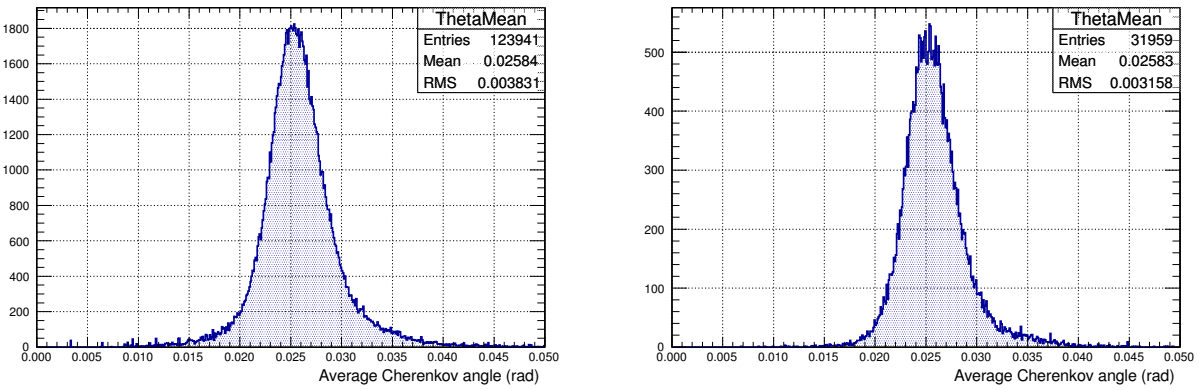

Fig.5. Average Cherenkov angle distribution at each beam momentum. (left) and (right) figures are Cherenkov angle distribution at beam momentum of 300 MeV/c and 700 MeV/c, respectively.

The angular distributions at each set angle are shown in Figure 6. In this case, radiator and incident momentum are fixed to be air and 700 MeV/c, respectively. As a results, angular resolution doesn't depend on mirror set angle so much.

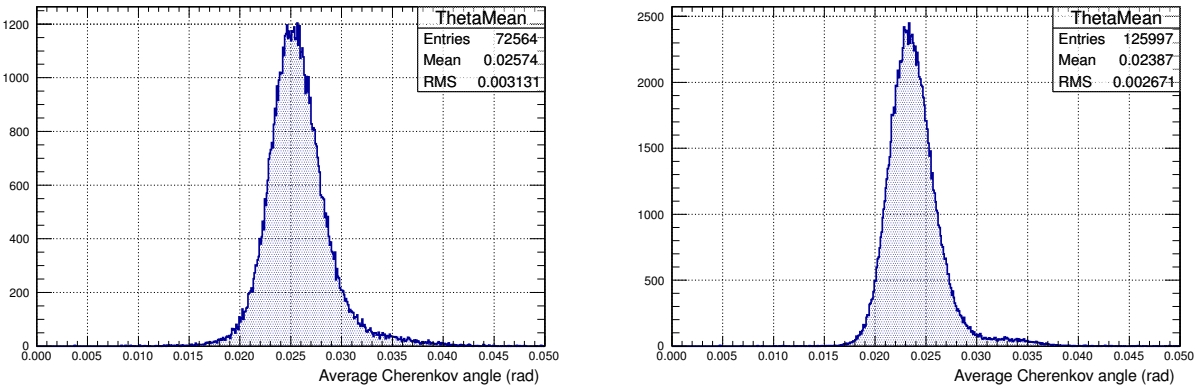

Fig.6. Average Cherenkov angle distribution at each mirror angle. (left) and (right) figures are Cherenkov angle distribution at mirror angel of 5 deg. and 12.5 deg., respectively.

3.3 Radiator dependence

In this experiment, because of only electron beam was used, the Cherenkov angle is fixed to be the maximum value even electron momentum is changed. Actually, the RICH counter identifies particles by measuring different Cherenkov angle from each particle. To investigate separation between different Cherenkov angles, we change refractive index of radiator. The refractive indices and calculated Cherenkov angles are listed on Table 1. Figure 7 shows the Cherenkov angle distribution for each radiator. The difference of Cherenkov angle between radiators is clearly observed.

Table 1. Refractive indices and calculated Cherenkov angles for each radiator

Radiator	n	θ_c (mrad)
Air	1.000293	24.2
CO_2	1.0005	31.6

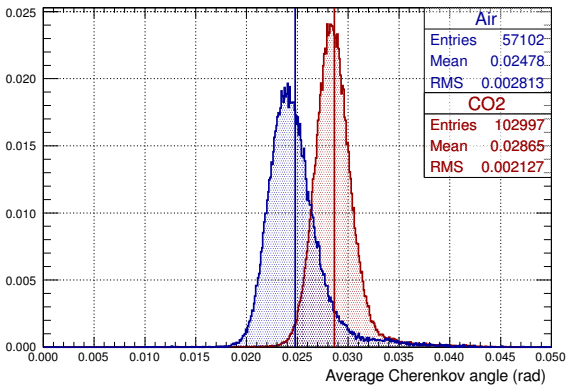

Fig.7. Average Cherenkov angle distribution with each radiator. Blue and Red spectra are Cherenkov angle distribution with Air and CO_2 radiator, respectively.

§4. Summary

The prototype RICH counter which has MPPC photo-detection plane was tested by using electron beam. Angular resolutions at each incident momentum, mirror set angle and radiator index were measured. As a results, MPPC photo-detection plane was useful for the RICH counter. More detail analysis is now ongoing.

Acknowledgment

We would like to thank staffs of ELPH for their supports and providing exellent experimental condition.

References

[1] H. Noumi *et al.*: J-PARC E50 proposal,
http://www.j-parc.jp/researcher/Hadron/en/pac_1301/pdf/P50_2012019.pdf

[2] T. Yamaga : Master's Thesis, Osaka university (2014)

Study for the charged particle detector using wave length shifting fibers and MPPC

M. Miyabe[1], T. Abe[1], Y. Inoue[1], M. Sasagawa[1], Y. Honda[1], T. Ishikawa[1], S. Kido[1], T. Suda[1], Y. Tajima[2], and A. O. Tokiyasu[1]

[1]*Research Center for Electron Photon Science, Tohoku University, Sendai, 982-0826, Japan*
[2]*Department of Physics, Yamagata University, Yamagata 990-8560, Japan*

The study for baryon spectroscopy and meson photo-production experiment has been carried out with an electro-magnetic calorimeter FOREST and BGOegg at Research Center for Electron Photon Science (ELPH), Tohoku University. High energy gamma detector is generally consists of inorganic scintillators and charged particle identification detectors like plastic scintillators. However, the space for the charged particle identification detector is often limited in the design process of the large acceptance electro-magnetic calorimeter. In this study, we developed a hodoscope detector using a plastic scintillator, wave length shifting fibers and multi-pixel photon counters. This hodoscope is designed for the charged particle detectors surrounding the 90mm-diameter Liquid Hydrogen target system to be installed inside BGOegg. It is produced by a 5mm-thickness plastic scintillator, which is covered by the wave length shifting fibers with the diameter of 1mm. Each 4 and 8 fibers are connected to multi-pixel photon counters. The position resolution of the hodoscope was examined by the positron beam at ELPH, Tohoku University. As a result of the analysis, we achieved the position resolution $\sigma = 1.17$mm with the 8mm interval read out.

§1. Introduction

The study of baryon resonance is one of the effective tool to understand the low energy Quantum chromodynamics (QCD). A nucleon excited by the incident particle emits mesons like π, η and K, and then de-excited to the ground state nucleon. With the detection of these emitted mesons, we study the intermediate state of these reactions. On these mesons, π^0 and η immediately decay into two gamma. With high accuracy measuring these high energy gamma, BGOegg enables detailed studies for the baryon resonance. A large acceptance electro-magnetic calorimeter BGOegg include the charged particle detectors on the inside(Fig.1). BGOegg is an egg-shaped gamma ray detector which consists of 1320 BGO inorganic crystal scintillators of 220 mm in length (equal to 20 radiation length). BGOegg has 22 layers and covers from 24 degrees to 144 degrees at polar angle. Each layer has 60 crystals and covers 360 degrees at azimuthal angle. The energy resolution for the positron at 1GeV is 1.3% and the position resolution amounts to 3 mm. These values are the highest performance in the world [1, 2]. To detect the gamma with high accuracy, charged particle detectors which has the equivalent position resolution are necessary. In this study, we developed and evaluated the charged particle detector using wave length shifting

fibers and multi-pixel photon counters for this purpose.

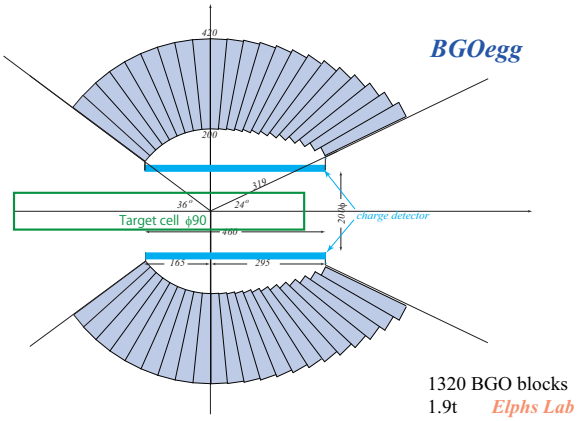

Fig.1. Cross Section view of BGOegg crystals and charged particle detectors

§2. Design of the detector

BGOegg has an egg-like-shape and consists of 1320 BGO inorganic crystal scintillators. BGOegg also include the target system and the charged particle detectors on the inside. For our Liquid Hydrogen target system has the 90 mm diameter and the smallest diameter of BGOegg is almost 200mm, these charged particle detectors have to cover the large acceptance and must not interfere BGOegg. In the present setup of BGOegg experiment, we use the cylindrically-located 30 plastic scintillators for the charged particle identification. But in this detectors only, we could not obtain the z position of a charged particle at all. To avoid this situation, we adopt the design which has a plastic scintillator covered by wave length shifting fibers with reasonable intervals and tilt angle. In this design, we could obtain not only ϕ-direction information but also the z position information. Figure2,3 shows the overview of the hodoscope consist of a plastic scintillator and wave length shifting fibers. The emitted light from the charged particle passed the plastic scintillator, are absorbed by the fibers at the surface of scintillator, and re-emitted with the long wave length light. Re-emitted light propagate to the photon detectors inside of wave length shifting fibers. Considering the efficiency of absorption, emission and the loss of the propagation, the number of photons at the photon detectors are very small(about a few photons). Therefore, the efficiency of the conversion from light to electric signal is important. For this reason, we adopt the multi-pixel photon counter as the photon detectors.

2.1 Plastic Scintillator and Wave Length Shifting (WLS) fibers

In this study, we use the wave length shifting (WLS) fibers Y-11 manufactured by Kuraray corporation [3]. The absorption wave length of Y-11 is about 430nm, emission wave length is 476nm. Y-11 has the multi-cladding configuration, Center core, Inner cladding and Outer cladding are polystyrene(index n=1.59), polymethylmethacrylate(n=1.49) and Fluorinated Polymer(n=1.42) respectively. An attenuation length is 3.5m. The base plastic scintillator of our hodoscope is EJ-212 [4] made by ELJEN Tech-

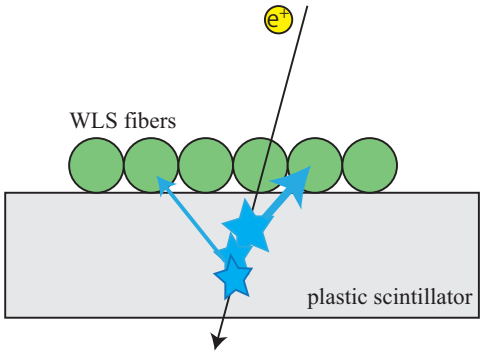

Fig.2. Overview of the photon detection with Plastic Scintillator and WLS fibers

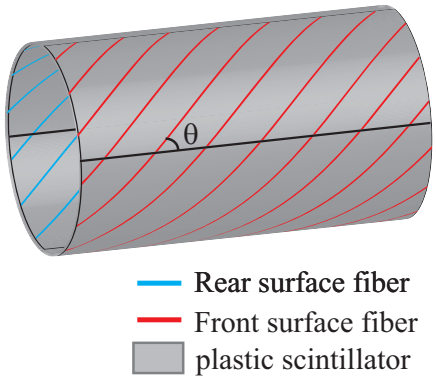

Fig.3. A simple design for 2 sided WLS fiber hodoscope

nology. The plastic scintillator is covered by 128 WLS fibers in both side. Each 8 fibers are read out by multi-pixel photon counter. Total number of channels is 16.

2.2 Multi-Pixel Photon Counter (MPPC)

Multi-Pixel Photon Counter (MPPC) is a recently well-developed photon counting device. MPPC is consist of many Geiger mode avalanche photo-diode (APD) and shows the high performance for photon counting. MPPC can be operated with low voltage and don't affected by the Magnetic field. For the efficiency of the photon detection will achieve the 40% with increasing the supply voltage, it is suitable for the low light yield detectors like this study. In addition, its small size and simple read out system of MPPC has advantage in the restricted geometry. In this study we use the S12572-050P manufactured by Hamamatsu Photonics [5]. The acceptance surface, pixel pitch, number of pixels, wave length of the maximum sensitivity are 3×3mm, 50μm, 3600 and 450nm respectively. These parameters are suitable for the light from WLS fibers. We use the 16 MPPC and 8 WLS fibers connect to each MPPC. Figure 4 shows the accomplished hodoscope picture. The plastic scintillator and WLS fibers were glued by EJ-500, WLS fibers and MPPC were fixed by the special handmade jig and the optical grease.

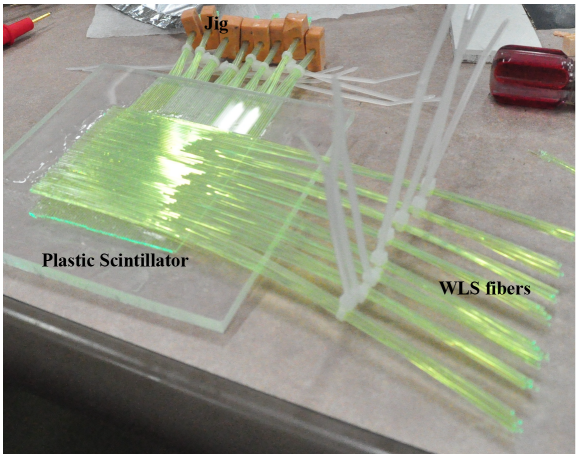

Fig.4. The double sided 16ch hodoscope without MPPC

§3. Experiment

The hodoscope detectors were tested by the positron beam at ELPH, Tohoku University. The experiment was carried out during a day at March 2014. We changed the position of positron beam by moving the detectors and signal conversion circuits inside of the light shielded black box. Beam profile monitor(BPM) which consist of 32 scintillating fibers(3 $\times$ 3mm) are located in upstream of the hodoscope. In the downstream of hodoscope detectors, a plastic scintillator with 10 $\times$ 10mm and 5mm-thickness were set up. Figure 5 shows the experimental setup.

Using the 4 scintillating fibers around the center of BPM and the downstream plastic scintillator, we made the trigger signals. From these trigger position information, we specified the position of the penetrated positron. We obtained the ADC and TDC data of all hodoscope channel. Output signal of MPPC went through the 160ns cable delay and input the photomultiplier amplifier ($\times$10). After the amplifying, the signals were connected to LeCroy 2249W(ADC) and REPIC RPC-060(TDC). Using these digitized data and beam position information, we estimate the position resolution of the hodoscope detector. In this experiment, irradiation position of beam is 13 point, 2mm interval for x and y direction, and we took 1000 event data at each position. We also took the pedestal data with the clock gate for ADC calibration. A typical trigger rate was about 2Hz.

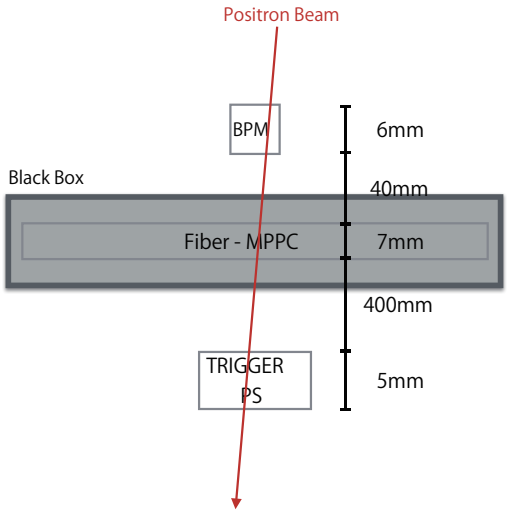

Fig.5. Overview of the detectors setup.

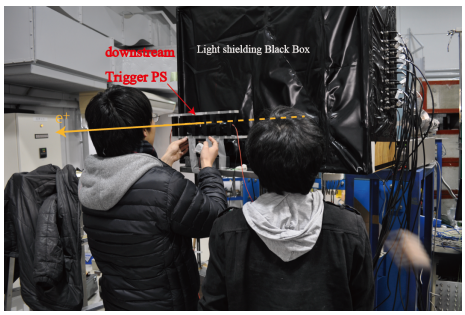

Fig.6. figure of the experimental setup

§4. Result and Discussion

At the first, we calculated the ADC distribution for each hodoscope channels with subtraction the pedestal value. These ADC distribution are fitted by the Moyal distribution function. As a result of fitting, we obtained the light output of hodoscope channels. Figure 7 shows the typical ADC distribution and the result of fitting. Figure 8 shows this obtained light output as a function of the distance from the positron beam. This light output distribution has a little fluctuation caused by the difference in the gain of each MPPC. After the correction of this fluctuation, we fitted the light output distribution with

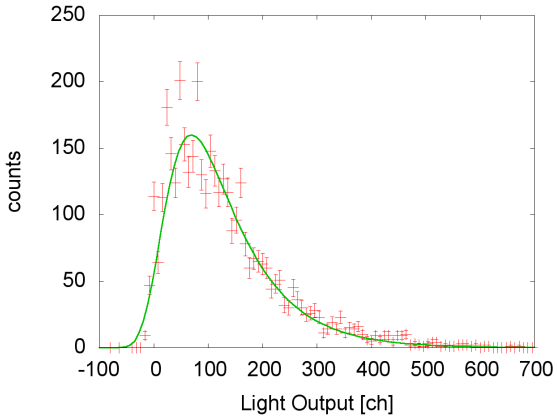

Fig.7. ADC distributions from the hodoscope channels. The solid line shows the Moyal distribution function.

the Lorentzian $f(x) = \frac{a}{1+(\frac{x-c}{b})^2}$ (Fig.9). The position dependence of the light output is well described

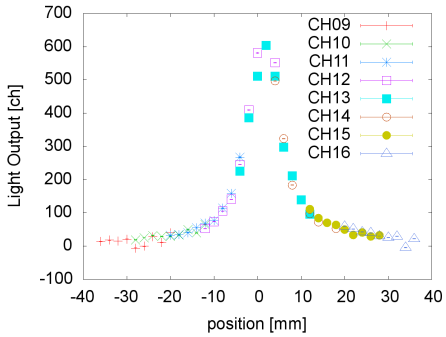

Fig.8. Light output distributions as a function of the distance from the beam center.

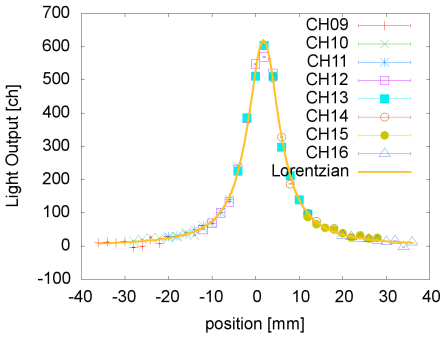

Fig.9. Normalized light output distributions as a function of the distance from the beam center.

by the Lorentzian function. The fitted width value(b) of Lorentzian is about 4.4mm. With fixing this fitted value b, the light output distribution is fitted by Lorentzian per event. As a result of this fitting, we can estimate the beam center position(c) from the light output. From the Gaussian fitting for the residual distribution of the reconstruct position and the beam position, we obtained the width $\sigma_{EXP} = 2.09 \pm 0.04mm$.

By the way, experimental result σ_{EXP} is related to the resolution σ_{BPM} of the beam position detector (BPM). We assume the relation as below,

$$\sigma_{EXP}^2 = \sigma_{HOD}^2 + \sigma_{BPM}^2$$

where, $\sigma_{BPM} = 2 \times 3/\sqrt{12}$, so the position resolution of our hodoscope detector σ_{HOD}

$$\sigma_{HOD} = 1.17 \pm 0.04mm$$

is obtained.

In the case of the previous design (Fig.3), the z-direction position resolution is estimated with $\sigma_z =$

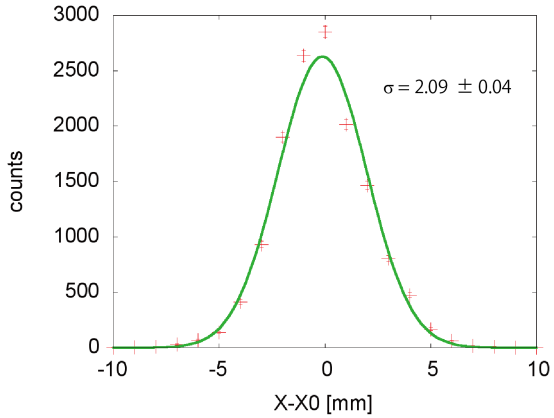

Fig.10. Residual distributions of the reconstruct position(X) and beam position(X_0). The solid line shows the fitting result of the Gaussian distribution function.

$1.17/\sin\theta$. On the other hand, the z position resolution of BGOegg itself at the hodoscope position is estimated with $\sigma_{BGO} = 3.1 \times r_{HOD}/200$ mm. For example, we suppose that r_{HOD} and θ are 100mm and 60°, the accomplished z position resolution σ_z is good enough compared to σ_{BGO}. Where θ is defined as the angular of z-axis and WLS fibers and r_{HOD} is the inner radius of the hodoscope.

References

[1] T. Ishikawa: Internal GeV-γ Analysis Note No. **231**$\mathcal{B}$ (2011)

[2] T. Ishikawa: Internal GeV-γ Analysis Note No. **238**$\mathcal{B}$ (2012)

[3] http://kuraraypsf.jp/psf/ws.html

[4] http://www.ggg-tech.co.jp/maker/eljen/ej-212.html

[5] http://www.hamamatsu.com/jp/ja/4004.html

The performance study of an electro-magnetic calorimeter BGOegg

Y. Matsumura[1], T. Ishikawa[1], M. Miyabe[1], N. Muramatsu[1], H. Shimizu[1], H. Hamano[2], T. Hashimoto[3], S. Kido[1], S. Masumoto[4], K. Mizutani[3], K. Ozawa[5], T. Shibukawa[4], K. Shiraishi[1], A. Tokiyasu[1], N. Tomida[3], N. Tran[2], Y. Tsuchikawa[1], H. Yamazaki[1], R. Yamazaki[1], and M. Yosoi[2]

[1]*Research Center for Electron Photon Science, Tohoku University, Sendai, Miyagi 982-0826*
[2]*Research Center for Nuclear Physics, Osaka University, Ibaraki, Osaka 567-0047*
[3]*Department of Physics, Kyoto University, Kyoto 606-8502*
[4]*Department of Physics, University of Tokyo, Tokyo 113-0033*
[5]*Institute of Particle and Nuclear Studies, High Energy Accelerator Research Organization(KEK), Tsukuba, Ibaraki 305-0801*

We are carrying out a meson photoproduction experiment at the SPring-8/LEPS2 facility. One of the main purposes of the experiment is to search for η' mesic nuclei. The peak structure of the formation of η' mesic nuclei will be observed in the missing energy spectrum of forward protons in the C(γ, p)X reaction. To reduce background events, we plan to tag the decay products of an η' mesic nucleus by using a large acceptance electro-magnetic calorimeter BGOegg. BGOegg can detect γ's coming from mesons with a high energy-resolution and a high position-resolution.

We have started to collect physics data with a carbon and a polyethylene target from 2014. We have performed energy and timing calibration of BGOegg and evaluated its performance. After the energy calibration, we can observe the peaks corresponding to π^0, η, and η' mesons in the $\gamma\gamma$ invariant mass distribution with high mass-resolutions of 6.7, 14.4 and 18.8 MeV, respectively. In this report, the calibration status and the performance of BGOegg are presented.

§1. Introduction

An η' meson has larger mass than other pseudo scalar mesons due to the $U_A(1)$ anomaly effect. In a high-density environment such as nuclear medium, the η' mass is expected to decrease significantly by partial restoration of chiral symmetry. By a theoretical calculation based on the Nambu-Jona-Lasinio (NJL) model, the decrease of an η' mass is estimated to be $\sim$150 MeV at the normal nuclear density (Fig.1 [1]). The large mass shift of the η' meson will cause a strong attractive potential in a nucleus, and will result in a bound state of an η' and a nucleus. This is called an "η' mesic nucleus".

We are carrying out an experiment to search for η' mesic nuclei at the SPring-8/LEPS2 facility using a multi-GeV photon beam. η' mesic nuclei are searched for in the missing energy spectrum of the C(γ, p)X reaction, where proton momenta are measured with TOF-RPCs. Figure.2 shows a theoretical prediction of the spectrum [1]. If η' mesic nuclei are formed, some peak structure will appear below

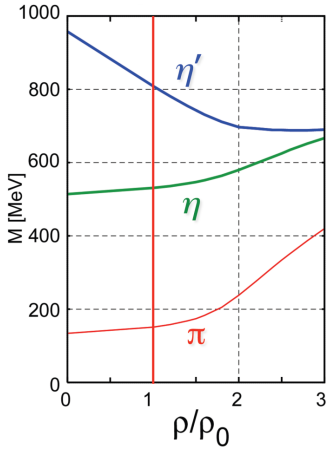

Fig.1. Theoretical prediction of mass shift of pseudo scalar mesons in a high-density environment based on NJL model. ρ_0 is the normal nuclear density. [1]

the η' production threshold in the missing energy spectrum. However, there will be a lot of background events such as a multi-π production reaction with only proton detection, and S/N ratio is estimated to be approximately 1/200. To reduce background events, we plan to tag the formation events of η' mesic nuclei by detectiong particles in the final state with a large acceptance electro-magnetic calorimeter BGOegg. η'N $\rightarrow$ ηN conversion is assumed as a tagged process, and the η is identified by detecting γ's by using BGOegg. To identify mesons in final state effectively, BGOegg is required to achieve a high resolution. We have performed the energy and timing calibration of BGOegg, and have studied the mass-resolution and the time-resolution achieved as a result of the calibration.

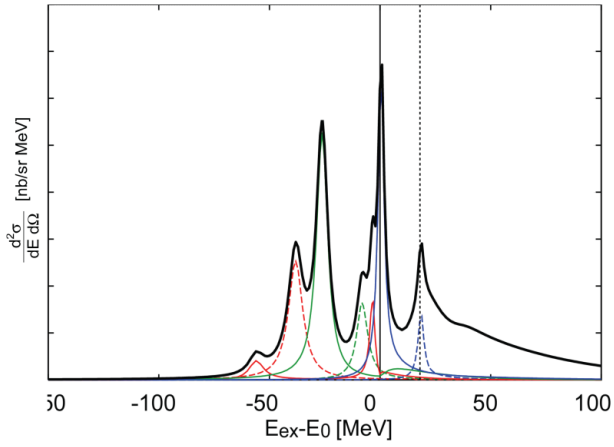

Fig.2. The expected spectrum of the ^{12}C(γ, p)^{11}B$\otimes\eta'$ as a function of the excited energy. E_0 is the η' production threshold energy. The imaginary part of the optical potential is assumed to be $W_0 = -5$ MeV. [1]

§2. LEPS2 beamline and BGOegg calorimeter

The experiment is carried out at the SPring-8/LEPS2 beamline (Fig.3). The photon beam is produced by backward Compton scattering with an ultra violet laser injected onto the 8 GeV electron beam

in the strage ring of SPring-8. We can use a tagged photon beam with energies from 1.3 to 2.4 GeV, which can produce nearly recoilless η' mesons. The beam intensity is now about 2 MHz with 4 lasers injection. We have started to collect physics data from April 2014.

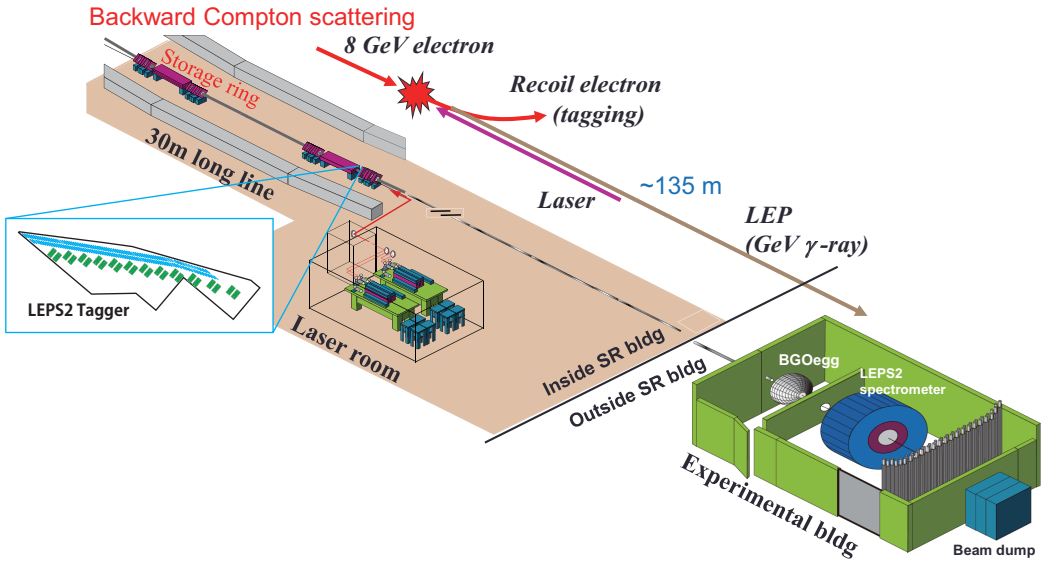

Fig.3. A schematic view of the LEPS2 beamline

BGOegg is an egg-shaped electro-magnetic calorimeter consisting of 1320 BGO crystals of 20 radiation length, which cover a polar angle from 24 to 144 degrees and the whole azimuthal angle surrounding the target (Fig.4). Since it has no housing material, there is no dead region between crystals. The details of the design and the construction of BGOegg can be found in [2, 3]. To detect charged particles, inner plastic scintillators(IPS) and a cylindrical drift chamber(CDC) are installed in front of the BGO crystals. BGOegg can detect γ's coming from photo-produced mesons with a high energy-resolution and a high position-resolutions of 1.3% and 3.1 mm at 1 GeV, respectively. The resolutions are the world highest values as an electro-magnetic calorimeter used in the energy region of 1 GeV.

§3. Energy calibration of BGOegg

The energy deposit for each crystal is measured by ADC information with

$$E_i = \alpha_i (A_i - A_{0i}) \tag{1}$$

where α_i, A_i, A_{0i} are the gain factor, ADC and the pedestal value for ith crystal, respectively. Since the gain factor is different value for each crystal, these values should be determined for all 1320 channels

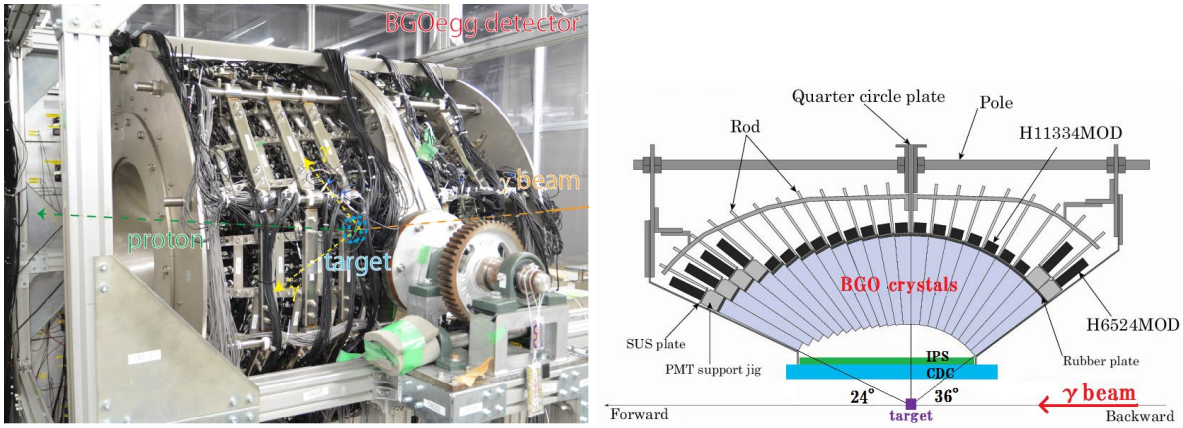

Fig.4. Left : The picture of the electro-magnetic calorimeter BGOegg. Right : Side view of the structure of BGOegg.

by calibration. We have performed the energy calibration of BGOegg using a real data of a carbon and a polyethylene target.

3.1 Clustering

To reconstruct the particle energy and the hit position, we put some crystals in which a particle deposits its energy together into a cluster. A cluster is defined as a set of adjacent crystals (See Fig.5). A particle energy is reconstructed by summing up the energy deposits of all crystals in a cluster, and a hit position is defined as an energy-weighted-mean of the positions of crystals in a cluster. When inner plastic scintillators corresponding to a cluster are fired, such events are ignored if we assume gamma hits.

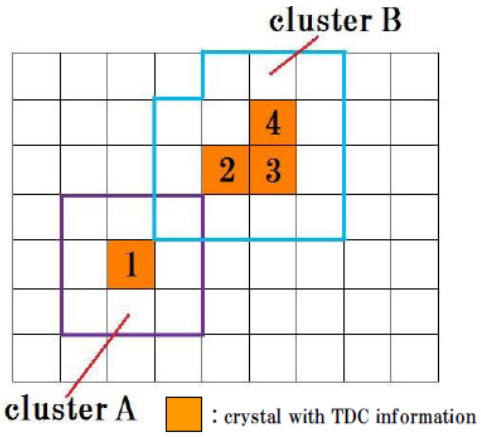

Fig.5. The definition of a cluster. In case of this figure, the cluster A consists of crystals inside the violet line, and the cluster B consists of crystals inside the blue line. Crystals in orange have TDC information.

We can reconstruct the invariant mass of a meson decaying to $\gamma\gamma$ from energies and hit positions of 2 neutral clusters by

$$M_{\gamma\gamma} = \sqrt{2E_{\mathrm{A}}E_{\mathrm{B}}(1-\cos\theta)} \tag{2}$$

where $E_{\mathrm{A}}, E_{\mathrm{B}}$ are the energy values of the clusters, and θ is the opening angle of the clusters.

3.2 Determination of gain factors

The gain factors have been determined using $\pi^0 \to \gamma\gamma$ events so that the π^0 peak position in the $\gamma\gamma$ invariant mass distribution should be consistent with the π^0 mass $m_\pi = 134.977$ MeV [4]. To determine the gain factors, we performed a successive approximation by iterating following procedures.

1, Reconstructing $\gamma\gamma$ invariant mass distribution of all combinations of 2 neutral clusters, and getting the mean value of π^0 peak for each crystal.
2, Adjusting gain factors by the following function.

$$\alpha_i^{\mathrm{new}} = \alpha_i^{\mathrm{old}} \left(\frac{m_\pi}{m_i} \right) \tag{3}$$

where $\alpha_i^{\mathrm{new}}, \alpha_i^{\mathrm{old}}$ are the old and new gain factor of ith crystal, respectively, and m_i is the mean value of π^0 peak for ith crystal obtained in 1.

These processes was iterated until convergence.

We checked the convergence with χ^2 defined by

$$\chi^2 = \sum_{i=1}^{1320} \left(\frac{m_i - m_\pi}{\delta m_i} \right)^2 \tag{4}$$

where m_i is the mean value of π^0 peak for ith crystal, and δm_i is the error of m_i. Convergence was achieved after 15th iteration because χ^2 almost stopped decreasing. After convergence, the mean values of π^0 peaks are within $m_\pi \pm 0.05$ MeV for all crystals (See Fig.6).

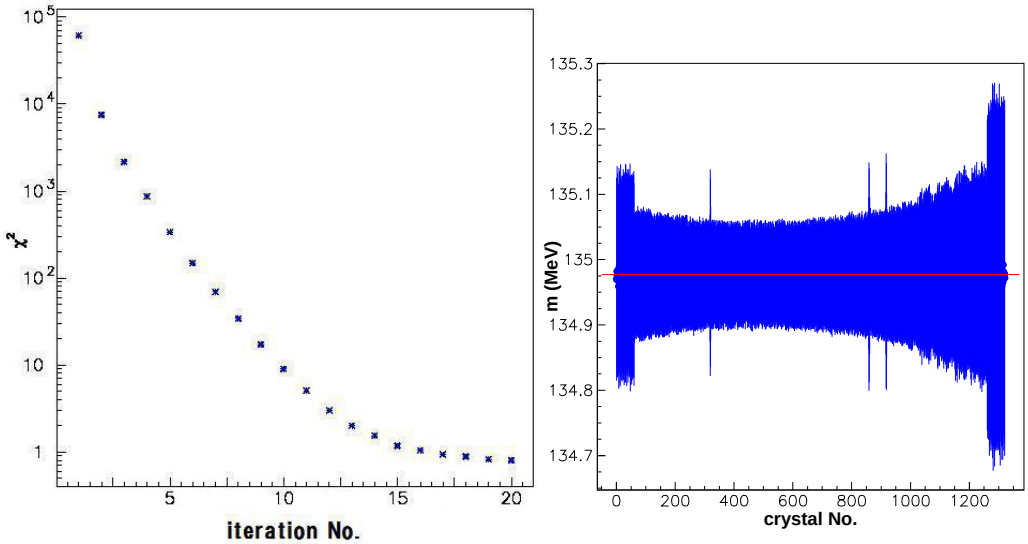

Fig.6. Left : Transition of χ^2 by iteration. Right : The mean values of π^0 peak after convergence.

3.3 Run dependence of gain factors and correlation with temperature

We checked the run dependence of gain factors. Fig.7 shows the transition of average gain factor and the room temperature. The gain factors are stable if the room temperature is kept constant, while the correlation between the room temperature and the gain factors is seen when the temperature changes significantly. The correlation can be explained by the light output of crystals and PMTs as a function of the tempearture $dL/dT \sim -1.5$ %/K.

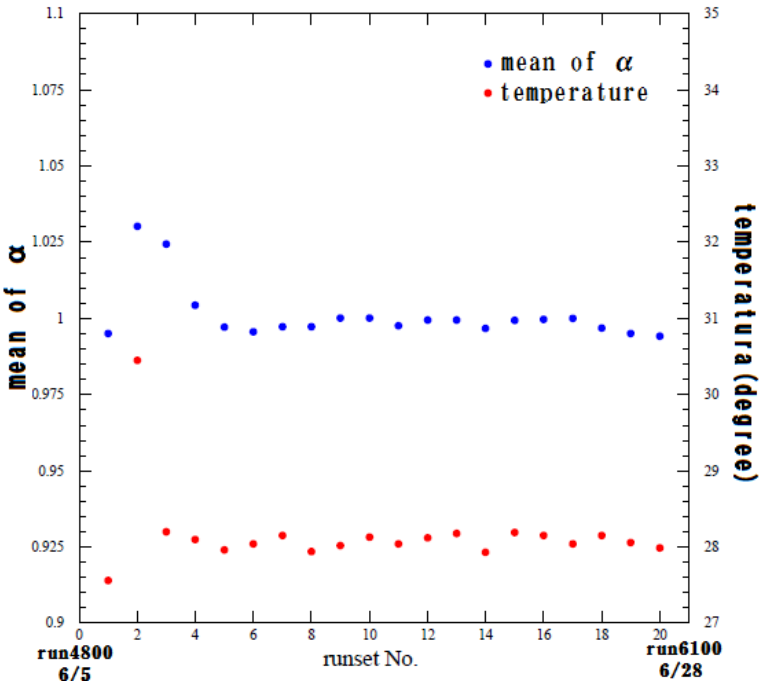

Fig.7. Run dependence of the average gain factor(blue) and the room temperature(red). The gain factor increases when the room temperature rises.

3.4 $\gamma\gamma$ invariant mass distribution and mass resolution

As a result of the energy calibration, the peaks corresponding to π^0 and η mesons are clearly observed in the $\gamma\gamma$ invariant mass distribution with a high mass-resollution of 6.7 MeV for π^0, and 14.4 MeV for η. η' mesons are also clearly observed with a mass-resolution of 18.8 MeV. This mass-resolution is enough to identify the η meson, and over 99% of multi-π events will be eliminated in search for η' mesic nuclei.

The mass resolution of BGOegg is significantly high compared with other detector systems used in the energy region of 1 GeV. Table 1 shows the comparison of the detector performance between BGOegg and some other detectors.

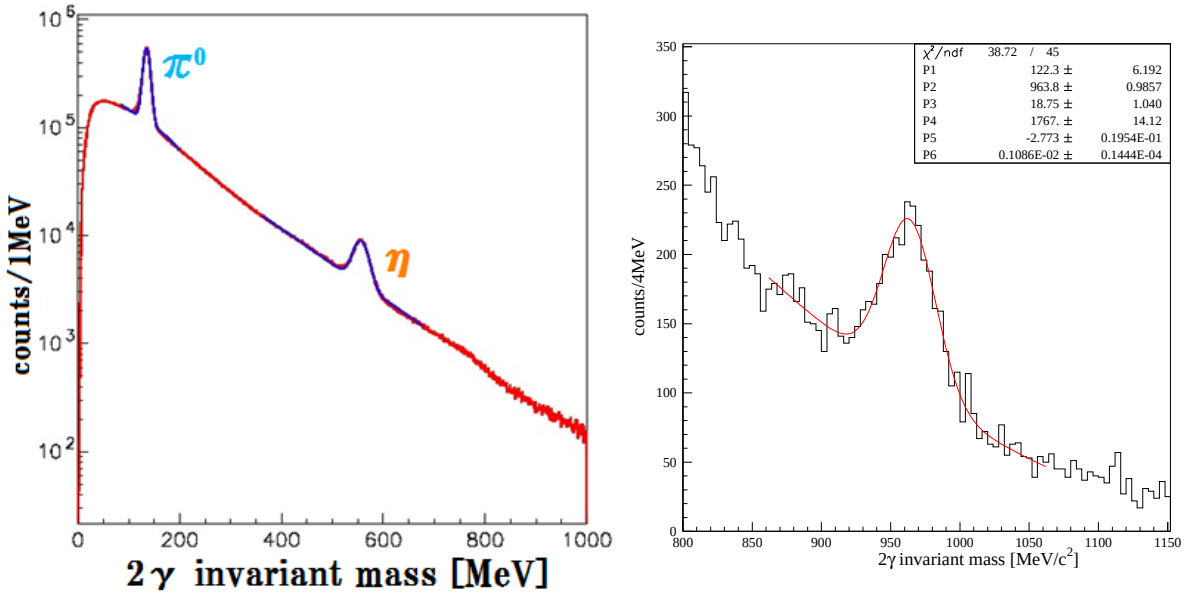

Fig.8. The $\gamma\gamma$ invariant mass distribution. Left : The overall distribution with logarithmic scale. π^0 and η are clearly observed. Right : The distribution of events with 2 neutral clusters with linear scale. η' is clearly observed.

	BGOegg [5]	Crystal Barrel [6]	Crystal Ball [7] [8]	GRAAL [9]
scintillator	BGO	CsI(Tl)	NaI(Tl)	BGO
number of crystals	1320	1380	672	480
energy resolution (1GeV γ)	1.3%	2.5%	1.7%	1.3%
π^0 mass-resolution σ_π(MeV) ($\gamma\gamma$ invariant mass, overall)	6.7	9.9	10	14
η mass-resolution σ_η(MeV) ($\gamma\gamma$ invariant mass, overall)	14.4	16.6	22	24

Table 1. Comparison of the photon energy-resolution and the meson mass-resolution among some calorimeters used in the energy region of 1 GeV.

3.5 More precise calibration

The energy calibration was performed to adjust the overall π^0 peak position in the $\gamma\gamma$ invariant mass distribution to π^0 mass m_π as explained above. However, the peak position of η mesons is a little higher than the η mass $m_\eta = 547.86$ MeV [4]. In addition, the peak position of π^0 is dependent on π^0 momenta, and shifts in the high momentum region (See Fig.9). The inconsistency of π^0 and η peak positions is caused by an energy leakage effect. When reconstructing a cluster of a gamma hit, a few % of energy leaks out of the cluster. Since the ratio of energy leakage is dependent on the photon energy and the polar angle of the hit position, a cluster energy should be corrected as a function of photon energies and polar angles. Fig.10 shows the leaked energy ratio $\Delta E/E$ estimated by MC simulation. We checked the leakage effect by MC simulation, and re-calibrated gain factors taking it into account.

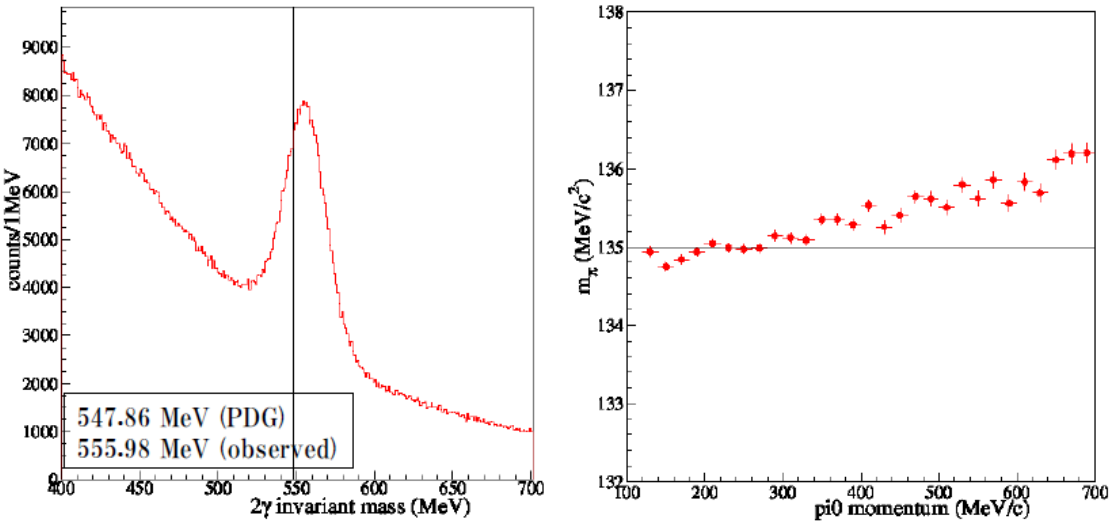

Fig.9. Left : The η peak in $\gamma\gamma$ invariant mass distribution. The mean value of the peak is 555.98 MeV, which is $\sim$8 MeV higher than η mass. Right : The momentum dependence of the π^0 peak position. The mean values of the π^0 peak become higher than π^0 mass as π^0 momenta become large.

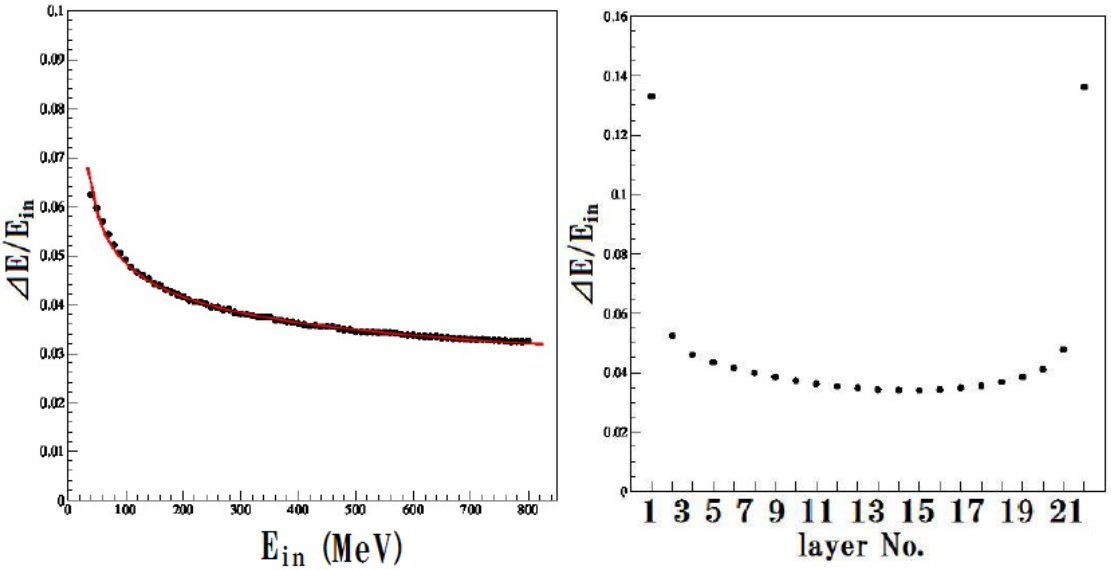

Fig.10. The leaked energy ratio $\Delta E/E$ as functions of photon energy(left) and the polar angle of the hit position(right) estimated by MC simulation.

Figure.11 shows the result of re-calibration. The mean value of the η peak has decreased and become close to the normal η mass after correction. In addition, the momentum dependence of the π^0 peak position has become almost constant.

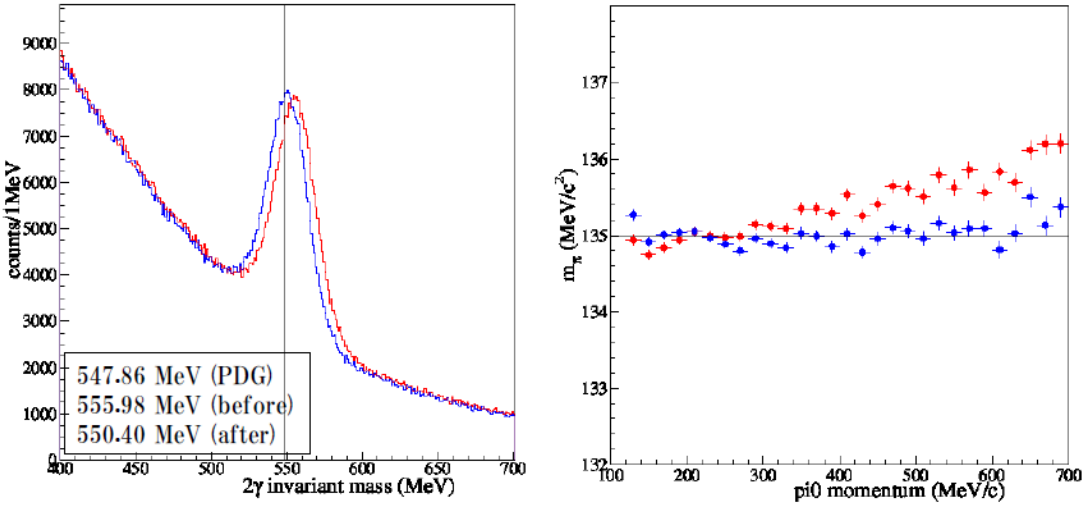

Fig.11. The effect of the energy correction taking leakage into account. The red and the blue show before and after correction, respectively. Left : The mean value of η peak is 550.40 MeV after correction becoming close to the normal η mass. Right : The π^0 peak position is almost independent of π^0 momenta after correction.

§4. Timing calibration of BGOegg

Timing information of BGOegg is used for the event selection or the separation of the RF bunches of 2ns interval. To obtain the timing information independently of the crystals, we have performed timing calibration so that the timing of a gamma hits returns 0. Since we used leading edge discriminators, there is correlation between timing information and ADC channels due to a time-walk effect (See Fig.12). Then we have performed a slewing correction by fitting the following function to ADC-timing correlation.

$$t_i = t_{0i} - \alpha_i \tanh(\beta_i(A_i - A_{0i})) - \gamma(A_i - A_{0i}) \tag{5}$$

where A_i, A_{0i} are ADC and pedestal values for ith crystal, respectively, and $t_{0i}, \alpha_i, \beta_i$ are free parameters for the fit. (γ is common in all crystals.)

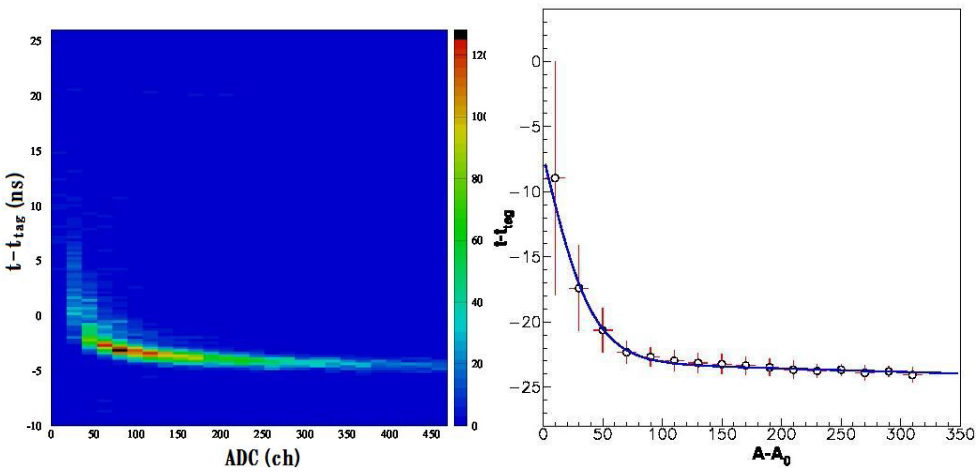

Fig.12. The ADC-timing correlation. The bule line in the right figure is a fitting function.

Figure.13 shows the timing difference distribution between 2 γ's from the same π^0 with energies over 200 MeV after the timing calibration. The timing difference resolution $\sigma_{\gamma\gamma}$ is 0.32 ns, corresponding to the time-resolution of a single crystal of 0.23 ns. This time-resolution is enough to separate the RF bunches, and also enough to eliminate accidental hits such as cosmic rays which is not negligible especially in the analysis of the LH_2 data.

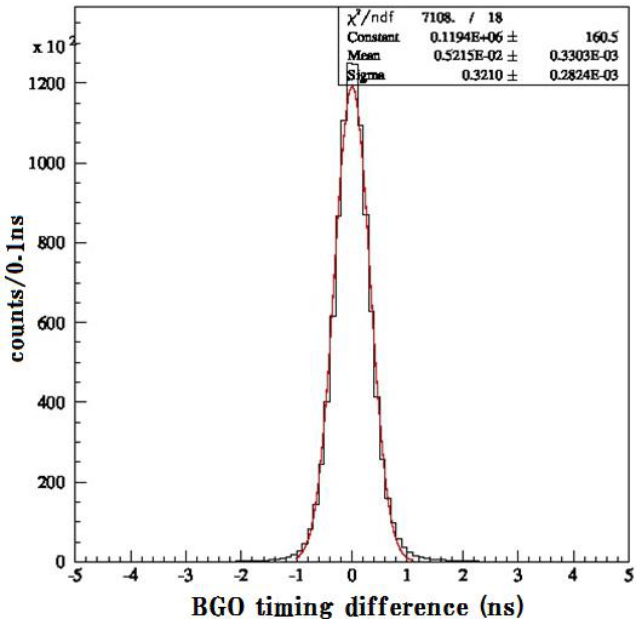

Fig.13. The timing difference distribution of 2 γ's from the same π^0. Sigma of the distribution is 0.32 ns.

§5. Summary

We are carrying out the LEPS2/BGOegg experiment aiming to search for η' mesic nuclei. A large acceptance electro-magnetic calorimeter BGOegg is used to detect γ's and identify mesons in final state. We have performed energy and timing calibration with a data of a carbon and a polyethylene target. As a result of energy calibration, the peaks corresponding to π^0, η and η' mesons have been observed in the $\gamma\gamma$ invariant mass distribution with a significantly high mass-resolutions of 6.7, 14.4 and 18.8 MeV, respectively. As a result of timing calibration, the time-resolution of a single crystal has been achieved to be 0.23 ns for γ's with energies over 200 MeV, which is enough to separate the RF bunches and to eliminate accidental hits of cosmic rays.

Acknowledgment

We greatly thank the SPring-8 staff for the stabel operation of the accelerators. This work was supported in part by Grants-in-Aid for Specially promoted Research (19002003), for Scientific Research (A) (24244022), and for Scientific Research (C) (26400287).

References

[1] H.Nagahiro *et al.*, Phys. Rev. C **74**, 045203 (2006)

[2] T.Ishikawa *et al.*, ELPH Annual Report **1**, Tohoku University, 61 (2012)

[3] M.Miyabe *et al.*, ELPH Annual Report **2-4**, Tohoku University, 144 (2014)

[4] Particle Data Group, Chin. Phys. C, **38**, 090001 (2014)

[5] T.Ishikawa, Internal GeV-γ Analysis Note, No.**231B** (2011)

[6] E.Aker *et al.*, Nucl. Instr. Meth. **A321**, 69 (1992)

[7] D.Watts The Crystal Ball and TAPS Detectors at the MAMI Electron Beam Facility, 11th International Conference On Calorimetry In High Energy Physics (2004)

[8] A.Thomas Recent result from the Crystal Ball Experiment at MAMI, HEPD Seminar (2010)

[9] https://bgo-od.physik.uni-bonn.de/ExperimentalSetup/BgoBall

Development of the liquid hydrogen target system for the electromagnetic calorimeter BGOegg

Norihito Muramatsu[1], Takeshi Ohta[2], Masaru Yosoi[2], Yuji Ohashi[3], Wen-Chen Chang[4], Jia-Ye Chen[5], Schin Daté[3], Hiroya Goto[2], Hirotomo Hamano[2], Toshikazu Hashimoto[6], Qing Hua He[1], Kenneth Hicks[7], Toshihiko Hiraiwa[2], Yuki Honda[1], Tomoaki Hotta[2], Hiroyuki Ikuno[2], Takatsugu Ishikawa[1], Igal Jaegle[8], Yuuto Kasamatsu[2], Satoshi Kido[1], Yukiyoshi Kon[2], Shinichi Masumoto[9], Yuji Matsumura[1], Manabu Miyabe[1], Keigo Mizutani[6], Takashi Nakano[2], Masayuki Niiyama[6], Yuki Nozawa[6], Haruo Ohkuma[3], Hiroaki Ohnishi[10,2], Masaya Oka[2], Kyoichiro Ozawa[11], Takuya Shibukawa[9], Hajime Shimizu[1], Ken'ichiro Shiraishi[1], Yorihito Sugaya[2], Shinsuke Suzuki[3], Shintaro Tanaka[2], Atsushi Tokiyasu[2], Natsuki Tomida[6], Nam Tran[2], Yusuke Tsuchikawa[1], Hirohito Yamazaki[1], Ryuji Yamazaki[1], and Tetsuhiko Yorita[2]

[1]*Research Center for Electron Photon Science, Tohoku University, Sendai, Miyagi 982-0826, Japan*
[2]*Research Center for Nuclear Physics, Osaka University, Ibaraki, Osaka 567-0047, Japan*
[3]*Japan Synchrotron Radiation Research Institute (SPring-8), Sayo, Hyogo 679-5198, Japan*
[4]*Institute of Physics, Academia Sinica, Taipei 11529, Taiwan*
[5]*National Synchrotron Radiation Research Center, Hsinchu 30076, Taiwan*
[6]*Department of Physics, Kyoto University, Kyoto 606-8502, Japan*
[7]*Department of Physics and Astronomy, Ohio University, Athens, OH 45701, USA*
[8]*University of Hawaii at Manoa, Honolulu, HI 96822, USA*
[9]*Department of Physics, University of Tokyo, Tokyo 113-0033, Japan*
[10]*RIKEN Nishina Center, Wako, Saitama 351-0198, Japan*
[11]*Institute of Particle and Nuclear Studies, High Energy Accelerator Research Organization (KEK), Tsukuba, Ibaraki 305-0801, Japan*

The liquid target system, which is usable for hydrogen and deuterium, was developed for the LEPS2/BGOegg experiments at SPring-8. It has a long nose with the 50 mm aperture for the beam path, in order to install the 40 mm-long target cell at the center of the electromagnetic calorimeter BGOegg. From 2014 November to 2015 February, the liquid hydrogen target was used for the physics data collection with the laser-backscattering photon beam, whose tagged counts reach about 3×10^{12} in total.

§1. Introduction

The LEPS2/BGOegg experiments at SPring-8 [1] has started the stable collection of physics data from 2014 April by using a few MHz photon beam, which is produced by the backward Compton scattering of the ultra-violet (UV) lasers and tagged in the energy range of 1.3–2.4 GeV [2]. The electromagnetic calorimeter BGOegg surrounds a target in the polar angle region of 24° to 144° with a good energy resolution (1.3% at 1 GeV). Charged particles are identified at the inner plastic scintillators (IPS) and the cylindrical drift chamber (CDC) inside the BGOegg, as shown in Fig. 1. The forward acceptance hole is covered by the planar drift chamber (DC, $\theta < 21°$) and the resistive plate chambers (RPC, $\theta < 7°$). The resolution of the time-of-flight measurement at the RPC is about 80 psec, so that the proton momentum can be calculated from the 12.5 m flight length with the resolution of $\sim$1% at 2 GeV/c. All of the detectors became finally ready in June.

From April to July, we used the 20 mm-thick nuclear targets of Carbon or polyethylene (CH_2) mainly for the η'-mesic nuclei search. The η' meson acquires a distinctively large mass by the $U_A(1)$ anomaly, appearing in the QCD Lagrangian, and receives special interests compared with usual Nambu-Goldstone bosons. By the partial restoration of chiral symmetry breaking, the large reduction of the η' mass by 80–150 MeV is theoretically calculated based on the Nambu-Jona-Lasinio (NJL) model [3] and the linear sigma model [4] even at the nuclear density.

The $U_A(1)$ anomaly possibly induces an attractive interaction between the η' and a nucleon ("N") in the QCD vacuum. Therefore, the measurement of the η'-N scattering length is desired near the production threshold of $\gamma p \to \eta' p$ reaction. In addition, the η' possesses a large content of $s\bar{s}$, whose

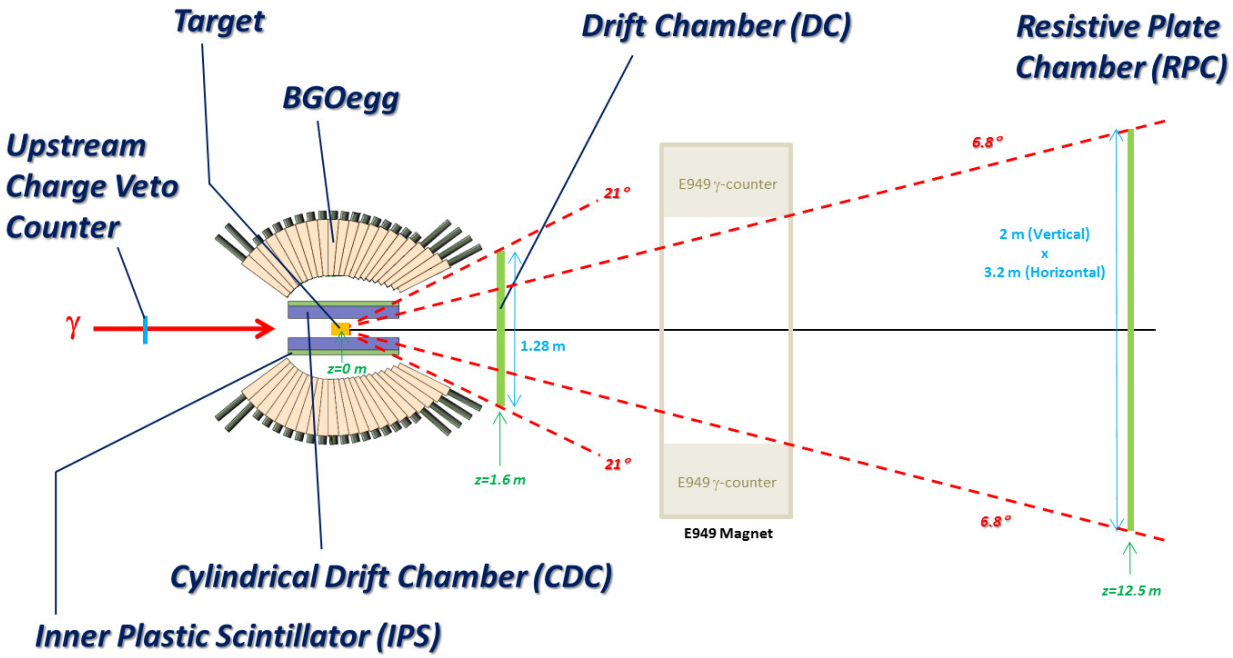

Fig.1. The detector setup of the LEPS2/BGOegg experiments.

phase relative to non-strange quark content $u\bar{u} + d\bar{d}$ is opposite to the case of η meson. It is expected that the cross sections of the η and η' photoproduction from a nucleon target are sensitive to the excited nucleon resonances, which strongly couple to strange quarks, along with clarifying the interference with the $s\bar{s}$ content in the nucleon. The measurements of the beam asymmetries relative to the linear polarization vector of photons also provide the spin information of the nucleon resonances.

The experimental data about the η' photoproduction from a nucleon target is still poor, and the LEPS2/BGOegg experiments intend to measure its total and differential cross sections and photon beam asymmetry by using a highly polarized photon beam. Such measurements of the elementary cross sections are necessarily important to understand the possible formation of the mesic nuclei, too. The experiments using the nucleon target is useful not only for the η' photoproduction but for various physics opportunities, including the excited nucleon resonance searches in the s-channel of single or double meson (ω, $\pi^0\pi^0$, $\pi^0\eta$, etc) photoproduction. Thus, we developed a liquid hydrogen target system, which is also usable for a deuterium target, in parallel with the nuclear target runs. The new liquid target system have been utilized at the physics data collection from 2014 November.

§2. Construction of the liquid hydrogen target system

The liquid hydrogen target system has a 1 m-long nose structure to place a 40 mm-long target cell at the center of the large acceptance electromagnetic calorimeter BGOegg. (See Fig. 2.) The nose part is extended from the chamber box, where the refrigerator (Sumitomo Heavy Industries, 4K GM refrigerator RDK-408D2) is mounted on the top. The refrigerator is connected to the buffer tanks, whose

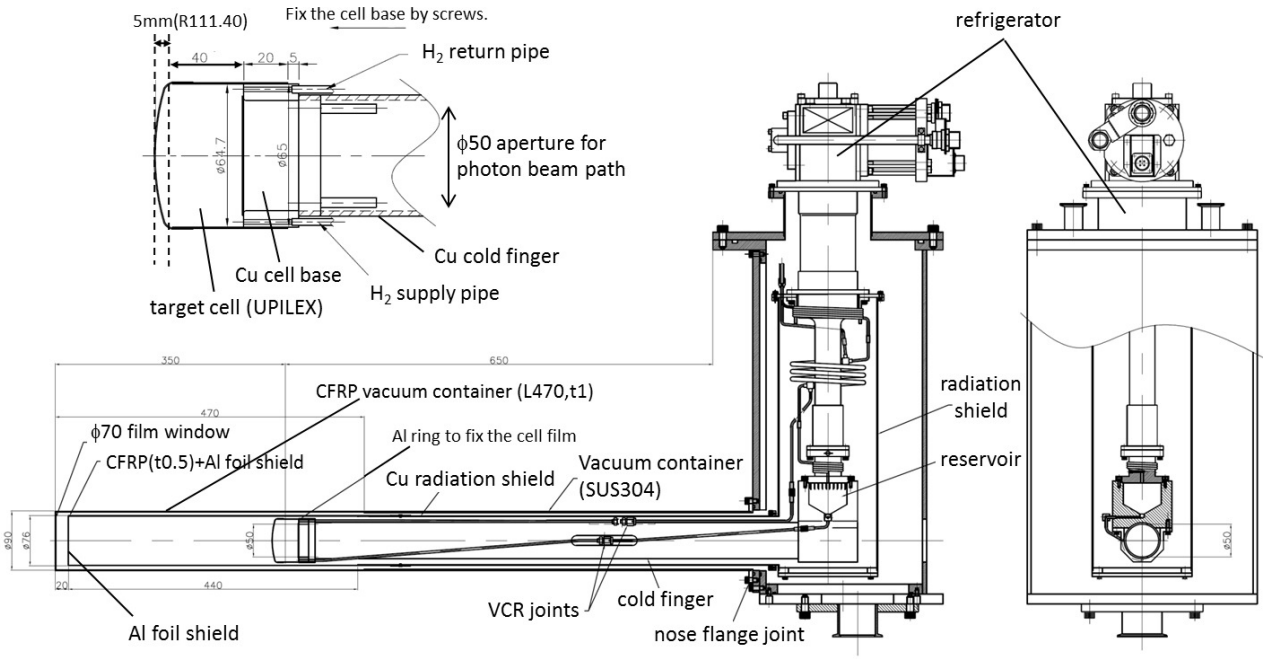

Fig.2. The side view (left) and the upstream end view (right) of the liquid hydrogen target system. The expanded side view of the target cell is also shown in the upper-left corner.

total volume is 300 L, by using the supply and return pipes made of Cu. The hydrogen gas is filled inside this closed volume at ∼1.7 atm, and partially liquefied at the 98 mL reservoir under the refrigerator. As a result of the liquefaction, the pressure of the remaining hydrogen gas becomes about 1 atm. The liquefied hydrogen is transferred to the target cell by the self-weight while the temperature is kept at ∼20 K with a heater and an automatic controller (LakeShore Model331).

The most outside of the chamber box and the ϕ90 nose structure is made of SUS304 to maintain the vacuum as a thermal shield. In order to reduce the material amount around the target cell, the front part (470 mm) of the nose is produced by a cylinder of carbon-fiber-reinforced plastic (CFRP) with the thickness of 1 mm. Inside these vacuum containers, the whole cooling system including the refrigerator, the reservoir, and the Cu cold finger is covered by radiation shields. The radiation shield around the target is also made by a 0.5 mm-thick CFRP support and Al foil. The cold finger is extended from the refrigerator inside the nose, and the cell base for the target mount is attached to the front part of the cold finger. In order to reserve the photon beam path (σ ∼6.5 mm), those structures have enough aperture at least with a 50 mm diameter. The front cap of the CFRP nose and the upstream wall of the SUS chamber box also have the windows covered by 75 μm-thick polyimide films (Ube Industries, UPILEX RN). The front faces of the CFRP nose and the Al foil radiation shield are apart from the target cell in order to achieve the better separation of the reaction products from the target and the background hits from the front materials at their detection by the BGOegg.

The target cell is produced by gluing 125 μm-thick UPILEX films to the cell base with Stycast. (See the upper-left part of Fig. 2.) The front cap of the cell is molded with moderate curvature, so that the real thickness becomes thinner to ∼50 μm. The cell volume is about 140 mL with a diameter of

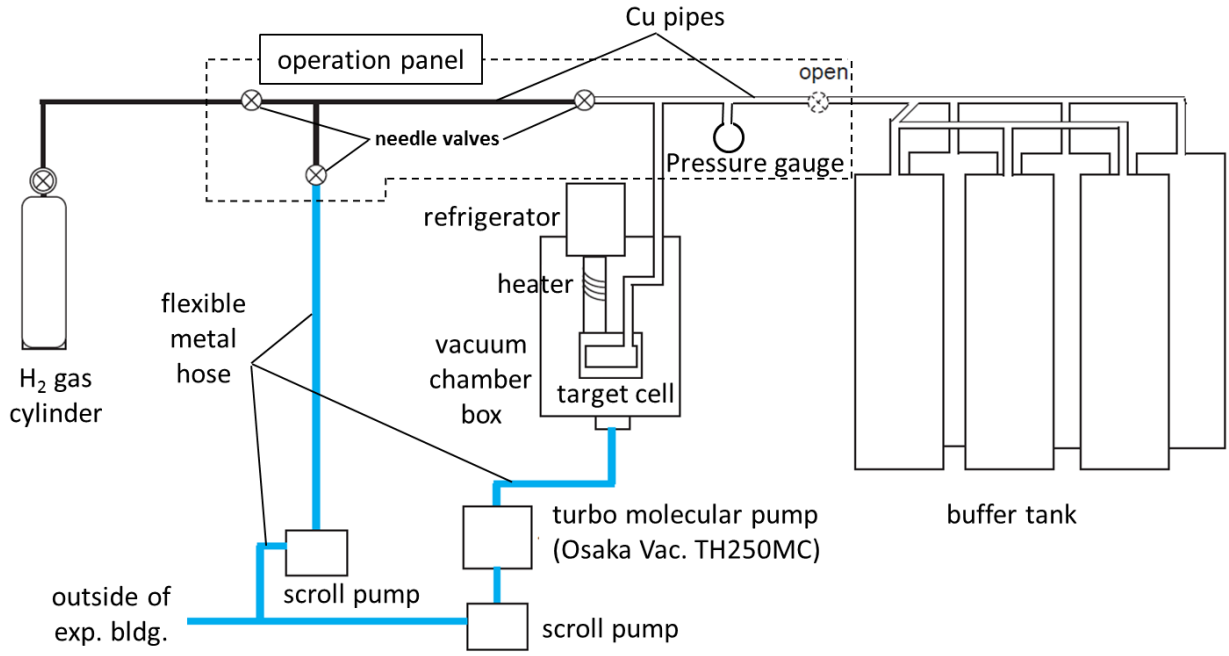

Fig.3. The schematic view of the hydrogen gas flow line and the vacuum control line.

65 mm. The liquid hydrogen is fully filled through the lower pipe hole of the cell base, and returns to the reservoir from the upper pipe hole. For the thermal insulation of the target cell and the cooling system, the vacuum is made inside the CFRP and SUS containers by using a turbo molecular pump and a scroll pump, connected with the bottom of the SUS chamber box. The possible leakage of the hydrogen gas from the cell is also exhausted by those pumps. Figure 3 shows the pipe connections for the vacuum control and the hydrogen gas flow at the constructed target system.

§3. Operation at the BGOegg experiments in 2014 Nov – 2015 Feb

In 2014 October, several tests were performed for debugging the cell structure, connecting the hydrogen gas and vacuum lines without any leakage, confirming the cooling system operation with the temperature and pressure monitors, and so on. Figure 4 shows the liquefaction status at the target cell in the view from the nose front. After the full liquefaction at the cell, the hydrogen gas pressure becomes $\sim$1 atm at the pressure gauge, located near the buffer tanks. The liquefied hydrogen volume at the target cell, the transfer pipes, and the reservoir was calculated to be 267 mL based on the pressures before and after the liquefaction. The temperatures at the target cell and the refrigerator head just above the reservoir were monitored by thermocouples, and the difference of the cell and head temperatures was a few K even with the nose structure.

The combination of the nose structure with the target cell and the vacuum chamber box with the refrigerator is placed on the sliding rail stage with many ball-type rollers. The nose structure was installed inside the BGOegg along the guide rail, which was fixed on the large plate for enabling the two-dimensional position adjustment by screws. (See Fig. 5.) The stage height was also optimized by the adjuster bolts, which were attached at the bottom of the individual stage leg and anchored to the floor of the experimental area. The target system was aligned by adjusting the cell position and the center of the upstream UPILEX window relative to the beam position markers. Further fine tuning was done by checking the azimuthal hit distribution at the BGOegg calorimeter with the injection of a photon beam. In the case of experiments with nuclear targets, this liquid target system can be slided away to the side space off the photon beam axis, so that the experimental setup should be easily changed depending on the physics plans.

Fig.4. The pictures of the target cell during the hydrogen liquefaction. The liquid surface increases while the gas pressure at the buffer tanks decreases from the left picture to the right picture.

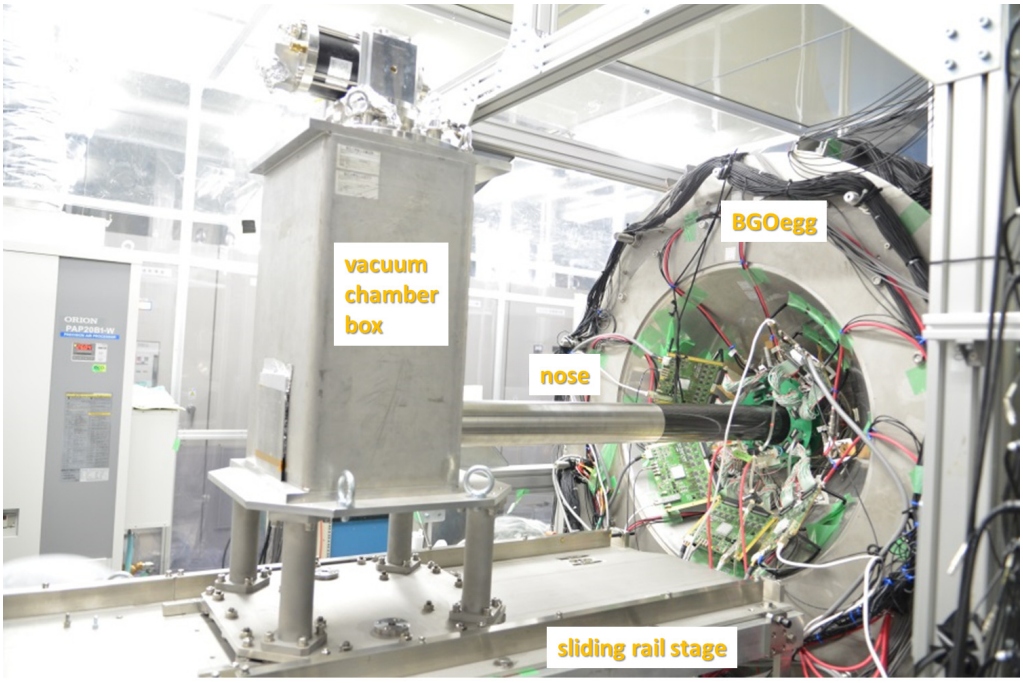

Fig.5. The picture of the hydrogen target system on the sliding rail stage. The nose part is installed into the BGOegg calorimeter.

The whole target system was stably working from 2014 November to 2015 February at the physics data taking. About 3×10^{12} of tagged photons were irradiated on the liquid hydrogen target in total. In order to study the possible systematics of the detector acceptances at the measurements of spin observables, the linear polarization vector of the photon beam was alternatively changed to the vertical or the horizontal directions. The energy and timing calibrations of individual detectors are being done by using the collected data. The π^0 and the η mesons will be identified in the invariant mass distibution of 2γ, which are detected at the BGOegg calorimeter. In the nuclear target data collected before the 2014 summer, those mesons have been already reconstructed with the good mass resolutions of 6.7 MeV/c^2 and 14.4 MeV/c^2, respectively. The ω meson also have been successfully reconstructed from the $\pi^0\gamma$ invariant mass (Br=8.3%) using the same nuclear target data. The photoproduction of the η' meson will be identified by the invariant mass distributions of $\pi^0\pi^0\eta$ (Br=21.6%) or 2γ (Br=2.2%). The 2γ decay mode has a smaller branching fraction, but the acceptance is a few times larger and covers the η' production angles in more forward region. A proton in the final state of the above meson photoproduction processes will be confirmed by the missing mass, which is calculated using the photon energy measured at the tagging detector of a recoil electron.

§4. Summary

The LEPS2/BGOegg experiments have started the physics data collection from 2014 April. First of all we used a Carbon or CH_2 target for the η'-mesic nuclei search, while the liquid hydrogen target system with a 1 m-long nose structure was developed to install the 40 mm target cell inside the electro-

magnetic calorimeter BGOegg. A part of the hydrogen gas, stored in the large volume buffer tanks, is liquefied at $\sim$20 K by the refrigerator, so that the liquid hydrogen is filled at the reservoir and the target cell. The target cell is made by 125 μm polyimide films and the material amount of the nose around the cell is reduced by using CFRP cylinders. The constructed target system was installed for collecting the γp reaction data from 2014 November to 2015 February. This data will be analyzed, for example, to measure the cross sections and the photon beam asymmetries in the photoproduction of η', η, ω, $\pi^0\pi^0$, $\pi^0\eta$, etc for the study of nucleon resonances.

Acknowledgment

We greatly thank to the staff at SPring-8 for the support to the beamline construction and commissioning and the stable operation of the accelerators. This research was supported in part by the Ministry of Education, Science, Sports and Culture of Japan and JSPS KAKENHI Grant No. 24244022.

References

[1] N. Muramatsu, ELPH Report 2044-13 (2013) or arXiv:1307.6411.

[2] N. Muramatsu *et al.*, Nucl. Instr. Meth. **A737** (2014) 184.

[3] H. Nagahiro *et al.*, Phys. Rev. C **74** (2006) 045203.

[4] S. Sakai and D. Jido, Phys. Rev. C **88** (2013) 064906.

Development of a charge-to-time (QTC) discriminator

T. Ishikawa[1]

[1]*Research Center for Electron Photon Science (ELPH), Tohoku University, Sendai 982-0826, Japan*

A charge integrating analog-to-digital converter (ADC) is too expensive only for the monitoring of the gain and applying a pulse-height time-walk correction. In addition, a very long cable for delaying analog signals is required for the ADC readout. It is difficult to introduce many ADC modules easily any more by taking into account the cost of ADC modules and long delay cables. Recently, a multi-hit time-to-digital converter (TDC) module is available, which can digitize both the timings of the leading and trailing edges of signals. Thus, it is not necessary to use an ADC module if the output width of a discriminator corresponds to the charge integration. The function converting the charge integration into the width of the logic signals is called as a charge-to-time converter (QTC). We have asked Fuji Diamond International Co. Ltd. to produce a discriminator with a QTC function fitted to the signals for plastic scintillators. The results of testing the developed QTC discriminator are given in this report. The QTC discriminator has been made into a product as GeVγ-1370.

§1. Introduction

The ordinary ADC module integrates the charge during the gate period, and digitizes the charge integration to give the energy deposit in a detector. The gate signal is often generated with a trigger circuit of a data acquisition system, and is delayed in a finite time. This delay determines the lengths of delay cables for analog signals to match them with the gate period. Long cables with an order of μs are required to obtain the energy deposit in scintillating fibers of STB-Tagger II at ELPH.

A flash ADC (FADC) module is a candidate to obtain the energy deposit. But A FADC chip with a very high frequency (more than several hundred MHz) is required for analog signals of plastic scintillators. We have a lot of difficulties to introduce very high frequency FADC chip:

1. high cost,
2. cooling FADC, and
3. very high speed processing of digitized data

are required. On the other hand, some filter circuits are necessary when low frequency FADC chips are adopted.

Recently, a multi-hit (MH) time-to-digital converter (TDC) module is available, which can digitize both the timings of the leading and trailing edges of signals. The V1190 and V1290 modules of CAEN SpA are often used MHTDC modules. Both the ADC and TDC modules are required for each signal to obtain the timing and the energy deposit. Yet, it is not necessary to use an ADC module if the output

width of a discriminator corresponds to the charge integration. The function converting the charge integration into the width of the logic signals is called as a charge-to-time converter (QTC). Generally, QTC is realized in the following way [1, 2]:

1. the input signal is amplified,
2. the charge is integrated in a capacitor,
3. The capacitor is discharged with a constant current.

Figure 1 shows the simplified circuit and charge in a capacitor.

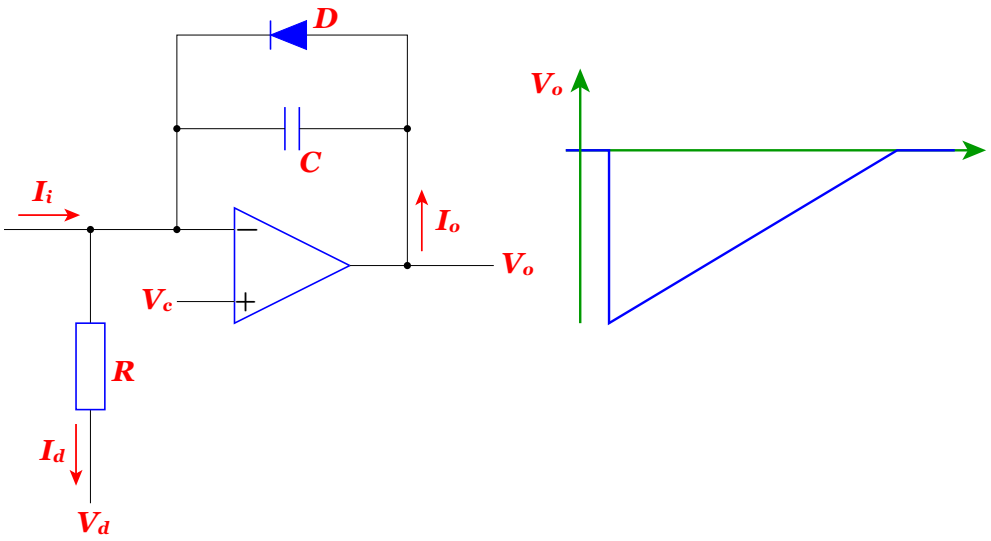

Fig.1. Simplified circuit and charge in a capacitor. The circuit consists of the integrator, and constant current source I_d which discharges the capacitor. The output voltage V_o of the circuit gives a linear triangle signal.

The quiescent voltage for the capacitor C is given by the diode D. The constant current I_d through a register R is defined as

$$I_d = \frac{V_c - V_d}{R} \tag{1}$$

from the difference between V_c and V_d. In the idle state, all the output current I_o from the operational amplifier (OPAMP) flows through the diode D, and makes $Id = I_o$. An input pulse makes I_o smaller according to the current of the input signal I_i, and the charge is integrated in the capacitor C. The circuit comes back to the idle state when the capacitor C is fully discharged by a constant current I_d.

The output current of the OPAMP is

$$I_o = I_d - I_i, \tag{2}$$

and $I_i = 0$ in the idle state. The charge Q_0 in the idle state is determined by the diode D, An input pulse makes the charge Q in the capacitor C becomes

$$Q = Q_0 - \int_t I_0(t)\, dt + I_d t, \tag{3}$$

and output voltage becomes

$$V_o = V_c + \frac{Q_0}{C} - \frac{1}{C}\int_0^t I_0(t)\, dt + \frac{I_d}{C} t. \tag{4}$$

If the current I_i according to the input pulse becomes 0 in a short time as compared with the discharging time, the behavior of V_o is expressed by the fourth term in eq. (4). A QTC discriminator should give a true state when V_o exceeds given threshold basically.

§2. Developed QTC discriminator

A QTC discriminator should be desired as a high precision leading edge discriminator. Therefore, the input signal is divided into two, and one is used for generating a leading edge of the output pulse, and the other is input to the integrator circuit giving a linear triangle pulse. This is realized by a flip-flop circuit so that the output signal is started by the comparator output for the former signal, and stopped by that for the latter triangle pulse. Figure 2 shows the behavior of the QTC discriminator, and Figure 3 shows its photo.

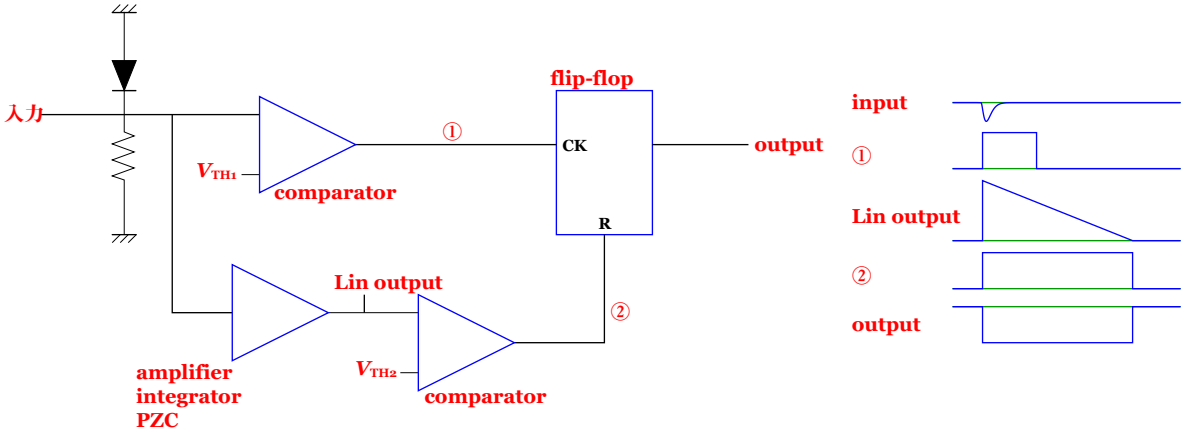

Fig.2. Behavior of the QTC discriminator. The main circuit of the QTC function described in §1 is given by an amplifier, integrator, and pole-cancellation circuit (PZC).

The V_{TH1} is a threshold for generating a output pulse, and V_{TH2} is that for determining of the width of the pulse. The requirements for the developed QTC discriminator are

1. the leading edges with high precision according to the given threshold V_{TH1}, and
2. the widths of the output pulses expressed by a (one polynomial) function according to the charge of the input signal.

The prototype QTC discriminator was produced by Fuji Diamond International Co. Ltd. to satisfy these conditions.

§3. Testing the prototype QTC discriminator

We tested the prototype QTC discriminator by using the output signals of photomultiplier tube (PMT) connected with a plastic scintillator. The plastic scintillator used was EJ-212 produced by ELJEN Technology, and it measured $30 \times 30 \times 20$ mm^3. It was connected to a PMT Hamamatsu H6410, and the supplied voltage is -1100 V with a current of 279 μA. The waveform of the input and output signals of the prototype QTC discriminator was acquired by employing a digital phosphor oscilloscope, Tektronix

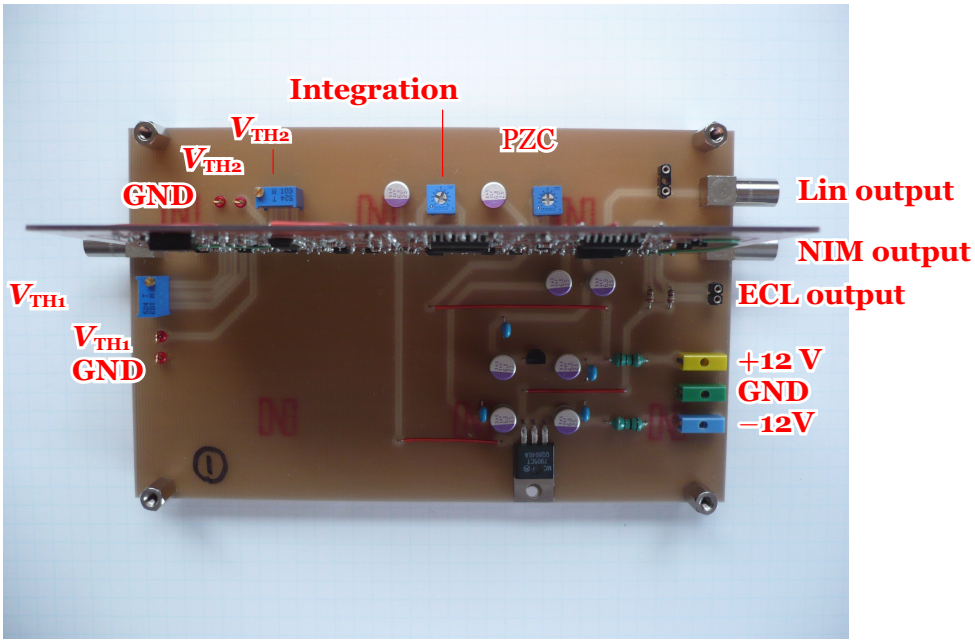

Fig.3. Photo of the prototype QTC discriminator produced by Fuji Diamond International Co. Ltd.

DPO-4104, with a sampling frequency of 5 GHz. Figure 4 shows the experimental setup for testing the prototype QTC discriminator.

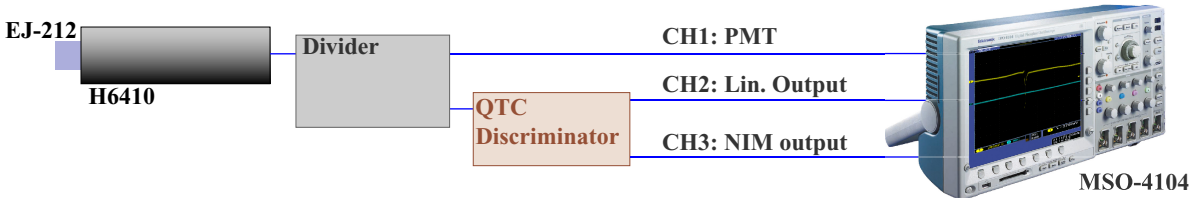

Fig.4. Experimental setup for testing the prototype QTC discriminator. The input signal to the QTC discriminator is given by the output signal of a photomultiplier tube (PMT) Hamamatsu H6410 connected with a plastic scintillator EJ-212 with a size of $30 \times 30 \times 20$ mm^3. The waveform of the input and output signals of the prototype QTC discriminator was acquired by employing a digital phosphor oscilloscope, Tektronix DPO-4104. The output signal of PMT is divided into two, one is delivered to CH1 of DPO-4104, and the other is input to the QTC discriminator. The linear and NIM outputs of it is given to CH2 and CH3 of DPO-4104, respectively.

The input signal to the QTC discriminator was given by the output signal of PMT. The output signal of PMT is divided into two, one was delivered to CH1 of DPO-4104, and the other was input to the QTC discriminator. The linear and NIM outputs of it was given to CH2 and CH3 of DPO-4104, respectively. The waveform acquisition was made by using a library [3] developed by T. Ishikawa *et al*. The trigger of DPO-4104 was the falling edge of CH3 (NIM output) with a threshold of -400 mV. The measured voltages are $[-270, +30)$, $[-100, +900)$, and $[-1800, +200)$ mV for CH1, CH2, and CH3, respectively. The waveform was recorded by 0.2 ns step with a time $[-379.8, 420.0]$ ns. Table 1 summarizes the acquired data. To reject the accidental double pulses in the analysis, The width of the output signals of

PMT with a -5 mV threshold is longer than 30 ns by checking CH1 waveform. The events was rejected that the voltage of -270 mV was recorded in CH1. Figure 5 shows the typical waveforms for the output signals of PMT and those of the QTC discriminator.

Table 1. Acquired data. The discriminator threshold (V_{TH1}), the number of events, the effective number of events which satisfy the conditions.

run	threshold	#events	#analyzed events
008	-19.9 mV	10,000	9,878
009	-6.8 mV	10,000	9,947
010	-45.0 mV	3,000	2,890
011	-60.9 mV	3,000	2,878
012	-31.9 mV	3,000	2,937

To obtain the amplitude V_0, timing t_0, rising time τ_R, and decay time τ_D, the function

$$V(t) = -V_0 \ \ \mathrm{freq}\left(\frac{t-t_0}{\tau_R}\right)\exp\left(-\frac{t-t_0}{\tau_D}\right) \tag{5}$$

is fitted to the waveform of the PMT output signal event by event. The error of each point is assumed to be 1.12 mV, which is the resolution corresponding to the least significant bit. The fitting process was made with a time range $[-20, -5)$ ns, and iterated five times with a time range $[t_0 - 4\tau_R, t_0 + 4\tau_D)$. Figure 6 shows the output waveforms of PMT together with a fitted functions.

The obtained parameters are

$$\begin{cases} V_0 = 60.6 \pm 0.7 \text{ mV} \\ t_0 = -14.76 \pm 0.10 \text{ ns} \\ \tau_R = 2.34 \pm 0.05 \text{ ns} \\ \tau_D = 4.62 \pm 0.10 \text{ ns} \end{cases} \tag{6}$$

for the first event in `run008`, and

$$\begin{cases} V_0 = 324.0 \pm 0.8 \text{ mV} \\ t_0 = -11.29 \pm 0.02 \text{ ns} \\ \tau_R = 2.33 \pm 0.01 \text{ ns} \\ \tau_D = 5.35 \pm 0.02 \text{ ns} \end{cases} \tag{7}$$

for the third event in the same run. The maximum pulse height V_{max} is determined from the maximum difference of the recorded pulse height in each event. The ground level V_{GND} is also determined by the average pulse height in a time $[-70, -30)$ ns. The charge integration is obtained by using a pulse height V over a time $[-30, +10)$ ns

$$Q = \int \frac{1}{50\ \Omega}\left(V(t) - V_{\mathrm{GND}}\right)\,dt = \sum_{[-30,+10)\ \mathrm{ns}} \frac{V(t)}{50\ \Omega}\,\Delta t - \sum_{[-70,-30)\ \mathrm{ns}} \frac{V(t)}{50\ \Omega}\,\Delta t, \tag{8}$$

where $\Delta t = 0.2$ ns stands for the period of the pulse height measurement. The V_{max} is 38.4 and 183.6 mV, and the charge integration Q is 6.8 and 37.5 pC for the first and third events in `run008`. Figure 7 shows the correlations between the charge integration Q and the amplitude V_0, that between Q and the

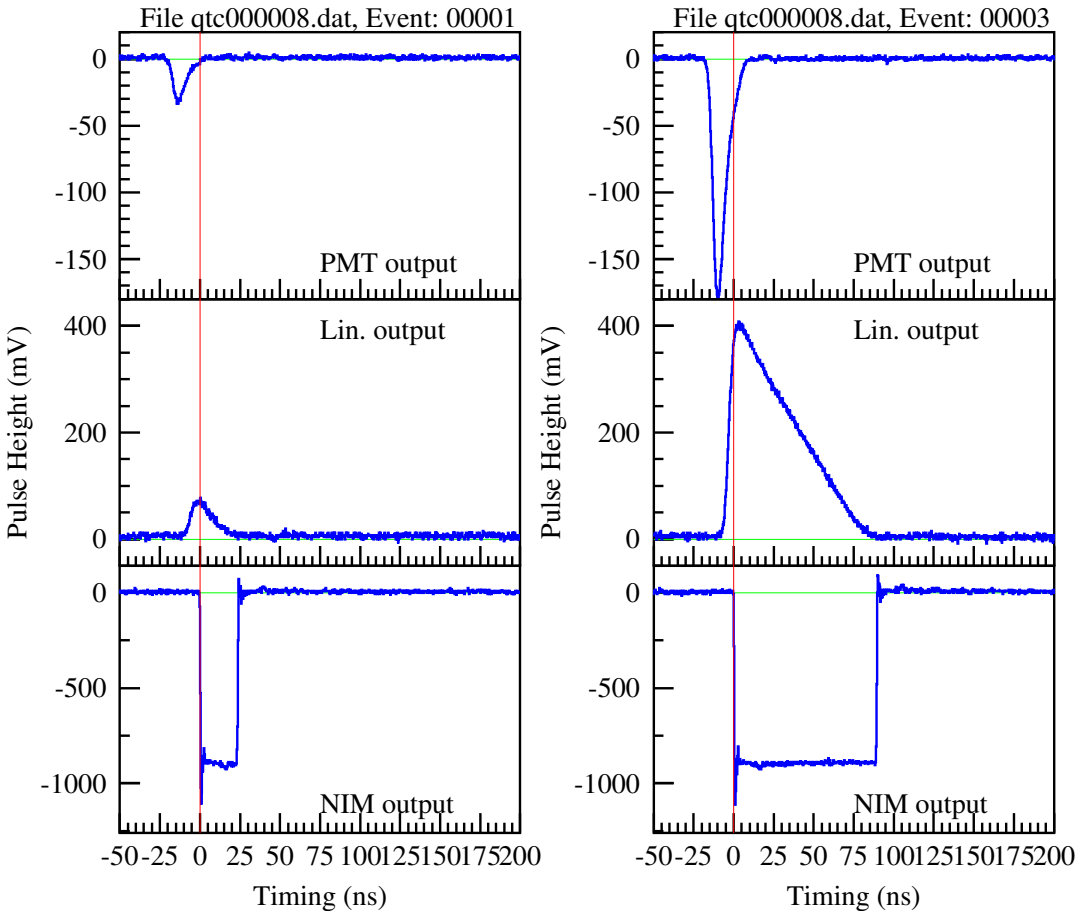

Fig.5. Typical waveforms for the output signals of PMT and those of the QTC discriminator. The left panel shows the waveforms of the first event in `run008`, and the right one shows those of the third event in the same run. The upper, central, and lower panels show the waveforms of the PMT output (CH1), the linear output (CH2), and the NIM output (CH3). The green and red lines correspond to the voltage of 0 mV and the timing of 0 ns, respectively.

maximum pulse height $V_{\max}$, and that between V_0 and $V_{\max}$. All the correlation shows a proportional function, and they give $V_0/Q = 8.5 \pm 0.2$ mV/pC, $V_{\max}/Q = 5.2 \pm 0.2$ mV/pC, $V_{\max}/V_0 = 0.61 \pm 0.03$ for all the events in `run008`.

Since the Q, V_0 and $V_{\max}$ are proportional each other, the waveforms of the output signals of PMT can be assumed to be the same. To confirm this, the rising and decay time parameters are also investigated. Figure 8 shows the rising time parameters τ_R and the decay time parameter τ_D. Both of them are constant, all the events in `run008` give $\tau_R = 2.3 \pm 0.1$ ns and $\tau_R = 5.2 \pm 0.2$ ns.

The set value of the threshold V_{TH1} and the effective value of the threshold V_{eff} are investigated by looking at the distributions of the maximum pulse height V_{rmmax}. Figure 9 shows the maximum pulse height (V_{rmmax}) distribution run by run. The effective threshold V_{eff} is determined by the minimum value of V_{rmmax}. The V_{eff} is -31, -13, -65, -83, and -47 mV for `run008`–`run012`. The correlation between V_{TH1} and V_{eff} is also plotted in Fig. 9. Although V_{TH1} and V_{eff} is different, V_{eff} can be expressed by a one dimensional polynomial function of V_{TH1}. Taking the error of V_{eff} to be 1 mV, V_{TH1} is expressed

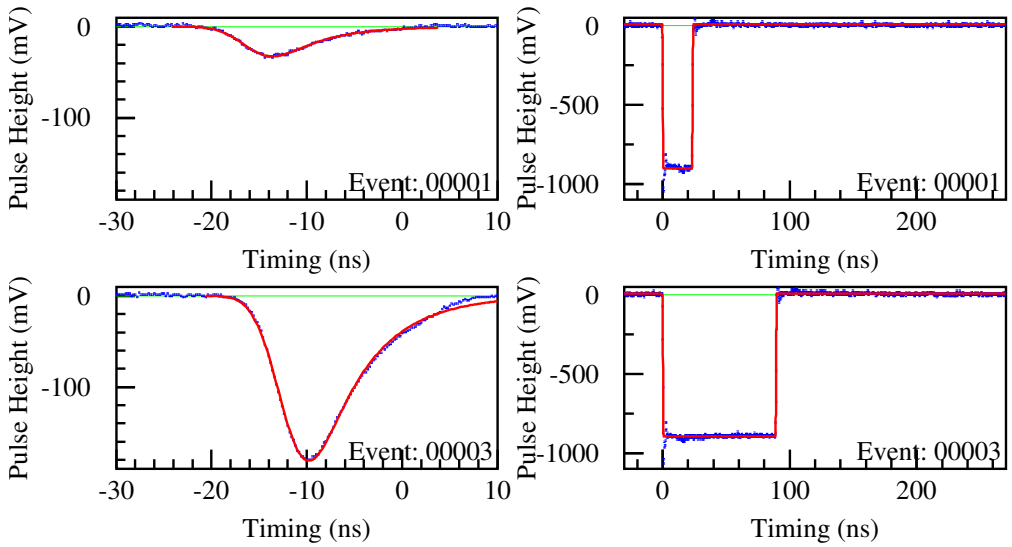

Fig.6. Typical waveforms of PMT output signals (left) and those of NIM output signals of the QTC discriminator. The upper panels show the waveforms for the first event in `run008`, and the lower show those for the third event in the same run. The green lines stand for the voltage of 0 mV, and the red curves show the fitted functions expressed in eq. (5) and (10).

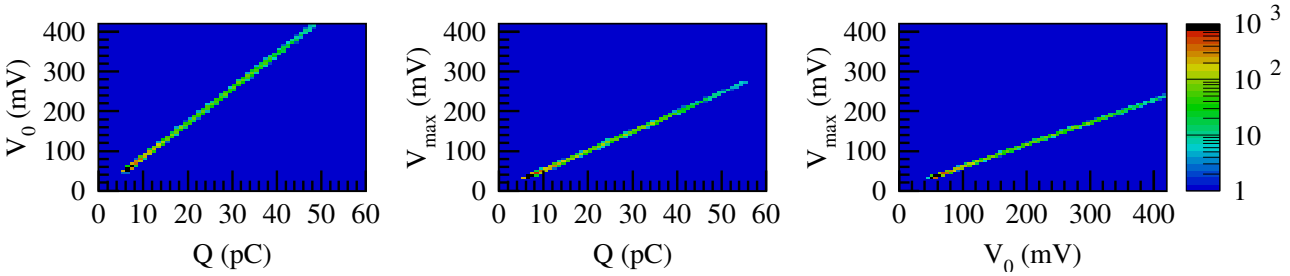

Fig.7. Correlations between the charge integration Q and the amplitude V_0 (left), that between Q and the maximum pulse height $V_{\max}$ (central), and that between V_0 and $V_{\max}$ (right). The correlations are given by the events in `run008`.

as a function of $V_{\rm eff}$

$$(-V_{\rm eff}) = (4.3 \pm 0.9) + (1.327 \pm 0.024)\,(-V_{\rm TH1})\,. \tag{9}$$

A function

$$V(t) = V_c - V_a \,\mathrm{freq}\left(\frac{t-t_l}{\tau_l}\right)\left\{1 - \mathrm{freq}\left(\frac{t-t_t}{\tau_t}\right)\right\} \tag{10}$$

is fitted to the NIM output of the QTC discriminator to obtain the ground level V_c, the amplitude V_a, the leading edge timing t_l, the rising time of the leading edge τ_l, the trailing edge timing t_t, and the falling time of the trailing edge τ_t event by event. The error of each point is assumed to be 7.81 mV, which is the resolution corresponding to the least significant bit. The fitting process was made five times with a time range $[-30, +270)$ ns. Figure 6 shows the waveform of the NIM output signals of the QTC discriminator

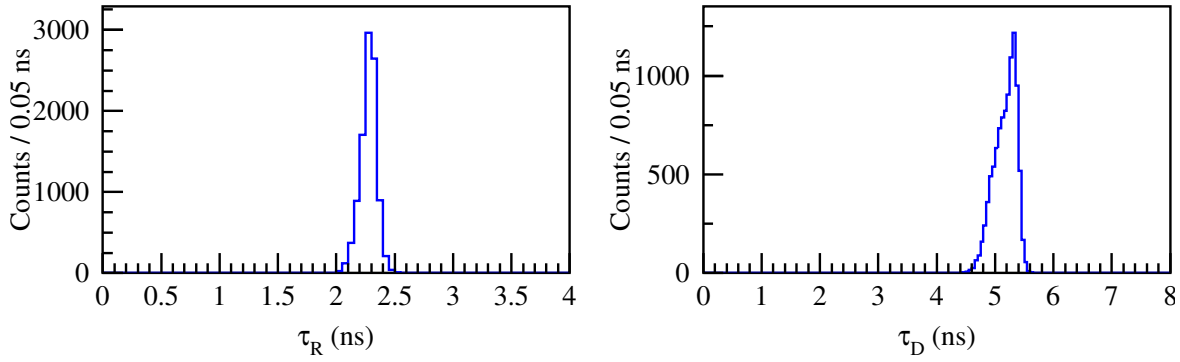

Fig.8. Rising time parameter τ_R (left) and decay time parameter τ_D (right). These parameters are given by the events in `run008`.

for the first and third events in `run008`. The obtained parameters are

$$\begin{cases} V_c = 5.3 \pm 0.2 \text{ mV} \\ V_a = 906.6 \pm 0.8 \text{ mV} \\ t_l = 0.14 \pm 0.00 \text{ ns} \\ \tau_l = 0.21 \pm 0.00 \text{ ns} \\ t_t = 23.62 \pm 0.00 \text{ ns} \\ \tau_t = 0.26 \pm 0.00 \text{ ns} \end{cases} \tag{11}$$

for the first event in `run008`, and

$$\begin{cases} V_c = 6.8 \pm 0.2 \text{ mV} \\ V_a = 902.3 \pm 0.4 \text{ mV} \\ t_l = 0.30 \pm 0.00 \text{ ns} \\ \tau_l = 0.20 \pm 0.00 \text{ ns} \\ t_t = 89.39 \pm 0.00 \text{ ns} \\ \tau_t = 0.26 \pm 0.01 \text{ ns} \end{cases} \tag{12}$$

for the third event in `run008`. The width of the NIM output signal t_W is determined by the time difference between the leading and trailing edges event by event. The width is 23.49 and 89.09 ns for the first and third events in `run008`, and becomes longer as the charge integration larger.

To confirm that the NIM output is stable. th ground level V_c, the amplitude V_a, the rising time of the leading edge τ_l, and the falling time of the trailing edge τ_t are investigated. Figure 10 shows the distributions for the ground level V_c, the amplitude V_a, the rising time of the leading edge τ_l and the falling time of the trailing edge τ_t. All the variables are constant, and $V_c = 6.0 \pm 0.7$ mV, $V_a = 905.9 \pm 2.4$ mV, $\tau_l = 0.18 \pm 0.05$ ns, and $\tau_t = 0.27 \pm 0.02$ ns in `run008`. The τ_l and τ_t is approximately the same value of the sampling period of DPO-4104 (0.2 ns), which indicate the transition time of the states is very short.

The correlation between the charge integration Q and the width of the NIM output signals t_w is investigated run by run. Figure 11 shows the correlation between Q and t_W. The t_W is proportional to Q for all the runs. The very small threshold deteriorates the linearity between Q and t_W at very close

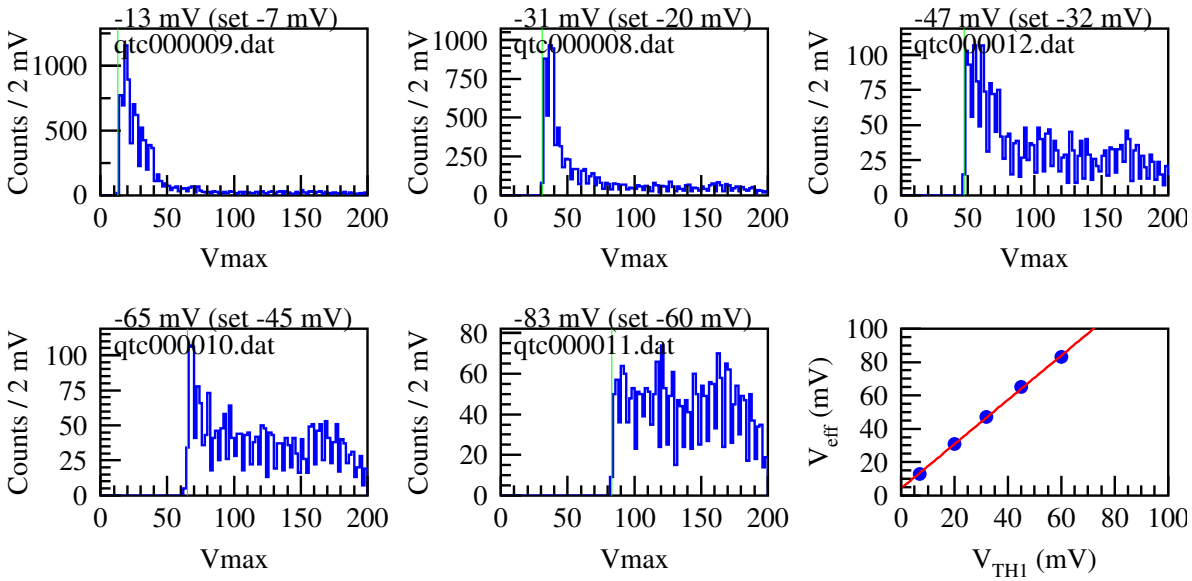

Fig.9. Maximum pulse height ($V_{\max}$) distributions for the runs, and the correlation between the set value of the threshold V_{TH1} and the effective value of the threshold V_{eff}. The panels show the $V_{\max}$ distributions for `run009`, `run008`, `run012`, `run010`, and `run011` from the upper left. The green lines show V_{eff}. The V_{TH1} and V_{eff} are described in each panel. The lower right panel shows the correlation between V_{TH1} and V_{eff}. The absolute value is adopted for these values.

to the threshold (`run009`). The t_W is fitted by a function of Q expressed

$$t_W(Q) = C_W Q + t_W^0, \tag{13}$$

and the charge to time conversion factor C_W and the minimum width corresponding to the charge integration of 0. The obtained parameters are

$$(t_W^0, C_W) = \begin{cases} (10.72\ \mathrm{ns},\ 2.10\ \mathrm{ns/pC}) & \text{for } V_{\mathrm{eff}} = -13\ \mathrm{mV}\ (\texttt{run09}), \\ (7.95\ \mathrm{ns},\ 2.15\ \mathrm{ns/pC}) & \text{for } V_{\mathrm{eff}} = -31\ \mathrm{mV}\ (\texttt{run08}), \\ (7.50\ \mathrm{ns},\ 2.15\ \mathrm{ns/pC}) & \text{for } V_{\mathrm{eff}} = -47\ \mathrm{mV}\ (\texttt{run12}), \\ (7.57\ \mathrm{ns},\ 2.14\ \mathrm{ns/pC}) & \text{for } V_{\mathrm{eff}} = -65\ \mathrm{mV}\ (\texttt{run10}),\ \text{and} \\ (7.85\ \mathrm{ns},\ 2.12\ \mathrm{ns/pC}) & \text{for } V_{\mathrm{eff}} = -83\ \mathrm{mV}\ (\texttt{run11}). \end{cases} \tag{14}$$

The t_W^0 is a little bit large, and C_W is a little bit small for the run with a very small threshold (`run008`). Except for this run, both the C_W and t_W^0 parameters are constant independently of the given threshold V_{TH1}.

The correlation between the charge integration Q and the leading edge timing of the NIM output of the QTC discriminator t_L are investigated. The leading edge timing of the NIM output of the QTC discriminator t_L is determined by $t_l - t_0$, where t_l and t_0 is the timings for the PMT and NIM output signals measured by DPO-4104. Figure 12 shows the correlation between Q and t_L. The correlation is similar to the ordinary leading edge discriminator. This is because the leading edge is determined only by a comparator. Since the t_W is a one dimensional polynomial function of Q, and t_0 can be given from t_L by using t_W.

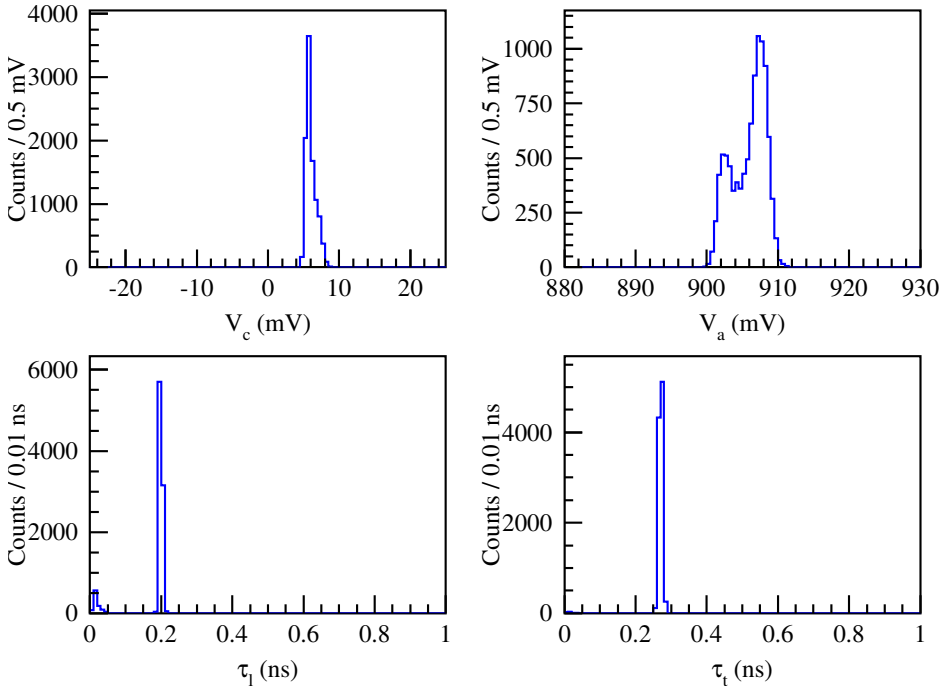

Fig.10. Distributions for the ground level V_c (upper left), the amplitude V_a (upper right), the rising time of the leading edge τ_l (lower left), and the falling time of the trailing edge τ_t (lower right) for the NIM output of the QTC discriminator. All the values are determined by the events in `run008`.

The details of the analysis for testing the prototype QTC discriminator are described elsewhere [4]. A slight problem on the difference between set and effective threshold values has been fixed, and a QTC discriminator has been made into a product as GeVγ-1370. GeVγ-1370 will be tested by using a time of flight measurement of the positron beam.

§4. Summary

A discriminator with a charge-to-time converter (QTC) has been designed, which converts the charge integration into the width of the output logic signals. The prototype QTC discriminator was manufactured by Fuji Diamond International Co. Ltd. The leading edge timing of the output logic signals given by the discriminator is similar to the ordinary leading edge one. The width of the output signals is expressed by a one dimensional polynomial function of the charge integration. This discriminator together with a multihit TDC is very useful for both the measurements of the timing and the energy deposit. A slight problem has been fixed, and a QTC discriminator has been made into a product as GeVγ-1370.

Acknowledgement

The author thanks Mr. Yasuo Takeda, and Mr. Toshimitsu Takeda in Fuji Diamond International Co. Ltd. for accepting the cooperation of the development of the QTC discriminator. This work was supported in part by Grant-in-Aids for Scientific Research (A) (24244022) and for Scientific Research (C)

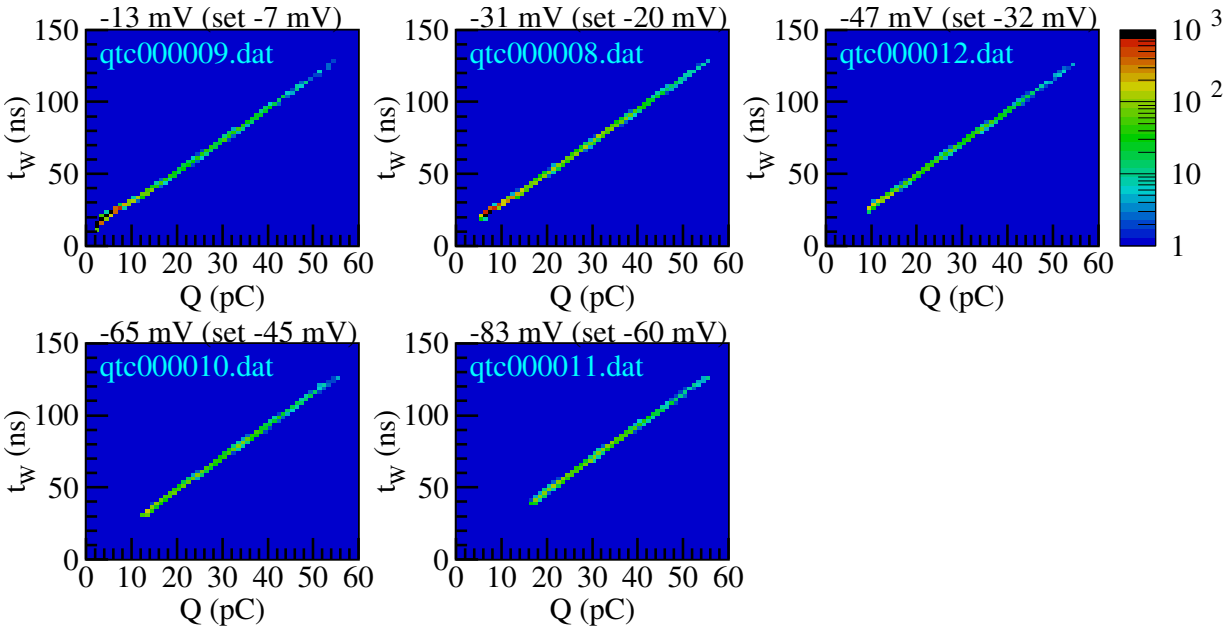

Fig.11. Correlation between the charge integration Q and the width of the NIM output signals t_w. The panels show the correlation between Q and t_W for `run009`, `run008`, `run012`, `run010`, and `run011` from the upper left. The V_{TH1} and V_{eff} are described in each panel. The lower right panel shows the correlation between V_{TH1} and V_{eff}. The t_W is proportional to Q for all the runs. The very small threshold deteriorates the linearity between Q and t_W at very close to the threshold (`run008`).

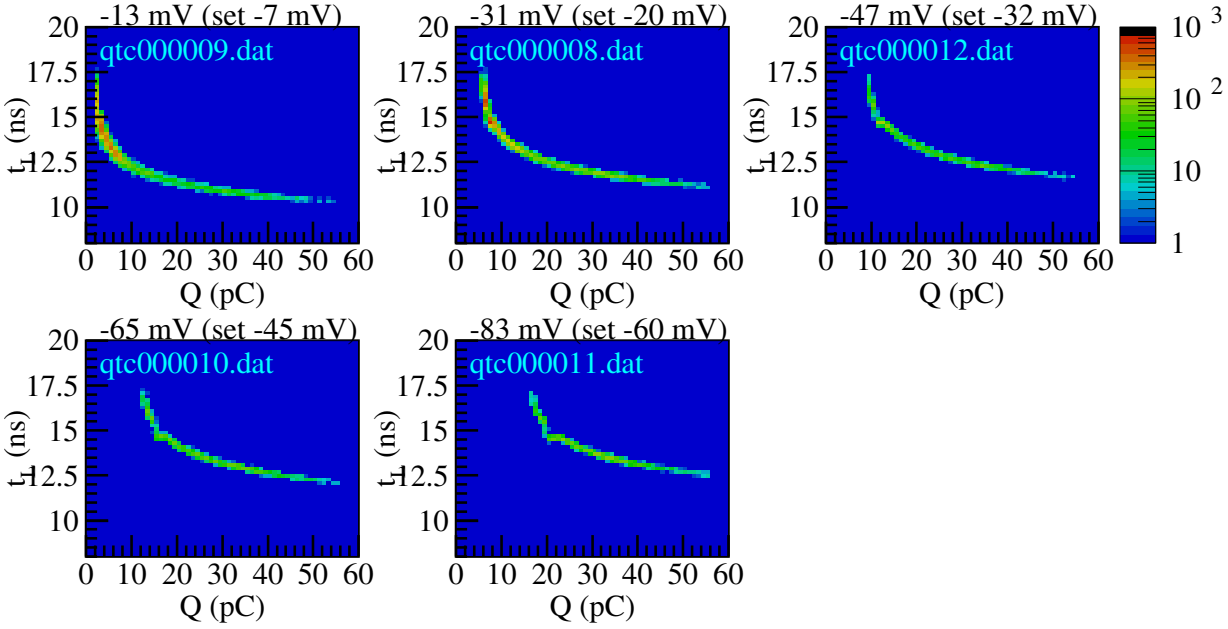

Fig.12. Correlation between the charge integration Q and the leading edge timing of the NIM output signals t_L. The panels show the correlation between Q and t_+ for `run009`, `run008`, `run012`, `run010`, and `run011` from the upper left. The V_{TH1} and V_{eff} are described in each panel.

(26400287).

References

[1] C. Parl *et al.*: Fast Charge to Pulse Width Converter for Monolith PET Detector, IEEE Trans. on Nucl. Sci. **59**, 1809 (2012).

[2] Y. Lin: Application of the Charge to Time Conversion Technique in Radiation Spectroscopy, Progress in Nuclear Science and Technology **1**, 206 (2011).

[3] T. Ishikawa: Internal GeV-γ Analysis Note No. **151**$\mathcal{A}$ (2009);
T. Ishikawa: Internal GeV-γ Analysis Note No. **177**$\mathcal{A}$ (2010).

[4] T. Ishikawa: Internal GeV-γ Analysis Note No. **356**$\mathcal{C}$ (2014).

Commissioning of the Electron spectrometer for the SCRIT electron scattering facility

K. Tsukada[1], A. Enokizono[3], K. Kurita[3], S. Matsuo[3], Y. Moriya[1], T. Ohnishi[2], T. Suda[1], T. Tamae[1], M. Togasaki[3], T. Tsuru[1], R. Toba[4], K. Yamada[3], S. Yoneyama[1], and M. Wakasugi[2]

[1]*Research Center for Electron Photon Science, Tohoku University, Sendai, 982-0826*
[2]*RIKEN Nishina Center for Accelerator-Based Science, Wako, 351-0198*
[3]*Department of Physics, Rokkyo University, Tokyo, 171-8501*
[4]*Department of Electrical Engineering, Nagaoka University of Technology, Niigata, 940-2137*

We have developed the SCRIT electron scattering facility to realize electron scattering experiments off unstable nuclei. In December 2014, a commissioning experiment was carried out using a tungsten wire target just after the construction of an electron spectrometer and new luminosity monitor system completed. The elastically scattered electrons were successfully identified with the electron spectrometer. The present status of analysis are reported here.

§1. Introduction

Electron scattering provides the most powerful and reliable information of the nuclear structure. Many stable nuclei have been investigated and our understanding of nuclear structures have been established by electron scattering experiments in the latter half of the 20th century after the Nobel-prize experiments by R. Hofstadter and his colleagues [1]. This method, however, could be applied almost only stable nuclei because of the difficulty to prepare the target material for unstable nuclei. Now, it is revealed that some of nuclei far from stability have exotic structures such as halo, skin, magicity loss, and new magic numbers, and many scientific efforts for understanding unstable nuclear structures are being made over the world. Because of the great advantages of electron scattering for the nuclear structure studies, actualization of electron scattering off unstable nuclei has been awaited.

Under these circumstances, we proposed a completely new target-forming technique, namely SCRIT (Self-Confining Radioactive isotope Ion Target) which makes electron elastic scattering off unstable nuclei possible [2]. After the success of the feasibility study of the SCRIT system [3, 4], we have developped the SCRIT electron scattering facility at RIKEN RI Beam Factory, Japan. In 2011 and 2012, a series of experiments has been performed, and the minimum required luminosity for elastic scattering, $\sim 10^{27}$ [/cm^2/s], was proved with using stable nuclei, ^{133}Cs and ^{132}Xe [5].

To realize electron scattering off unstable nuclei, a high resolution and wide acceptance electron spectrometer have also been developped. In this report, the first measurement of electron scattering with the electron spectrometer is reported.

§2. Experimental apparatus

2.1 overview of the facility

The facility consists of a 150-MeV injector racetrack microtron, an ISOL system, 700-MeV electron storage ring equipped with the SCRIT system, and the electron spectrometer. The electron beam energy can be controlled from 100 MeV to 700 MeV. The current of the stored electron beam is currently 350 mA at the maximum. Details of the electron accelerators and ISOL system can be found elsewhere [5, 6].

2.2 Electron spectrometer (WiSES)

The electron spectrometer (WiSES:Window-frame Spectrometer for Electron Scattering) consists of a dipole magnet [7], FDC (Front Drift Chamber), RDC (Rear Drift Chamber), plastic scintillator hodoscope, and a helium bag. Figure 1 shows a schematic view of WiSES and the SCRIT system.

The geometrical parameters and materials of the drift chambers are listed in Table1 and 2. By using FDC and RDC, we can reconstruct trajectories of scattered electrons in the magnetic field and estimate their momenta. Our goal of momentum resolution is δp/p $\sim 1\times10^{-3}$ for 300 MeV electron. The plastic scintillator hodoscope generates trigger signals. The solid angle of the spectrometer is evaluated to be about 80 msr by GEANT4 simulation. In order to reduce the multiple scattering of electrons, a beryllium plate of thickness 2 mm is used as the SCRIT chamber window, and the helium bag made of vinyl sheets of thickness 30 μm is installed between FDC and RDC.

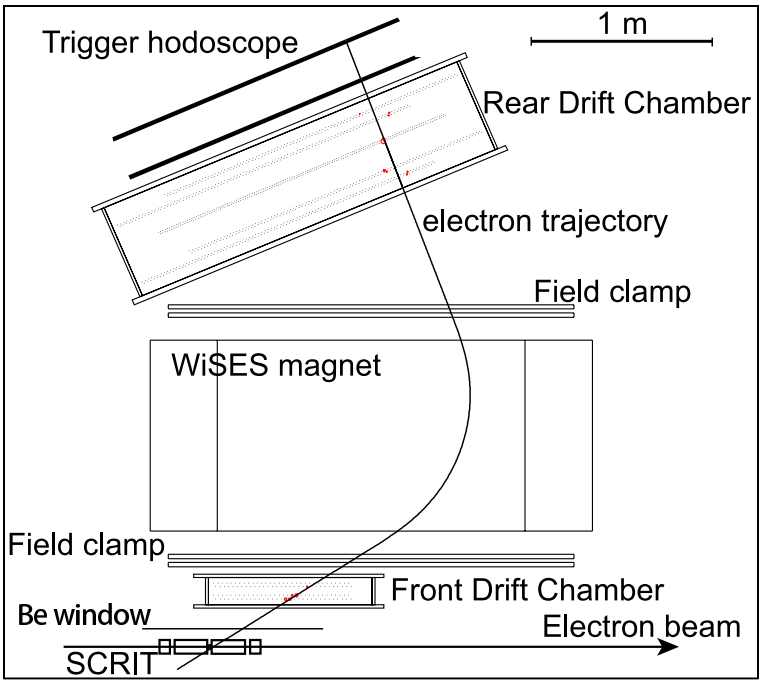

Fig.1. Schematic view of WiSES. A window of the SCRIT chamber is made of the beryllium plate of thickness 2 mm. The space between FDC and RDC was filled with helium. A trajectory between FDC and RDC was reconstructed by a Runge-Kutta calculation.

Figure 2 shows an acceptance map of WiSES which covers a wide angular region, 30$< \theta <$55 [deg.] and -10$< \phi <$10 [deg.]. At the forward region, especially, the vertical acceptance become large because

of a vertical focusing by the magnetic fringe field.

Table 1. Geometrical parameters of FDC and RDC.

	#readout	Layer configuration	Cell type	Cell size
RDC	1002	UU'VV'XX'UU'VV'	honeycomb	10 [mm]
FDC	128	XX'XX'	honeycomb	18 [mm]

Table 2. Materials of FDC and RDC.

	Window	Gas	Sense wire	Field (Shield) Wire
RDC	Al-mylar 25μm	He+CH_4 (50:50)	Au-W 30μmϕ	Au-Al 80μmϕ
FDC	Al-mylar 20μm	He+CH_4 (50:50)	Au-W 30μmϕ	Au-BeCu 100μmϕ

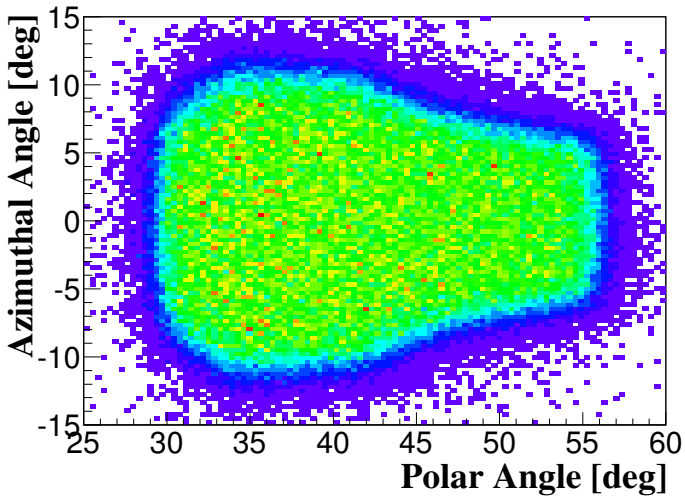

Fig.2. Acceptance map of WiSES evaluated by a GEANT4 simulation. It is assumed that electrons are scattered at the center of the SCRIT system. Because of the vertical focusing due to the fringe field at the entrance and exit of the magnet, the vertical acceptance become large in the forward region.

§3. Commissioning run

In December 2014, a commissioning experiment was performed to evaluate the perfomance of WiSES. Metal wires of diameter 50 μm made of tungsten and titanium were separately mounted as stable nuclear targets in the SCRIT chamber, and their position could be remotely controlled. Because their differential cross sections for elastic scattering are known, the perfomance of the spectrometer could be evaluated by checking the reproducibility of the differential cross sections. Figure 3 shows the inside of the SCRIT chamber.

The titanium wire was, unfortunately, found to be broken after the chamber baking, so the experiment was done with only the tungsten wire. The stored electron beam energy of 150 MeV was mainly used because the differential cross section has an inflection point in the acceptance region and reasonable magnitude for that beam energy. The differential cross section calculated by DREPHA code [8] which is a DWBA calculation is shown in Fig. 4.

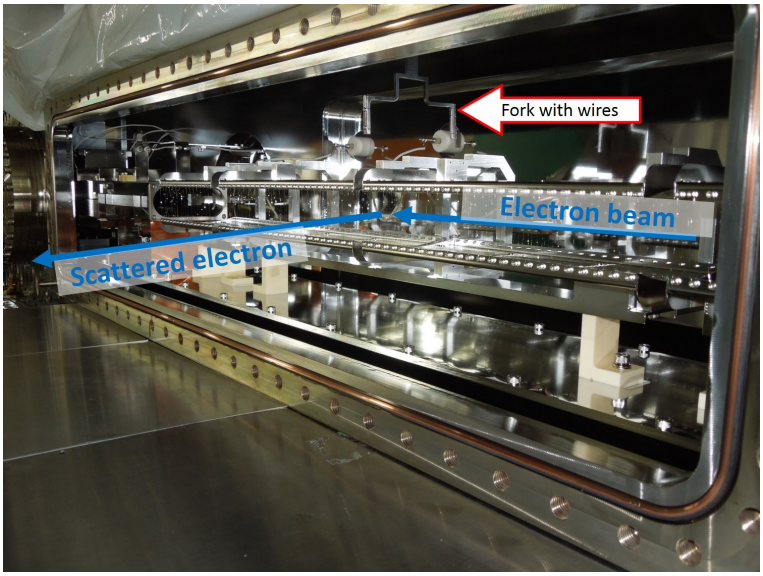

Fig.3. A picture of the SCRIT chamber's inside. The beryllium window was removed to replace the SCRIT electrode. The electron beam goes through the SCRIT system, and scattered by nuclear ions trapped along the beam line. During the commissioning experiments, the tungsten wire attached on the fork was used as a stable nuclear target.

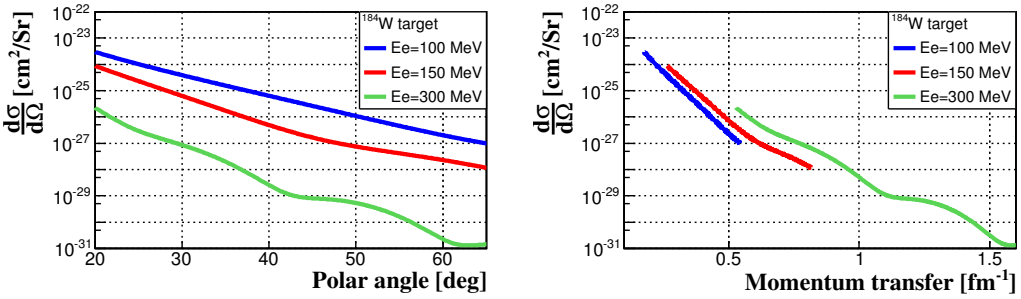

Fig.4. The differential cross sections for ^{184}W target calculated by DREPHA code. Left figure shows the angular dependence, and right one the momentum transfer dependence.

§4. Data analysis

Because RDC has tilted wires, the electron tracks can be three-dimensionally reconstructed. On the other hand, because FDC has only vertical wires, only horizontal information is available. Note that the time origin for FDC must be calculated using the flight length information between FDC and RDC since the trigger counter defining the timing was set beyond RDC.

The most probable trajectory between FDC and RDC is derived by the MINUIT program included in cern ROOT library. The position and direction differences from reconstructed tracks at RDC (δx_{RDC}, $\delta x'_{RDC}$, δy_{RDC}, $\delta y'_{RDC}$) and a momentum difference from that of the electron beam, $\delta p/p$, are used as parameters. Then, the position and direction difference at FDC (δx_{FDC}, $\delta x'_{FDC}$) can be calculated by

the 4th Runge-Kutta method. In the MINUIT, the following χ^2 is minimized,

$$\chi^2 = \frac{1}{N-1}\left[\left(\frac{\delta x_{RDC}}{\sigma_{x_{RDC}}}\right)^2 + \left(\frac{\delta x'_{RDC}}{\sigma_{x'_{RDC}}}\right)^2 + \left(\frac{\delta y_{RDC}}{\sigma_{y_{RDC}}}\right)^2 + \left(\frac{\delta y'_{RDC}}{\sigma_{y'_{RDC}}}\right)^2 + \left(\frac{\delta x_{FDC}}{\sigma_{x_{FDC}}}\right)^2 + \left(\frac{\delta x'_{FDC}}{\sigma_{x'_{FDC}}}\right)^2\right].$$

In present analysis, the magnetic field calculated by a finite element method, OPERA-3D, is used, and the magnitude of the field is scaled with the measured value by an NMR. After the minimization, the momentum of trajectory is defined, and the vertex point and direction on the beam line are derived from position and direction at FDC. Figure 5 shows the vertex point distributions. A peak at the center is corresponding to the tungsten wire, and one beside the target is a shadow of one side of the fork fixing the wire. Because the fork is located off the beam axis and the vertex points are reconstructed with an oblique angle, the shadow is projected upstream target. Two peaks at $V_Z = \pm 400$ [mm] are corresponding to entrance and exit electrodes of the SCRIT system. Structures at $V_Y = \pm 25$ [mm] are also the parts of the SCRIT system. The vertical and horizontal resolutions are evaluated to be 7.1 [mm] and 11.5 [mm] in σ, respectively.

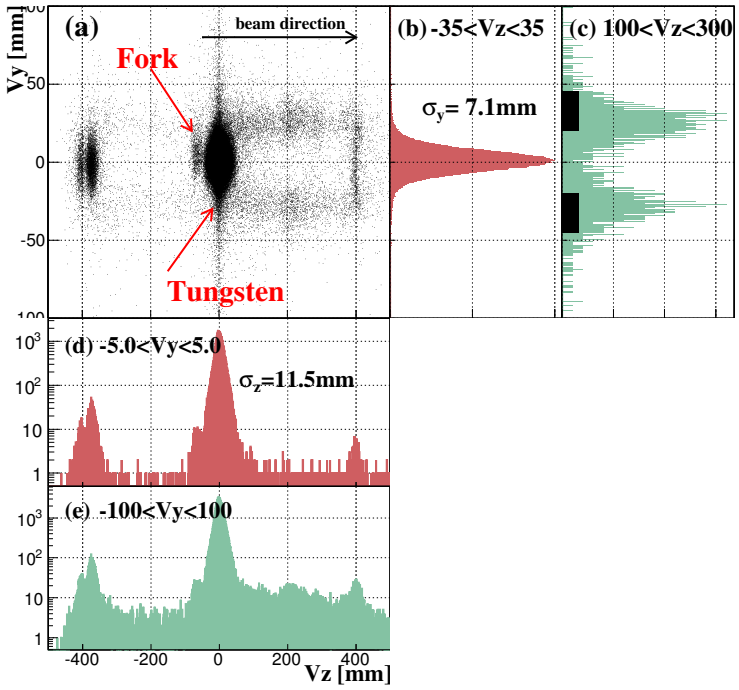

Fig.5. (a) Vertex point distribution reconstructed by FDC and RDC for the 150-MeV data set. A clear enhancement at the center corresponds to the tungsten target. A peak beside target is shadow of the fork fixing tungsten wire. Other structures correspond to the SCRIT electrodes. (b) A projection onto Vy within $-35 < Vz < 35$ [mm]. Vertical resolution is evaluated to be 7.1 [mm]. (c) A projection onto Vy within $100 < Vz < 300$ [mm]. Black blocks represent materials position of the SCRIT electrode. (d) A projection onto Vz within $-5 < Vy < 5$ [mm]. Horizontal resolution is evaluated to be 11.5 [mm]. (e) A projection onto Vz within $-100 < Vy < 100$ [mm].

Figure 6 shows a reconstructed momentum distribution with the vertex point cuts, -35<Vz<35 [mm] and -21<Vy<21 [mm]. A clear peak corresponding to the elastic scattering can be seen. Low momentum tail in Fig. 6 can be roughly explained by considering the effects of radiation (radiative tail) at the reaction and the energy deposit at the beryllium window. Figure 7 shows angular dependence of the momentum distributions. Black line shows the experimental results, and red one the simulation. In the simulation, the angular distribution was calculated by DREPHA code [8], and the radiative tail is included [9] in a particle generator of the simulation.

Although each simulation data is scaled by the number of events in Fig. 7, those scaling factors are slightly different each other so far. This is due to a lack of knowledge of geometries of the spectrometer and the magnetic field map. We need more study to decide the acceptance.

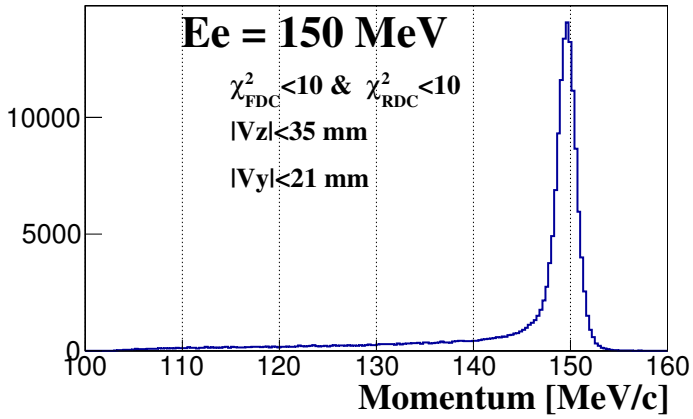

Fig.6. Reconstructed momentum distribution. Vertex point cuts, -35<Vz<35 [mm] and -21<Vy<21 [mm], are applied.

§5. Conclusions and future prospects

The SCRIT electron facility will realize electron scattering off unstable nuclei for the first time. The primary goal for this facility is to determine their charge density distributions by elastic electron scattering. Construction of the electron spectrometer, WiSES, completed and the commissioning experiment with a tungsten wire target was carried out in December 2014. The elastically scattered electrons were successfully identified, and the momentum distributions can be roughly explained by the simulation taking into account the angular distribution by the DWBA calculation and the radiative tail.

Because the target ion transport line from the ISOL system will be ready soon, the electron scattering experiment with series of the Xe isotopes and ^{132}Sn trapped by the SCRIT system will be performed this year.

Acknowledgment

This work is supported by Grants-in-Aid for Scientific Research (S) (Grands No. 22224004) from JSPS.

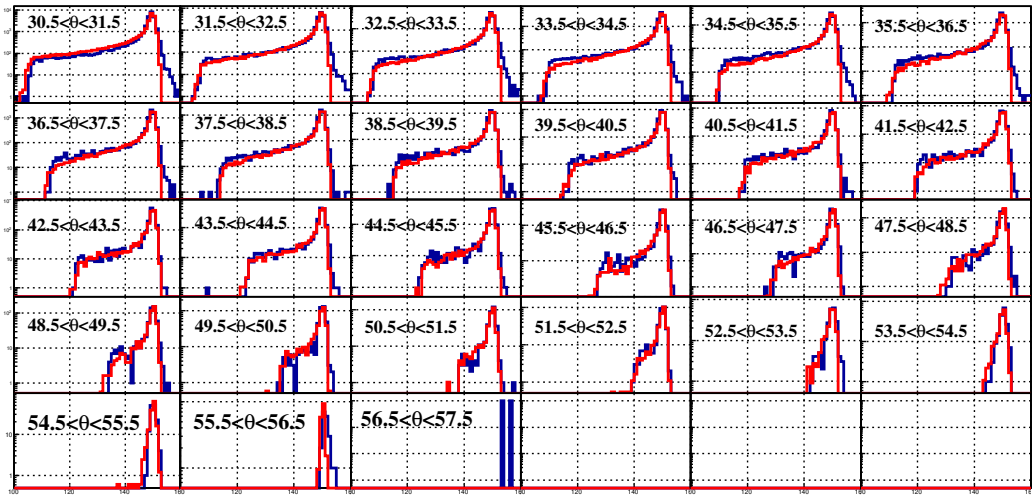

Fig.7. Angular dependence of the momentum distributions. Black histogram shows the experimental results. Red histogram shows the simulation taking into account the radiative tail and the energy deposit at the beryllium window. Each simulation is scaled by the surface of histogram.

References

[1] B. Hahn, D. G. Ravenhall and R. Hofstadter: Phys. Rev. 101 (1956) 1131.

[2] M. Wakasugi *et al.*: Nucl. Instr. and Meth. A 532 (2004) 216.

[3] M. Wakasugi *et al.*: Phys. Rev. Lett. 100 (2008) 164801.

[4] T. Suda *et al.*: Phys. Rev. Lett. 102 (2009) 102501.

[5] T. Suda *et al.*: ELPH Annual Report 2011-2013 Vol. 2, Tohoku University, 201 (2013).

[6] T. Ohnishi *et al.*: Nucl. Instr. and Meth. B 317 (2013) 357.

[7] T. Tamae *et al.*: ELPH Annual Report 2011-2013 Vol. 2, Tohoku University, 1 (2013).

[8] B. Drepher, DREPHA: a phase-shift calculation code for elastic electron scattering, communicated by J. Friedrich.

[9] J. Friedrich: Nucl. Instr. Meth. 129 (1975) 505.

(ELPH Experiment : #2775)

Radiochemical Determination of Photonuclear Reaction Yields for Photon Activation Analysis

Yasuji Oura[1], Yuki Yamaguchi[1], and Yoshihisa Tanaka[1]

[1]*Department of Chemistry, Tokyo Metropolitan University, Hachioji, 192-0397*

Relative reaction yields of (γ, n) reaction induced by bremsstrahlung of maximum end-point energy of 30 MeV and 20 MeV were reported for the target nuclides with mass number from 12 to 204. Relative yields were systematically increased with an increase of target mass number. With this correlation, any yield ratio is roughly able to be estimated.

§1. Introduction

We have been determining yields of photo nuclear reaction, especially (γ, n) reaction, to be valuable for photon activation analysis (PAA) because of a lack of useful data set of yields of (γ, n) and (γ, pxn) reactions induced by bremsstrahlung, which are used for an elemental analysis by PAA. Segebade et al. published a textbook on photon activation analysis in 1988 [1], in which induced radioactivity ratios normalized with radioactivity of ^{57}Ni produced by ^{58}Ni(γ, n) reaction are listed. As far as we know, this list is an only useful data set for PAA.

Our measurement was started at first with bremsstrahlung from an electron linac at Kyoto University Research Reactor Institute and yields of photo nuclear reaction producing radionuclides with a long half life ($>$ 8 hours) were determined [2, 3]. In FY2013 yields of photo nuclear reaction producing radionuclides with a short half life ($<$ 8 hours) as well as a longer half life for target nuclides with $\geq$ 35 of mass number were determined by using a linac at Research Center for Electron Photon Science (ELPH), Tohoku University.

In FY2014 we continuously determined photo nuclear reaction yields at ELPH and a main objective in this study was that yields for target nuclides with $<$ 40 of mass number was determined.

§2. Experimental

About 50 to 100 mg of high purity powder reagents such as C, KF, NaCl, Sc_2O_3, Cr, Fe_2O_3, Mn, Co, Cu, ZnO, Ga_2O_3, $SrCl_2$, Y_2O_3, ZrO_2, Mo, CdO, $Na_2H_4TeO_6$, KI, CsCl, Yb_2O_3, and PbO_2were wrapped in aluminum foil to be formed a disk (10 mmϕ) shape. For Au target and Ni monitor, 10 mmϕ of Au foil (0.01 mm thick) and 10 mmϕ of Ni foil (0.04 mm thick) were used, respectively.

The targets together with Ni monitors in a quartz tube were irradiated for 5 min and 10 min with bremsstrahlung beam of maximum end-point energy (E_0) of 30 and 20 MeV, respectively. After irradiation, target disks were subjected to gamma-ray spectrometry by a Ge detector. To reduce true coincidence

effect, a sample was placed at about 20 cm far from a detector. Since the bremsstrahlung beam flux was not determined, reaction yields normalized with one of ^{58}Ni(γ, n)^{57}Ni were calculated.

§3. Results and discussion

Target mass yield ratios of (γ, n) reactions for E_0 = 30 MeV and 20 MeV studied at ELPH are shown in Fig.1 1 together with data obtained in experiment #2757. (Some data obtained in experiment #2757 were made corrections.) Yield ratios of reactions producing meta-stable nuclides are shown separately by open circles. Yield ratios (^{58}Ni $\equiv$ 1) shown by solid circles generally increase smoothly with increasing target mass number from ^{12}C to ^{204}Pb both for E_0 = 30 and 20 MeV, although some yield ratios are scattered. On the contrary, yield ratios of reactions producing meta-stable nuclides shown by open circles are smaller than systematic yield ratios for ground state nuclides.

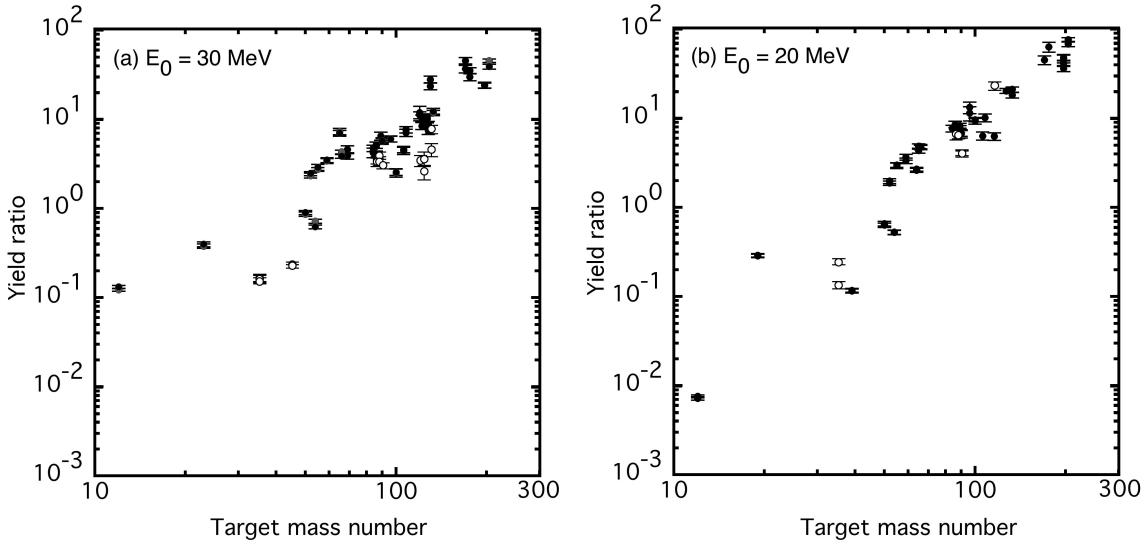

Fig.1. Target mass yield for (γ, n) reactions at E_0 = 30 MeV and 20 MeV. Relative yield values normalized with a yield of ^{58}Ni(γ, n)^{57}Ni are shown. Open circles show yield ratios of reaction producing a meta-stable nuclides

Yield ratios at E_0 = 20 MeV were roughly consistent with those at E_0 = 30 MeV except for some target nuclides. The yield ratio of ^{12}C(γ, n)^{11}C at E_0 = 20 MeV was about 10 times smaller than one at E_0 = 30 MeV. A high threshold energy (18.7 MeV) of ^{12}C(γ, n)^{11}C probably results in this low ratio observed at E_0 = 20 MeV, because bremsstrahlung with E_0 = 20 MeV have little photons inducing ^{12}C(γ, n)^{11}C reaction. Yield ratio of ^{39}K(γ, n)^{38}K at E_0 = 20 MeV was also about 10 times smaller than an estimated systematic yield. Since yield ratio of ^{39}K(γ, n)^{38}K at E_0 = 30 MeV was not determined yet, we should determine a yield ratio at E_0 = 30 MeV to confirm that the deviation for ^{39}K at E_0 = 20 MeV is caused by a difference of irradiation energy.

Specific radioactivity of ^{57}Ni induced by ^{58}Ni(γ, n) reaction for 1 hour at E_0 = 30 MeV and 20 MeV were about 48 kBq/mgNi and 6 kBq/mgNi, respectively. Using these specific radioactivity and induced radioactivity ratio values compiled by Segebade et al. [1], we can estimate radioactivity produced by (γ,

n) reaction at ELPH.

Although observed values at less than 50 of a target mass number are not enough, the systematic correlation between relative reaction yield ratio and mass number observed in this study can help an estimation of (γ, n) reaction yield ratios for various elements. We are going forward to determine yield ratios especially at less than 50 and apply yield ratios to photon activation analysis using an internal standard method.

Acknowledgment

The authors are indebted to Dr. H. Kikunaga and the accelerator operating crew members of Tohoku University for their invaluable cooperation in irradiation of samples and/or accelerator operation.

References

[1] C. Segebade *et al.*: Photon Activation Analysis, Walter de Gruyter (1988).

[2] Y. Oura *et al.*: CO2-1 in KURRI Progress Report 2012 (2013).

[3] Y. Oura *et al.*: CO5-5 in KURRI Progress Report 2013 (2014).

(ELPH Experiment : #2785)

Study on Metallofullerene Encapsulating Artificial Radio Element of Promethium

K. Akiyama and S. Miyauchi

Graduate School of Science and Engineering, Tokyo Metropolitan University, 1-1 Minami-Ohsawa, Hachioji, Tokyo 192-0397

The metallofullerenes encapsulating artificial radio element of Promethium (**Pm**) was studied. Promethium isotopes were produced from natural **Sm** by the photon irradiation at Research Center for Electron Photon Science, Tohoku University. The highest productivity of produced **Pm** isotopes was found to be that of ^{143}**Pm**. Promethium metallofullerene was produced by an arc discharge method. The valence state of **Pm** in the metallofullerene was strongly suggested to be trivalent from the similarity of HPLC elution behavior for **Pm** metallofullerenes with those for trivalent metallofullerenes.

§1. Introduction

Endohedral metallofullerenes (EMFs) are known as a clathrate compound and are attracting interest of the expectation for the potential application brought from their unique physical and chemical properties. The large number of studies about the EMFs have been reported, so far. Especially for the EMFs of lanthanide, it has been studied for a variety of encapsulated elements from the dawn of metallofullerene research. However, only metallofullerene of promethium (**Pm**) has been still missing [1]. It is well known that **Pm** is one of the artificial elements belonging to lanthanide elements and do not have any naturally occurred stable isotope. The chemical property of **Pm** is considered to be almost same as those of other neighboring lanthanides, actually most stable oxidation state in water is +3 similar to neighboring element of **Nd**. In general, **Pm** is produced from processing nuclear fuel and neutron irradiation of Nd in High Flux Isotope Reactor. However, ^{147}**Pm** produced by these methods is not suitable for the metallofullerene research because of their small γ-ray emission rate and their long half life.

Some of lanthanide elements in fullerene cage are reduced by the electron rich environment of fullerene inside. Actually, the valence state of **Sm**, **Eu**, **Tm**, and **Yb** in fullerenes is divalent even though most stable valence state of these elements in the air is trivalent [1]. **Pm** is located between **Nd** and **Sm** on the periodic table. Considering about the chemical properties of **Pm** as mentioned above, it is very important to investigate the valence state of **Pm** in fullerene cage from the view point of lanthanide chemistry. In this paper, we report the synthesis of **Pm** metallofullerene and their properties observed from elution behavior on the high performance liquid chromatography (HPLC).

§2. Experimental

2.1 Production of promethisum

To investigate the optimal condition for the irradiation and the produced radio activity of each **Pm** isotope from natural **Sm** isotopes by (γ, n) and (γ, p) reaction with bremsstrahlung converted from electron beam, we employed ^{nat}**Sm** oxide for the production of **Pm**. About 0.1 **g** of **Sm** oxide was sealed into quartz tube under reduced pressure. Photon irradiation of the samples was performed at Research Center for Electron Photon Science, Tohoku University with the beam energy of 20, 30, 40, and 50 **MeV** for 0.5 hours.

2.2 Pm Metallofullerene production

Irradiated **Sm** oxide was dissolved into concentrated nitric acid and ^{147}**Nd** radio tracer was added in this solution for the comparison. This solution was heat to dryness and then EtOH was added to dissolve resultant nitrate salts. This EtOH solution was dropped on a porous carbon rod with 10 **mm** diameters and 60 **mm** length to adsorb the nitrate salts and then dried. This porous carbon rod was placed in an electric tubular furnace and sintered at 700 ^{o}**C** under $\mathbf{N}_2$ gas flow. After the sintering, this rod was set into the fullerene generator as an anode for the arc discharge. The promethium EMFs were produced by the arc discharge method [2], [3] with DC 100 **A** under 60 **kPa** of He atmosphere. The produced soot containing **Pm** EMFs was dissolved to $\mathbf{CS}_2$ and then filtered to remove insoluble substance. After filtration, $\mathbf{TiCl}_4$ was added in this solution for the pre-separation of EMFs [4]. This pre-separated EMFs solution was evaporated to dryness and then toluene was added to dissolve fullerene species for the HPLC analysis.

2.3 HPLC analysis

The EMFs toluene solution was injected into HPLC system (Pump: Hitachi L-7110, flow rate: 3.2 **mL/min**, UV detector: GL-Science GL-7450, λ = 340 **nm**) with a HPLC column of Buckyprep (Nakarai tesque inc., size: 10 ϕ**mm** $\times$ 250 **mm**). The eluate from HPLC was collected for every 1 minute with the range from 38 to 90 minute of the retention time. The γ-ray from each fractionated sample was determined by a germanium semiconductor detector (SEIKO EG&G, GEM25P4).

§3. Results and Discussion

3.1 Produced radioactivity of Pm

Figure 1 shows γ-ray spectrum of irradiated $\mathbf{Sm}_2\mathbf{O}_3$ sample with beam energy of 50 **MeV**. From this spectrum ^{143}**Pm** (742 **keV**), ^{144}**Pm** (618 **keV**), ^{146}**Pm** (454 **keV**), ^{148m}**Pm** (630 **keV**), ^{145}**Sm** (61 **keV**), and ^{153}**Sm** (103 **keV**) were observed in this **Sm** sample. The productivities of each promethium isotope with each beam energy were listed in table 1. The highest radioactivity was found to be that of ^{143}**Pm** among these **Pm** isotopes. So the suitably longer half-life and higher radioactivity are required for the metallofullerenes synthesis, we employed ^{143}**Pm** for the metallofullerenes synthesis.

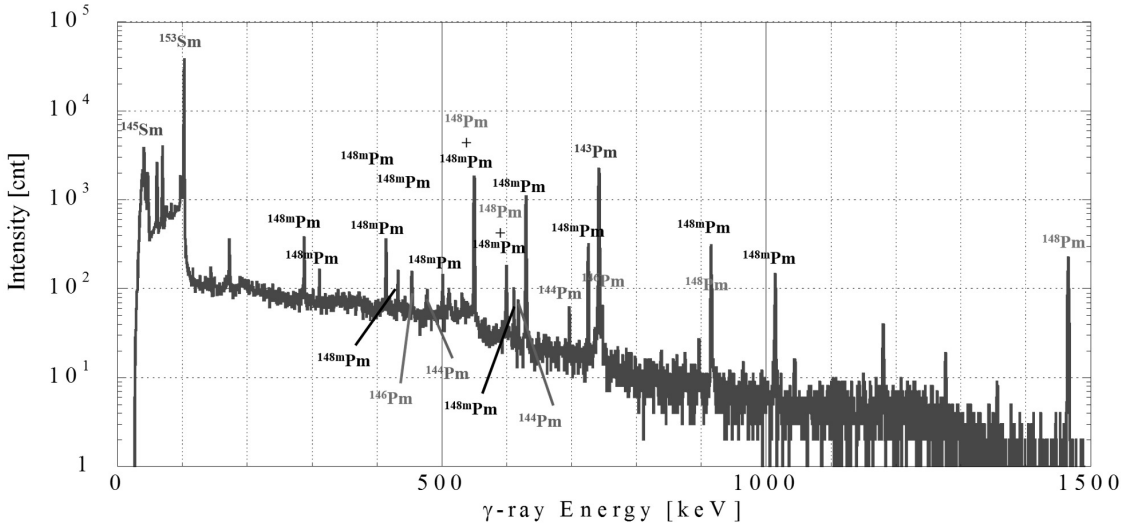

Fig.1. γ-ray spectrum of $\mathbf{Sm_2O_3}$ sample irradiated at the beam energy of 50 **MeV**.

Table 1. Determined productivity of each **Pm** isotopes.

Productivity [**Bq/g·h**]	Beam Energy [**MeV**]			
	20	30	40	50
^{143}**Pm**	$(1.2\pm0.1)\times10^3$	$(3.4\pm0.3)\times10^3$	$(8.8\pm0.9)\times10^3$	$(1.5\pm0.1)\times10^4$
^{144}**Pm**	NA	NA	NA	$(1.4\pm0.2)\times10^2$
^{146}**Pm**	NA	36 ± 7	$(1.5\pm0.3)\times10^2$	$(2.5\pm0.3)\times10^2$
^{148m}**Pm**	80 ± 7	$(6.1\pm0.3)\times10^2$	$(2.1\pm0.1)\times10^3$	$(3.9\pm0.2)\times10^3$
Target weight [**g**]	0.1069	0.1046	0.1064	0.1043

3.1.1 HPLC elution behavior of Pm EMFs

According to the above mentioned results, ^{143}**Pm** was produced by the 50 **MeV** photon irradiation of $\mathbf{Sm_2O_3}$ for 6 hours. Figure 2 shows observed radioactivity of ^{143}**Pm** and ^{147}**Nd** for each HPLC fraction together with obtained HPLC profile monitored by UV detector. The radioactivity of both ^{143}**Pm** and ^{147}**Nd** was only observed at 62 min. In general, the metallofullerene $\mathbf{M@C_{82}}$ encapsulating trivalent lanthanide, such as $\mathbf{La@C_{82}}$, $\mathbf{Ce@C_{82}}$, $\mathbf{Pr@C_{82}}$, $\mathbf{Nd@C_{82}}$, etc., have almost same chemical properties as each other and is observed around the HPLC retention time of 60 min under the studied condition (surrounded by an open square) [5]. On the other hand, metallofullerene encapsulating divalent lanthanide, such as **Sm** metallofullerenes, is known to be mainly eluted with empty fullerenes of $\mathbf{C_{84}}$ (around 40 min in this condition) [6], [7]. Considering about the HPLC elution behavior of trivalent and divalent metallofullerenes, our results strongly suggest that observed radioactivity of ^{143}**Pm** together with that of ^{147}**Nd** is derived from metallofullerene $\mathbf{Pm@C_{82}}$ encapsulating trivalent **Pm**.

Conclusion

Artificial element of **Pm** was produced by the photon irradiation at Research Center for Electron Photon Science, Tohoku University. The highest productivity of **Pm** isotopes were found to be that of

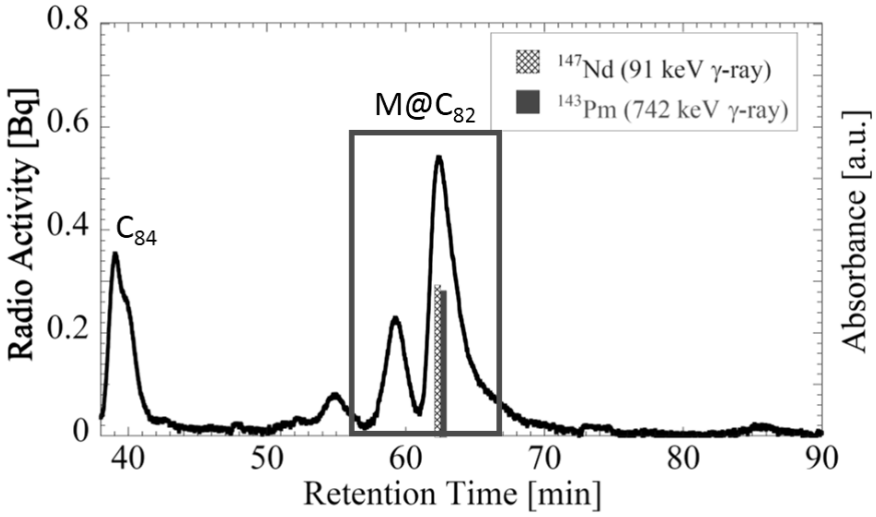

Fig.2. HPLC elution behavior of **Pm** metallofullerene.

^{143}**Pm** among the produced **Pm** isotopes in this study. Promethium metallofullerene was successfully produced by arc discharge method. The valence state of **Pm** in produced metallofullerenes was strongly suggested to be trivalent from the similarity of HPLC elution behavior for **Pm** metallofullerenes with those for trivalent metallofullerenes.

Acknowledgment

We deeply thank to the facility staffs of research center for electron photon science at Tohoku University for supplying the high-quality electron beam. And also we thank to Professor Hidetoshi Kikunaga and Doctor Kyo Tsukada for helping us in the sample irradiation.

References

[1] H. Shinohara: Rep. Prog. Phys. **63** (2000) 843.
[2] W. Kratschmer *et al.*: Nature **347** (1990) 354.
[3] K. Akiyama *et al.*: J. Am. Chem. Soc. **123** (2001) 181.
[4] K. Akiyama *et al.*: J. Am. Chem. Soc. **134** (2012) 9762.
[5] K. Akiyama *et al.*: J. Phys. Chem. A **104** (2000) 7224.
[6] K. Sueki *et al.*: Chem. Phys. Lett. **291** (1998) 37.
[7] T. Okazaki *et al.*: Chem. Phys. Lett. **320** (2000) 435.

(ELPH Experiment : #2787)

Measurements of thicknesses of Ce targets for (p,γ) reaction

Norikazu Kinoshita[1], Shingo Ueno[2]

[1]*Institute of Technology, Shimizu Corporation, Koto-ku, Tokyo 135-8530*

[2]*Graduate School of Natural Science and Technology, Kanazawa University, Kanazawa 920-1192*

The thicknesses of ^{136}Ce and ^{138}Ce targets for the cross section measurements of the proton capture reaction were determined using a photon activation analysis. The targets prepared with a plasma sputtering process were activated together with natural Ce as a standard using a bremsstrahlung with a maximum energy of 20 MeV. Activities of ^{139}Ce produced by the ^{140}Ce(γ,n) reaction were determined with a gamma-ray spectrometry. The thicknesses of ^{136}Ce and ^{138}Ce atoms were derived from the ^{139}Ce activities, number of ^{140}Ce atoms in the standard, and nominal isotopic abundance used for preparation of the targets.

§1. Introduction

Most elements heavier than iron are synthesized via neutron capture processes known as the *s* process and *r* process [1,2]. However, in the solar system, there are 35 neutron-deficient stable isotopes between Se and Hg with low isotopic abundance. These nuclei, not created by the *s* process or *r* process, are termed *p* nuclei. The *p* process, by which *p* nuclei are synthesized, proceeds via a photo-disintegration reaction [3-5], proton capture reaction [6,7], and neutrino process [8] on the pre-existing heavy *s* and *r* seed nuclei at temperatures between 1.5 – 3.5 GK. This high temperature can be obtained in explosive environments, such as in the O/Ne layers of Type II supernovae and in the deflagration flame fronts of Type Ia supernovae [9,10].

From the investigation of the isotopic abundance relative to atomic number Z, the *p* nuclei was found to possess approximately 1% abundance for lighter nuclei with Z = 34 – 50 and 0.01 – 0.3% abundance for medium and heavier nuclei with Z > 50 [11]. The *p* nuclei with a larger atomic number have thus a smaller isotopic abundance than that with a smaller atomic number. On the other hand, ^{92}Mo and ^{144}Sm with neutron magic numbers present abundances of 14.77% and 3.07%, respectively. The neutrino process is a strong candidate for the nucleosynthesis of ^{92}Nb, $^{136, 138}$Ce, and ^{138}La in the Type II supernovae [12,13]. The ^{12}C(^{12}C,p)^{23}Na reaction is one of candidate for the proton source in the Type Ia supernovae [6]. The neutrino process is hard to explain the greater abundance of ^{92}Mo and ^{144}Sm. Photo-disintegration as well as the proton capture reaction has a key for understanding isotopic abundances of the overall *p* nuclei.

Our group have measured cross sections of (p,γ) and (p,n) reactions on $^{136, 138}$Ce, $^{142, 143}$Nd, ^{144}Sm at energies between ~3 MeV and ~8 MeV for an accurate numerical computation of abundances of the *p* nuclei with mass numbers of 130 – 150 in the stellar environment. Thin targets of the isotopes will be bombarded by the proton beam for the cross section measurement. The thin targets were prepared using a molecular plating method

for isotopes of Nd and Sm [14]. Thicknesses of the targets are determined by measuring the solutions before and after the molecular plating with an ICP-MS. On the other hand, targets of the Ce isotopes cannot be prepared by the molecular plating method. Thus, we prepared the Ce targets with a plasma sputtering process [15]. The prepared target is hardly dissolved in HCl or HNO_3 because Ce is a refractory element; thickness of the target cannot be determined with an ICP-MS. Activation analysis which allows to determine trace amount without sample digestion, is only method for measurement of the refractory element. In the present work, we intended to determine the thicknesses of ^{136}Ce and ^{138}Ce target prepared by the plasma sputtering process using a photon activation analysis.

§2. Experiment

Targets of enriched isotopes of ^{136}Ce and ^{138}Ce with a diameter of 7 mm were prepared using a plasma sputtering process. The Ce isotopes were deposited on a 50-μm-thick aluminum foil with a purity of 99.999%. Several targets of ^{136}Ce and 10 mg of natural CeO with a purity of 99.9% sandwiched by Au foils as a flux monitors with a diameter of 7 mm and thickness of 10 μm, were encapsulated in a quartz tube. The stack for activation of ^{138}Ce was prepared with the same manner as that of ^{136}Ce mentioned above. A schematic diagram of the target stacks is shown in Fig. 1.

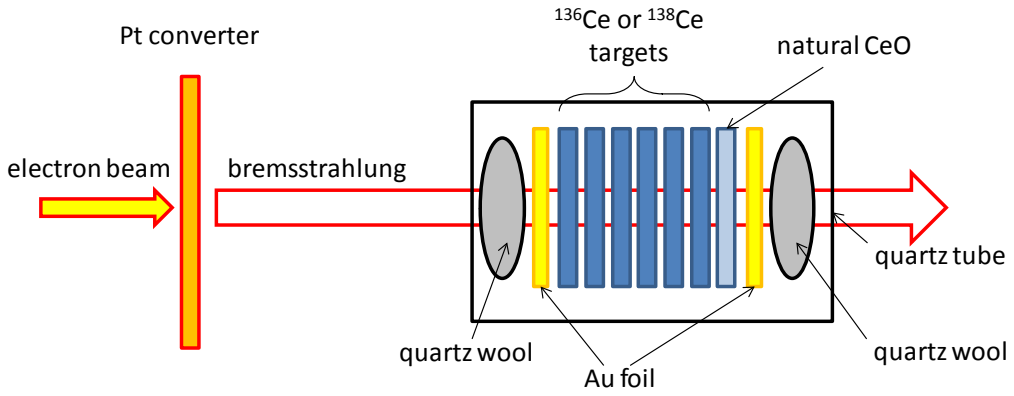

Fig. 1 Configuration of target stack for activation using bremsstrahlung

The isotopic compositions of ^{136}Ce and ^{138}Ce enriched isotopes are summarized in Table 1 together with a natural Ce. The Ce has 4 isotopes of mass numbers 136, 138, 140, and 142. In an photon activation analysis, activity of ^{139}Ce with a half-life of 137.6 days produced by (γ,n) reaction from the most abundant nuclei of ^{140}Ce is the best for a gamma-ray spectrometry. The ^{139}Ce can be produced by the ^{142}Ce(γ,3n)^{139}Ce reaction as well as the ^{140}Ce(γ,n)^{139}Ce reaction. The thresholds of ^{140}Ce(γ,n)^{139}Ce and ^{142}Ce(γ,3n)^{139}Ce are 9.2 MeV and 21.8 MeV, respectively. In the present work, bremsstrahlung with a maximum energy of 20 MeV was bombarded to suppress ^{142}Ce(γ,3n)^{139}Ce reaction.

Table 1 Isotopic abundances of ^{136}Ce, ^{138}Ce, and natural Ce.

	136	138	140	142
Ce-136	21.5%	1.3%	70.8%	6.4%
Ce-138	0.2%	12.9%	83.5%	3.4%
natural Ce	0.185%	0.251%	88.450%	11.114%

Electron beams with 20 MeV for an energy and 100 μA for a beam current were bombarded to a 2-mm-thick Pt converter. The stacks were individually activated for 4 hours with bremsstrahlung with a maximum energy of 20 MeV at 10 cm downstream of the Pt converter. After the activation, a gamma-spectrometry was carried out using an HPGe detector at Kanazawa University.

§3. Results and discussion

Thicknesses of six targets each of ^{136}Ce and ^{138}Ce were determined in the present work. As an example, gamma-ray spectra of natural Ce sample and one of targets of ^{136}Ce and ^{138}Ce are shown in Fig. 2. Gamma-ray peaks of ^{139}Ce produced by ^{140}Ce(γ,n)^{139}Ce reaction and ^{141}Ce produced by ^{142}Ce(γ,n)^{141}Ce reaction were identified in all samples. Many peaks observed in the ^{136}Ce sample were assigned to be ^{135}Ce. Other significant gamma-ray peaks were not identified in the spectra. Activities of ^{196}Au, as of the end of irradiation, in the Au monitor foils placed at downstream and upstream of samples were determined to be 23.8 ± 0.3 kBq/mg and 23.3 ± 0.3 kBq/mg for the ^{136}Ce stack, respectively. The activities in the ^{138}Ce stack were determined to be 24.9 ± 0.3 kBq/mg and 24.9 ± 0.4 kBq/mg. We ignored variation of the bremsstrahlung flux in the stacks because the ^{196}Au activity in the foils placed at downstream and upstream of samples agreed well each other within the errors.

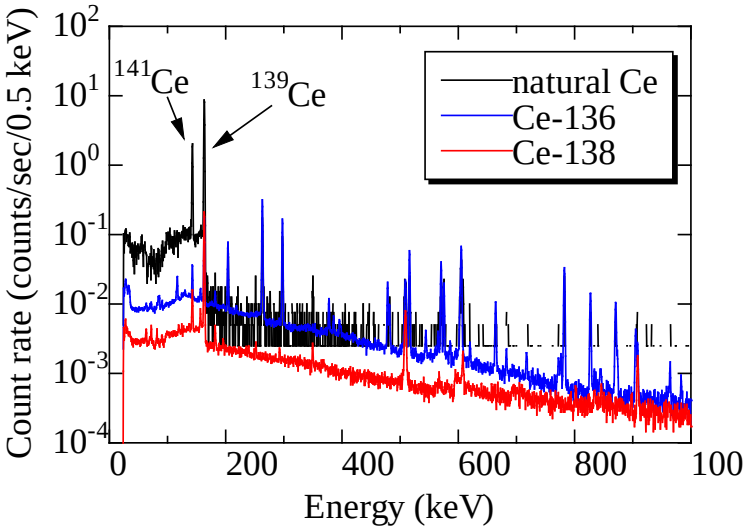

Fig. 2 Examples of gamma-ray spectra of natural Ce, ^{136}Ce, and ^{138}Ce activated with the bremsstrahlung.

Amounts of ^{140}Ce atoms in each sample were determined by comparing number of ^{140}Ce atoms in natural Ce as a standard, count rates of ^{139}Ce in target samples and natural Ce as a standard. Thicknesses of ^{136}Ce and ^{138}Ce in each target prepared by a plasma sputtering process were calculated using the amount of ^{140}Ce atoms and nominal isotopic abundance as shown in Table 1. The thicknesses of ^{136}Ce and ^{138}Ce targets are summarized in Table 2. Thickness of ^{136}Ce and ^{138}Ce in each target were determined to be ~10^{17} atoms/cm^2 for ^{136}Ce targets and ~10^{16} atoms/cm^2 for ^{138}Ce targets. We'll determine cross sections of (p,γ) and (p,n) reaction on these targets using proton energies of 3 – 8 MeV.

Table 2 Thicknesses of the Ce isotopes in ^{136}Ce and ^{138}Ce targets prepared by a plasma sputtering process

	^{136}Ce (atoms/cm^2)	^{138}Ce (atoms/cm^2)	^{140}Ce (atoms/cm^2)	^{142}Ce (atoms/cm^2)
^{136}Ce target-1	(5.00±0.15)×10^{16}	(3.02±0.09)×10^{15}	(1.65±0.05)×10^{17}	(1.49±0.04)×10^{16}
^{136}Ce target-2	(5.07±0.10)×10^{16}	(3.07±0.06)×10^{15}	(1.67±0.03)×10^{17}	(1.51±0.03)×10^{16}
^{136}Ce target-3	(1.44±0.03)×10^{17}	(8.71±0.19)×10^{15}	(4.74±0.11)×10^{17}	(4.29±0.10)×10^{16}
^{136}Ce target-4	(1.52±0.03)×10^{17}	(9.16±0.19)×10^{15}	(4.99±0.11)×10^{17}	(4.51±0.10)×10^{16}
^{136}Ce target-5	(7.03±0.14)×10^{16}	(4.25±0.08)×10^{15}	(2.31±0.04)×10^{17}	(2.09±0.04)×10^{16}
^{138}Ce target-1	(5.86±0.13)×10^{14}	(3.78±0.09)×10^{16}	(2.45±0.06)×10^{17}	(9.97±0.23)×10^{15}
^{138}Ce target-2	(7.39±0.13)×10^{14}	(4.77±0.09)×10^{16}	(3.08±0.06)×10^{17}	(1.26±0.23)×10^{15}
^{138}Ce target-3	(2.88±0.07)×10^{14}	(1.86±0.04)×10^{16}	(1.20±0.03)×10^{17}	(4.90±0.12)×10^{15}
^{138}Ce target-4	(5.78±0.11)×10^{14}	(3.73±0.07)×10^{16}	(2.41±0.05)×10^{17}	(9.83±0.19)×10^{15}
^{138}Ce target-5	(5.63±0.13)×10^{14}	(3.63±0.09)×10^{16}	(2.35±0.06)×10^{17}	(9.57±0.23)×10^{15}

Acknowledgement

We wish to acknowledge the assistance of Dr. Kikunaga and the staff of ELPH, Tohoku University, with regard to the activation experiment and operation of the electron linac. This work was supported in part by a Grant-in-Aid for Scientific Research Program of Japan Society for the Promotion of Science (26800161).

References

[1] M. Arnould *et al*.: Phys. Rep. **450** (2007) 97.

[2] F. Käppeler *et al*.: Rev. Mod. Phys. **83** (2011) 157.

[3] M. Rayet *et al*.: Astron. Astrophys. **227** (1990) 271.

[4] T. Rauscher *et al*.: Astrophys. J. **576** (2002) 323.

[5] H. Utsunomiya *et al*.: Nucl. Phys. A **777** (2006) 459.

[6] C. Travaglio *et al*.: Astrophys. J. **739** (2011) 93.

[7] H. Schatz *et al*.: Phys. Rep. **294** (1998) 167.

[8] C. Fröhlich *et al*.: Phys. Rev. Lett. **96** (2006) 142502.

[9] T. Plewa *et al*.: Astrophys. J. **612** (2004) L37.

[10] W. Rapp *et al*.: Astrophys. J. **653** (2006) 474.

[11] J. Magill *et al*.: *Chart of the Nuclides, 8th Edition*, (EC-DG JRC-ITE, Karlsruhe, Germany, 2012).

[12] T. Hayakawa *et al*.: Phys. Rev. C **77** (2008) 065802.

[13] T. Hayakawa *et al*.: Astrophys. J. Lett. **779** (2013) L9.

[14] W. Parker *et al*.: Nucl. Instr. Meth. **26** (1964) 61.

[15] A. Caillard *et al*.: Pow. Sour. **162** (2006) 66.

Profile measurement of bremsstrahlung at the irradiation site for RI production.

H. Kikunaga for Radioactive-Isotope Science Group[1]

[1]*Research Center for Electron Photon Science, Tohoku University, Sendai, 980-8578*

Profile measurement of bremsstrahlung at the irradiation site for RI production in the 1st Experimental Hall has been carried out by using a photon-activation method and autoradiography. The beam profile is essential for estimation of the amount of the radioactivity produced in the photo-nuclear reactions.

§1. Introduction

Radioactive isotopes are useful for various applications in medical, pharmaceutical, chemical, physical, and biological sciences. Most of those are artificially produced in nuclear reactions using accelerators. In the Research Center for Electron Photon Science, Tohoku University, many radioactive isotopes have been produced in the photo-nuclear reactions. However, the measurements of the production yields of the photo-nuclear reactions, which is essential for estimation of the amount of the radioactivity produced in a target, is difficult because that changes depending on the experimental setup. In many cases, the production yields have been determined as the ratio of the production yield of a monitor reaction and that of a reaction of interest. In other words, it is necessary for estimation of the amount of the radioactivity produced in the objective reactions to determine the production rate of the radioactivity produced in the monitor reaction with the experimental setup. In this report, we determined the production rate of a monitor reaction, namely ^{nat}Ni(γ,n)^{57}Ni reaction using our experimental setup.

§2. Experimental

The nickel foils with 10 μm thickness, 17 mm width, and 100 mm length were used as profile monitors. The 70 MeV electron linear accelerator at Research Center for Electron Photon Science, Tohoku University was used. The accelerator was operated at electron energies of 20, 30, 40, and 50 MeV with a mean current of around 0.1 mA. The monitor foils were set in the water-cooling irradiation system shown in Fig. 1 and were placed in 30 mm away from a platinum converter. The irradiation was carried out for 3 minutes for each foils.

After the irradiation, the monitor foils were subjected to autoradiography using an imaging plate to measure the distribution of radioactivities, which are mainly Ni-57 ($T_{1/2}$ = 35.6 h [1].) produced in the (γ,n) reaction. The imaging plate (BAS-IP-SR2025) was exposed by the monitor foils for 35 min after approximately 25 hours from the end of bombardment.

Based on the results of the autoradiography, samples pieces with 10 mm diameter around the center of the radioactivity distribution were punched out from the Ni monitor foils, and then were subjected to γ-ray spectrometry using a high-purity Ge semiconductor detector after 3 days from the end of bombardment.

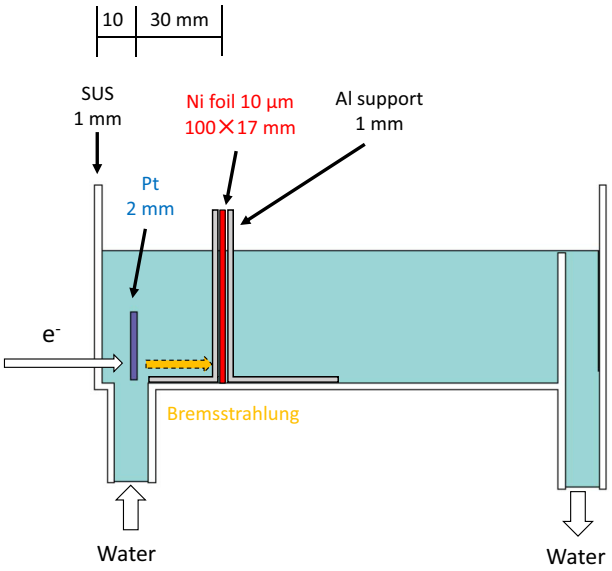

Fig.1. Schematic diagram of the water-cooling irradiation system in the 1st Experimental Hall.

§3. Results

Fig. 2 shows photographic images taken using an imaging plate with a read-out spatial resolution of 50 μm and their vertical and horizontal profiles. The photographic images are arranged in the order of the electron energies of 20 MeV, 30 MeV, 40 MeV, and 50 MeV from the left side. The beam size of the bremsstrahlung at the irradiation site for RI production became smaller up to 40 MeV, and was almost the same at 40 MeV and 50 MeV. A typical γ-ray spectrum for the Ni sample with 10 mm diameter is shown in the Fig. 2. The γ-peak of ^{57}Ni, which is the most prominent nuclide, ^{56}Ni, ^{57}Co, and ^{56}Co are observed in the spectrum. The specific activities of ^{57}Ni normalized to the mass of irradiated material, beam current and duration of irradiation are 1.97(6) $\times$ 10^3 Bq/mg/μA/h for 50 MeV, 1.23(4) $\times$ 10^3 Bq/mg/μA/h for 40 MeV, 6.00(17) $\times$ 10^2 Bq/mg/μA/h for 30 MeV, and 1.04(3) $\times$ 10^2 Bq/mg/μA/h for 20 MeV. Note that these values notably depends on the beam condition such as focus of the electron beam. Unfortunately, the operation parameters of the accelerator have not determined due to the instability of its aging components. To provide for a stable supply of radioactive isotopes, the stabilization of the accelerator is one of the necessary improvement.

References

[1] R. B. Firestone and V. S. Shirley: *Table of Isotopes, 8th ed.*(John Wiley and Sons, New York, 1996).

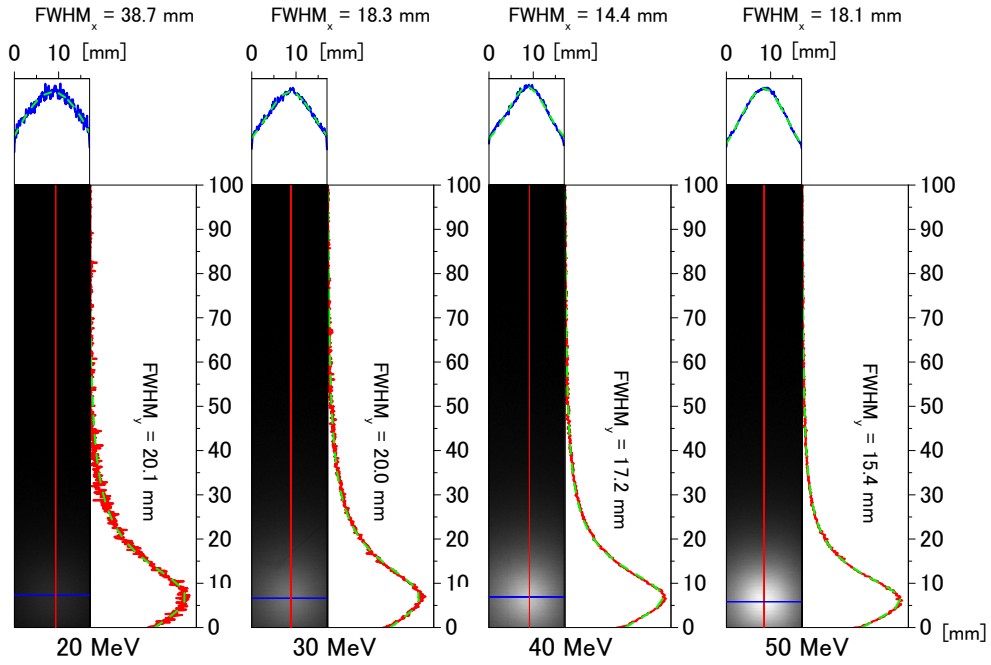

Fig.2. Photographic images taken using an imaging plate

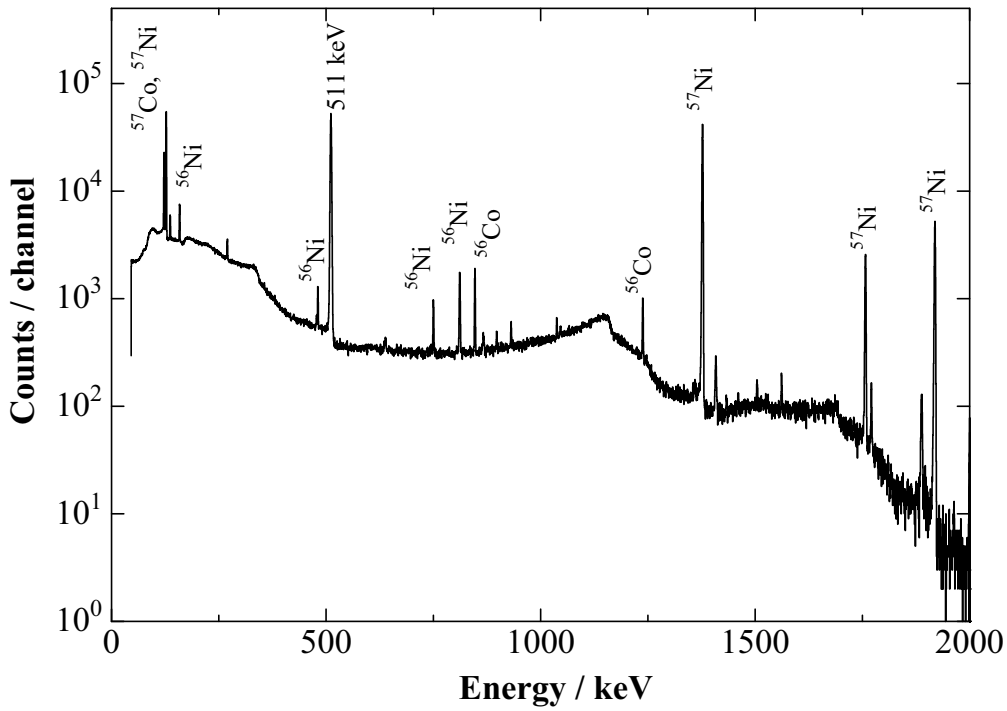

Fig.3. An example of a γ-ray spectrum of a Ni sample.

Status of Accelerator Facilities in FY2014

Accelerator group

Research Center for Electron Photon Science, Tohoku University, Sendai, 982-0826

The electron accelerator complex in this center consists of high intensity 60 MeV linac, 90 MeV injector linac, 1.3 GeV booster synchrotron and 50 MeV linac as a test accelerator for coherent THz source. Since the restart of user time in Dec. 2013, these machines have been well operated without any significant trouble. In this report, machine status and some improvements performed in FY2014 are presented.

§1. Low Energy Linac for RI Production

1.1 Overview of machine operation

Stable operating energies were 20, 30, and 50MeV with Linac repetition 300pps at the beginning. As users requested the irradiation of a target with various energies, it is now extended 10 to 50MeV by 10MeV steps, and the beam currents are ranged from 80 μA to 120μA depending on the operated energy. The machine is optimized for the mass production of radioactive isotopes that as much electron beam should be transported to the target. Currently, the electron beam with $\pm 10\%$ of the operating energy is transported to the experimental hall. Beam line at the experimental hall is only straight line along upstream an accelerator beam line to achieve maximum transportation. Overall layout of 60MeV Linac and the Experimental hall #1 is shown in Fig.1.

1.2 Guide electron beam to the target

The operation of 60MeV Linac is scheduled once or twice a week, and everything is shutdown while there is no operation. Currently, it takes about an hour for starting-up a Linac before it is ready to irradiate the target. Comparing to the past, starting-up time is greatly reduced by employing 2 profile monitors to the downstream of experimental beam line. Beryllium plate with ϕ30mm and 0.5mm thickness is used for tuning beam size and profile, and one with same dimension with ϕ10mm inner hole is used as a beam position monitor. Fig.2 shows Electron beam profile extracted to air (left), and its position before the target (right).

1.3 Beam extraction window

The electron beam is extracted from vacuum by 50 μm Ti film. The film was used to be sandwiched by flat surfaces of a conflate flange with ϕ 50mm inner opening and an air blower for cooling sealed with indium paste. The flange was outdated standard, and the detail of Ti film was unknown except

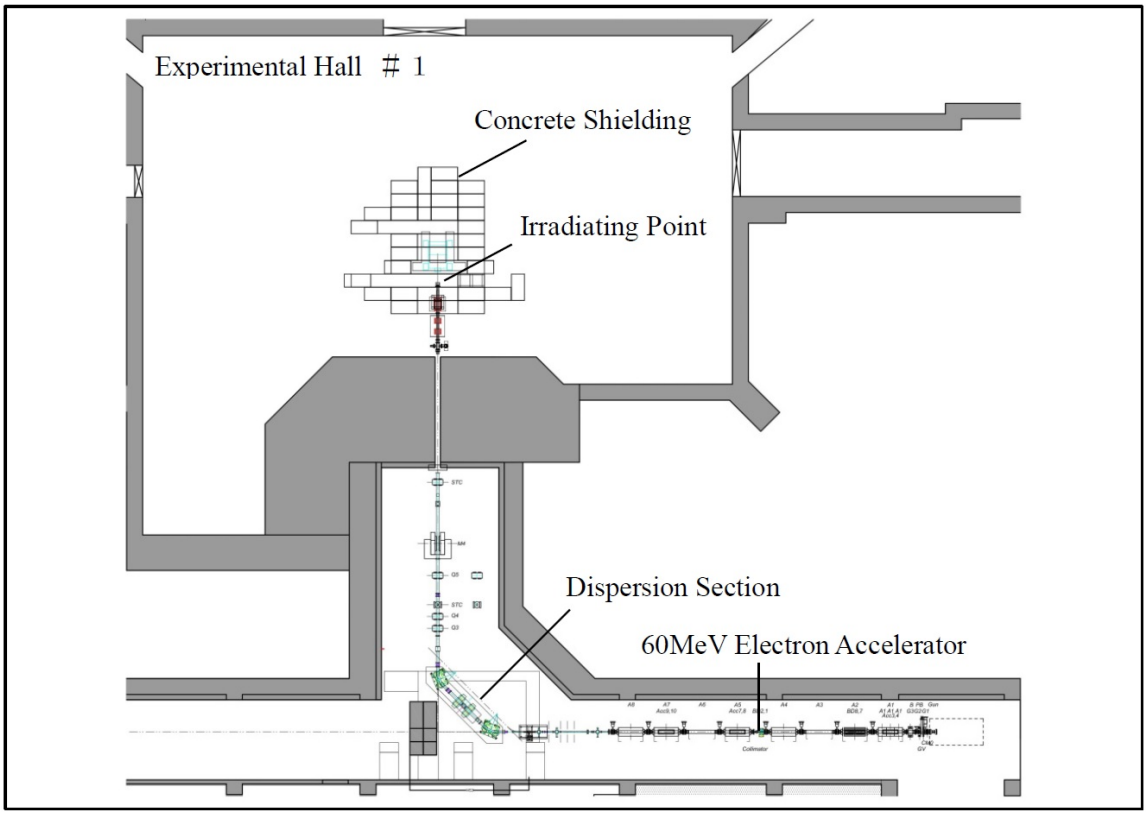

Fig.1. Overall 60MeV Linac and the Experimental hall #1.

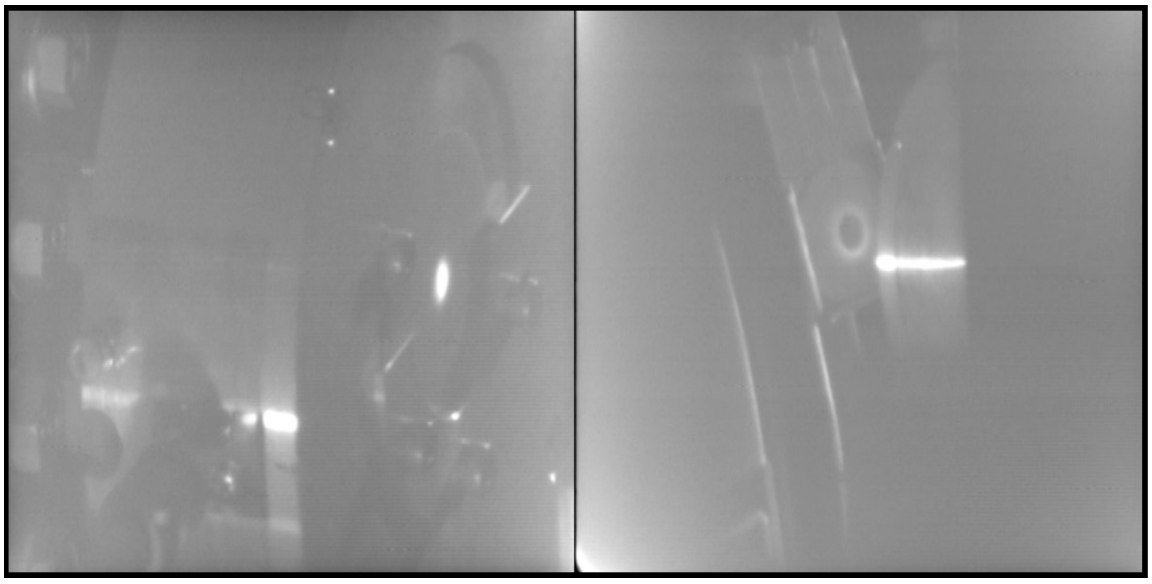

Fig.2. Electron beam profile extracted to air (left), and its position before the target (right).

its thickness. This is now redesigned and replaced with the ICF152 conflate flange with ϕ 50mm inner opening brazed Ti 99.5% film with 50μm thickness as shown in Fig.3.

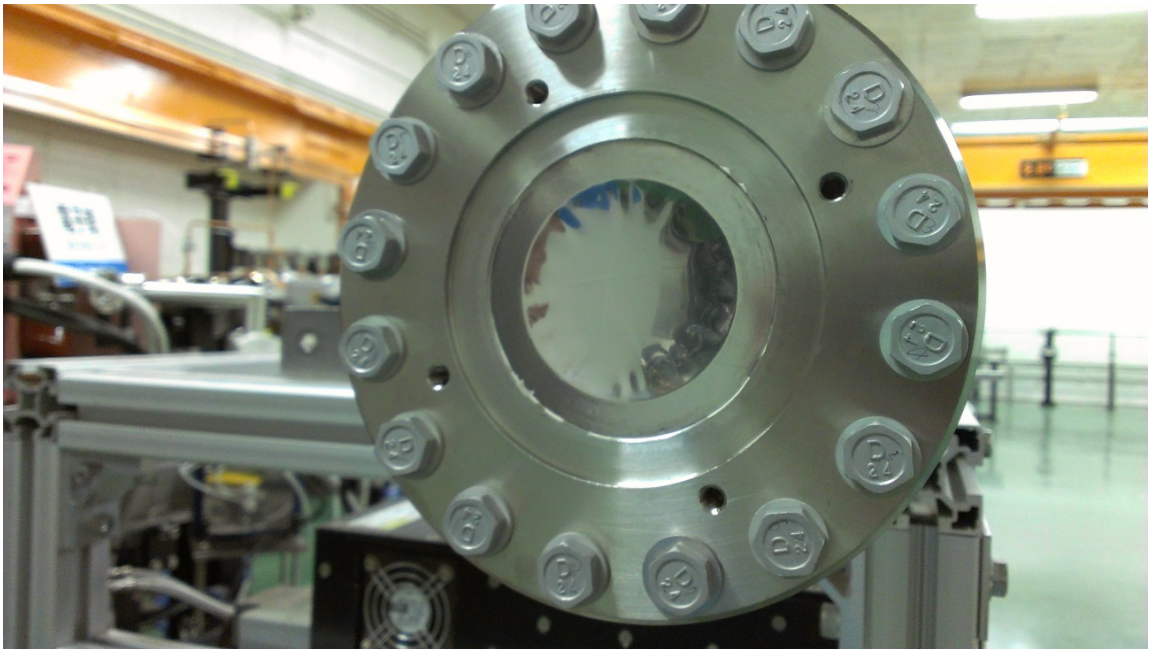

Fig.3. Beam extraction window brazed Ti film with 50μm thickness.

1.4 Beam Current Monitor

Beam current had been logged by an analog current averaging module and a digital current integrator. Now the system had been replaced with an oscilloscope averaging 4μs region of interest as shown in Fig.4. Logging is coincident with the control software of the Linac operation. It averages current per a pulse every a minute, and saves in user pc with time stamp. It would be automatically stopped when an operator turned off a beam. Fig.5 shows an example of the current log after Ti window.

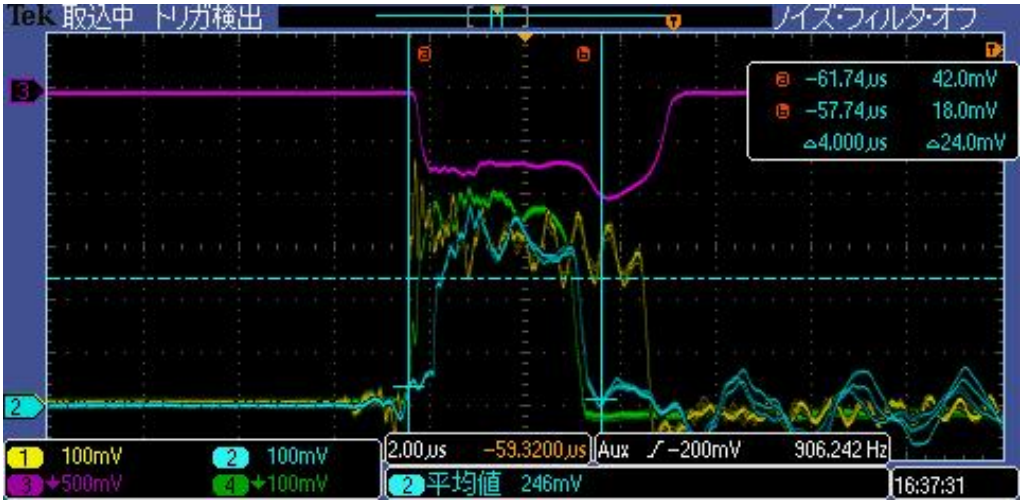

Fig.4. Typical beam pulse of 50MeV operation. Channel 1: beam current at gun exit, Channel 2: beam current after Ti window, Channel 3: RF pulse, and Channel 4: beam current after A8.

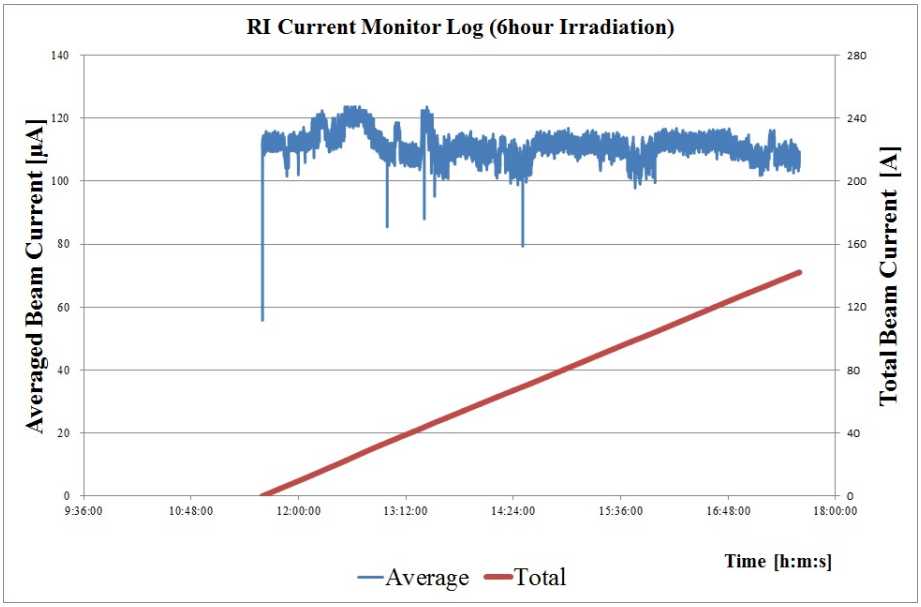

Fig.5. Current log after Ti window. Averaged (Blue) and total beam current irradiated (Red)

§2. 90 MeV Injector Linac for the 1.3 GeV Booster Synchrotron

The injector linac employs a thermionic cathode RF gun with an alpha magnet as its electron source. It consists of two independent cavities designed to manipulate the longitudinal phase space distribution of electron beam, named the Independently-Tunable Cells (ITC) RF gun. To obtain low emittance beam, a LaB_6 single crystal cathode with a diameter of 1.78 mm had been used.

In the last year, it was observed that an emission current of the gun periodically drop during beam operation, and it was not possible to perform a stable beam injection to the booster synchrotron. The problem was short circuit of the cathode heater line with the ground, and it was found that temporally revising an insulation of the cathode heater line helps to suppress this phenomena. For the best stable operation, it was decided to replace the RF gun.

New RF gun is almost equivalent to the previous gun except it employs a CeB_6 single crystal cathode with a diameter of 3.0 mm. It adopted the cathode of a size larger than the previous one. It is aim to suppress a back-bombardment effect for a stable operation without emittance deterioration. Main parameters of new ITC RF gun are shown in Table 1.

Table 1. Main parameters of ITC RF gun.

	Design	Measured
Resonant frequency [MHz] (cathode cell / accelerating cell)	2856 / 2856	2855.9906 / 2856.0063
Coupling (β)	$4 \sim 5$	4.185 / 4.4071
Quality factor (Q_0)	9500 / 12500	8721 / 12000
Shunt impedance (R_s) [MΩ]	> 0.8 / >1.1	0.886 / 1.271

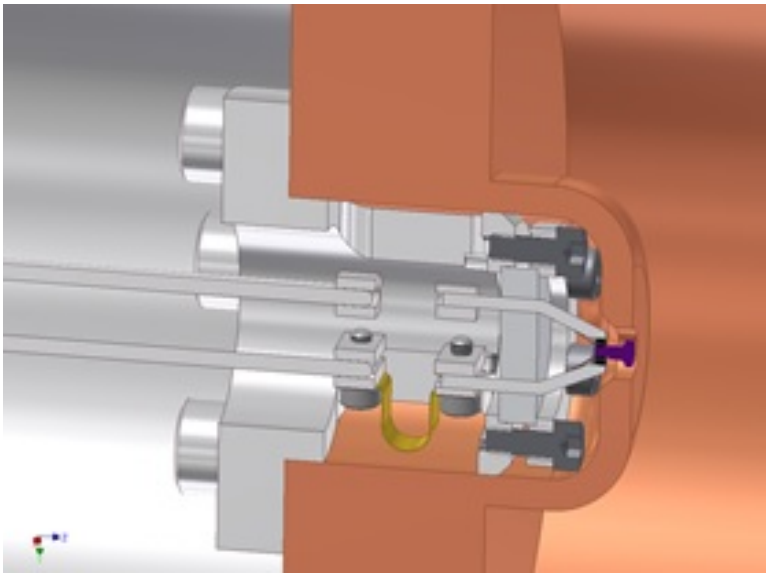

Fig.6. Cathode folder of new ITC RF gun

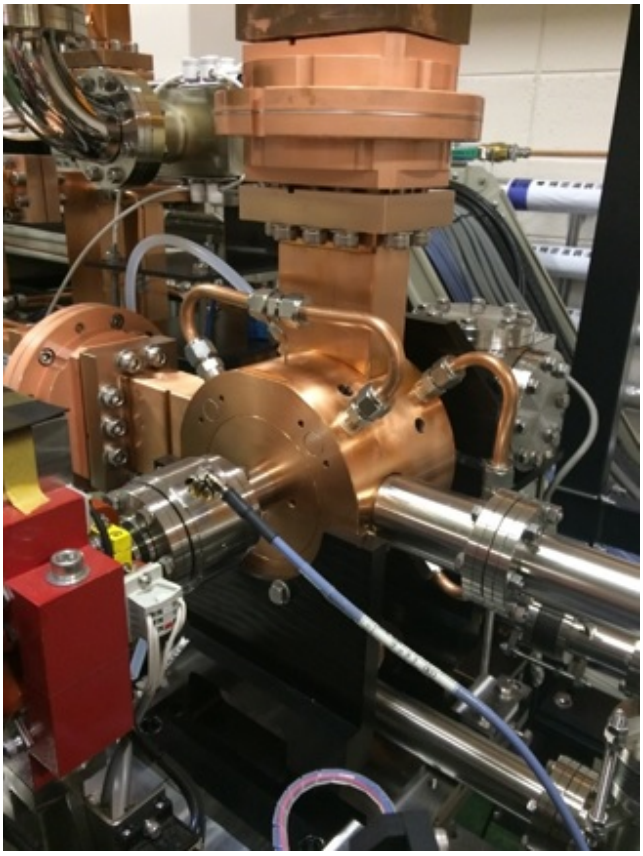

Fig.7. Installed new ITC RF gun cavities

In new RF gun, a ceramic insulator was inserted into the cathode heater line to prevent a short circuit. In order to absorb the extension and distortion of the cathode posts due to thermal expansion, a metal spring was also adopted to the heater line as shown in Fig.6. In addition, a cooling efficiency

of the RF gun cavities was improved by increasing the number of water channel to keep a constant temperature of gun cavities for stable operation. New RF gun had been installed in the injector linac in February, 2015 (Fig.7).

§3. 1.3 GeV Booster-storage ring (BST ring)

One of the main issues performed in FY2014 is the realignment of the synchrotron magnets. In the early beam commissioning of the BST ring, we had encountered the problem of very large bare COD (closed orbit distortion), and then we could not circulate the beam without the steering magnets in spite of the proper alignment accuracy. Furthermore, there are only four steering magnets for each plane to correct the COD, so that we were forced to move two dipole magnets (BM4 and BM5) to inside the ring more than 15 mm to mitigate the large horizontal COD. After some study to improve the machine performance, it was turned out that the wrong positioning in some combined function magnets caused this large COD. In some of these combined magnets to bring the sextupole component into the ring optics, the mechanical fiducial plate had unusually large rotation angles with respect to the beam axis, and thus these magnets should have to be positioned with their proper rotation angles. However, those magnets had been actually placed with wrong rotation angle due to the mishandling of the reference coordinates based on the fiducial plate, so that it caused the large offset of magnetic center for those combined function magnets. In order to correct such offsets realignment was performed for all magnets in February 2015, employing a laser tracker, Leica AT401, which has excellent resolution of the order of 0.01 mm for our typical situation.

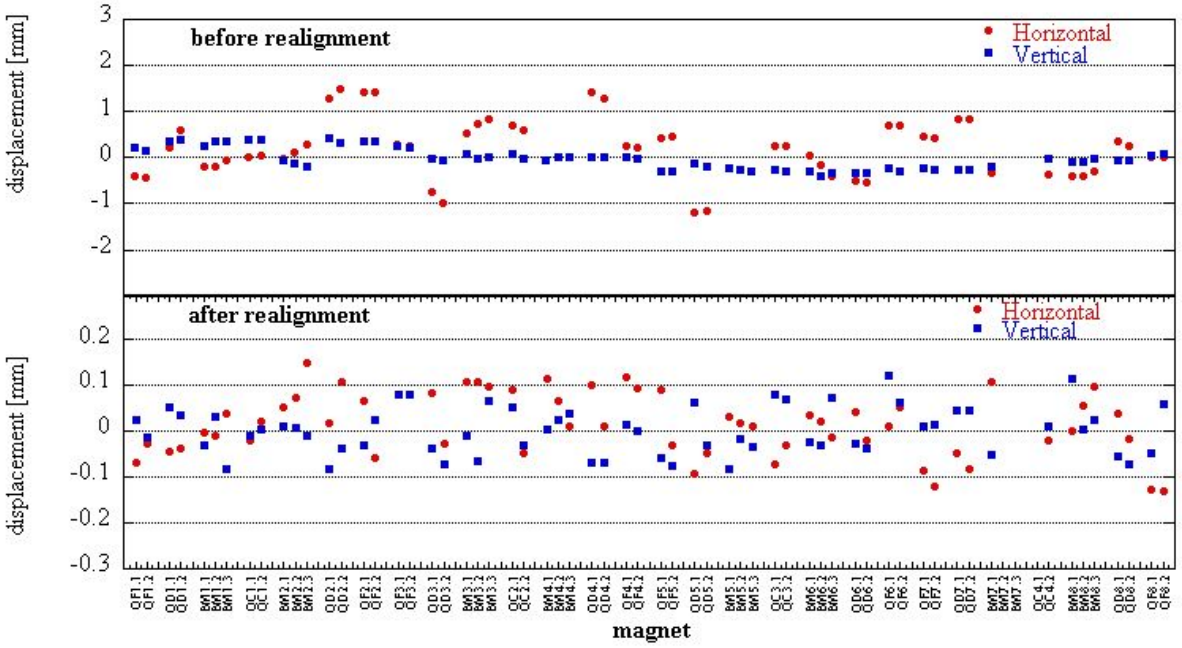

Fig.8. Displacements of the magnetic center in the reference coordinate system before (upper) and after realignment work (lower). Red and blue plot show horizontal and vertical displacement, respectively. Note that the vertical scale is ten times magnified in lower graph.

Fig. 8 shows displacements of the magnetic center with respect to the reference position, which were obtained by using the reflector target mounted on the fiducial plate of each magnet. All the positions of the magnets were carefully measured before moving those magnets for the realignment, and then it was confirmed that some combined function magnets had actually large horizontal offsets more than 1 mm, which were consistent with the estimated values to explain the measured bare COD. It can be also seen in the figure that the vertical displacement shows a sinusoidal behavior due to a slight tilt of the reference median plane. After the realignment work, displacements of the magnetic center were corrected fairly well as shown in Fig. 8. Note that the vertical scale is ten times magnified in lower graph.

Fig. 9 shows bare CODs before and after the realignment. As a result of the realignment, the large bare COD more than 20 mm in horizontal plane was improved drastically. Vertical bare COD was also improved, and thus it became possible to accelerate some fraction of the injected beam to the maximum energy without steering magnets. Two dipole magnets had been moved so far, however, those could go back to their original positions by the realignment. After the tuning work such as correction of COD, phase-space matching for injection beam and modification of ramp-up patterns of synchrotron magnets etc., the ring current more than 20 mA has been obtained with the maximum energy, which is almost the same as the operated current before the disaster in spite of the much lower injection energy.

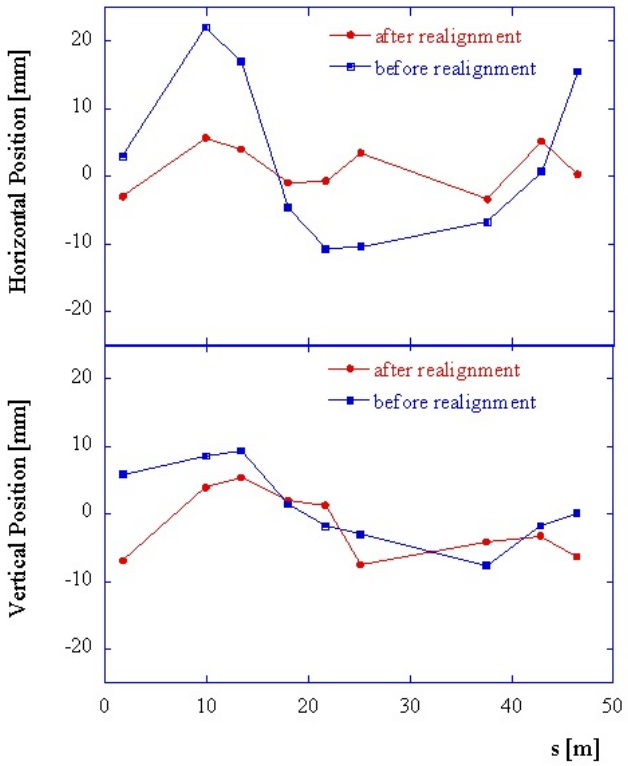

Fig.9. Measured bare CODs before (blue) and after realignment work (red). Upper and lower graph show horizontal and vertical CODs, respectively.

§4. Improvements of control system and other infrastructure

4.1 Control system

Because of the limited human resources, we employed LabVIEW and EPICS for the control system with CA-lab to minimize the workload for developing the control software. The CA-lab was written by Carsten Winkler and Tobias Hoff at BESSY and which can connect between LabVIEW and EPICS without any complicated procedure. Since all control and monitoring information of accelerators is shared on the control system via the EPICS, our control system has a high extensibility for beam diagnosis, data logging etc. Subcomponents of control system are roughly classified into the 90MeV injector, the beam transport line, the BST-ring and the utility. Figure 10 shows schematic block diagram of the control system. It is easy to find the failure component in the accelerator by the logged data of about 2000 items of accelerator components. A snapshot of the parameter and status of the accelerators are saved at intervals of every five minute, so that the condition of accelerator is easily understood. Since the maintenance of beam and the simple operation, such as beam on/off and change of duty cycle, have to be also done by certified beam user in addition to the accelerator stuff in our facility, it is also important to prepare a safe and simple program as a user interface for the less matured operator. Some tentative programs for the beam commissioning still survive presently, and then further development for stable, easier and reliable operation of the accelerator is ongoing.

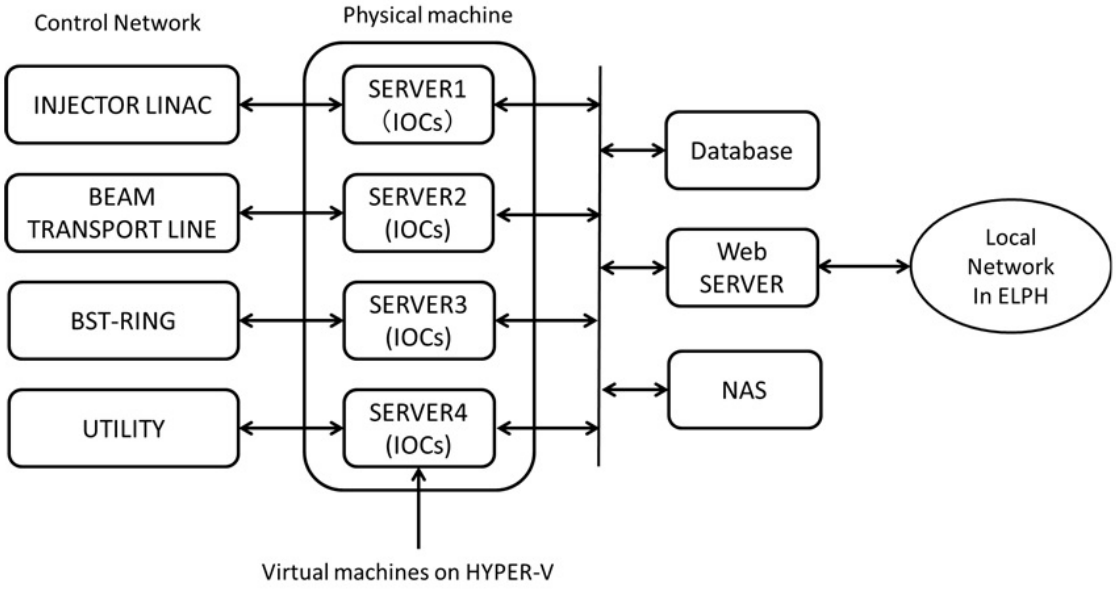

Fig.10. Servers are operated on the virtual machine using Hyper-V. Network-attached storage (NAS) is used for backup of control system. The Database server is built using MySQL. The Web server has distributed the information of accelerator status for users. To provide a secure operation of the accelerators, the control system accepts commands from specific consoles.

4.2 Substation

There were some old substations and switchboards in the facility which were used exceeding their service lives, and thus it was difficult to keep the required functions with such old equipment. These substations and switchboards provide the electric power for accelerators, experimental systems and air handling units. Therefore there will be significant impacts on a controlled area for radiation in the facility, if the power is cut off by failure of substation and switchboard. To avoid these potential risks on safety management, we decide to replace the substation and the switchboard. However, due to the limited budget for the replacement of such old equipment, we replaced the switchboard as a first step, because the old protection relays were severely deteriorated. Next, the old substations will be replaced as soon as possible for providing the stable electric power safely. Figure 11 shows the photograph of the new switchboard.

Fig.11. (left) Old switchboards, (right) new switchboards include vacuum circuit breakers (VCB) and protection relays. An automatic power factor controller is also installed in the new switchboard for proper control of the power system.

§5. Summary and prospect

Since the restart of user machine time on late in 2013, the approved beam time have been consumed smoothly as scheduled. There were some improvements in FY2014, i.e. improvement of monitor system, installation of new RF gun, realignment of synchrotron magnets, etc., which brought more reliable and stable operation for user. However there are still many instruments to be replaced or updated especially for 60 MeV linac and BST ring, and thus it is important to pursue such improvement work continuously not only to provide the regular user time but also to realize the higher performance of accelerator.

User Support Office Report in FY2014

T. Ishikawa on behalf of the user support office[1]

[1]*Research Center for Electron Photon Science (ELPH), Tohoku University, Sendai 982-0826, Japan*

The User Support Office coordinates communication between the users and scientists at ELPH and management of the beamtime. The bremsstrahlung photon beam came back in the end of December 2013 after the recovery of the 2011 Earthquake, and the experiments using electron/positron beams for testing detectors started. The high intense low energy electron beam also came back, and the experiments using it started in the end of February 2014.

§1. Introduction

Our facility has a 70 MeV electron linear accelerator (linac), a 1.3 GeV electron scynchrotron called BooSTer (BST) ring with a 93 MeV injector. The two accelerator complexes providing electron and photon beams are open to all the users in Physics and Chemistry. The beams utilized by the experimentalists can be classified into three:

1. high intense low energy electrons ($\sim 100\mu$ A and 30 MeV, $\sim 120\mu$ A and 50 MeV at maximum) for producing radio active sources (Radiochemistry),
2. high energy tagged photons for meson photoproduction experiments (Hadron Physics), and
3. positrons (electrons) with the variable energy for testing detectors (Particle Physics, Nuclear Physics, and so on).

There was basically no difference between the latter two in the operation of the accelerator complex.

§2. Beamtime operated

The radiation time was 124.2 hours for the RI linac operation and 1130.9 hours for the BST operation, and it was 1255.1 hours in total. The beam provided time (user beamtime) was 154.0 and 822.4 hours for the RI linac and BST operations, and it was 976.4 hours in total. When the several experimental groups use the beamtime, the user beamtime is doubly counted. Table 1 summarizes the radiation times, and user beamtimes in FY2014.

The 70 MeV electron linear accelerator was used for the Radiochemistry experiments. In November, producing extraordinary low energy beam down to 10 MeV was succeeded, and 10 MeV electrons were provided to users. The high voltage supply controller for the 70 MeV electron linear accelerator was out of order on 22nd in December. Low energy electron beams also came back in February after It was repaired.

Table 1. Radiation times, and user beamtimes in FY2014. They are given by the sum of the times that the beam is coming to the beamline, and that the beam is provided to the users. The beamtimes are classified to RI linac and BST used ones.

month	RI linac		BST	
	radiation (h)	user (h)	radiation (h)	user (h)
April	13.7	6.9	113.7	73.8
May	3.0	7.2	141.4	91.6
June	22.1	29.1	121.7	112.2
July	0.0	0.0	21.6	0.0
August	0.0	0.0	29.5	0.0
September	0.0	0.0	207.4	173.1
October	25.0	21.0	3.7	0.0
November	22.2	40.3	182.9	146.2
December	7.2	7.4	213.6	204.3
January	0.0	0.0	3.5	0.0
February	3.2	2.8	14.2	0.0
March	27.8	39.3	77.8	21.2
sum	124.2	154.0	1130.9	822.4

Many experiments for testing detectors (mainly tracking devices, and particle identification counters) were made by using bremsstrahlung photon beams from the synchrotron. Although these photon beams were provided in the parallel direction with respect to the temporary beamline ($dx/dz = +0.14$ mrad and $dy/dz = +0.01$ mrad) by moving the $\mathcal{R}$TAGX magnet and the beam dump [1], the photon beam intensity as a function of the spent time in a spill was different for different spills, namely the intensity of the provided positron beams was unstable. An increase of the intensity and an improvement of the profile of the positron beams especially for the low energy ones were made due to the installation of the vacuum chamber in March 2014 [2].

The meson photoproduction experiments did not start after the earthquake since the photon tagging counter was not ready for the photon beam course I and since a stable operation of the electron synchrotron was not available for the photon course II. The unstable operation was thought to come from the mis-alignment of the magnets for the synchrotron. The rotation of the quadrupole magnets were made step by step over this fiscal year to obtain a stable operation. The alignment of the magnets was adjusted from the beginning in February and the BM4 and BM5 magnets (20–30 mm shift for the temporary operation) became to the nominal position. The corresponding machine study was made in March, and also will be made in coming April of the next fiscal year. The injector linac was unstable in June, and it did not produce electrons for a while out of several minutes. It was replaced and this phenomenon disappeared after the summer shutdown. The R&D works were still on-going for the new tagging counters for the two photon beam courses. The modification of the control system of the booster ring was still continued.

Two experiments were proposed, and carried out for the undergraduate students. The first one (#2794: T. Ishikawa, ELPH, Tohoku University) is for the third school for giving an opportunity using an accelerator to young undergraduate students (Y. Sakemi) [3], which was supported by High Energy

Accelerator Research Organization (KEK) for the corporations between Tohoku University and KEK (H. Tamura). The second one (#2796: M. Miyabe, ELPH, Tohoku University) is for the education of the undergraduate students in ELPH.

§3. ELPH workshops and ELPH seminars

In this fiscal year, ELPH supported three ELPH workshops: the first on hadron physics (C009: H. Fujioka, Kyoto University), the second on an electromagnetic calorimeter for particle, hadron, nuclear, and cosmic ray physics (C010: K. Miyabayashi, Nara Woman University), and the third on an application of the high intense low energy electrons (C010: Y. Oura, Tokyo Metropolitan University). Three ELPH seminars were held at ELPH: the first one on the development of a silica-aerogel (H. Kawai, Chiba University, and M. Tabata, JAXA and Chiba University), the second one on the J-PARC hadron experiments (K. Ozawa, KEK), the third one on the exotic hadrons from the point of the lattice QCD (T. Hatsuda, RIKEN).

References

[1] T. Ishikawa *et al.*: Commissioning of the photon beamline II after the recovery of the earthquake in FY2013, ELPH annual report 2011–2013, 28 (2014).

[2] T. Ishikawa *et al.*: Commissioning of the positron beamline for testing detectors after the recovery of the earthquake in FY2013, ELPH annual report 2011–2013, 33 (2014).

[3] Y. Sakemi: Web site ⟨`http://cycgw1.cyric.tohoku.ac.jp/ sakemi/cyric2014.html`⟩.

放射線安全管理室報告

放射線安全管理室

Radiation Safety Report 2014

Radiation Control Office

2014 年度（平成 26 年 4 月～平成 27 年 3 月）

§1．変更申請

2014 年度の変更承認申請はない。

§2．個人管理

2.1 放射線業務従事者登録

190 人（東北大 68 人、学外 104 人、研究者以外 18 人）

2.2 個人被ばく管理

1 年間の個人被ばく線量 5 mSv 以下 190 人

2.3 教育訓練

定期講習

平成 26 年 6 月 13 日　新規教育 16 人、　再教育 83 人

特別講演の内容：独立行政法人理化学研究所　仁科加速器研究センター

安全業務室長　上蓑 義朋 氏

「加速器施設の安全ー理研 RIBF の経験からー」

不定期の講習

32 回　　112 人

§3．自主点検

年 2 回実施　　平成 26 年 9 月 16 日、平成 27 年 3 月 26 日

§4. 製造核種と数量

2014 年度に本加速器施設で製造され、共同研究に使用された放射性同位元素は次のとおり。

核種	数量 (kBq)
C-11	3000 kBq
N-13	3000 kBq
O-15	1000 kBq
Na-22	0.4 kBq
K-43	100 kBq
Sc-44m	110 kBq
Ca-47	201 kBq
Sc-47	200 kBq
V-48	100 kBq
Cr-51	1500 kBq
Fe-52	1000 kBq
Mn-54	1 kBq
Co-57	1729.5 kBq
Ni-57	4300 kBq
Co-58	50 kBq
Zn-65	451.9 kBq
Ga-68	200 kBq
Sr-85	59.5 kBq
Y-88	21.9 kBq
Mo-99	710 kBq
Cd-109	10.4 kBq
Sb-124	5 kBq
Ce-139	1 kBq
Pm-143	100 kBq
Nd-147	100 kBq
W-181	200 kBq
Au-196	2100 kBq
Pt-197	200 kBq
全 28 核種	計 20,451.6 kBq

§5. そ の 他

第一実験室のγ線エリアモニタを更新（2013 年度実施）

第二実験室，光源加速器棟にγ線エリアモニタを増設（2013 年度実施）

第一実験室，第二実験室，光源加速器棟に中性子エリアモニタを新設

List of Publication (論文リスト) (2014)

Papers Published in Refereed Journals

Backward-angle photoproduction of ω and η' mesons from protons in the photon energy range from 1.5 to 3.0 GeV

Y. Morino, Y. Nakatsugawa, M. Yosoi, M. Niiyama, M. Sumihama, T. Nakano, D.S. Ahn, J.K. Ahn, S. Ajimura, W.C. Chang, J.Y. Chen, S. Daté, H. Fujimura, S. Fukui, K. Hicks, T. Hiraiwa, T. Hotta, S.H. Hwang, K. Imai, T. Ishikawa, Y. Kato, H. Kawai, M.J. Kim, H. Kohri, Y. Kon, P.J. Lin, K. Mase, Y. Maeda, M. Miyabe, N. Muramatsu, H. Noumi, Y. Ohashi, T. Ohta, M. Oka, J.D. Parker, C. Rangacharyulu, S.Y. Ryu, T. Saito, T. Sawada, H. Shimizu, E.A. Strokovsky, Y. Sugaya, K. Suzuki, K. Tanida, A. Tokiyasu, T. Tomioka, T. Tsunemi, M. Uchida, R. Yamamura and T. Yorita

Prog. Theor. Exp. Phys. (2015) 013D01. DOI: 10.1093/ptep/ptu167

Experiments at ELPH/Sendai before and after the disaster

H. Shimizu

International Journal of Modern Physics 26 (2014) 1460092. DOI: 10.1142/S2010194514600921

Search for the K^-pp bound state via $\gamma d \to K^+\pi^-X$ reaction at E_γ =1.5-2.4 GeV

A.O. Tokiyasu, M. Niiyama, J.D. Parker, D.S. Ahn, J.K. Ahn, S. Ajimura, H. Akimune, Y. Asano, W.C. Chang, J.Y. Chen, S. Date, H. Ejiri, H. Fujimura, M. Fujiwara, S. Fukui, S. Hasegawa, K. Hicks, K. Horie, T. Hotta, S.H. Hwang, K. Imai, T. Ishikawa, T. Iwata, Y. Kato, H. Kawai, K. Kino, H. Kohri, Y. Kon, N. Kumagai, D.L. Lin, Y. Maeda, S. Makino, T. Matsuda, T. Matsumura, N. Matsuoka, T. Mibe, M. Miyabe, M. Miyachi, N. Muramatsu, R. Murayama, T. Nakano, Y. Nakatsugawa, M. Nomachi, Y. Ohashi, H. Ohkuma, T. Ohta, T. Ooba, D.S. Oshuev, A. Sakaguchi, C. Rangacharyulu, S.Y. Ryu, T. Sawada, P.M. Shagin, Y. Shiino, H. Shimizu, E.A. Strokovsky, Y. Sugaya, M. Sumihama, J.L. Tang, Y. Toi, H. Toyokawa, T. Tsunemi, M. Uchida, M. Ungaro, A. Wakai, C.W. Wang, S.C. Wang, K. Yonehara, T. Yorita, M. Yoshimura, M. Yosoi, R.G.T. Zegers

Phys. Lett. B728 (2014) 616-621. http://dx.doi.org/10.1016/j.physletb.2013.12.039

Development of High Intensity Laser- Electron Photon Beams up to 2.9 GeV at the SPring-8 LEPS Beamline

N. Muramatsu, Y. Kon, S. Daté, Y. Ohashi, H. Akimune, J.Y. Chen, M. Fujiwara, S. Hasegawa, T. Hotta, T. Ishikawa, T. Iwata, Y. Kato, H. Kohri, T. Matsumura, T. Mibe, Y. Miyachi, Y. Morino, T. Nakano, Y. Nakatsugawa, H. Ohkuma, T. Ohta, M. Oka, T. Sawada, A. Wakai, K. Yonehara, C.J. Yoon, T. Yorita, M. Yosoi

Nucl. Instr. Meth. A737 (2014) 184-194. http://dx.doi.org/10.1016/j.nima.2013.11.039

Performance test of a lead-glass counter for the J-PARC E36 experiment

Y. Miyazaki, S. Shimizu, S. Bianchin, C. Djalali, D. Gill, J. Jiang, M. Hasinoff, K. Horie, Y. Igarashi, J. Imazato, A. Ivashkin, M. Kohl, R. Narikawa, R. Pywell, S. Strauch, M. Tabata, A. Toyoda, H. Yamazaki, T. Yoshioka Nucl. Instr. Meth. A779 (2015) 13-17.

Time-of-Propagation Counter for the LEPS

C.J. Yoon, H. Hamano, T. Hotta, Y. Kasamatsu, Y. Morino, Y. Nakatsugawa, T. Nakano, T. Nam, H. Noumi, M. Oka, S.Y. Ryu, M. Yosoi, K. Matsuoka, Y. Kato, Y. Arita, K. Inami, K. Suzuki, T. Hyakawa, T. Iijima, R. Maeshima, S. Hirose, Y. Horii, M. Niiyama, Y. Nozawa, N. Muramatsu, E.A. Strokovsky, M. Uchida, M. Barrett, T. Browder, M. Jones, S. Korpar IEEE Transactions on Nuclear Science, Vol. 61 (2014) 2601.

Electron Scattering for Exotic Nuclei

T. Suda

Pramana Journal of Physics 83, 2014, 739-747.

Production of ^{88}Nb and ^{170}Ta for chemical studies of element 105, Db, using the GARIS gas-jet system

M. Huang, H. Haba, M. Murakami, M. Asai, D. Kaji, J. Kanaya, Y. Kasamatsu, H. Kikunaga, Y. Kikutani, Y. Komori, H. Kudo, Y. Kudou, K. Morimoto, K. Morita, K. Nakamura, K. Ozeki, R. Sakai, A. Shinohara, T. Sumita, K. Tanaka, A. Toyoshima, K. Tsukada, Y. Wakabayashi, A. Yoneda

Journal of Radioanalytical and Nuclear Chemistry 304 (2015), 845-849

Coprecipitation behaviors of Zr, Hf, and Th with Sm hydroxide for chemical study of element 104, Rf

Y. Kasamatsu, K. Toyomura, N. Shiohara, T. Yokokita, Y. Komori, A. Kino, T. Yoshimura, N. Takahashi, H. Haba, Y. Kudou, H. Kikunaga, T. Mitsugashira, T. Ohtsuki, K. Takamiya, A. Shinohara

Journal of Nuclear and Radiochemical Sciences 14 (2014), 7-11

Comparison of the decay constants of ^{51}Cr with metal, oxide, and chromate chemical states

H. Kikunaga, K. Takamiya, K. Hirose, T. Ohtsuki

Journal of Radioanalytical and Nuclear Chemistry 303 (2015), 1581-1583

Production of ^{256}Lr in the ^{249,250,251}Cf + ^{11}B, ^{243}Am + ^{18}O, and ^{248}Cm + ^{14}N reactions

N. Sato, T.-K. Sato, M. Asai, A. Toyoshima, K. Tsukada, Z.-J. Li, K. Nishio, Y. Nagame, M. Schaedel, H. Haba, S. Ichikawa, H. Kikunaga

Radiochimica Acta 102 (2014), 211-219

Production of ^{262}Db in the ^{248}Cm(^{19}F,5n)^{262}Db reaction and decay properties of ^{262}Db and ^{258}Lr

H. Haba, M. Huang, D. Kaji, J. Kanaya, Y. Kudou, K. Morimoto, K. Morita, M. Murakami, K. Ozeki, R. Sakai, T. Sumita, Y. Wakabayashi, A. Yoneda, Y. Kasamatsu, Y. Kikutani, Y. Komori, K. Nakamura, A. Shinohara, H. Kikunaga, H. Kudo, K. Nishio, A. Toyoshima, K. Tsukada

Physical Review C: Nuclear Physics 89 (2014), 024618/1-024618/11

Development of a Fast Timing Counter with a Monolithic MPPC Array

T. Nishizawa, Y. Fujii, H. Kanda, M. Kaneta, Y. Kasai, J. Kusaka, K. Maeda, S. Nagao, S.N. Nakamura, K. Tsukada, F. Yamamoto

IEEE Trans.Nucl.Sci. 61 (2014) 3, 1278-1283

Experiments with the High Resolution Kaon Spectrometer at JLab Hall C and the new spectroscopy of 12ΛB hypernuclei

L. Tang, C. Chen, T. Gogami, D. Kawama, Y. Han, L. Yuan, A. Matsumura, Y. Okayasu, T. Seva, V.M. Rodriguez, P. Baturin, A. Acha, P. Achenbach, A. Ahmidouch, I. Albayrak, D. Androic, A. Asaturyan, R. Asaturyan, O. Ates, R. Badui, O.K. Baker, F. Benmokhtar, W. Boeglin, J. Bono, P. Bosted, E. Brash, P. Carter, R. Carlini, A. Chiba, M.E. Christy, L. Cole, M.M. Dalton, S. Danagoulian, A. Danie, R. De Leo, V. Dharmawardane, D. Doi, K. giyan, M. Elaasar, R. Ent, H. Fenker, Y. Fujii, M. Furic, M. Gabrielyan, L. Gan, F. Garibaldi, D. Gaskel, A. Gasparian, E.F. Gibson, P. Gueye, O. Hashimoto, D. Honda, T. Horn, B. Hu, Ed V. Hungerford, C. Jayalath, M. Jones, K. Johnston, N. Kalantarians, H. Kanda, M. Kaneta, F. Kato, S. Kato, M. Kawai, C. Keppe, H. Khana, M. Koh, L. Kramer, K.J. Lan, Y. Li, A. Liyanage, W. Luo, D. Mack, K. Maeda, S. Malace, A. Margaryan, G. Marikyan, P. Markowitz, T. Maruta, N. Maruyama, V. Maxwel, D.J. Millener, T. Miyoshi, A. Mkrtchyan, H. Mkrtchyan, T. Motoba, S. Nagao, S.N. Nakamura, A. Narayan, C. Neville, G. Niculescu, M.I. Niculescu, A. Nunez, Nuruzzaman, H. Nomura, K. Nonaka, A. Ohtani, M. Oyamada, N. Perez, T. Petkovic, J. Pochodzalla, X. Qiu, S. Randeniya, B. Raue, J. Reinhold, R. Rivera, J. Roche, C. Samanta, Y. Sato, B. Sawatzky, E.K. Segbefia, D. Schott, A. Shichijo, N. Simicevic, G. Smith, Y. Song, M. Sumihama, V. Tadevosyan, T. Takahashi, N. Taniya, K. Tsukada, V. Tvaskis, M. Veilleux, W. Vulcan, S. Wells, F.R. Wesselmann, S.A. Wood, T. Yamamoto, C. Yan, Z. Ye, K. Yokota, S. Zhamkochyan, and L. Zhu

Phys.Rev. C90 (2014) 3, 034320

Grid pulser for an electron gun with a thermionic cathode for the high-power operation of a terahertz free-electron laser

S. Suemine, K. Kawase, N. Sugimoto, S. Kashiwagi, K. Furukawa, R. Kato, A. Irizawa, M. Fujimoto, H. Ohsumi, M. Yaguchi, S. Funakoshi, R. Tsutsumi, K. Kubo, A. Tokuchi, G. Isoyama

Nuclear Instruments and Methods in Physics Research A 773 (2015) 97-103

The high-power operation of a terahertz free-electron laser bsased on a normal conducting RF linac using beam conditioning

K. Kawase, R. Kato, A. Irizawa, M. Fujimoto, S. Kashiwagi, S. Yamamoto, F. Kamitsukasa, H. Osumi, M. Yaguchi, A. Tokuchi, S. Suemine, G. Isoyama

Nuclear Instruments and Methods in Physics Research A 726 (2013) 96-103

Local structure around Ge in lithium germanate glasses analyzed by AXS and EXAFS techniques

H. Arima, T. Kawamata, K. Sugiyama, J. Miner

Petrol. Sci. Adv. Pub., 2015 ,100, 141022f.

Temperature effect on screening effects and stopping power for low-energy d-6Li interaction in liquid Li

K.H. Fang, J. Zou, E. Yoshida, T.S. Wang and J. Kasagi

Europhys. Lett. 109 (2015) 22002-p1-p5; DOI: 10.1209/0295-5075/109/220

Papers Published in International Conference Proceedings

Investigation of Strangeness Photoproduction near the Threshold at ELPH, Tohoku University

M. Kaneta, B. Beckford, P. Bydžovský, T. Fujibayashi, T. Fujii, Y. Fujii, K. Futatsukawa, T. Gogami, Y. Han, O. Hashimoto, K. Hirose, K. Hosomi, R. Honda, A. Iguchi, T. Ishikawa, H. Kanda, Y. Kaneko, Y. Kasai, T. Kawasaki, C. Kimura, S. Kiyokawa, T. Koike, K. Maeda, N. Maruyama, M. Matsubara, K. Miwa, Y. Miyagi, S. Nagao, S.N. Nakamura, T. Nishizawa, A. Okuyama, M. Sotona, T. Tamae, H. Tamura, K. Tsukada, N. Terada, T. Wang, F. Yamamoto, T.O. Yamamoto, H. Yamazaki, and the NKS2 collaboration

JPS Conf.Proc. 1 (2014) 013045.

Study of Double Delta Photoproduction on the Deuteron in the Energy Region of $E_\gamma = 0.65 - 1.1$ GeV

F. Yamamoto, B. Beckford1, T. Fujibayashi, T. Fujii, Y. Fujii, K. Futatsukawa, T. Gogami, Y.C. Han, O. Hashimoto, K. Hirose, K. Hosomi, R. Honda, A. Iguchi, T. Ishikawa, H. Kanda, M. Kaneta Y. Kaneko, T. Kawasaki, C. Kimura, S. Kiyokawa, T. Koike, K. Maeda, N. Maruyama, M. Matsubara, K. Miwa, Y. Miyagi, S. Nagao, S.N. Nakamura, A. Okuyama, H. Shimizu, K. Suzuki, T. Tamae, H. Tamura, K. Tsukada, N. Terada, M. Ukai, T.S. Wang, and H. Yamazaki

JPS Conf.Proc. 1 (2014) 013072.

Measurement of Charged Pion Photoproduction at ELPH

H. Kanda, B. Beckford, T. Fujibayashi, T. Fujii, Y. Fujii, K. Futatsukawa, T. Gogami, Y.C. Han, O. Hashimoto, K. Hirose, K. Hosomi, R. Honda, A. Iguchi, T. Ishikawa, M. Kaneta, Y. Kaneko, Y. Kasai, T. Kawasaki, C. Kimura, S. Kiyokawa, T. Koike, K. Maeda, N. Maruyama, M. Matsubara, K. Miwa, Y. Miyagi, S. Nagao, S.N. Nakamura, T. Nishizawa, A. Okuyama, H. Shimizu, K. Suzuki, T. Tamae, H. Tamura, K. Tsukada, N. Terada, M. Ukai, T.S. Wang, F. Yamamoto, and H. Yamazaki

JPS Conf.Proc. 1 (2014) 013075.

Water/CH neutrino cross section measurement in J-PARC

T. Koga, N. Chikuma, F. Hosomi, M. Yokoyama, A. Bonnemaison,O. Drapier, O. Ferreira, M. Gonin, Th. A. Mueller,B. Quilain,I. Aizenberg, A. Izmaylov, I. Karpikov, M. Khabibullin, A. Khotjantsev, Y. Kudenko, S. Martynenko,A. Mefodiev,O. Mineev, T. Ovsjannikova,S. Suvorov, N. Yershov, T. Hayashino, A. K. Ichikawa, A. Minamino,K. Nakamura, T. Nakaya, K. Yoshida, Y. Seiya, K. Wakamatsu, K. Yamamoto, Y. Hayato

Proceedings of the 2nd International Symposium on Science at J-PARC, to be published.

Production of Quasi-monochromatic GeV Photons by Compton Scattering using Undulator X-ray Radiation at SPring-8

H. Ohkuma, A. Mochihashi, M. Oishi, S. Suzuki, K. Tamura, T. Nakano, N. Muramatsu, H. Shimizu

Proceedings of IPAC2014 (2014), 941-943.

The SCRIT Electron Scattering Facility

T. Suda, A. Enokizono, M. Hara, Y. Haraguchi, S. Ichikawa, K. Kurita, S. Matsuo, T. Ohnishi, T. Tamae, M. Togasaki, K. Tsukada, T. Tsuru, S. Wang, S. Yoneyama, M. Wakasugi
Proceedings of the 2nd Conference on " Advances in Radioactive Isotope Science 2014 ", in press

Study of Femtosecond Electron Bunch Generation at t-Acts, Tohoku University
S. Kashiwagi, F. Hinode, T. Muto, Y. Shibasaki, K. Nanbu, K. Takahashi, I. Nagasawa, S. Nagasawa, C. Tokoku, A. Lueangaramwong, H. Hama
Proc. of LINAC2014, (2014), pp1178-1181

Linear Focal Cherenkov-Ring Camera for Single Shot Observation of Longitudinal Phase Space Distribution for Non-Relativistic Electron Beam
K. Nanbu, H. Hama, F. Hinode, S. Kashiwagi, A. Lueangaramwong, T. Muto, I. Nagasawa, S. Nagasawa, Y. Shibasaki, K. Takahashi, C. Tokoku
Proc. of IBIC2014, (2014), TUPF26

Lattice Design of a Sub-nm Emittance Storage Ring for a Compact High Brilliant Light Source, SLiT-J
H. Hama and SLiT-J Design Team
Proceeding of Advanced Lasers and Their Applications Workshop, Seogwipo, Jeju, Korea, May 8-10, 2014, pp

Structural Study of Fe80B20 Amorphous Alloy by Anomalous X-ray Scattering Coupled with Neutron Diffraction
H. Arima, T. Kawamata, Y. Yokoyama, S. Kazumasa, T. Otomo
Proceedings of the J-PARC Symposium 2014, in press.

Invited Talk and Oral Presentations at International Conferences

Lattice Design of a Sub-nm Emittance Storage Ring for a Compact High Brilliant Light Source, SLiT-J
H. Hama
Advanced Lasers and Their Applications Workshop, Seogwipo, May 8-10, 2014, Jeju, Korea

Design strategy of a 3 GeV low emittance storage ring and a full energy injector linac for SLiT-J project
H. Hama
The 8th Asia Oceania Forum for Synchrotron Radiation Research (AOFSRR 2014), September 15 -18, 2014, Hsinchu, Taiwan

Design concept and expected performance of a 3GeV high brilliant synchrotron light source, SLiT-J
H. Hama
The 5th International Symposium of Advanced Energy Science, September 30 October 2. 2014, Uji, Kyoto

Conceptual Design of Variable Polarized THz Source Based on Crossed Undulator Superradiant
H. Hama
The 6th Asian Forum for Accelerators and Detectors (AFAD2015), January, 26-27, 2015, Hsinchu, Taiwan

Peculiar Physics by Intense Gamma Rays

H. Shimizu

International Workshop of Laser Compton Scatter Gamma Rays at Electron Storage Rings Nov. 7-11, 2014, Saskatoon, SK, Canada.

Search for the η'n bound state in the d(γ,p) reaction

N. Muramatsu

APS-JPS Joint Meeting, 7-11 Oct 2014, Hawaii

Baryon spectroscopy at ELPH and LEPS2

T. Ishikawa

APS-JPS Joint Meeting, 7-11 Oct 2014, Hawaii

Recent status and Physics overview at SPring-8 LEPS2/BGOegg

M. Miyabe

APS-JPS Joint Meeting, 7-11 Oct 2014, Hawaii

SCRIT Electron Scattering Facility

T. Suda

The 59th Annual Conference of the South Africa Institute of Physics, 7-11 July 2014,Johannesburg

Electron Scattering for Exotic Nuclei

T. Suda

The 38th Symposium on Nuclear Physics, January 6 11, 2015, Cocoyoc, Mexico

SCRIT Electron Scattering Facility

T. Suda

ARIS2014 (Advances in Radioactive Isotope Science)、June 1-6, 2014, Tokyo

Photonuclear Reaction of Exotic Nuclei at the SCRIT Electron Scattering Facility

T. Suda

International collaboration SAMURAI meeting、September 8-9, 2014, Sendai

SCRIT Electron Scattering Facility

K. Tsukada

APS-JPS Joint Meeting, 7-11 Oct 2014, Hawaii

A luminosity monitor for the SCRIT electron scattering facility

S. Yoneyama

The 13th CSN summer school, Wako, August 21-27, 2014

The $\gamma n \to K^0\Lambda$ photoproduction studied with an electromagnetic calorimeter complex FOREST

Y. Tsuchikawa

APS-JPS Joint Meeting, 7-11 Oct 2014, Hawaii

Screening potential of the d(d,p)t reaction in liquid In and Sn measured for 10 ED3+ 60 keV

Y. Honda

APS-JPS Joint Meeting, 7-11 Oct 2014, Hawaii

The performance study of an electromagnetic calorimeter BGOegg

Y. Matsumura

APS-JPS Joint Meeting, 7-11 Oct 2014, Hawaii

Near threshold $\Lambda(1115)$ photo production on a deuteron

B. Beckford

APS-JPS Joint Meeting, 7-11 Oct 2014, Hawaii

Proposal of an experiment about $\Lambda - n$ interaction via FSI in $\gamma + d$ reaction at ELPH, Tohoku University

M. Kaneta

APS-JPS Joint Meeting, 7-11 Oct 2014, Hawaii

Test Experiment of Velocity Bunching in Accelerating Structure toward THz Superradiant

H. Saito

Korea-Japan Workshop on Accelerator Based Advanced Light Sources 2015, Korea, March 13, 2015

学位論文 (電子光理学研究センター所属)

博士論文「Bose-Einstein Correlations between two neutral pions from photoproduction below 1.2 GeV」

何 慶華（HE Qinghua）, 平成 26 年, 東北大学

修士論文 「Development of Linear Focal Cherenkov-ring Camera for Direct Observation of Longitudinal Phase Space of Non-relativistic Electron Beam」

Anusorn Lueangaramwong, 平成 26 年, 東北大学

修士論文 「進行波加速構造中における速度集群法を用いた極短パルス電子ビーム生成の研究」

永沢　聡, 平成 26 年, 東北大学

修士論文 「制動輻射を用いた SCRIT 実験用ルミノシティモニタ」

米山 俊平, 平成 26 年, 東北大学

修士論文 「電磁カロリメータ BGOegg の性能評価」

松村 裕二, 平成 26 年, 東北大学

学位論文 (他機関所属)

修士論文「GeV 領域 γ 線ビームプロファイルモニターへの X 線ピクセル型検出器の応用研究」

尾関啓一,　平成 26 年度，東北大学

修士論文「中間子光生成反応実験に用いる内部標的型光子標識化装置の開発」

佐々木貴之,　平成 26 年度，東北大学

修士論文「J-PARC E07 実験用 momentum trigger に用いる ホドスコープ検出器の性能評価」

大植健一郎,　平成 26 年度，大阪大学

修士論文「ミューオン g-2/EDM 実験に用いるシリコン検出器の読み出し ASIC の開発」

調 翔平,　平成 26 年度，九州大学

修士論文「Development of a new GEM detector for a Cerenkov Counter application」

Hikari Murakami,　平成 26 年度，Graduate School of Science University of Tokyo

修士論文「セリウム同位体の（p, γ）反応実験及び陽子捕獲反応による p プロセスのモデル計算」

上野 慎吾,　平成 26 年度，金沢大学

修士論文「Research and development of a new neutrino detector for precise measurement of neutrino-nucleus cross sections」

Taichiro Koga,　平成 26 年度，東京大学

修士論文「三次元格子構造を持つ新型ニュートリノ検出器 WAGASCI の開発」

吉田健人,　平成 26 年度，京都大学

修士論文「KOTO 実験における高レート多線式比例計数管のための波形整形機能をもつ信号増幅器の開発」

上路 市訓,　平成 26 年度，京都大学

修士論文「KOTO 実験の中性ビーム中で荷電粒子を検出する Thin Gap Chamber の開発」

中桐 洸太,　平成 26 年度，京都大学

学士論文「光量子放射化分析のための光核反応収率の測定 (II)」

山口優貴,　平成 26 年度，首都大学東京

Steering Committee

2014

Hajime SHIMIZU*	ELPH
Hiroyuki HAMA	ELPH
Toshimi SUDA	ELPH
Fujio HINODE	ELPH
Shigeru KASHIWAGI	ELPH
Norihito MURAMATSU	ELPH
Hidetoshi KIKUNAGA	ELPH
Hirokazu TAMURA	Graduate School of Science
Teruya ISHIHARA	Graduate School of Science
Kazushige MAEDA	Graduate School of Science
Kouichi HAGINO	Graduate School of Science
Fuminori MISAIZU	Graduate School of Science
Yasushi KINO	Graduate School of Science
Asuka FUJII	Graduate School of Science
Atsuki TERAKAWA	Graduate School of of Engineering
Masaki FUJITA	Institute for Materials Research
Mihiro YANAGIHARA	Institute of Multidisciplinary Research for Advanced Materials
Keiichi EDAMATSU	Research Institute of Electrical Communication
Yasuhiro SAKEMI	Cyclotron and Radioisotope Center
Tetsuo TANIUCHI	Center for Interdisciplinary Research

* Chairperson

General Advisory Committee

2014

Hajime SHIMIZU*	ELPH
Hiroyuki HAMA	ELPH
Toshimi SUDA	ELPH
Hidetoshi KIKUNAGA	ELPH
Hirokazu TAMURA	Graduate School of Science
Yasushi KINO	Graduate School of Science
Yasuhiro SAKEMI	CYRIC
Tetsuo TANIUCHI	CIR
Hiroaki OHNISHI	RIKEN
Kyoichiro OZAWA	IPNS, KEK
Daisuke JIDO	Tokyo Metropolitan University
Takashi NAKANO	RCNP, Osaka University
Hideaki OHGAKI	IAE, Kyoto University
Shigemi SASAKI	HSRC, Hiroshima University
Atsushi SHINOHARA	Osaka University
Keisuke SUEKI	University of Tsukuba

* Chairperson

Program Advisory Committee

2014

Hiroyuki HAMA	ELPH
Toshimi SUDA	ELPH
Hidetoshi KIKUNAGA	ELPH
Kazushige MAEDA	Graduate School of Science
Satoshi N. Nakamura	Graduate School of Science
Asao YAMAMURA	Institute for Materials Research
Yasuhisa TAJIMA	Yamagata University
Toshiyuki TAKAHASHI *	IPNS, KEK
Tomoaki HOTTA	RCNP, Osaka University
Yoshihiko SHOJI	LASTI, University of Hyogo
Keisuke SUEKI	University of Tsukuba
Yasuji OURA	Tokyo Metropolitan University

* Chairperson

平成26年度前期採択課題一覧

課題番号	課　　題　　名	申込責任者
原子核関連分野		
2773	T2K 実験前置検出器施設に設置する新型ニュートリノ検出器のテスト実験	南野 彰宏
2776	大強度標識化ガンマ線ビームの透過率モニターの開発	石川 貴嗣
2777	FOREST 中央部における荷電粒子の極角測定装置の開発	石川 貴嗣
2779	Test experiment for new detector systems for the J-PARC E07 experiment	Sanghoon Hwang
2780	FOREST 検出器の再整備とアップグレード	石川 貴嗣
2781	J-PARC E34 実験 (ミューオン g-2/EDM 実験) のためのシリコン飛跡検出器および読み出し回路の性能評価試験	三部　勉
2782	J-PARK E21 実験 (COMET 実験) のためのチェレンコフトリガー検出器の開発	東城 順治
放射化学関連分野		
2774	光量子放射化法による 57 Co メスバウアー線源の作成	秋山 和彦
2775	光量子放射化分析のための光核反応収率の測定 (II)	大浦 泰嗣
2778	電子ライナックを用いた有用放射性トレーサー製造法の開発 II	菊永 英寿
随時申込		
2783	J-PARC E05 実験用 水チェレンコフ検出器の性能評価	永江 知文
2784	J-PARC E13 実験用 PWO 検出器読み出し回路の性能評価	鵜養 美冬

平成26年度後期採択課題一覧

課題番号	課　　題　　名	申込責任者
原子核関連分野		
2789	小型 Multigap Resistive Plate Chamber (MRPC) の性能評価	金田 雅司
2790	小型 ビームを用いた NKS2 実験スペクトロメータの動作確認及び調整	金田 雅司
2791	Photo-production of a Neutral Kaon and/or a Lambda Hyperon on a deuteron near the threshold	金田 雅司
2793	J-PARC E14 実験用サンプリングカロリメータの性能評価	外川 学
2794	偏向電磁石のコイル電流と運動量分析される電子の運動量 [学生実験]	石川 貴嗣
2795	300 MeV 標識化光子ビーム生成のテスト	石川 貴嗣
2796	シンチレーションカウンターの基本的特性の研究 [学生実験]	宮部 学
2797	FOREST アップグレードのための粒子識別用チェレンコフ検出器の開発	河合 秀幸
2798	J-PARC E21 実験（COMET 実験）のためのドリフトチェンバー（CDC) の開発	坂本 英之
2799	Feasibility study for Lambda-n interaction via FSI in gamma+d reaction	金田 雅司
2800	BM4 用 光子標識化装置の性能評価 （#2767 NKS2 実験のための光子ビームの調整の一部として）	神田 浩樹
2801	$500 < E_\gamma < 800$ MeV 領域における重水素原子核標的での $\pi^+\pi^-$ 光生成反応の研究	神田 浩樹
2802	チャームバリオン分光実験 (J-PARC E50) 用粒子識別チェレンコフ検出器のテスト実験	野海 博之
2803	光子ビームによる η メソン原子核の探索	石川 貴嗣
放射化学関連分野		
2785	光量子放射化法によるプロメチウム（Pm）内包金属フラーレンの合成を目的とした RI 製造	秋山 和彦
2786	軽元素の閾エネルギー近傍での光核反応断面積の測定	桝本 和義
2787	太陽系内同位体組成解明を目的とした光量子放射化分析	木下 哲一
2788	光核反応による核医学核種 Sc-44 の製造	福地 知則
2792	放射性バナジウム V-48 を用いたバナジウム・レドックスフロー電池の隔膜の研究 ～加速器による V-48 の製造～	白崎 謙次
随時申込		
2804	放射性ストロンチウムの化学分離法検討のための RI トレーサの製造	大浦 泰嗣